



Terms and Conditions of Use of Digitised Theses from Trinity College Library Dublin

Copyright statement

All material supplied by Trinity College Library is protected by copyright (under the Copyright and Related Rights Act, 2000 as amended) and other relevant Intellectual Property Rights. By accessing and using a Digitised Thesis from Trinity College Library you acknowledge that all Intellectual Property Rights in any Works supplied are the sole and exclusive property of the copyright and/or other IPR holder. Specific copyright holders may not be explicitly identified. Use of materials from other sources within a thesis should not be construed as a claim over them.

A non-exclusive, non-transferable licence is hereby granted to those using or reproducing, in whole or in part, the material for valid purposes, providing the copyright owners are acknowledged using the normal conventions. Where specific permission to use material is required, this is identified and such permission must be sought from the copyright holder or agency cited.

Liability statement

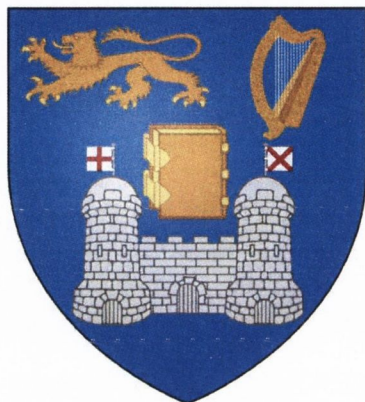
By using a Digitised Thesis, I accept that Trinity College Dublin bears no legal responsibility for the accuracy, legality or comprehensiveness of materials contained within the thesis, and that Trinity College Dublin accepts no liability for indirect, consequential, or incidental, damages or losses arising from use of the thesis for whatever reason. Information located in a thesis may be subject to specific use constraints, details of which may not be explicitly described. It is the responsibility of potential and actual users to be aware of such constraints and to abide by them. By making use of material from a digitised thesis, you accept these copyright and disclaimer provisions. Where it is brought to the attention of Trinity College Library that there may be a breach of copyright or other restraint, it is the policy to withdraw or take down access to a thesis while the issue is being resolved.

Access Agreement

By using a Digitised Thesis from Trinity College Library you are bound by the following Terms & Conditions. Please read them carefully.

I have read and I understand the following statement: All material supplied via a Digitised Thesis from Trinity College Library is protected by copyright and other intellectual property rights, and duplication or sale of all or part of any of a thesis is not permitted, except that material may be duplicated by you for your research use or for educational purposes in electronic or print form providing the copyright owners are acknowledged using the normal conventions. You must obtain permission for any other use. Electronic or print copies may not be offered, whether for sale or otherwise to anyone. This copy has been supplied on the understanding that it is copyright material and that no quotation from the thesis may be published without proper acknowledgement.

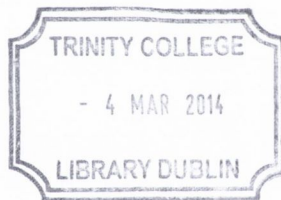
Charge and spin transport through organic semiconductors



Sandip Bhattacharya

A thesis submitted for the degree of
Doctor of Philosophy
School of Physics
Trinity College Dublin

September 2013



Thesis 10172

Declaration

I, Sandip Bhattacharya, hereby declare that this dissertation has not been submitted as an exercise for a degree at this or any other University.

It comprises work performed entirely by myself during the course of my Ph.D. studies at Trinity College Dublin. I was involved in a number of collaborations, and where it is appropriate my collaborators are acknowledged for their contributions.

A copy of this thesis may be lent or copied by the Trinity College Library upon request by a third party provided it spans single copies made for study purposes only, subject to normal conditions of acknowledgement.

S Bhattacharya

Sandip Bhattacharya

September, 2013

Abstract

Over the past decade a great body of research has been devoted to the field of *organic spintronics*. This is primarily because of its potential to open new ways to cheap, low weight, mechanically flexible, chemically inert and bottom up fabricated spin-devices for high density data storage and logic applications. The main advantage of using organic semiconductors (OSCs) for spintronics applications is that the device structure can be conveniently designed based on the experiences from an industrially well established field, namely that of *organic electronics*. However, the intrinsic transport properties of OSCs are poorly understood from both an experimental and a theoretical perspective. The work presented in this thesis provides the first comprehensive and robust procedure to investigate in detail the charge and spin transport properties of such OSCs from first principles.

The technique involves representing all the essential interactions in OSCs with a tight binding model including in particular the coupling of the charge carriers to phonons. Thereafter the *ab initio* Hamiltonian parameters are extracted from Density Functional Theory (DFT) and the maximally localized Wannier functions scheme. Furthermore, the Hamiltonian representing the organic material also incorporates carriers' spin relaxation mechanisms, i.e. hyperfine interactions and spin-orbit coupling. We evaluate the finite temperature properties of the system by evolving the classical fields in the Hamiltonian via Monte Carlo simulations. Thereafter the mobility is obtained from the Kubo formula and the spin diffusion length from a Landauer-Büttiker approach, implemented within

the Monte Carlo scheme.

The results from the work in this thesis can be divided into three main parts. Firstly, we explore in detail the phase diagram of the model to understand the effect of the various parameters on the physical observables. This is particularly crucial in order to optimize the different interactions in the OSC. Furthermore, we also understand the charge and spin transport properties of the model from such a microscopic approach. Secondly, we present in detail a DFT characterization of rubrene molecular crystals, which has the highest charge carrier mobility among OSCs. We shall then demonstrate that the first principles estimates of its carrier mobilities are very close to those measured in single-crystal rubrene-based organic field effect transistors and the spin diffusion lengths are also similar to that estimated in experiments on rubrene-based spin valves.

Thirdly, we will discuss the use of a similar multiscale procedure to predict the *ab initio* charge and spin transport characteristics of triarylamine based organic nanowires. Such organic nanowires were recently synthesized from a light activated self-assembly process and were demonstrated to have almost metallic type transport characteristics. We obtain exceptional estimates for the hole mobilities in such nanowires thereby confirming the experiments. Also the spin transport properties of such nanowires that we obtain are quite exceptional. As such, we predict that triarylamine based self-assembled organic nanowires can be promising candidates for organic spintronics.

Acknowledgements

I am indebted to a number of people for their help and guidance during the time spent working on this dissertation. First and foremost I would like to thank my supervisor Prof. Stefano Sanvito for his continuous guidance during my Ph.D. studies. His enthusiasm, understanding and dedication to research will stay with me forever as a source of inspiration. Working under him is indeed an incredible privilege. Periodic discussions with him on specific problems related to my work, sometimes enabled me to get a completely different perspective into the problem, which were incredibly helpful to bring projects forward. Furthermore, his kind hearted behavior was an encouragement throughout the last four years.

Secondly, I would like to thank my co-supervisor Prof. Mauro Ferreira for helpful comments and inspiring discussions which were also helpful to my work. I would like to thank Akinlolu Akande with whom I had the pleasure to work with in the organic nanowires project (also co-authored two papers with him). Also Dr. Claude Ederer and Dr. Roman Kovacic for introducing me to the world of Wannier functions.

Next I would like to thank my examiners Prof. Alessandro Troisi and Prof. Werner Blau for interesting discussions and essential suggestions on the work presented in this thesis. I thank them for appreciating the work that I have done during my PhD.

Special thanks goes to Lia Beverige and Stefania Negro for handling my accounts and administrative duties respectively. Their help was extremely useful over the years. The computational resources for this work have been provided by TCHPC. In particular I am

thankful to Darach Golden for his generous and patient help whenever I needed consultations regarding issues with my Monte Carlo and quantum transport codes. Furthermore, I would like to thank Paddy Doyle for his support with the queueing system. I also gratefully acknowledge the funding support from Science Foundation of Ireland's CSET grant underpinning CRANN, which made the work possible.

I owe a great deal of gratitude to my colleagues in the Computational Spintronics Group. They were not only my colleagues but the best of friends, over the years. In particular, Ivan Rungger and Nadjib Baadji who have been very patient and incredibly helpful to me in discussions relating to my work. I would like to thank Ivan who provided important encouragement to me and my work, during the last months. Also, Awadhesh Narayan with whom I had the pleasure to share my house with. Other members of the group include Anna Pertsova, Maria Stamenova, Amaury Melo Souza, Thomas Archer, Nuala Caffrey, Kapildeb Dolui, Maria Stamenova, Sri Chaitanya Das Pemmaraju, Gokhran Shukla, Meilin Bai, Thomas Cathcart, Andrea Droghetti (with whom I had some very inspiring discussions on work), Carlo Motta, Igor Popov, Jacopo Simoni, Mario Zuc, Tilde Cucinotta, Rajharshri Tiwari and Subhayan Roychoudhury. I am also thankful to the friendship of my colleagues and fellow PhD students in CRANN, Jose Manuel Caridad Hernandez, Stephen Connaughton, Sinead Winters, Elisa del Canto, Manwell Natali, Dania Movia, Stephen Power, Luiz Fillepe Perreira, Brendan O'Dowd and Carlos Ritter.

I would like to mention the late-night shows of Jon Stewart and Stephen Colbert which were a perfect source of light hearted fun as well as news, after a days work!

I am forever grateful to my family, my parents who have supported, encouraged and helped me throughout my life. It is their love that has enabled me to cross the finish line. Special mention to two of my colleagues Rohit Mishra and Mauro Mantega who have been incredible friends to me over the years.

Finally, I must thank Annemarie whose continuous support and encouragement is extremely precious to me and is more than I could ever express in words.

Contents

Abstract	i
Acknowledgements	iii
1 General Introduction	1
1.1 Spintronics	2
1.2 Magnetic read heads	4
1.3 Organic Semiconductor based devices	6
1.4 Understanding the operation of an Organic Spin Valve	10
1.5 Thesis layout	15
2 Theoretical Framework	18
2.1 Multiscale modelling of organic semiconductors	18
2.2 Monte Carlo simulations	20
2.2.1 Importance sampling	22
2.2.2 Markov process	24
2.2.3 Metropolis algorithm	27
2.2.4 Ground state techniques	28
2.2.5 Summary	30
2.3 Density Functional Theory	30
2.3.1 Non-interacting systems	33

2.3.2	Hartree-Fock method	35
2.3.3	Hohenberg-Kohn theorem	37
2.3.4	The Kohn-Sham scheme	38
2.3.5	Spin polarized DFT	43
2.3.6	Exchange-correlation functionals	44
2.3.7	Implementation of Van der Waals interactions in DFT	48
2.3.8	Ingredients in solving the Kohn-Sham equations	53
2.3.9	DFT codes	57
2.3.10	Spin-orbit interactions in DFT: an on-site approximation	57
2.4	Summary of this chapter	59
3	Towards modelling Organic Semiconductors: first steps	60
3.1	Computational methods	62
3.1.1	Tight binding Hamiltonian matrix: an example	66
3.2	Phase diagram of the model	67
3.2.1	Ground state	67
3.2.2	Finite temperature phase diagram	70
3.2.3	Spin crossover phase	73
3.3	Summary	76
4	Charge and Spin transport in Organic Semiconductors: a microscopic study	78
4.1	Introduction	78
4.2	Charge transport through OSCs	82
4.2.1	Linear Response Kubo Formula	85
4.2.2	Results and discussions	89
4.3	Spin transport	96
4.3.1	Spin relaxation mechanisms in organic materials	96

4.3.2	Theoretical setup for spin transport	104
4.3.3	Results and discussions	113
4.4	Summary	120
5	Charge and spin transport properties of Rubrene from first principles	122
5.1	Charge transport experiments on single crystalline rubrene based OFETs .	123
5.1.1	Experimental estimation of carrier mobilities in OFETs	129
5.2	Electronic and structural characterization of rubrene from DFT	135
5.2.1	Gas phase rubrene molecule	136
5.2.2	Rubrene crystal	140
5.3	First principles estimation of charge and spin transport in rubrene molec- ular crystals	144
5.4	Wannier Functions	147
5.5	TB Hamiltonian parameters	151
5.5.1	On-site energies and transfer integrals	153
5.5.2	Electron-phonon and stiffness constants	157
5.6	<i>Ab initio</i> transport observables	160
5.6.1	Charge carrier mobility	160
5.6.2	Spin diffusion length	163
5.7	Summary	171
6	First principles study of Organic Nanowires synthesized from light sen- sitive triarylamine derivatives	172
6.1	Light triggered self-assembly of supramolecular organic nanowires: the ex- periments	174
6.2	Charge transport properties	179
6.2.1	Single molecules in the gas phase	182
6.2.2	Charge transport properties from Marcus theory	187

6.2.3	Charge transport properties from linear response theory	193
6.3	Spin transport properties	201
6.4	Summary	208
7	Current projects, Conclusions and Future works	210
7.1	Project in progress: investigating the organic magnetoresistance effect . . .	210
7.2	General conclusions and achievements of this thesis	215
7.3	Future works	216
A	Derivation of the spin-orbit Hamiltonian for the $\pi - \pi$ model	222
B	$sp^2 - p_z$ model	227
C	Publications stemming from this work	230

List of Figures

1.1	Data storage over the years.	2
1.2	Tunnel magnetoresistance read heads used in hard disks.	5
1.3	Working mechanism of a spin valve using the resistor model.	11
2.1	Schematic cartoon of a lateral organic spin valve.	19
2.2	Concept of pseudopotential approximation.	55
3.1	α - U phase diagram at $T = 0$ for a finite chain of length $L = 10$ of a 1D model polymer.	68
3.2	$T = 0$ phase boundary in the ground state phase diagram for the model system.	69
3.3	Finite temperature α - U phase diagram for the model 1D polymers.	71
3.4	On-site Coulomb repulsion, U_C , needed for the phase boundary, as a function of temperature.	72
3.5	Entropy difference between the nSP and SP phases explaining the existence of the spin crossover phase observed in the model.	74
4.1	Concept of ballistic and diffusive transport.	79
4.2	Illustration of an organic field effect transistor, the prototypical charge transport device for OSCs.	81

4.3	Temperature dependence of charge carrier mobility as a function of the microscopic parameters in the model, charge carrier density ρ and el-el interaction U	90
4.4	Temperature dependence of charge carrier mobility as a function of el-ph interaction strengths (α) for a chain of length $L = 256$ atoms.	91
4.5	Carrier mobility different 1D segments (molecular chains).	92
4.6	Cartoon of a 2D rectangular slab containing five layers of 1D chain with a interlayer hopping t_{il}	94
4.7	Temperature dependence of mobility of the 2D rectangular slab.	95
4.8	Semi-classical model to explain spin relaxation due to random hyperfine fields.	97
4.9	Summary of experimental results on the role of hyperfine interactions (HI) in controlling spin transport through OSCs : Part I	99
4.10	Summary of experimental results on the role of hyperfine interactions (HI) in controlling spin transport through OSCs : Part II	100
4.11	Summary of experimental results on the role of spin orbit coupling (SO) in controlling spin transport through OSCs.	102
4.12	Summary of experimental results countering the role of SO interactions in controlling spin transport through OSCs.	103
4.13	Illustration of our $\pi-\pi$ model which represents all the essential interactions in OSCs.	104
4.14	Cartoon illustrating the concept of spin diffusion length, l_s , and how it is extracted in experiments.	108
4.15	Cartoon illustrating our spin transport setup.	110
4.16	Results for spin mixing transmission probability, T_{sm} , vs L evaluated at different temperatures when only HIs are the source of spin scattering. . .	113

4.17	Results for spin polarization, SP , vs L evaluated for different HI strength when only HIs are the source of spin scattering (for all t and T).	115
4.18	Comparison between HI and SO coupling for different magnitudes of spin relaxations.	116
4.19	Results for l_s vs $1/t$ evaluated at different t and T when only SO are the source of spin scattering.	118
5.1	The evolution of carrier mobility in single-crystalline OFETs over the years.	123
5.2	Structure of rubrene molecular crystal.	124
5.3	Illustration of an experimental method to fabricate high performing OFETs.	125
5.4	Cartoon describing carrier transport in OSCs for band transport and activated hopping mechanisms.	128
5.5	Circuit diagram for a four-terminal conductivity measurement in OFETs. .	130
5.6	Experimental results on the Hall-effect in rubrene molecular crystals. . . .	133
5.7	Kohn-Sham HOMO-LUMO gap for the rubrene molecule in the gas phase, for different DFT functionals.	135
5.8	DFT band structure and PDOS of rubrene crystal.	143
5.9	DFT and Wannier band structure of rubrene along with an illustration of its real space MLWF and molecular wavefunctions.	148
5.10	Illustration of the different transfer integrals in rubrene crystal, obtained from our Wannier analysis.	154
5.11	The magnitudes of all the transfer integrals in rubrene for the HOMO and LUMO bands along the different crystallographic directions.	155
5.12	Sliding phonon mode along which α and K are evaluated in our approach.	159
5.13	The statistical distribution of the two main hopping integrals in rubrene crystal.	161
5.14	The temperature dependence of <i>ab initio</i> charge carrier mobility, μ , of rubrene.	162

5.15	<i>SP</i> vs <i>L</i> graphs to obtain the <i>ab initio</i> estimate of l_s for rubrene molecular crystals, when only HIs are the source of spin relaxation.	165
5.16	Spin transport setup to incorporate SO coupling in rubrene molecular crystals.	167
5.17	<i>SP</i> vs <i>L</i> graphs to obtain the <i>ab initio</i> estimate for l_s of rubrene molecular crystals, when both HI and SO coupling are the source of spin diffusion. . .	170
6.1	Structure of triarylamine derivatives.	175
6.2	The nanodevice architecture constructed in the experimental work and microscopy images, when light is switched on and off.	177
6.3	Experimental results illustrating the transport properties of the nanodevice fabricated with self-assembled triarylamine based organic nanowires.	178
6.4	Energy level diagram of the frontier molecular orbitals for all the precursors and the TPA	182
6.5	Schematic diagram of the potential energy surface of a neutral and cationic radical precursor as a function of reaction coordinate.	183
6.6	DFT density of states for triarylamine P1 molecule and the P1 ⁺ radical in the gas phase.	186
6.7	Variation of the binding energy and charge transfer integral of TPA calculated by using different DFT functionals.	188
6.8	Binding energy and charge transfer integrals for all the precursors calculated at the geometry provided by the Grimme's functional evaluated using Markus theory.	189
6.9	Band structures of the nanowire P1 evaluated using DFT.	195
6.10	Illustration of the molecular displacement of the different phonon modes in the triarylamine molecule.	196
6.11	The statistical distributions of the transfer integral shown at two different temperatures.	198

6.12	Our <i>ab initio</i> estimate of charge carrier mobility as a function of temperature for the P1 nanowire, in the linear response limit.	199
6.13	Illustration of the organic nanowire and the DOS on a single molecule. . .	201
6.14	Schematic cartoon of a $sp_2 - p_z$ model to represent spin transport through organic nanowires.	203
6.15	Schematic cartoon of a spin valve comprising a triarylamine based organic nanowire sandwiched between ferromagnetic leads, that we model.	206
6.16	SP vs L graph from which the <i>ab initio</i> estimates of l_s for the nanowires can be calculated.	207
7.1	Experimental results for Organic Magnetoresistance effect (OMAR).	211
7.2	Our results for the <i>ab initio</i> estimation of OMAR for rubrene molecular crystals.	214
7.3	Concept of <i>spinterface</i> physics.	217

List of Tables

1.1	OSC molecular crystals used in organic electronics and opto-electronics.	8
5.1	The ionization potentials, electron affinity and the band gap ($\Delta = \text{I.P.} - \text{E.A.}$) of rubrene molecule in the gas phase, for different DFT functionals.	137
5.2	Geometrical properties of gas phase rubrene molecule for different DFT functionals.	139
5.3	Kohn-Sham HOMO-LUMO gap and unit cell geometry of rubrene crystal for different vdW DFT functionals.	141
5.4	The <i>ab initio</i> TB parameters for the rubrene molecular crystal obtained from our Wannier analysis of rubrene.	157
6.1	List of the triarylamine precursors and if they self-assemble in the presence of light to form nanowire structures.	176
6.2	DFT-B3LYP estimates of the ionization potentials, $\text{IP}(\text{v})$ and $\text{IP}(\text{a})$, the hole extraction potential, HEP, the internal reorganization energy, λ_{int} , and the localization radius, d_0 , for all the precursors and for TPA.	184
6.3	Comparison between the estimated J values at the binding energy minimum calculated by using the Grimme and the B3LYP functional for all the precursors, in the Marcus theory limit.	192
6.4	Estimates of α/t calculated using finite difference for the phonon mode C-I.	197

Chapter 1

General Introduction

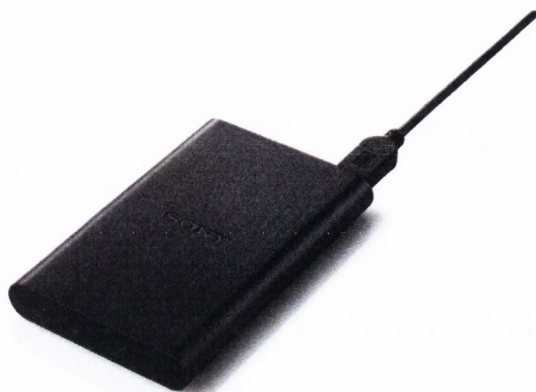
It has been estimated that the total data generated by humanity today in two days is greater than that produced throughout the entire human civilization till the year 2003. This very interesting fact highlights the sheer volume of data that is produced as a result of human day to day basic activities. Most of this falls into the category of user generated contents in popular websites. There is therefore an urgent need to store large volumes of data in as little space as possible and the solution must be as cost effective as possible. In fact, this mode is termed as high density data storage.

Additionally, in this day and age, we are living through a technology revolution and at every moment in time a plethora of information is available literally at our finger tips using "smart devices". These devices which make human lives comfortable from a technological point, include smart phones, tablets and laptop computers. Over the years these devices have become increasingly popular, cheaper, smaller and lighter. This is also made possible through new routes to high density data storage.

Let us pictorially illustrate the perspective of the success story of high density data storage over the last half century. Fig. 1.1a shows a 5 megabytes hard disk drive (HDD) designed by IBM in 1956 for a supercomputer 305 RAMAC. This was deemed as the world's first HDD, weighed more than a ton, and in today's money (accounting for inflation) costed \$160,000. On the right-hand side panel of Fig. 1.1b we show an external 1



1956
(a)



2013
(b)

Figure 1.1: The left panel (a) shows the world's first hard disk drive (5 megabytes) designed by IBM while the right panel shows a typical 1 terabyte (10^6 megabytes) external hard disk that one can purchase now a days.

terabyte HDD that one can purchase today. Such hard disks are the size of our palm and costs just under \$100.

High density data storage has been possible through a field known as *Spintronics* and now we will now spend some time introducing it.

1.1 Spintronics

Spin is an intrinsic angular momentum carried by elementary particles. Spin is a solely quantum mechanical property. It is precisely the result of the spin, that elementary particles possess a magnetic moment. In fact, a single electron's spin \mathbf{s} can be measured by detecting the associated magnetic moment $-g\mu_B\mathbf{s}$, where μ_B is Bhor magneton and g

is the electron g -factor in the material. Spintronics is a branch of electronics exploiting both the intrinsic spin and the associated magnetic moment of carriers, together with their fundamental charge in solid state devices for data storage applications. Spintronics offers a massive advantage of reduced dimensions. Thus, in this process spintronics promises smaller and cheaper devices with low power consumption. The latter is because spins can be manipulated by very little differences in magnetic fields.

The field of spintronics concerns the creation, manipulation and detection of spin polarization through solid-state materials. Generating spin polarization involves producing a non equilibrium population of spins in a particular material. Traditionally this was done optically by directing circularly polarized light onto direct bandgap semiconductors, which transfers its angular momentum to carriers. However, in modern spintronic devices, which are known as spin valves (Giant Magnetoresistance -GMR- junctions), electrical spin injection is achieved. This can be accomplished in spin valve like devices with the help of ferromagnetic (FM) electrodes which already boast a spin polarized density of states at their fermi level. The spin valve is the prototypical device for spin transport in spintronics and is a vital component of HDDs as we will discuss in the next section. It comprises two FM electrodes sandwiching a central spacer which can be either metallic (GMR junctions) or insulating (Tunnel Magnetoresistance -TMR- junctions). The electrical resistance through the device depends on the direction of magnetization of the two FM electrodes. Some examples of FM metals used in GMR junctions include Co, Ni, Fe, CoFe Alloys, $\text{La}_x\text{Sr}_{1-x}\text{MnO}_3$ (LSMO), etc. Thus, simply by passing current through such devices, spin polarized carriers can be generated within the spacer. If now, one wants to use the spin valve for injecting carriers into a semiconductor the combination of materials chosen must ensure that there is an appropriate level alignment between the conduction and valence bands of the semiconductor and the chemical potentials of the ferromagnetic electrodes. This is to ensure that the spin injection from the ferromagnets into the semiconductor material is efficient, i.e. that spins enter the semiconductor.

The next important problem is how effectively these spin polarized carriers move through the semiconductor, which will decide the functioning of a spin valve. We explain this in more detail in the coming sections of this introduction chapter. Moreover, this is a principal question we wish to address through the work presented in this entire thesis.

Let us now discuss the use of *spintronics* in HDD.

1.2 Magnetic read heads

Modern HDDs are capable of storing and retrieving large volumes of data, with the help of rapidly rotating disks coated with a magnetic material. Furthermore, in the HDD design there is a very tiny read/write head "floating" above the disks which enables reading and writing information onto/from the hard disk in the forms of bits (0's and 1's). The writing operation is facilitated relatively conveniently with the help of nanomagnets or tiny electromagnetic coils. However, the success of high density data storage in the present day lies in the use of *spintronics* for creating efficient read-heads which are sensitive to very small changes in magnetic field. Let us now explore how this is achieved in practice.

Fig. 1.2 shows the top view of the interior of a modern HDD. As we have discussed the key component of such hard disks is the tiny read head. In present hard disks, tunneling magnetoresistance (TMR) heads are used. The cartoon of a TMR head is illustrated in the right panel of Fig. 1.2 which also depicts the basic principle of the TMR. The materials set for the TMR read heads used in modern hard disks is Fe/MgO/Fe [131]. The very tip of the read head is comprised of this structure, with a thick Fe layer, whose magnetization direction is always fixed and hence it is termed as the fixed layer. Next there is a few nanometers wide insulating barrier (MgO). Finally, the last component of the TMR structure is a thin Fe layer, which is termed as the free layer since the direction of its magnetization can be easily altered by a stray magnetic field from the data written on the particular part of the magnetic disk.

The current through the TMR junction comprising the read head is monitored during

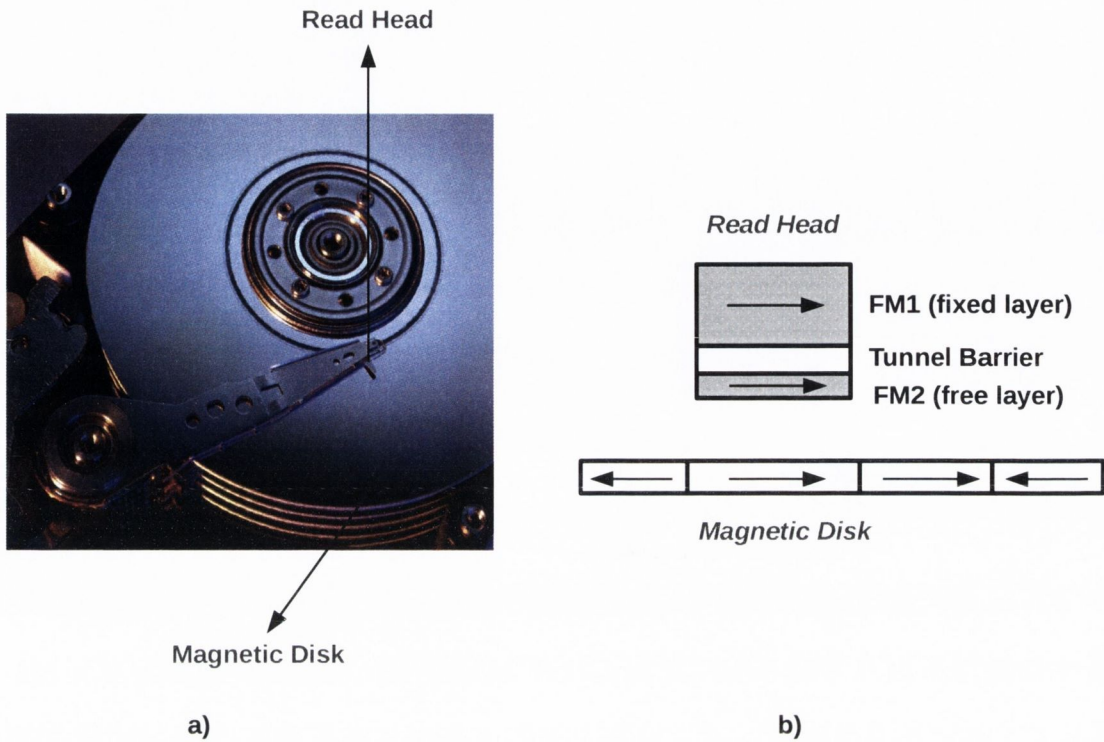


Figure 1.2: The inside of a HDD is shown here with the magnetic disk and the tiny read head in the left panel. Cartoon illustrating a snapshot of a reading operation in the hard disk is shown in the right panel. In present day HDD, the read head is made up of a Tunnelling Magneto Resistance (TMR) junction which is highly sensitive to small magnetic fields and hence is very effective in reading data from the disk. In order to cope with the demand for HDD storage, significant research is invested into improving the configuration of such read heads.

the reading operation of a hard disk. The electrical resistance through the TMR junction depends on the relative direction of magnetization of the two ferromagnetic layers. If they are parallelly aligned, the device is in the low resistance state and current can flow through the TMR junction. In contrast, if the alignment of the magnetizations of the two ferromagnetic layers is anti-parallel, the junction is in the high-resistance state and no current flows. This phenomenon by which electrical resistance of the TMR junction depends on the magnetic configuration is known as Tunnel Magneto Resistance and the two resistance states of the junction are used for reading information from the magnetic

disk.

So what exactly will ensure high density data storage in modern HDD? The areal density of the data stored in hard disks can be increased by making the bit size in a disk as tiny as possible. This means that the read heads should also be as small as possible. Furthermore, the magnetoresistance effect should be as large as possible in order to make the read heads extremely sensitive to tiny changes in magnetic field while reading data from the disk. As mentioned previously, in present generation HDDs Fe/MgO/Fe TMR junctions are used as read heads. In the past thicker junctions relying on the GMR effect have been used as read heads. Such spin valve structure included the following configuration, antiferromagnetic exchange bias layer /Co (pinned layer)/ Cu spacer / NiFe (free layer). This was based on the pioneering work of Nobel laureates Albert Fert and Peter Grünberg [1, 2].

The need for HDD storage has led to periodic updating of these read heads over the last decade. There is also a substantial amount of research devoted in academia and industry in newer and better materials for the design of the next generation read heads. One such set of materials is represented by organic semiconductors (OSCs). The essential idea behind this was to use the knowledge from an already experienced field of organic optoelectronics and exploit the advantages of using organic materials. We will now discuss in detail this emerging and enticing field of *Organic Spintronics*.

1.3 Organic Semiconductor based devices

The work presented in this thesis is on researching the use of organic materials for spintronics. This was possible with the discovery of spin polarized transport through organic semiconductors [70]. Although this very exciting field is quite nascent, the most important advantage of organic spintronics is that organic based solid state devices could be conveniently fabricated based on the experience accumulated in the already well-established fields of organic electronics and organic optoelectronics.

Let us now talk about OSCs and organic electronics before we start our discussions on organic spintronics. π -conjugated polymers are leading OSC materials because of their modest bandgaps and also because of the ease with which they can be manufactured in large area devices. Such polymers have a delocalized π -electron in their molecular plane, which serve as the itinerant charge carrier. In fact, organic molecular crystals which contain these molecular planes held together in the structure by Van der Waals forces are presently ubiquitous in the optical display panels of devices such as laptops, TVs, mobile phones and tablet screens. They make use of a large number of tiny but high quality Organic Light Emitting Diodes (OLEDs), providing high contrast display. A table summarizing the most common organic molecular crystals used in organic electronics is shown in Table. 1.1. Out of these Alq₃ is the most widely used OSC in such display panels because thin films out of Alq₃ can be conveniently manufactured on a large scale.

There are unique advantages which organic materials have over their inorganic counterparts. In comparison to inorganic semiconductors, OSCs are cheap, low weight and most importantly they can be conveniently synthesized and are non-toxic. Furthermore, they are mechanically flexible and chemically inert, which is very advantageous in device fabrication. Moreover, their optical and electronic properties can be chemically tuned.

Organic light emitting diodes (OLEDs) have a similar device configuration as organic spin valves. However, instead of ferromagnetic electrodes (as in organic spin valves) OLEDs have hole and electron injecting electrodes sandwiching a thick layer of OSC(s). The hole-injecting electrode is comprised of high workfunction materials like indium tin oxide (ITO) while the electron-injecting electrode can be low workfunction alkali metals like calcium, magnesium, etc. OLEDs work by hole and electron transport (at finite applied bias) respectively through a hole transport layer (HTL) and an electron transport layer (ETL) where they meet and form quasi particles known as excitons. The HTL and ETL are made up of OSC. The two carriers (electron and hole) with spins can combine together to form triplets (with total spin $S = 1$) or singlets ($S = 0$). Only the singlet

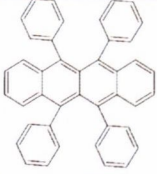
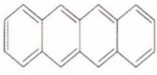
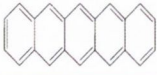
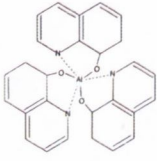
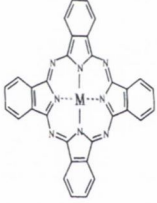
Organic molecular crystal	Chemical Formula	Structure
Rubrene	$C_{42}H_{28}$	
Tetracene	$C_{18}H_{12}$	
Pentacene	$C_{22}H_{14}$	
Metal Quinolates e.g. Alq ₃	$C_{27}H_{18}AlN_3O_3$	
Metal Phthalocyanine e.g. CuPc	$C_{32}H_{18}MN_8$	

Table 1.1: Table depicting the chemical and structural formula of common molecular crystals used as OSC for optoelectronic and spintronic applications.

excitons radiatively decay to produce light. However, the bulk of excitons produced in an OLEDs have a triplet character (singlet to triplet ratio is 1:3).

In 2002, Alek Dediu and Carlo Taliani [70] combined their expertise in OLEDs and half metallic oxides to increase the yield of singlet excitons by injecting spin polarized charge carriers through the OSCs. Although their original experiment was controversial, they managed to observe a finite magnetoresistance (MR^1) in a device made up of ferromagnetic LSMO electrodes and a π -conjugated polymer known as sexithiophene

¹ $MR = \frac{R_{AP} - R_P}{R_P}$; with AP=Antiparallel and P=Parallel.

T_6 . Their device configuration was LSMO/ T_6 (120 nm)/LSMO. A couple of years later, other groups [71] also observed a similar resistance variation in a spin valve type device, LSMO/Alq₃ (160 nm)/Co, at low temperatures. Subsequently, for a similar device configuration, LSMO/Alq₃ (200 nm)/Al₂O₃ (1.5 nm)/Co, finite MR was confirmed also at room temperatures [139]. Furthermore, there have also been demonstrations of a TMR effect using OSC material as the tunneling barrier. For example, a TMR of about 4% was reported [170] at room temperature for a device structure, Co/Al₂O₃ (0.5 nm)/Rubrene (4.6 nm)/ Co. More recently [68] in LSMO/Alq₃ (2 nm)/Co based TMR junctions magnetoresistances of 300% were observed which is comparable with the best inorganic tunneling junctions.

Note, that in these organic spin valves generally a few nanometers of an insulating barrier like Al₂O₃ or LiF [148] is inserted between the organic spacer and the top Co electrode. This has two advantages. Firstly, it prevents the contact between the fragile organic structure and the top electrode, which is typically deposited on the organic layer via vapour deposition techniques. Normally, based on the experience on working with such devices, it was observed that deposition of Co on unprotected organic surfaces lead to metal inclusions of the hot metal through the OSC layer thereby short circuiting the device. Thus the deposition of Al₂O₃ between the organic and the top Co electrode prevents this problem. Secondly, a few nanometers of insulators serves as an additional tunneling barrier. This facilitates the injection or removal of spin polarized carriers to/from the organic semiconductor thereby circumventing a problem which plagues organic device known as the resistance mismatch problem. We shall now describe this.

Normally if there were no tunneling barrier between the organic and the metal, the movement of carriers from the organic to the metal would be impeded. This is because, when a carrier moves through the metal it faces very little resistance but when it travels through the organic its flow is met with a large amount of resistance. Therefore the entry and subsequent transport of the carrier into (and through) the organic can be entirely

impeded due to this resistance mismatch. Both these problems could be eliminated with the use of a ferromagnetic organic material (at room temperature) Vanadium tetracyanoethylene, $V(\text{TCNE})_x$ [16, 17], as a magnetic electrode.

Uptill now in this introductory section we have discussed the basic concepts of read heads in hard disk drives and organic spin valves. We have also discussed the advantages of using OSCs over their inorganic counterparts. Moreover, we have also mentioned the performance of organic spin valves made by different research groups over the past decade. However, note that we have also mentioned that the working of an organic spin valve is because of an efficient spin polarized transport through the organic media. In the next section of this introductory chapter we will talk about the operation of an organic spin valve.

1.4 Understanding the operation of an Organic Spin Valve

A spin valve is simply a resistor whose electrical resistance depends on the direction of magnetization of the two ferromagnets. Let us elaborate upon the explicit mechanism of the working of a spin valve in a little more detail, since this will form the basis of much of the discussions on transport through the OSC in this thesis.

Electrical current flowing through a material is constituted by electrons of opposite spin types. In a non-magnetic metal or a semiconductor the resistance faced by each of these spin currents are the same. However, this is not the situation in a magnetic material, where the resistances experienced by the two different spin species are different depending on the orientation of the electron spins with respect to the internal magnetization [130].

In a spin valve, when the direction of the magnetization of the two ferromagnetic electrodes are the same, the electrical resistance of the device is low. In contrast, when the ferromagnets are antiparallely aligned with respect to each other, the electrical resistance

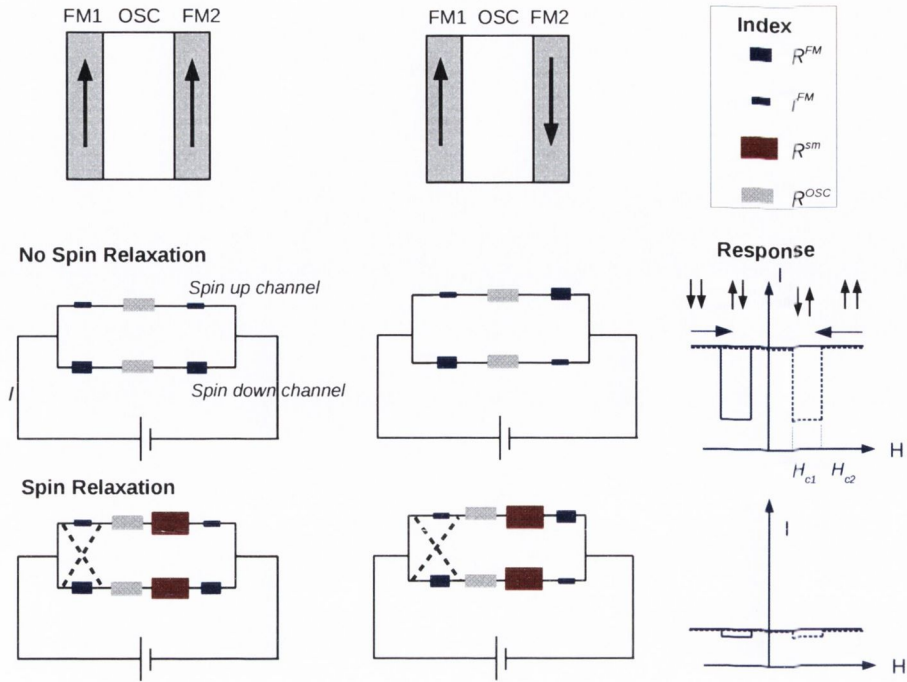


Figure 1.3: The working mechanism of a spin valve is illustrated. An organic spin valve consists of two ferromagnets FM1 and FM2 sandwiching a central spacer made up of an OSC. The device in the parallel (P) and antiparallel (AP) configurations are depicted in the top panel. In the absence of any spin relaxation events (middle panel) it can be worked out that $R_P < R_{AP}$ and the spin valve exhibits a characteristic bi-stable I vs H response which is desired. However, when relaxation of the carrier spins are taken into consideration (bottom panel), the spins fail to reach the opposite electrode (FM2) due to spin mixing of the two spin channels. As a result, the resistances R_P and R_{AP} will be indistinguishable and the device will not exhibit the desired spin valve effect. Here the size of the resistors directly correlate to the magnitude of that particular resistances in the circuit diagrams.

of the device is high. There are some cases (different configuration of magnetic electrodes) when the opposite is true and an inverse spin valve effect is observed [71, 139]. However, for the description in this section we will stick to the conventional picture. In a device, typically one of the ferromagnet has its direction of magnetization fixed (it is the pinned layer) by exchange biasing it with a strong antiferromagnet. The other ferromagnet, the free layer, is allowed to change its magnetization direction upon application of an external magnetic field, H . The current through the device I is monitored as a function of the applied magnetic field and the response is summarized in the right most panel of Fig. 1.3. As evident from the response, the device will exist in a two distinct resistance states,

which can be effectively used for storing information.

Let us examine the working mechanism of a spin valve with the help of a simple resistor model, first in the ideal case ignoring any spin relaxation mechanisms. This is illustrated in the middle panel of Fig. 1.3. We can assume that the electrical resistance of the spin current is low when the electron spin is oriented along the direction of the magnetization (say spin up) and it is high when the electron spin is oriented against the direction of magnetization (spin down). In the parallel configuration of the ferromagnets, the spin-up electrons experience low resistance in both the ferromagnets, while the spin down experiences high resistance in both the ferromagnets. Therefore the overall resistance (R_P) of the device in the parallel configuration can be worked out [8] to be equal to

$$\frac{1}{R_P} = \frac{1}{r_{\uparrow}^{\text{FM1}} + R^{\text{OSC}} + r_{\uparrow}^{\text{FM2}}} + \frac{1}{R_{\downarrow}^{\text{FM1}} + R^{\text{OSC}} + R_{\downarrow}^{\text{FM2}}}. \quad (1.1)$$

Here the arrows (\uparrow, \downarrow) mean the spin direction of the carriers with respect to the local magnetization. Furthermore, R^{OSC} is the resistance of the carriers through the organic channel, $r_{\uparrow}^{\text{FM1/FM2}}$ are the resistance of the carriers with the same spin direction with respect to the local magnetization (hence their magnitudes are low) and $R_{\downarrow}^{\text{FM1/FM2}}$ are the resistance of the carriers with the opposite spin direction with respect to the local magnetization (hence their magnitudes are high). Therefore in the parallel configuration spin up electrons carry the current.

Similarly, in the antiparallel configuration one can work out [8] the effective resistance R_{AP} as

$$\frac{1}{R_{AP}} = \frac{1}{r_{\uparrow}^{\text{FM1}} + R^{\text{OSC}} + R_{\downarrow}^{\text{FM2}}} + \frac{1}{R_{\downarrow}^{\text{FM1}} + R^{\text{OSC}} + r_{\uparrow}^{\text{FM2}}}. \quad (1.2)$$

Please note that neither of the two spin components experience the low resistance path in the antiparallel configuration of the two ferromagnets.

Now in Eq. (1.1) and Eq. (1.2), provided that the resistance of the electronic current

through the OSC, R^{OSC} , is small enough² R_P will always be smaller than R_{AP} . Thus the device will exhibit a bi-stable response in its I vs H profile as shown in the middle-right panel of Fig. 1.3. This is a very simple explanation of the spin valve effect.

In what we have discussed till now no spin relaxation has been included. This is the perfect circumstance as far as the functioning of the device is concerned. However in reality, electron spins undergo decoherence as a result of their interaction with the environment. There are several spin relaxation mechanisms, some of which are pertinent to the discussions in this thesis. These include interaction of electron spin with nuclear spins of the atoms constituting a material, which is known as hyperfine interaction; interaction between the spin and orbital components of the angular momenta of the itinerant electron, which is termed as spin-orbit interactions; interaction between electron spins and that of paramagnetic impurities or defects. In this thesis we shall discuss in detail the different spin relaxation mechanisms in OSCs, in particular the former two. For now, we should keep in mind that spin diffusion causes mixing of the spin-up and spin-down channels in the spin valve, as illustrated in the bottom panel of Fig. 1.3 and also leads to a resistance contribution R_{sm} . Here the subscript sm stands for spin mixing. Therefore in an OSC with substantial spin mixing, R_{sm} will be large and will dictate both R_P and R_{AP} . In such an scenario R_P and R_{AP} can be indistinguishable. This is a situation that is undesired in a spin valve based spintronic device.

Alternatively, one could also write down the resistances in the parallel (R_P) and the antiparallel (R_{AP}) configurations by the following two equations in the limit of zero temperature

$$R_P = R_0 (1 + \kappa \cdot e^{-L/l_s}), \quad (1.3)$$

$$R_{AP} = R_0 (1 - \kappa \cdot e^{-L/l_s}), \quad (1.4)$$

here L is the length of the semiconducting channel, l_s (spin diffusion length) is the average length electron spins travel through the channel before losing their spin polarization and

²The organic material is a good semiconductor.

κ is a constant that will depend on the electronic structure of the materials comprising the spin valve and external field [12]. Therefore in the above equations if L is large and there is spin mixing, $R_P - R_{AP} \rightarrow 0$. Consequently, the device will not exhibit the desired spin valve effect.

When significant spin mixing takes place the spin valve effect would be minimal as illustrated in the I vs H response in the bottom-right panel. Needless to say, a proper understanding of the spin diffusion mechanisms through OSCs is quintessential in organic spintronics. Furthermore, it is also crucial that we understand the factors which control R^{OSC} . In order to do so, we must comprehensively understand the intrinsic charge carrier transport behavior in OSCs. These are the facets we wish to explore in this thesis.

The above explanations for the bi-stable response of organic spin valves (as a function of magnetic field) is attributed to an efficient spin dependent transport through the OSC layer. This is what is assumed in experiments by the organic spintronics community. Unfortunately, Hanle effect in organic semiconductors is not yet been observed [9]. Hanle effect is the demonstration of spin precession and dephasing in a magnetic field non-collinear to the injected spin orientation within a semiconductor [10]. Therefore it is the only conclusive evidence of spin transport within the semiconductor layer.

Therefore, in practice, the working of an organic spin valve could also be due to interface effects [7]. However, in this thesis since we are interested in investigating the charge and spin transport through the bulk OSC layer, we assume perfect metal-organic contacts. Under experimental conditions, such a scenario could be due to the presence of a tunneling barrier between the injecting electrode and the OSC, in which case the charge carriers are expected to be injected into the molecular levels of the organic from the electrode without any metal-organic interface effects [170, 139]. Note that the metal-organic interface effects i.e. the problem of an organic molecule on metallic surface, using state of the art theoretical techniques, is an exciting research field in itself and is one of the possible future work of this thesis, especially after one has fully understood transport

through the bulk OSC layer.

Let us now discuss briefly the general layout of the thesis.

1.5 Thesis layout

We will explore from first principles the charge and spin transport properties of OSCs, which are used in devices like organic spin valves. We will make an *ab initio* estimate of the charge carrier mobility, which epitomizes the ease with which carriers travel through a particular organic media and hence characterizes charge transport. We will also estimate the spin diffusion length of organic semiconductors, which is the average length that carriers travel through the organic material before losing their spin polarization. The spin diffusion length characterizes spin transport through OSCs. Furthermore, we aim to obtain a comprehensive understanding from a microscopic point of the charge and spin transport mechanisms through OSCs. The work presented in this thesis is a significant step in achieving the goal of modelling a full organic spintronic device.

The approach which we use in this work, is to represent all the interactions in a particular OSC including the spin relaxation effects using a microscopic tight binding Hamiltonian. Next the tight binding Hamiltonian parameters are obtained from first principles calculations either directly or with the help of Wannier functions. The Hamiltonian has classical terms accounting for physical phenomena in OSCs. These classical terms in the Hamiltonian are evolved via Monte Carlo simulations and subsequently the spin and charge transport properties are estimated using the Kubo and the Landauer-Büttiker formulae respectively.

First principles modelling of the transport properties through the OSC is a challenging task particularly because it is a multiscale problem and involves several different degrees of freedom. In this work we have developed a comprehensive understanding of those parameters and hence have performed a careful optimization of them. The general layout of the thesis is as follows

Chapter 2 In Chapter 2 we will discuss the two main computational techniques implemented in the work presented in this thesis. These include stochastic methods namely Monte Carlo and energy minimization techniques which are used to statistically evolve the microscopic Hamiltonian describing the OSCs. Next we will discuss in detail about a very powerful tool known as Density Functional Theory (DFT), which is used to predict the properties of systems from first principles. We have made extensive use of DFT in exploring the electronic and geometric properties of organic molecular crystals. Furthermore, in our multiscale approach DFT calculations also form the basis for obtaining *ab initio* information.

Chapter 3 We will take a first step towards modelling OSCs in Chapter 3. This includes representing all the essential interactions in OSCs with the help of a microscopic Hamiltonian for a linear chain of atoms. Thereafter we will explore the effect of the different Hamiltonian parameters on the properties of the model and summarize the results in the form of a phase diagram. This chapter gives us a comprehensive understanding of the role played by all the different model parameters.

Chapter 4 In Chapter 4 we will introduce the procedure by which we compute the charge carrier mobility using Kubo Formula and the spin diffusion length using an algorithm based on the spin polarized Landauer-Büttiker formula. We will explore in detail the charge transport phase diagram for a one-dimensional chain, one-dimensional segments (molecular chains) and two-dimensional networks. Here we wish to understand the charge transport behavior for different morphologies as a function of the model Hamiltonian parameters. In the second part of the chapter we explore the spin transport phase diagram for a one-dimensional chain. Here we introduce the spin transport Hamiltonian, which accounts for the principal spin scattering effects in OSCs. We will investigate in detail the dependance of spin diffusion length on the model Hamiltonian parameters.

Chapter 5 In Chapter 5 and Chapter 6 we will investigate the *ab initio* charge and spin transport observables for real OSCs. Firstly, in Chapter 5 we will introduce a method to obtain the *ab initio* tight binding Hamiltonian for rubrene using a Wannier functions based projection scheme. Next we compute the carrier mobility and the spin diffusion length from the *ab initio* Hamiltonian of rubrene. We find that the first principles estimates for the charge carrier mobility and the spin diffusion length are quite close to those obtained from experiments. The choice for rubrene in our investigation is because it is the OSC with the highest charge carrier mobility and hence the best performing OSC.

Chapter 6 In Chapter 6 we will perform a detailed first principle analysis of the electronic structure as well as the charge and spin transport properties of triarylamine-based organic nanowires. These were recently synthesized through a self-assembly procedure and were found to have metallic type transport behavior. We will theoretically confirm this and also provide the *ab initio* estimates for the carrier mobility and the spin diffusion length in such organic nanowires.

Chapter 7 Finally, in Chapter 7 we will describe some of our ongoing projects, we will draw some conclusions and highlight the achievements of the work presented in this thesis. We will also mention our perspective for some possible future research directions based on what we have learnt throughout the course of this thesis.

Chapter 2

Theoretical Framework

2.1 Multiscale modelling of organic semiconductors

Fig. 2.1 shows a schematic illustration of a lateral organic spin valve, which is the prototypical device in organic spintronics [181]. It comprises two metallic electrodes (leads) sandwiching a central spacer made up of an OSC material which is typically 100-200 nm thick (see Fig. 2.1). Modelling such a nanodevice from first principles requires multiscale techniques (due to the OSC thickness) and hence it is a challenging task. In this respect, the very first problem which needs to be addressed is what happens at the metal-organic interface. Here we essentially need information at a length scale of less than 2 nm. Indeed, the characteristics of the metal-organic interface can be appropriately described by DFT up to a very high degree of accuracy. Some very interesting problems such as investigating the geometrical and electronic structure properties of organic molecules on a metallic surface fall into this category [3, 4, 5]. Moreover, interfaces can play a crucial role in governing transport through the entire device as indicated by the pioneer explanation of *spininterface physics* [7], which we shall explain in the subsequent chapters. Using the appropriate *ab initio* technique to describe the interfaces accurately in such hybrid inorganic-organic systems (HIOS) is an exciting and ambitious field in itself. Furthermore, electronic transport properties across different organic molecules deposited on metallic surfaces or insulating

islands in a Scanning Tunneling Microscope (STM) setup, can now be extensively studied using state of the art *ab initio* transport codes like SMEAGOL [13], which is developed in our group.

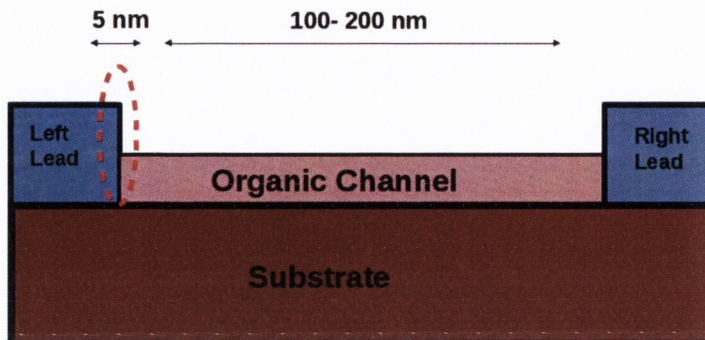


Figure 2.1: Schematic cartoon of a lateral organic spin valve, which is the prototypical device in organic spintronics [181]. The work presented in this thesis is a crucial step towards developing a robust computational architecture to describe *ab initio* transport properties in such OSC based nanodevices. Our computational tools involve MC simulations and DFT, which shall be discussed in detail in this section.

The second most important issue at hand when modelling an organic nanodevice (depicted in Fig. 2.1) is how well can we describe the electronic structure and the transport properties across the rest 100–200 nm of the OSC channel. The fundamental complication that one faces is that this is a length scale not accessible by DFT. Hence, this is where the work presented in this thesis expects to make an essential contribution to the field of organic spintronics. At the very heart of our multiscale scheme to represent OSCs, lies a set of numerical methods that will be extensively employed throughout this thesis, which fall into the category of Monte Carlo (MC) techniques. They form a powerful class of stochastic methods which can be used to accurately simulate large physical systems at finite temperature. We will discuss such stochastic methods in the first part of this chapter. Subsequently, in the second part we will discuss the basics of DFT which we make an extensive use of in our multiscale modelling of OSCs.

2.2 Monte Carlo simulations

The aim of MC simulations performed in this thesis is to estimate the temperature dependent value of a physical observable Q , of a system. For example, in this work Q can be the charge carrier mobility or the conductance. Such an expectation value for the observable, $\langle Q \rangle$, can be obtained according to the following expansion [11]

$$\langle Q(t) \rangle = \sum_{\mu} Q_{\mu} w_{\mu}(t), \quad (2.1)$$

where $w_{\mu}(t)$ is the probability of a state μ occurring in a real system at time t and Q_{μ} is the value of the observable when the system is in the state μ . For example, the state μ can be characterized by a set of displacements vectors of the molecules constituting the system or by the (classical) nuclear spins on an atom. In general we are assuming that the particle state μ is defined by a set of classical vectors $\{x_i\}$. In principle, the summation is over all the possible states that the system can access. This can be an intractably large number. However, one can circumvent this problem by selecting a finite number of states, which provide a sufficient representative sampling of the states that the system can explore. This representative selection of states must be met in such a way that the frequency of their occurrence in the simulation is the same as it would be in a "real system". The precise way in which this is described, is by a Markov process, which we shall explain in the coming subsections. Thereafter the expectation value $\langle Q \rangle$ is measured by averaging over a large number of these states.

Indeed keeping in mind that each state must appear with the correct frequency, care should be taken in the time evolution of the states so as to describe the correct dynamics of the system and the rules in transition of the system from one state to another. The system's dynamics is governed by the *Master Equation* [14] under the condition of only

including incoherent effects [235],

$$\frac{dw_\mu}{dt} = \sum_{\eta} [w_\eta(t)R(\eta \rightarrow \mu) - w_\mu(t)R(\mu \rightarrow \eta)], \quad (2.2)$$

where $R(\eta \rightarrow \mu)$ are the transition rates from the state η to the state μ and $w_\eta(t)$ is the weight or the probability of the system to be found in state η at time t . The first term on the right hand side of the Master equations represents the rate at which the system is undergoing a transition from the state η into the state μ , while the next term represents the rate at which the system is leaving state μ . Since the system must exist in some state after transition, all the probabilities must obey the criterion $\sum_{\mu} w_\mu(t) = 1$.

Now, since the system at hand is examined in its equilibrium state $\frac{dw_\mu}{dt}$ vanishes (at equilibrium the state population does not change with time) which implies that the rate takes constant values at all time. The values of w_μ must be known at all time during the simulation and their equilibrium value is $p_\mu = \lim_{t \rightarrow \infty} w_\mu(t)$. In fact, p_μ can be obtained for a system at thermal equilibrium with a reservoir at temperature T , according to the following expression given by Gibbs

$$p_\mu(E_\mu) = \frac{e^{\frac{-E_\mu}{k_B T}}}{Z}, \quad (2.3)$$

where E_μ is the energy of the state μ and k_B is the Boltzmann's constant. Here, Z is the partition function of the system which is $Z = \sum_{\mu} e^{\frac{-E_\mu}{k_B T}}$. Eq. (2.3) is in fact the single particle probability distribution function for a *canonical ensemble* of the quantum states of the system, when the volume V , the number of particles N and the temperature T of the system are fixed. In this case the system exchanges only energy with the reservoir.

For a *microcanonical ensemble* when the internal energy U , V and N are fixed all the states occur with equal probability. We shall demonstrate in the next subsections why the choice of microcanonical ensemble of states of the system is poor in terms of simulating the dynamics of the system. Finally, for a *grand canonical ensemble* V , the

chemical potential μ_o (which controls the number of particles in the system, N_μ) and T are fixed. In this case the system exchanges both energy and particles with the reservoir. For a grand canonical ensemble the single particle probability distribution function is:

$$p_\mu(E_\mu, N_\mu) = \frac{e^{\frac{-(E_\mu - \mu_o N_\mu)}{k_B T}}}{Z}. \quad (2.4)$$

where the partition function is given by $Z = \sum_{E_\mu} \sum_{N_\mu} e^{\frac{-(E_\mu - \mu_o N_\mu)}{k_B T}}$.

If the system evolves through a representative sample of states then the measured average must be close to the theoretical expectation value of the observable $\langle Q \rangle$. In the following subsections we shall explain in detail a set of rules which ensures that a representative sample of the states are generated during a MC simulation.

2.2.1 Importance sampling

The estimation, Q_M , of the observable $\langle Q_M \rangle$, made during the MC simulations is,

$$Q_M = \frac{\sum_{i=1}^M Q_{\mu_i} p_{\mu_i}^{-1} e^{-\beta E_{\mu_i}}}{\sum_{j=1}^M p_{\mu_j}^{-1} e^{-\beta E_{\mu_j}}}, \quad (2.5)$$

where M is the complete finite number of states sampled by the MC algorithm, p_μ is the probability distribution from which those states are randomly sampled. In other words the probability p_{μ_i} defines the likelihood of the state μ_i to occur in the simulation and hence depends on the nature of the algorithm used to evolve the system from one state to the next. Also $\beta = \frac{1}{k_B T}$ is the inverse temperature¹. Needless to say that when a large number of states are sampled, $M \rightarrow \infty$, $Q_M \rightarrow \langle Q \rangle$.

One alternative is to neglect the concept of importance sampling and choose all the states

¹ β is eV⁻¹, T in K and the Boltzmann's constant is $k_B = 8.6173 \times 10^{-5}$ eV/K.

with the same probability (as for a microcanonical ensemble of states), which results in

$$Q_M = \frac{\sum_{i=1}^M Q_{\mu_i} e^{-\beta E_{\mu_i}}}{\sum_{j=1}^M e^{-\beta E_{\mu_j}}}. \quad (2.6)$$

As one can notice this will be a poor choice in an algorithm, especially if the selected number of states M are a tiny fraction of the total number of states the system can be found in. In such a scenario there may be a very high possibility that the states selected by the algorithm are not a good representation of the behavior of the system thereby yielding a very poor estimate of Q_M from Eq. (2.6).

Fortunately, the probability of a state occurring in a real system is known, i.e. it is given by Boltzmann distribution, i.e. by Eq. (2.3) and Eq. (2.4). Therefore if the simulation is biased towards sampling states that are given by the Boltzmann's probability distribution one can ensure that only the high probability states and therefore the ones which contribute the most to $\langle Q \rangle$ are examined in the simulation.

By maintaining the probability of the state chosen in our MC simulations as the Boltzmann's probability, i.e. $p_{\mu_i} = \frac{e^{-\frac{E_{\mu_i}}{k_B T}}}{Z}$ (for a canonical ensemble of states) we obtain,

$$Q_M = \frac{1}{M} \sum_{i=1}^M Q_{\mu_i}. \quad (2.7)$$

Thus, this ensures that the states occur with a correct probability distribution as in a real system and a simple average of the observable over those states (ensemble average) will yield quite an accurate estimation of the value of the observable. Furthermore, from here on we only provide the example for a canonical ensemble of states. If one wants to obtain the expressions for the corresponding grand canonical ensemble of states, one can simply use Eq. (2.4) instead of Eq. (2.3) and the corresponding values of partition function Z .

Since importance sampling provides the sampling of most probable states (only a small fraction of the total number of possible states) this procedure also provides a route to estimate the partition function Z of the system. However, the partition function calculated

in this manner will be noisy and therefore the expectation values of an observable, which will be calculated as a derivative of the partition function would be erroneous. A much better and accurate alternative is to calculate the observables directly with Eq. (2.7), for example by averaging during the simulation (ensemble average) rather than from the partition function [11].

The next question is how exactly one can select the states which occur with the Boltzmann's probability. An inefficient procedure to do this would be to select states at random, as in this manner a vast majority of states considered would be rejected. A second possible method of generating states is to again select states at random but now decide whether or not to accept or reject the states based on Boltzmann's probability proportional to $e^{-\frac{E_\mu}{k_B T}}$. The latter method is a much more efficient. The procedure used in most MC simulation is known as the Markov process which ensures an efficient sampling of the states.

2.2.2 Markov process

Until now we have established that in order to describe the dynamics of the system one needs to solve the master equation, Eq. (2.2). This is achieved by requiring that the transition rates between the states are fixed in such a way that the equilibrium solution for the accessible states are given by the Boltzmann's probability distribution.

Markov process is a method by which a new state η can be obtained from an old state μ during the simulation based on the probability distribution of the occurrence of those states (probability distribution function). The newly generated state η must be selected at random from all the possible states accessible to μ and the probability of the particular selection, $P(\mu \rightarrow \eta)$ is known as the transition probability. For a transition to be described by Markov process it must not depend on time and must also be memoryless. This means that the transition probability $P(\mu \rightarrow \eta)$ must only depend on the states μ and η and not on the history of states before them during the course of the simulation.

Moreover the sum rule for all the other possible accessible states, $\sum_{\eta} P(\mu \rightarrow \eta) = 1$ must hold, since we are dealing with normalized probabilities and the system must end up in some state. We must keep in mind that although a Markov process must generate a state, $P(\mu \rightarrow \mu)$ need not be zero as during a Markov process the system can remain in the same state for that particular iteration in the algorithm, without violating the above mentioned criterion. The series of states generated in the process is known as a Markov chain.

To ensure that each state occurs with the correct probability as in a Markov process two additional conditions must be specified which we shall now describe in detail. Firstly, the simulation must be ergodic, i.e. all the states of the system should be in principle accessible from the current state. This means that even though some of the transition probabilities between certain specific states may be zero, at least one path joining those states must exist. In other words even if the transition between two states is restricted they must be accessible via a intermediate set of states. The second condition is known as detailed balance which ensures that it is the Boltzmann's probability distribution that is generated during the MC simulations.

Let us consider the master equation at equilibrium

$$\sum_{\mu} p_{\mu} P(\mu \rightarrow \eta) = \sum_{\eta} p_{\eta} P(\eta \rightarrow \mu). \quad (2.8)$$

This gives us the transition probabilities p_{μ} in an equilibrium Markov process. However, this alone is not sufficient to generate the required probability distribution for the states in which the system can be found. This is because the system may end up in a dynamic equilibrium. When this occurs during the algorithm the situation is described as a limit cycle whereby the system will alternate between a fixed number of states, satisfying the above equation but not necessarily the correct equilibrium distribution. The second condition (also mentioned above) respected by any Markov process is the condition of detailed balance which ensures that such limit cycles are not formed. According to the

condition of detailed balance the following holds true

$$p_\mu P(\mu \rightarrow \eta) = p_\eta P(\eta \rightarrow \mu). \quad (2.9)$$

The left-hand side of the Eq. (2.9) represents the probability of transition from the state μ to η and the right-hand side gives the probability of the opposite situation i.e transition from state η to μ . By requiring that these two probabilities are equal, we are ensuring that the limit cycles are not formed during the course of the simulation. This is because in a limit cycle when the system is changing between a fixed number of states in a cyclic manner, the conditions of detailed balance and ergodicity themselves are violated.

Now, subject to the condition that the system transition during the course of the MC simulation observes detailed balance and that the Boltzmann's distribution gives the desired probability distribution of the states the system can be found in, the following relation holds true

$$\frac{P(\mu \rightarrow \eta)}{P(\eta \rightarrow \mu)} = \frac{p_\eta}{p_\mu} = e^{-\beta(E_\eta - E_\mu)}. \quad (2.10)$$

In practice, the transition probabilities can be manipulated in a few ways to make the algorithm computationally efficient and yet satisfying the conditions of ergodicity and detailed balance. For instance one can adjust the transition rates in the numerator and the denominator individually preserving the ratio. Moreover, so as to satisfy the condition of detailed balance, $P(\mu \rightarrow \eta)$ can be adjusted by making an opposite change to $P(\eta \rightarrow \mu)$, thus ensuring that the sum rule is still obeyed. Finally, $P(\mu \rightarrow \mu)$ can be set to any value as the detailed balance condition will always be satisfied.

The next step in the actual realization of the MC simulations is to split the transition probabilities into two components, $P(\mu \rightarrow \eta) = g(\mu \rightarrow \eta) \cdot A(\mu \rightarrow \eta)$, where, $g(\mu \rightarrow \eta)$ is the likelihood of the algorithm generating the Markov chain attempting to evolve the state μ to the state η . The second component $A(\mu \rightarrow \eta)$ is the acceptance probability,

which is an input in the simulation, indicating whether a particular transition is accepted or rejected. Therefore Eq. (2.10) may be recasted into the following form

$$\frac{P(\mu \rightarrow \eta)}{P(\eta \rightarrow \mu)} = \frac{g(\mu \rightarrow \eta)A(\mu \rightarrow \eta)}{g(\eta \rightarrow \mu)A(\eta \rightarrow \mu)}. \quad (2.11)$$

In principle, the acceptance probability can be chosen as any number between zero and one. Therefore $\frac{A(\mu \rightarrow \eta)}{A(\eta \rightarrow \mu)}$ can take any values between zero and infinity and so can $g(\mu \rightarrow \eta)$ and $g(\eta \rightarrow \mu)$. In the next section we shall discuss the well established Metropolis algorithm used in choosing these different probability components in a MC simulation.

2.2.3 Metropolis algorithm

The algorithm used for most of the MC calculations presented in this thesis is the Metropolis algorithm [15], described here for a particular set of classical configurations corresponding to the displacement of the individual molecules comprising the system. A particular displacement configuration is selected at random and is then changed to a new value based on selection probabilities, $g(\mu \rightarrow \eta)$ chosen via a random number generator. This ensures that all possible states are equally accessible hence,

$$\frac{P(\mu \rightarrow \eta)}{P(\eta \rightarrow \mu)} = \frac{A(\mu \rightarrow \eta)}{A(\eta \rightarrow \mu)} = e^{-\beta(E_\eta - E_\mu)}. \quad (2.12)$$

We should mention that, although in every iteration during a MC simulation only states differing from μ by change of a single molecules' displacement (for example) are considered, the ergodicity criterion is still maintained because a path always exists connecting all those possible states. From Eq. (2.12) it can be seen that during the simulation when transitioning from one state to another the only constraint is the ratio of their acceptance rates. This allows for considerable flexibility in the algorithm in particular the largest factor in the acceptance ratio can be set to unity and the other factor can be made to

compensate, i.e.

$$A(\mu \rightarrow \eta) = e^{-\beta(E_\eta - E_\mu)}, \quad \text{if } E_\eta - E_\mu > 0, \quad \text{otherwise } A(\mu \rightarrow \eta) = 1. \quad (2.13)$$

Alternatively, during the course of the simulation, if the new state has an energy lower than that of the current state it is always accepted. Otherwise if the new state has energy higher than that of the current state it is accepted based on the probability given by Eq. (2.13). This is a terse description of the very powerful Metropolis algorithm. The Metropolis algorithm ensures that new states are generated on a regular basis and states that are potential candidates for the system are not rejected, i.e. importance sampling is always respected.

2.2.4 Ground state techniques

In many scenarios the properties of the system in the ground state is required to be simulated. In principle, by executing MC simulations at a very low temperature the ground state properties of the system can be recovered. However, most energy landscapes of real systems comprises numerous local minima. Therefore running a MC simulation at low temperature will be highly inefficient as the system may spend a long time being stuck in one of these local minima, instead of probing the actual global minimum. We have used two ground state techniques in this thesis.

Conjugate gradient

One of the most commonly implemented method for energy minimization in condensed matter physics is the conjugate gradient method. Consider for example the case of variable vectors corresponding to atomic displacement $\{q_i\}$. In this algorithm we minimize the

energy function by moving the atom positions q_i , as follows:

$$q_i^t = q_i^{t-1} + \kappa \cdot h_i^{t-1} \quad \text{with } i = 1, \dots, N. \quad (2.14)$$

Here $h_i^t = F(q_i^t) + \gamma_i^t h_i^{t-1}$ and γ is updated from the Fletcher-Reeves formula as

$$\gamma_i^t = \frac{F(q_i^t) \cdot F(q_i^t)}{F(q_i^{t-1}) \cdot F(q_i^{t-1})}. \quad (2.15)$$

where $F(q_i^t)$ are the forces corresponding to the particular displacement configuration, q_i^t , h_i^t is the search direction vector and κ is a constant in the simulations. At the beginning of calculation (when $t = 1$), we can make the search direction vector $h_0 = 0$. Therefore in conjugate gradient method energy minimization is carried out in the following manner. At every iteration for a particular configuration of atoms the potential energy and the net forces on all the atoms are evaluated. If every force vanishes the minimum energy solution is obtained. If not, atoms are moved according to Eq. (2.14) and Eq. (2.15) respectively and the cycle is repeated.

Despite the broad applicability of this method in energy minimization, in many circumstances conjugate gradient methods may fail as the algorithm can get trapped in local minima. This is primarily because in that situation the method does not provide any option to get out of the said local minima.

Simulated annealing

Simulated Annealing provides a robust procedure of reaching the global minimum of the system with complicated energy landscapes. The algorithm evolves the system at hand based on a probability that depends on the difference in energy between the current state and a neighboring state, and also temperature. In practice, the Metropolis algorithm with temperature being a variable can also be used. The main advantage lies in the essential rule governing the process, a system can move to a state with higher energy during the

course of the simulation. This ensures that the system is not trapped in any local minima for a long time as it can escape such a situation by moving out to an intermediary higher energy state. Thus, simulated annealing is quite an efficient algorithm in comparison to conjugate gradient or the steepest descent method.

2.2.5 Summary

In this section we have discussed the essential theory behind one of the main statistical methods that we will make extensive use of in our computational framework to model transport through OSCs. In the next chapter we shall discuss the tight binding model, which describes all the different interactions in organic materials. Some of the interactions are associated with classical variables. These classical terms in the tight binding Hamiltonian will be evolved via MC simulations to give the finite temperature properties of our system.

We will now shift our focus to the second computational technique used in our multi-scale modelling of OSCs. This is known as Density Functional Theory.

2.3 Density Functional Theory

In solid state theory many important electronic structure information of different systems can be obtained by describing their essential interactions in the form of microscopic models. These models require parameters which are generally obtained by some sort of a fitting procedure to experimental results or by the use of computationally heavy theoretical schemes (e.g. many-body techniques). For example, in this thesis we will describe the phase diagram and transport properties of OSC using microscopic models in Chapters 3 and 4.

However, in order to obtain "realistic" quantitative information about the electronic structure of materials, one requires a self-contained theory that does not rely on any fitting

parameters. Moreover, the route to this should be computationally inexpensive and must describe a broad range of systems from atoms to molecules and also solids, surfaces and crystals. Based on pioneering works in the last few decades [20, 21], the solution for such a "realistic" method lies on a well-tested route, which is known to give results with good levels of accuracy in predicting material properties. This electronic structure theory is known as DFT. Here we shall provide an outline to this powerful and ubiquitous theory.

In quantum mechanics, the Hamiltonian is an operator corresponding to the total energy of the system and describes all the interactions in the problem. The Hamiltonian operator \hat{H} , for an ensemble comprising N_e electrons of mass m_e , moving in a potential generated by N_N nuclei each with mass M_I (and atomic number Z_I) is given by :

$$\hat{H} = T_e(\mathbf{r}) + T_n(\mathbf{R}) + V_{ee}(\mathbf{r}) + V_{en}(\mathbf{r}, \mathbf{R}) + V_{nn}(\mathbf{R}) \quad (2.16)$$

where the independent contributions to \hat{H} (above) are as follows:

Electronic Kinetic Energy

$$T_e(\mathbf{r}) = \sum_{i=0}^{N_e} -\frac{\hbar^2}{2m_e} \nabla_{\mathbf{r}_i}^2 \quad (2.17)$$

Nuclei Kinetic Energy

$$T_n(\mathbf{R}) = \sum_{I=0}^{N_N} -\frac{\hbar^2}{2M_I} \nabla_{\mathbf{R}_I}^2 \quad (2.18)$$

Electron-Electron Coulomb energy

$$V_{ee}(\mathbf{r}) = \frac{1}{2} \sum_{i \neq j}^{N_e} \frac{e^2}{|\mathbf{r}_i - \mathbf{r}_j|} \quad (2.19)$$

Electron-Nuclei Coulomb energy

$$V_{en}(\mathbf{r}, \mathbf{R}) = -\frac{1}{2} \sum_{i,j}^{N_e, N_N} \frac{e^2 Z_I}{|\mathbf{r}_i - \mathbf{R}_i|} \quad (2.20)$$

Nuclei-Nuclei Coulomb energy

$$V_{nn}(\mathbf{R}) = \sum_{i,j} \frac{Z_i Z_j}{|\mathbf{R}_i - \mathbf{R}_j|}. \quad (2.21)$$

Here the coordinates of the i th electron is \mathbf{r}_i and that of the I th nucleus is \mathbf{R}_I .

The central problem in condensed matter physics is to solve the many-body Schrödinger equation for a large number of nuclei and electrons described by the Hamiltonian of, Eq. (2.16). In order to make such a problem tractable, several approximations need to be introduced. Firstly, since electrons and nuclei are bound to each other, one may assume that they travel at non-relativistic speeds and hence the dynamics of the system is governed by the non-relativistic Schrödinger equation. The problem can be described by the time-independent Schrödinger equation as

$$\hat{H}\Psi = E\Psi. \quad (2.22)$$

Here E is the energy and $\Psi = \Psi(\mathbf{r}_1, \mathbf{r}_2, \dots, \mathbf{r}_n, \mathbf{R}_1, \mathbf{R}_2, \dots, \mathbf{R}_n)$ is the many-body wavefunction of the system. Eq. (2.22) is the starting point for all many-body problems in quantum mechanics.

The second approximation assumes the following: since nuclei are many times heavier than electrons, i.e. $M_I \gg m_e$, the nuclear dynamics occur at a timescale much longer than the corresponding electron dynamics. Accordingly the nuclei can be described as classical particles. They thus generate a static potential in which electrons move. The total wavefunction Ψ can thus be decomposed into electronic and nuclear constituent

components, namely

$$\Psi(\mathbf{r}, \mathbf{R}) = \psi(\mathbf{r}; \mathbf{R})\phi(\mathbf{R}). \quad (2.23)$$

The equation (2.23) describes the so called Born-Oppenheimer approximation [18]. Consequently, the Schrödinger equation can be separated into an electron and a nuclear component

$$\hat{H}_e \psi(\mathbf{r}; \mathbf{R}) = E_e(\mathbf{R}) \psi(\mathbf{r}; \mathbf{R}) = \quad (2.24)$$

$$= (T_e + V_{ee} + V_{en}) \psi(\mathbf{r}; \mathbf{R}), \quad (2.25)$$

and

$$\hat{H}_N \phi(\mathbf{R}) = E \phi(\mathbf{R}) = \quad (2.26)$$

$$= (T_n + V_{nn} + E_e(\mathbf{R})) \phi(\mathbf{R}), \quad (2.27)$$

where $\psi(\mathbf{r}; \mathbf{R})$ and $\phi(\mathbf{R})$ are the electronic and nuclear wavefunctions respectively. $E_e(\mathbf{R})$ is the total electron energy for a fixed nuclei configuration, while E is the total energy of the system.

Thus, in all the DFT calculations described in this thesis the Born-Oppenheimer approximation holds true.

2.3.1 Non-interacting systems

The Born-Oppenheimer approximation massively simplifies the electronic structure problem. However, the Schrödinger equation in Eq. (2.24) is far from being solved. For the special case when the electron-electron interaction term, V_{ee} , can be neglected, the solution is trivial. The Hamiltonian of the system will then reduce to a sum of single particle

Hamiltonians, each of them described by single particle Schrödinger equation as

$$\left[-\frac{1}{2} \nabla_{\mathbf{r}}^2 - \sum_{i=1}^{N_N} \frac{Z_I}{|\mathbf{r} - \mathbf{r}_i|} \right] \psi_{\alpha}(\mathbf{x}) = e_{\alpha} \psi_{\alpha}(\mathbf{x}). \quad (2.28)$$

Here we have introduced a coordinate $\mathbf{x}_n = (\mathbf{r}_n, \sigma_n)$ which includes both electron position and spin respectively and the index α in Eq. (2.28) represents the corresponding single particle states.

In order to satisfy Pauli exclusion principle which restricts the occupation of a single orbital to two electrons carrying opposite spins, the non-interacting many particle wavefunction of the system can be written down as an anti-symmetrized product or a Slater determinant of N_e occupied single-particle wavefunctions $\{\psi_{\alpha}\}_{\alpha=1,2,\dots,N_e}$. Thus this takes the following form

$$\psi(\mathbf{X}) = \frac{1}{\sqrt{N!}} \begin{vmatrix} \psi_1(\mathbf{x}_1) & \psi_1(\mathbf{x}_2) & \dots & \psi_1(\mathbf{x}_{N_e}) \\ \psi_2(\mathbf{x}_1) & \psi_2(\mathbf{x}_2) & \dots & \psi_2(\mathbf{x}_{N_e}) \\ \cdot & \cdot & \cdot & \cdot \\ \cdot & \cdot & \cdot & \cdot \\ \cdot & \cdot & \cdot & \cdot \\ \psi_{N_e}(\mathbf{x}_1) & \psi_{N_e}(\mathbf{x}_2) & \dots & \psi_{N_e}(\mathbf{x}_{N_e}) \end{vmatrix}.$$

The single-particle orbitals can be expressed as products of the spacial (radial) and the spin components as $\psi_{\alpha}(\mathbf{x}_n) = \psi_{\alpha}(\mathbf{r}_n) \psi_{\alpha}(\sigma_n)$. Moreover, the ground state energy of the system, E_0 , is simply the sum of the eigenvalues of the occupied single particle eigenstates.

$$E_0 = \sum_{\alpha=1}^{\text{occupied}} e_{\alpha} \quad (2.29)$$

2.3.2 Hartree-Fock method

One way to tackle the electronic structure problem is by using the variational principle [19]. The variational principle states that the ground state energy of the system, E_0 , is always less than or equal to the expectation value of \hat{H} calculated with any trial wavefunction ψ . Mathematically this reads $E_0 \leq \langle \psi | \hat{H} | \psi \rangle$.

Thus, by varying the trial wavefunction, ψ within the full Hilbert space, until the expectation value of \hat{H} is minimized, one can obtain the wavefunction as well as the energy corresponding to the ground state. The variational principle can also be expressed in the following functional way:

$$E[\psi] = \frac{\langle \psi | \hat{H} | \psi \rangle}{\langle \psi | \psi \rangle}, \quad (2.30)$$

where

$$\langle \psi | \hat{H} | \psi \rangle = \sum_{\sigma_1 \dots \sigma_{N_e}} \int d\mathbf{r}_1 \dots d\mathbf{r}_{N_e} \psi^*(\mathbf{x}_1, \mathbf{x}_2, \dots, \mathbf{x}_{N_e}) \hat{H} \psi(\mathbf{x}_1, \mathbf{x}_2, \dots, \mathbf{x}_{N_e}) \quad (2.31)$$

and

$$\langle \psi | \psi \rangle = \sum_{\sigma_1 \dots \sigma_{N_e}} \int d\mathbf{r}_1 \dots d\mathbf{r}_{N_e} |\psi(\mathbf{x}_1, \mathbf{x}_2, \dots, \mathbf{x}_{N_e})|^2. \quad (2.32)$$

According to variational principle, every eigenstate of the Schrödinger equation in Eq. (2.24) is a stationary point of the functional $E[\psi]$. Alternately, the excited states of the system are saddle points, while the ground state ψ_0 corresponds to the absolute minimum.

In the Hartree-Fock (HF) method the subspace of the trial wavefunctions is chosen to be a single Slater determinant. In order to solve the problem, the expectation value of \hat{H} is minimized with respect to single-particle orbitals $\psi_\alpha(\mathbf{r})$. The Hartree-Fock equations

are as follows

$$\epsilon_\alpha \psi_\alpha(\mathbf{r}) = \left[-\frac{1}{2} \nabla_{\mathbf{r}}^2 + V_{eN}(\mathbf{r}) \right] \psi_\alpha(\mathbf{r}) + \sum_{\beta=1}^{N_e} \int d\mathbf{r}' \frac{|\psi_\beta(\mathbf{r}')|^2}{|\mathbf{r} - \mathbf{r}'|} \psi_\alpha(\mathbf{r}) - \sum_{\beta=1}^{N_e} \delta_{\sigma_\alpha, \sigma_\beta} \int d\mathbf{r}' \frac{\psi_\beta^*(\mathbf{r}') \psi_\beta(\mathbf{r}')}{|\mathbf{r} - \mathbf{r}'|} \psi_\beta(\mathbf{r}), \quad (2.33)$$

where ϵ_α are Lagrange multipliers of the orthonormal single-particle orbitals. These equations need to be solved self-consistently. The first term in Eq. (2.33) accounts for the kinetic energy of the electron and the electron-ion potential, while the final two terms outline the electron-electron interaction. Describing in more detail, the second term in Eq. (2.33) is the Hartree term which is simply the electrostatic potential arising from a charge distribution of N electrons. As such, the Hartree term includes the unphysical self-interaction of an electron with itself when $j = i$. This is exactly canceled out by the fourth term which is the exchange potential. This arises from the Pauli principle which imposes the wavefunction to be anti-symmetric. In practice, the effect of the exchange interaction is to make electrons with like spins to avoid each other.

The difference between the ground state solution E_0 and the Hartree-Fock energy E_{HF} is the correlation energy $E_c = E_0 - E_{HF}$. This contains quantum many particle contribution to the total energy which is not accounted for by the Pauli principle. We shall discuss in detail the different approximate forms of the correlation energy in the coming sections of this chapter.

Finally, an effective way for interpreting the eigenvalues of the HF solution is by removing an electron from a particular eigenstate without perturbing the rest of the system, also commonly recognized as the vertical ionization energy. As a matter of fact, in HF theory the first ionization energy of the system is equal to the negative of the orbital energy of the highest occupied molecular orbital (HOMO). This is known as the Koopmans' theorem [24], which is exactly satisfied for the HF approach.

2.3.3 Hohenberg-Kohn theorem

The main ground work behind DFT was laid by Hohenberg and Kohn [20]. The essential idea behind DFT, is to have the ground state electronic density $n(\mathbf{r})$ as the principal quantity in the theory instead of the complicated many-body wavefunction. Therefore in this fashion, the problem is more tractable, as it now depends only on three spacial variables instead of $3N_e$ variables of the many-body wavefunction. The electron density $n(\mathbf{r})$, which is the probability of finding an electron at a position \mathbf{r} is given by

$$n(\mathbf{r}) = \int |\psi(\mathbf{x}_1, \mathbf{x}_2, \mathbf{x}_3, \dots, \mathbf{x}_n)|^2 d\mathbf{r}_2 d\mathbf{r}_3, \dots, d\mathbf{r}_n. \quad (2.34)$$

The number of electrons in the system is

$$N_e = \sum \int n(\mathbf{r}) d\mathbf{r}. \quad (2.35)$$

The first Hohenberg-Kohn theorem states that the external potential $V_{ext}(\mathbf{r})$ is a unique functional of $n(\mathbf{r})$. This means that the electron density determines both the number of electrons in the system and the external potential $V_{ext}(\mathbf{r})$. Alternately, this implies that any ground-state observable of a particular system is uniquely determined by the ground-state electron density $n(\mathbf{r})$. The total energy can therefore be written as a functional of the density,

$$E = E[n] = T[n] + V_{ee}[n] + V_{en}[n], \quad (2.36)$$

where $T[n]$ is the functional of the electron kinetic energy, $V_{ee}[n]$ is the functional describing the electron-electron interactions and $V_{en}[n]$ is the functional corresponding to the electron-nuclear interactions.

The second Hohenberg-Kohn theorem is essentially a variational principle, which states that the energy functional of Eq. (2.36) can be minimized only for the true ground state

density n_0 . Mathematically this means that when $n \neq n_0$ then $E_0 < E[n]$, where E_0 is the ground state energy. Therefore assuming that the total energy functional is known [i.e. all the components of Eq. (2.36)] the ground state density can be calculated by this theorem.

Although the Hohenberg-Kohn theorems are extremely powerful they do not offer a procedure to minimize Eq. (2.36), to obtain the ground state density.

2.3.4 The Kohn-Sham scheme

About one year after the Hohenberg-Kohn theorem was proposed, Kohn and Sham formulated a systematic method to minimize the total energy functional, which forms the basis of modern DFT calculations. They established that the fully interacting many-body problem can be mapped onto an auxiliary system of non-interacting electrons with a requirement that the latter one has the same ground state density, and thus the same ground state energy, as the interacting system under examination.

The density of a system of non-interacting electrons under the influence of an external potential, V_{ext} , can be expressed in terms of single-particle wavefunctions, ψ_i as

$$n(\mathbf{r}) = \sum_{i=1}^{N_e} |\psi_i(\mathbf{r})|^2. \quad (2.37)$$

The Kohn-Sham energy functional can now be written down as

$$E_{KS}[n] = T_s[n] + \int n(\mathbf{r})V_{ext}(\mathbf{r})d\mathbf{r} + E_H + E_{xc}, \quad (2.38)$$

where $T_s[n]$ is the kinetic energy of the reference system of non-interacting particles:

$$T_s[n] = -\frac{\hbar^2}{2m} \sum_i \langle \psi_i | \nabla^2 | \psi_i \rangle. \quad (2.39)$$

The second term in Eq. (2.38) represents the interaction of the electron with the external

potential V_{ext} . Next, the classical Coulomb repulsion (Hartree) energy is given by

$$E_H = \frac{e^2}{2} \int \frac{n(\mathbf{r})n(\mathbf{r}')}{|\mathbf{r} - \mathbf{r}'|} d\mathbf{r}d\mathbf{r}'. \quad (2.40)$$

Finally E_{xc} is the exchange and correlation (xc) energy. The xc energy includes all the remaining contributions to the energy that are not already included in the other terms.

All the contributions in Eq. (2.38) can be explicitly written down for any given system except for the final term. Indeed in DFT, the exact functional dependence of the E_{xc} is unknown and must be approximated. These approximations will be discussed in detail in the next subsection.

In order to obtain the ground state energy, Eq. (2.38) must be minimized under the condition that the wavefunctions are normalized, i.e. $\langle \psi_i | \psi_j \rangle = \delta_{ij}$. This alternately means that the density is integrated to the correct number of electrons given by Eq. (2.35). This gives us the following Kohn-Sham equation

$$\hat{H}_{KS} \psi_i(\mathbf{r}) = \varepsilon_i \psi_i(\mathbf{r}), \quad (2.41)$$

$$\left[\frac{\hbar^2}{2m_e} \nabla^2 + V_{\text{eff}}(\mathbf{r}) \right] \psi_i(\mathbf{r}) = \varepsilon_i \psi_i(\mathbf{r}). \quad (2.42)$$

The effective Kohn-Sham potential V_{eff} , is essentially the functional derivative of the energy functional in Eq. (2.38) with respect to $n(\mathbf{r})$. It can be broken down as

$$V_{\text{eff}}(\mathbf{r}) = V_{\text{ext}}(\mathbf{r}) + V_H(\mathbf{r}) + V_{xc}(\mathbf{r}), \quad (2.43)$$

where the electrostatic Hartree potential is

$$V_H(\mathbf{r}) = e^2 \int \frac{n(\mathbf{r}')}{|\mathbf{r} - \mathbf{r}'|} d\mathbf{r}', \quad (2.44)$$

and the xc potential is

$$V_{xc}(\mathbf{r}) = \frac{\delta E_{xc}[n]}{\delta n(\mathbf{r})}. \quad (2.45)$$

The Kohn-Sham equations must be solved self-consistently with respect to the density $n(\mathbf{r})$. In practice, the Kohn-Sham approach used in DFT certainly has its advantage over Hartree-Fock. Firstly, the Kohn-Sham effective potential is a local operator (at least for some flavors of DFT) which makes DFT computationally much less expensive than Hartree-Fock. Moreover in many cases DFT performs better than Hartree-Fock because, although DFT describes correlation effects of a many-body system in an approximate fashion, it recovers part of the electron correlation energy, neglected in Hartree-Fock.

Estimation of the total energy

The eigenvalues, ε_i which are introduced in the minimization procedure in Eq. (2.41) and Eq. (2.42) are the Lagrange multipliers imposing charge conservation. In the Kohn-Sham equation they appear as single-particle energies. In order to obtain the total electronic energy we sum up these single particle Kohn-Sham eigenvalues but include the so called, double counting corrections. Thus the total energy of the system is

$$E = \sum_{i=1}^{N_e} \varepsilon_\alpha + E_{xc}[n] - \int d\mathbf{r} V_{xc}(\mathbf{r})n(\mathbf{r}) - \frac{1}{2} \int d\mathbf{r}d\mathbf{r}' \frac{n(\mathbf{r})n(\mathbf{r}')}{|\mathbf{r} - \mathbf{r}'|}. \quad (2.46)$$

Estimation of the forces

As discussed earlier, due to the Born-Oppenheimer approximation the position of the atomic nuclei only enters into the electronic Hamiltonian. After solving the Kohn-Sham equations for a particular nuclear configuration, the forces acting on the static nuclei can

be obtained by using the Hellman-Feynmann theorem [22] as

$$F_i = -\frac{\partial(E + V_{NN})}{\partial \mathbf{R}_i}, \quad (2.47)$$

where V_{NN} is the classical nuclear-nuclear interaction energy:

$$V_{NN} = \sum_{i < j}^{N_N} \frac{Z_i Z_j}{|\mathbf{R}_i - \mathbf{R}_j|}. \quad (2.48)$$

Eq. (2.47), can be used to calculate the equilibrium geometry of molecules and solids within the Born-Oppenheimer approximation, by changing \mathbf{R}_i until the forces F_i vanish (they are negligible).

Interpretation of Kohn-Sham eigenvalues

In the previous section we have outlined that the Kohn-Sham scheme is a method to map the real many-body problem onto a fictitious system of non-interacting electrons. Strictly speaking the ground state electron density obtained by self-consistently solving the Kohn-Sham equations do not represent the molecular orbitals of any "real" (many electron) system. Moreover, ε_i are merely Lagrange multipliers used to enforce the orthonormality of the Kohn-Sham states. The Koopmans' theorem [24] is not valid for DFT but instead Janak's theorem [23] is applicable. This establishes that the Kohn-Sham eigenvalues ε_i are equal to the derivative of the total energy functional with respect to the occupation, f_i , of the Kohn-Sham eigenstates ψ_i , i.e.

$$\varepsilon_i = \frac{\delta E}{\delta f_i}. \quad (2.49)$$

The occupations f_i are defined by the following expression

$$n(\mathbf{r}) = \sum_{i=1}^{\text{occupied}} |\psi_i|^2 = \sum_{i=1}^{\infty} f_i |\psi_i|^2. \quad (2.50)$$

Although the Kohn-Sham eigenvalues do not have any physical meaning and ϵ^{KS} are not excitation energies, the highest occupied molecular orbital (HOMO) associated with the Kohn-Sham eigenvalue ϵ^{HOMO} is equal to the ionization energy (I.E.) of the real system

$$\text{I.E.} = -\epsilon^{\text{HOMO}}. \quad (2.51)$$

However, the above relation is only true if the xc energy is an exact one. In general I.E. can be always obtained as:

$$\text{I.E.} = E_0(N_e - 1) - E_0(N_e), \quad (2.52)$$

and in a similar manner the electron affinity (E.A.) can be calculated as

$$\text{E.A.} = E(N_e) - E(N_e + 1) \quad (2.53)$$

where $E_0(N_e)$ is the ground-state energy of a system of N_e electrons (neutral). The resultant band-gap of the real system comprising of N_e electrons is

$$E_g^{\text{real}} = -\text{E.A.} + \text{I.E.} \quad (2.54)$$

In contrast the Kohn-Sham band gap, $E^{\text{KS}} = \epsilon_{\text{LUMO}} - \epsilon_{\text{HOMO}}[2]$, differs from the real bandgap due to a derivative discontinuity [31, 32, 33]. This is defined as

$$\left. \frac{\delta E_{xc}[n]}{\delta n(\mathbf{r})} \right|_{N_e+\delta} - \left. \frac{\delta E_{xc}[n]}{\delta n(\mathbf{r})} \right|_{N_e-\delta} = \Delta \quad (2.55)$$

where δ is an infinitesimal shift of the number of electrons in the system, N_e . Δ is a system dependent quantity. The ambiguity due to derivative discontinuity apparent in

²HOMO: Highest Occupied Molecular Orbital and LUMO: Lowest Unoccupied Molecular Orbital.

the Kohn-Sham bands can be summarized as

$$E_g^{\text{real}} - E_g^{\text{KS}} = \Delta > 0. \quad (2.56)$$

Thus due to the derivative discontinuity one must be conscious that the DFT band gap is incorrect because the Kohn-Sham band gap will never be equal to the real one unless $\Delta = 0$. However it must be said that despite the lack of any physical meaning associated to the Kohn-Sham eigenlevels it has been found that in practice they provide an excellent description (first approximation) of the experimental band structure for a large number of molecules and solids.

2.3.5 Spin polarized DFT

DFT can be extended to spin polarized systems [25, 26] by decomposing the charge density $n(\mathbf{r})$, into its spin components

$$n(\mathbf{r}) = n^\uparrow(\mathbf{r}) + n^\downarrow(\mathbf{r}), \quad (2.57)$$

where $n^\uparrow(\mathbf{r})$ and $n^\downarrow(\mathbf{r})$ are respectively the density of the majority and minority electrons. Therefore the magnetic density can be defined as

$$m(\mathbf{r}) = n^\uparrow(\mathbf{r}) - n^\downarrow(\mathbf{r}). \quad (2.58)$$

Majority and minority electrons must now satisfy two separate Kohn-Sham equations

$$\hat{H}_{KS}^\sigma \psi_i^\sigma = \epsilon_i^\sigma \psi_i^\sigma, \quad (2.59)$$

where σ is the spin index, $\sigma = (\uparrow, \downarrow)$. For situations which causes mixing between the majority and minority electrons (for example due to spin-orbit coupling) additional terms

are needed in the spin polarized Hamiltonian (like relativistic corrections and the spin-orbit Hamiltonian) [27]. Thus the spin dependent effective Kohn-Sham potential now takes the following form

$$V_{\text{eff}}^{\sigma}(\mathbf{r}) = V_{\text{ext}}(\mathbf{r}) + \int \frac{e^2 n(\mathbf{r}')}{|\mathbf{r} - \mathbf{r}'|} d\mathbf{r}' + \frac{\delta E_{\text{xc}}[n^{\uparrow}(\mathbf{r}), n^{\downarrow}(\mathbf{r})]}{\delta n^{\sigma} \mathbf{r}}. \quad (2.60)$$

As evident from Eq. (2.60), for non-relativistic calculations in the absence of an external magnetic field, the external potential $V_{\text{ext}}(\mathbf{r})$ and the Hartree potential $V_H(\mathbf{r})$ are not spin dependent. The Kohn-Sham equations can also be extended to account for non-collinear magnetism with the introduction of two component spinor wavefunction. However, the materials studied in this thesis do not exhibit non-collinear magnetism under any circumstances and hence this will not be discussed any further.

2.3.6 Exchange-correlation functionals

In principle, DFT formalism is exact, i.e. the ground-state total energy and density of a fully interacting system can be exactly obtained by minimizing the energy functional. However, this would only be true if the exact functional dependence of E_{xc} on $n(\mathbf{r})$ is known. In this section we shall discuss the several approaches to an approximate xc energy, which work quite well in predicting the properties for a wide variety of materials.

Local spin density approximation (LSDA)

The most simple approximation is the local spin density approximation (LSDA). This approximation was proposed in the original work of Kohn and Sham and is one of the most widely used DFT functionals till date. As evident from Eq. (2.41) and Eq. (2.42), the value of $V_{\text{xc}}[n]$ also depends on $n(\mathbf{r}')$ for all \mathbf{r}' , however LDA assumes that it only depends on $n(\mathbf{r})$, i.e. the density calculated at that particular point \mathbf{r} . Furthermore the xc energy is assumed to be the same as that of a homogeneous electron gas with the same

density, which is known explicitly. Therefore

$$E_{xc}^{\text{LSDA}}[n^\uparrow, n^\downarrow] = \int d\mathbf{r} n(\mathbf{r}) e_{xc}^{\text{hom}}(n^\uparrow(\mathbf{r}), n^\downarrow(\mathbf{r})), \quad (2.61)$$

where $e_{xc}^{\text{hom}}(n^\uparrow(\mathbf{r}), n^\downarrow(\mathbf{r}))$ is the xc energy density of the uniform (interacting) homogeneous electron gas, which is known. The exchange part of the energy is given by the following expression

$$\epsilon_x = -\frac{e^2}{4\pi\epsilon_0} \frac{3}{4} \left(\frac{3n}{\pi} \right)^{\frac{1}{3}}, \quad (2.62)$$

while the correlation part ϵ_c can be computed by using Quantum Monte Carlo (QMC) techniques. In general LSDA works really well for systems with slowly varying densities, for example metals. Moreover, LSDA also gives reasonable results for other materials because of a systematic error cancellation, namely LSDA underestimates the exchange energy, but it overestimates the correlation one, with the two having opposite signs.

The most commonly used parameterization for LDA is by Perdew and Zunger [34]. The numerous strengths and weaknesses of LSDA have been well documented in literature [37] in particular the structural and vibrational properties such as bond lengths, bond angles and phonon vibrational frequencies are well predicted by the functional. The principal drawback of LSDA is its underestimation of the bandgap of semiconductors and insulators. In many cases this can be so drastic that LSDA may predict an unphysical metallic ground state for semiconductors and insulators!

Generalized gradient approximation (GGA)

If the density of the system under investigation is inhomogeneous such as in molecules, it is a sensible approach to describe the xc energy as a function of the density and its gradient. In practice, such a semi-local approach is included in the generalized gradient approximation (GGA), where the xc energy is a functional of the density and its gradient.

For the spin polarized case the energy functional can be expressed as

$$E_{xc}^{\text{GGA}}[n^\uparrow, n^\downarrow] = \int d\mathbf{r} f(n^\uparrow(\mathbf{r}), n^\downarrow(\mathbf{r}), \nabla n^\uparrow(\mathbf{r}), \nabla n^\downarrow(\mathbf{r})). \quad (2.63)$$

There are several formulations of the GGA and the most commonly utilized one is that of Perdew, Burke and Ernzerhof (PBE) [35]. In general, both LDA and GGA fail in describing materials with localized electrons for example *d* and *f* electrons. Also both LDA and GGA fail in describing systems where Van der Waals (vdW) interactions play an important role such as in organic materials, which will be investigated in this thesis. However, GGA does perform better than LDA in describing chemical bonds by correcting the tendency of LDA to overbind molecules.

Meta GGA

There are a number of post GGA methods, which fall in the category of orbital based DFT functionals. One such important functional is meta-GGA [36] where the xc energy functional, in addition to depending on the density and its gradient also depends on the Kohn-Sham kinetic energy density. It must be noted that there are a few varieties of the meta GGA methods. In this thesis, however, we have not made an extensive use of meta GGA. Hence we will keep the discussions limited to this.

Hybrid Functionals

A class of important functionals which are especially popular in the chemistry community is known as hybrid functionals. The xc energy in such hybrid functionals has the following contributions: a fraction from Hartree-Fock exact exchange and the rest from DFT exchange, as well as DFT correlation energy according to the general formula

$$E_{xc}^{\text{hybrid}} = aE_x^{\text{exact}} + (1 - a)E_x^{\text{LDA(GGA)}} + E_c^{\text{LDA(GGA)}}. \quad (2.64)$$

The constant a is either produced theoretically or obtained by fitting to experimental data. The subscripts x and c in Eq. (2.64) stand respectively for the exchange and correlation part of the energy functional. Please note that, strictly speaking because of the fitting parameters, hybrid DFT functionals are not in the spirit of *ab initio* theory. However, for a range of different systems hybrid functionals perform better than standard LDA or GGA functionals due to a partial self-interaction correction.

B3LYP The most important hybrid functional is B3LYP where the xc energy is given by

$$E_{xc}^{\text{B3LYP}} = 0.8E_x^{\text{LDA}} + 0.2E_x^{\text{HF}} + 0.72\Delta E_x^{\text{B88}} + 0.19E_c^{\text{VWN3}} + 0.81E_c^{\text{LYP}}, \quad (2.65)$$

where E_x^{LDA} is the LDA exchange, ΔE_x^{B88} is the exchange of the Becke88 functional (GGA) [37]. E_c^{VWN3} and E_c^{LYP} are Vosko-Wilk-Nusair III [38] and the Lee-Yang-Parr correlation [39] functionals, respectively.

PBE0 Another popular hybrid functionals is PBE0 [41] where the xc energy is defined as

$$E_{xc}^{\text{PBE0}} = \frac{1}{4}E_x^{\text{HF}} + \frac{3}{4}E_x^{\text{PBE}} + E_c^{\text{PBE}}, \quad (2.66)$$

where E_x^{PBE} and E_c^{PBE} are the PBE exchange and correlation energies respectively. This functional is, in principle, parameter free and no fitting to experimental data is required in its derivation.

HSE Another prominent hybrid functional employed by condensed matter physicists is the HSE06 (Heyd-Scuseria-Ernzerhof) [42] one. This functional is designed to include the effect of electron screening in real solids while maintaining computational efficiency, and it is known to work very well for semiconducting systems. In the HSE xc energy the long

range part of the Hartree-Fock exchange is replaced by the corresponding part obtained from PBE as follows

$$E_{xc}^{\text{HSE}} = \frac{1}{4} E_x^{\text{HF},\text{sr},\mu} + \frac{3}{4} E_x^{\text{PBE},\text{sr},\mu} + E_x^{\text{PBE},\text{lr},\mu} + E_c^{\text{PBE}}, \quad (2.67)$$

where lr and sr denote the long range and short range part of the exchange interaction respectively (HF or PBE exchange energy) and μ is the range separation. The short and long range part of the exchange interaction are identified by decomposing the Coulomb kernel [42].

Functionals for strongly correlated systems

For weakly correlated systems LDA and GGA work perfectly in describing their electronic structures accurately. However for strongly correlated systems with well localized states, several DFT functional, exists which improve upon LDA or GGA based methods. These include DFT+ Hubbard U [28, 29, 30] and self-interaction correction [34] methods. Since the systems investigated in this thesis do not fall into this category, we shall not elaborate upon these methods any further. Please note that hybrid functionals are also quite suitable for strongly correlated systems because of a partial (or even significant) cancellation of the self-interaction error.

2.3.7 Implementation of Van der Waals interactions in DFT

Van der Waals (vdW) interactions are ubiquitous in nature playing a crucial role in determining the structure and stability of a wide range of molecules and solids. In particular, vdW interactions or London dispersions have profound importance in organic materials. Local and semilocal Kohn-Sham DFT, are incapable of including any such long-range vdW interactions (interactions which have a long tail) and therefore an accurate first principles description of such interactions is a very challenging problem. This is primarily

because the vdW dispersion energy arises from a correlated motion of electrons resulting in fluctuating charge distributions and, in principle, must be described by many-electron quantum mechanical techniques. Since many Kohn-Sham DFT functionals approximate the correlation energy they fail to accurately describe vdW interactions. Indeed, at present vdW interactions can only be accurately accounted for by high level quantum chemical wavefunction-based methods or by QMC.

The drive for an accurate description of vdW interactions in DFT to achieve chemical accuracy in calculating the binding between molecules as well as in large and complex systems, is becoming an enticing research field in itself. The primary intention here is for a better description of vdW interaction in molecules and solids, while simultaneously maintaining the computational costs similar to the one as incurred with standard (LDA/GGA) DFT calculations. Broadly speaking present day vdW DFT techniques can be divided into three categories:

1. Non local density functionals, which are constructed to capture the pair-wise (two-body) part of the vdW energy [46].
2. Interatomic (pairwise) vdW energy added to the DFT Kohn-Sham energy in a post processing fashion [43, 47].
3. DFT functionals, which have the capacity to describe Coloumb interactions and many-body vdW [48].

We shall now elaborate upon some of the vdW functionals implemented in DFT, which we have made extensive use of in the calculations presented in this thesis.

DFT-D method of Grimme

A pioneering method to incorporate vdW interactions in DFT was introduced by Grimme in his seminal works [43, 45]. This consists of adding a semi-empirical dispersion potential

to the PBE Kohn-Sham DFT energy

$$E_{\text{Grimme}} = E_{\text{KS-DFT}} + E_{\text{disp}}. \quad (2.68)$$

Here the vdW interactions are described by a simple pair-wise interatomic force field. The dispersion energy E_{disp} , for periodic systems can be described by the attractive part of the Lennard-Jones potential [44] as follows

$$E_{\text{disp}} = -\frac{s_6}{2} \sum_{i=1}^{N_{\text{at}}} \sum_{j=1}^{N_{\text{at}}} \sum_L \frac{C_6^{ij}}{|r^{i,0} - r^{j,L}|^6} f_{\text{damp}}(|r^{i,0} - r^{j,L}|), \quad (2.69)$$

where the sums are over all the atoms, N_{at} , in the system and all translations of the unit cell are $L = (l_1, l_2, l_3)$, s_6 is a global scaling factor, C_6^{ij} is the dispersion coefficient for the atom pair $i - j$ (simply referred to as C_6 coefficient by the community), $r^{i,L}$ is a position vector of the atom i after performing L translations of the unit cell along the lattice vectors. The above equation is not valid for $i = j$ and for $L = 0$.

In practice, the terms corresponding to the interactions between atoms that are further apart, i.e. beyond a particular cut-off radius (R_0) contribute to a negligible E_{disp} and thus can be ignored. Finally, the term $f_{\text{damp}}(r^{ij})$ is a short range damping function, which removes the inherent singularity in Eq. (2.69) at small distances. This damping function can be expanded as

$$f_{\text{damp}}(r^{ij}) = \frac{1}{1 + e^{-d(r^{ij}/R_0^{ij}-1)}}. \quad (2.70)$$

Thus, the role of the damping term is to scale the force field so as to minimize the contributions from interactions within a typical bonding distance. The combination rules for C_6^{ij} and vdW radii R^{ij} are $C_6^{ij} = \sqrt{C_6^i C_6^j}$ and $R_0^{ij} = R_0^i + R_0^j$, respectively.

Most components of the dispersion energy of Eq. (2.69) have a default value already incorporated into popular codes like Quantum Espresso, VASP, etc. The method is however

semi-empirical as Eq. (2.69) requires inputs for the element specific C_6^m coefficients and the corresponding vdW radii R_0^m , where m is the element index.

Grimme's method works really well for systems having dispersion effects at medium and short ranges, where conventional DFT functionals underestimate the binding energy. Indeed Grimme has proved this method to be accurate for a range of molecular systems [43]. Most importantly in this procedure no additional computational costs are incurred with respect to the underlying PBE calculation.

However the main drawback of Grimme's method is in its empirical nature. Since the parameters do not depend on the underlying electronic structure but are to be obtained by fitting to the experimental C_6 coefficients and/or to HF binding energy data. Strictly speaking Grimme's method is not an *ab initio* one. These equations [in particular Eq. (2.69)] forms the basis of many attempts to accurately include vdW interactions in DFT.

Tkatchenko and Scheffler (TS) functional

The essential idea behind the work of Tkatchenko and Scheffler [47] is to obtain the C_6 and vdW radii from mean-field ground-state electron density for the specific molecules and solids under investigation. Therefore the C_6 and vdW radii are estimated at an *ab initio* level. In their method, the atomic C_6^{atom} coefficients are calculated as a functional of the electron density of the specific molecule or solid under examination and from a reference data for the corresponding C_6 coefficients for the free atoms. Thereafter, the molecular C_6^{mol} coefficients are calculated by summing the various atomic C_6^{atom} coefficient contributions. The authors have shown that their estimation of C_6^{mol} for a range of different systems agree quite well with those obtained from experiments in the DOSD³ database. The systems tested also include water molecules, a range of H₂ bonded systems, as well as graphene. This is a recently implemented vdW functional, therefore tests are still being

³Dipole Oscillator Strength Distribution.

performed for different molecular crystals and layered materials

For systems where short range vdW interactions are prevalent, a Fermi type damping factor is introduced similar to that proposed by Grimme work in Eq 2.70. Thus the vdW radius of an atom in a molecular system can be related to that of the free atom (which is known) by the concept of an effective atomic volume. Finally, the dispersion energy term similar to that in Eq. (2.69) is added to an underlying Kohn-Sham DFT energy functional.

Van der Waals density functional (vdW-DF)

Another popular implementation of vdW interactions in DFT, which ensures a good performance in terms of balancing speed, accuracy and scalability is a non-local correlation functional named van der Waals density functional (vdW-DF) [46]. This method includes long range dispersion effects as a perturbation to the DFT correlation energy. This correction is a function of the density. The standard DFT functional used within vdW-DF, is the revised Perdew-Burke-Erzenhoff functional (revPBE)⁴ [49]. Unfortunately the use of revPBE as the underlying DFT functional gives too much repulsion at short distances. There are proposals to replace revPBE by Hartree-Fock and PW86 functionals, which improves vdW-DF inter-species separation distances but at the cost of overbinding the entities, in comparison to Quantum Chemistry wavefunction-based (CCSD calculations).

Despite these problems the vdW-DF functional is a true *ab initio*, universal, and widely accepted general-purpose functional. It is capable of describing quantitatively the weak dispersion interactions, without compromising the accuracy of the best GGA functionals for stronger ionic, covalent as well as metallic bonds. Moreover, the vdW-DF functional has been successful in describing the properties of a diverse group of materials, from molecules to bulk polymers as well as the problem of molecules on surfaces and also in describing accurately the cohesive energies of layer compounds.

⁴There are also versions of vdW-DF with PBE, PBEsol, etc.

2.3.8 Ingredients in solving the Kohn-Sham equations

In the previous sections we have introduced the central idea behind Kohn-Sham DFT as well as discussed the different flavors of xc functionals. In this section we shall talk about the ingredients that are required to solve the said Kohn-Sham problem.

Basis Set

In order to solve the Kohn-Sham equations, the corresponding eigenstates must be expanded over a finite number of basis functions. The choice of the basis can be plenty ranging from plane-waves to local orbitals or linearized Muffin-Tin orbitals. Let us discuss the essential concepts of the two most commonly used classes of basis sets in modern DFT codes.

Plane-wave basis set The system wavefunctions and operators are described as a Fourier expansion over a set of plane-waves

$$\psi_j^{KS}(\mathbf{r}) = \sum_k C_{k,j} e^{i\mathbf{k}\mathbf{r}}. \quad (2.71)$$

Thus the concept behind the application of plane-wave basis set is very simple. The desired number of k points are chosen such that the wavefunctions are accurately represented. In practice, this is done by deciding a value for the kinetic energy cutt-off, $E_{\text{cut}} = \frac{\hbar^2 |k|^2}{2m}$, which establishes the maximum value for the kinetic energy associated to any plane-wave that is chosen in the expansion. As one would expect, a plane-wave basis set is most efficient for periodic solids. However, in systems with highly localized electrons⁵, a very hefty E_{cut} is required to achieve convergence. Thus, the computational cost incurred using plane-wave basis sets will be large in this case. Moreover, in systems such as isolated molecules, plane-waves will also be ineffecient as they cannot describe vacuum regions which have a vanishingly small charge density.

⁵Hence a large kinetic energy.

Linear combination of atomic orbitals (LCAO) Another popular strategy is to expand the wavefunction over a linear combination of localized atomic-like orbitals. This is illustrated by the following equation

$$\psi_j(\mathbf{r}) = \sum_n C^{j,n} \phi_n(\mathbf{r}), \quad (2.72)$$

where $\phi_n(\mathbf{r})$ are radial functions with a finite radius beyond which they are strictly zero. These could be Slater-type orbitals or Gaussian functions. By using localized basis sets one can excellently describe localized systems as well as molecules and clusters. Moreover, the number of basis functions required for the calculation are usually small. The only disadvantage of using localized atomic-like orbitals is that unlike plane-waves there is no single parameter with which the convergence of the DFT calculation can be tuned.

Furthermore, it is common to represent the different valence orbitals with more than one basis function (each of which can in turn be composed of a linear combination of localized functions). This is known as the split valence scheme [50] which characterizes LCAO type basis sets. Some examples are as follows, single Zeta- ζ (SZ) basis set has single radial function per angular momentum channel. Double Zeta- ζ (DZ) basis set has two radial function per angular momentum channel. There are also many other ways to introduce multiple zetas. High angular momenta radial functions are generated by polarizing the radial orbitals with an electric field.

Pseudopotentials

The electrons in atoms constituting molecules and solids can be classified into two categories, namely valence and core electrons. The core electrons are strongly bound to the nuclei and form close shells. They are only slightly affected by the changes in the chemical environment. Hence, the nuclear and core potentials can be replaced by a single effective potential namely pseudopotential, which describes the resultant effect of the core on the valence electrons. The principal advantage of pseudopotentials is that it massively

reduces the number of electronic states in the calculation.

”*Ab initio*” pseudopotentials can be obtained by inverting the free atom Schrödinger

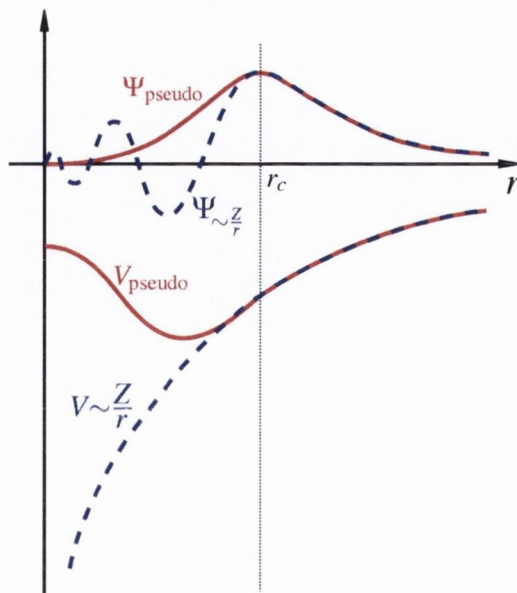


Figure 2.2: The pseudo (red) and all-electron (blue) wavefunctions are illustrated in the upper part of the graph as a function of the radius r of a specific atom. The corresponding Coulomb potential of the nucleus (blue) and pseudopotential (red) are shown in the lower half. The real and pseudo wavefunctions and potentials match above a certain cutoff radius r_c .

equation for a particular electronic configuration and enforcing the pseudo wavefunction to coincide with the true valence wavefunction⁶ beyond a certain cut-off radius, $r > r_c$ [51] (see Fig. 2.2). Moreover the pseudopotential also matches the all-electron potential beyond r_c . The pseudo-wavefunction is a nodeless function (Fig. 2.2), which has the same norm as the all-electron wavefunction, i.e. $\int_0^{r_{c,l}} |\psi_{PS}^l(r)|^2 dr = \int_0^{r_{c,l}} |\psi_{AE}^l(r)|^2 dr$. Here l is the angular momentum quantum number for the particular electronic state in question. Also the pseudo-energy eigenvalues must match with the valence eigenvalues.

In principle, the pseudopotentials constructed for an atomic species must appropriately describe the core of that particular atom in a range of different atoms, molecules as well as solids. This property of the pseudopotential is known as its transferability, which is an important condition when judging the quality of pseudopotentials used in a particular

⁶Also referred to as all-electron wavefunction.

DFT calculation. In order to satisfy this condition, the pseudopotential must be *semi-local*, i.e. to accurately represent the combined effect of the nucleus and the core electrons, the pseudopotential must be acting differently on different angular momentum states l, m (as they are scattered differently). There are numerous ways how this can be ensured for pseudopotentials and the most important method is the one worked out by Kleinman and Bylander [52].

In plane-wave codes, sometimes the so called ultra-soft pseudopotentials are also used [202]. These produce much smoother (softer) pseudo-wavefunctions and hence fewer plane-waves are needed to represent the charge density. This is achieved by releasing the norm conservation constraint and therefore DFT calculations performed using ultra soft pseudos are computationally lighter.

***K*-point Sampling**

In order to obtain the ground state energy in the Kohn-Sham scheme a real space integral needs to be solved, and the extent of the real space is in principle infinite. However by the virtue of Bloch theorem any real space integral can be replaced by an integral over reciprocal space, which is finite in the first Brillion Zone (BZ). However this integral must be done over an infinite number of points constituting the reciprocal point, known as k -points. Since the electron wavefunction does not change a lot in the k -space, this can be taken into our advantage by replacing the integral over infinite number of k -points by a summation over a finite mesh of k -points. Let us consider an integration function $f(r)$, which upon integration yields the density or total energy. The integration can be computed as a discrete sum as

$$\int_{BZ} F(k) dk = \frac{1}{V} \sum_j w_j F(k_j), \quad (2.73)$$

where $F(k)$ is the Fourier transform of the integration function $f(r)$, V is the unit cell volume, and w_j are the weight factors. Eq. (2.73), requires that the BZ must be accurately

represented by the k -mesh chosen, hence in every DFT calculation one must ensure that the total energy is fairly converged with respect to the number of k -points.

Hence, the position of the k -points must be carefully chosen for a particular system. In this work we employ the Monkhorst-Pack method [56], where the k -points are distributed homogeneously in the BZ and can be divided into rows and columns

$$k_i = x_{1i}b_1 + x_{2i}b_2 + x_{3i}b_3 \quad (2.74)$$

where b_1, b_2 and b_3 are the reciprocal vectors and $x_{ij} = \frac{l_i}{n_j}$. Here l_i are the length of the reciprocal lattice vectors and n_j are the number of special points in the set. This results in a uniform sampling of the k -space used in the summations.

2.3.9 DFT codes

For most of the results presented in this thesis the plane-wave code Quantum Espresso [201] is used. In Quantum Espresso we have made extensive use of both norm conserving and ultrasoft pseudopotentials. Additionally, calculations are also performed using the Gaussian 09 [199] code as well as SIESTA [55], both of which implement localized basis sets and norm conserving pseudopotentials. Furthermore, some of the DFT calculations presented in this thesis are also performed by using the FHI-aims code [168], which is an all-electron code with no pseudopotentials. We shall describe in detail, the specific parameters used for every DFT calculation presented in this thesis, whenever appropriate.

2.3.10 Spin-orbit interactions in DFT: an on-site approximation

Spin-orbit coupling is one of the mechanisms by which the itinerant carrier's spin polarization is lost as it travels through a semiconductor. Since the central point of our work is to investigate the spin transport properties of OSCs, at several instances during the course of this thesis we have made use of spin-orbit implementation in DFT [53] to check

its effect on the electronic structure of the OSC. We shall discuss briefly in this section as to how spin-orbit interactions are incorporated in DFT.

Kleinman and Bylander have shown that the generation of non-relativistic pseudopotentials can be extended to account for relativistic effects, by solving the Dirac equation [54]. Relativistic pseudopotentials thus depend on the total angular momentum $j = l \pm \frac{1}{2}$, and can be written down as:

$$V = \sum_{j, m_j} |j, m_j\rangle V_j \langle j, m_j|. \quad (2.75)$$

The above pseudopotential includes all the relativistic corrections and $|j, m_j\rangle$ are the total angular momentum states. The above expression can be reformulated into the following form, in terms of the real spherical harmonics

$$V_{\sigma, \sigma'} = V_{\sigma, \sigma'}^{\text{sc}} + V_{\sigma, \sigma'}^{\text{so}} = \sum_{l, M} \bar{V}_l I_{\sigma, \sigma'} + \bar{V}_l^{\text{so}} \vec{L} \cdot \vec{S} |l, M\rangle \langle l, M|, \quad (2.76)$$

where

$$\bar{V}_l^{\text{sc}} = \frac{1}{2l+1} [(l+1)V_{l+1/2} + V_{l-1/2}], \quad (2.77)$$

$$\bar{V}_l^{\text{so}} = \frac{2}{2l+1} [V_{l+1/2} - V_{l-1/2}]. \quad (2.78)$$

Here \bar{V}_l^{sc} accounts for scalar non-relativistic pseudopotential plus relativistic corrections, while \bar{V}_l^{so} is the corresponding relativistic spin-orbit correction.

Furthermore, $|l, M\rangle$ are the real spherical harmonics obtained from the corresponding complex ones $|l, m\rangle$ (please refer to Appendix 1 for more details). Here l and m are respectively the more familiar angular momentum and magnetic quantum numbers, from atomic physics.

Finally, the spin-orbit corrected Kohn-Sham equation can be written as

$$H_{\sigma,\sigma'}^{\text{KS}} = T_{\sigma,\sigma'} + V_H + V_{\sigma,\sigma'}^{\text{xc}} + V_{\sigma,\sigma'}^{\text{sc}} + V_{\sigma,\sigma'}^{\text{so}}. \quad (2.79)$$

When the above Kohn-Sham equation is solved self-consistently in the linear combination of atomic orbital (LCAO) scheme over a set of localized pseudoatomic (relativistic) orbitals $|\phi_i\rangle$, the spin-orbit part will be $V_{ij}^{\text{so}} = \langle \phi_i | \bar{V}^{\text{so}} | \phi_j \rangle$. This has an angular component, which can be obtained in a similar fashion as shown in Appendix A. Moreover, V_{ij}^{so} also has a radial part for which only the on-site terms are considered [53]. The authors [53] claim to get the correct results for the overall bandstructure and splittings for materials with strong spin-orbit coupling (i.e. group IV and III-IV semiconductors and $5d$ metals).

2.4 Summary of this chapter

In this chapter we have provided the basic groundwork behind two very powerful methods that are used in our multiscale approach to model OSCs. These include DFT which is used to extract the *ab initio* parameters in a model for OSCs. Furthermore we have also discussed MC techniques, which are used to evolve the model and thereafter compute the finite temperature statistical average of the observable. Please note that the exact procedure with which we can extract the *ab initio* information for a model describing OSCs will be discussed in Chapter 5 and 6 of this chapter.

Chapter 3

Towards modelling Organic Semiconductors: first steps

π -conjugated molecules

Amongst the various possible materials for organic spintronics, π -conjugated OSC molecules appear very appealing [70, 71]. This is because of their very long and relatively temperature independent spin relaxation time and their ability to form good interfaces with metal electrodes when incorporated in spin valve like devices [181]. Some prominent π -conjugated OSC molecules and their chemical and structural units were listed in the previous section. The most relevant structural feature of such molecules is their planar shape. The π -electron wavefunction distends over the molecular plane and it can easily interact with the wavefunction of adjacent molecules due to the conjugation. Therefore a face-to-face molecular configuration is usually stabilized through π - π bonding and diffusive Van der Waals interaction. This leads to a molecular stacking arrangement resulting in the formation of a low dimensional lattice [73]. Because of this peculiar structural conformation many of the π -conjugated organic molecular crystals can be described by simplified one-dimensional (1D) model Hamiltonians [180, 72, 218].

In this section we explore a minimal model describing the principal interactions in organic π -conjugated polymers. This is based on the repulsive Hubbard model incorporating both electron-phonon (el-ph) coupling and hyperfine interaction. It is solved for finite molecules by using a combination of energy minimization techniques and MC simulations over a vast region of its parameter space. Indeed, in the work presented in the rest of this chapter the detailed phase diagram of the model is explored and the effect of all the Hamiltonian parameters on the property of the system is explored. This is the very first step in the computational machinery which we have developed in the work presented in this thesis. It involves understanding in detail the different aspects of the tight binding model representing OSCs. In doing so, intriguingly we find that the interplay between on-site Coulomb repulsion and electron-phonon coupling, leading to Peierls distortion, can be responsible for spin crossover transition in small-sized molecules.

Spin Crossover transitions are an interesting, intriguing and a crucial spintronic phenomenon [78, 79, 80]. This is because an important aspect for the successful integration of organic materials in magnetic memories and in magnetic switching devices is the feasibility of manipulating the spin orientation in the organic media. It is difficult to achieve this in non-magnetic molecules because of the tiny non-equilibrium spin population originating from spin injection (little spins are inserted). Furthermore, the standard techniques for manipulation used in inorganic semiconductors, for example optical methods, are ineffective because of the weak spin-orbit interaction. A more promising option is that of manipulating the internal spin degrees of freedom of the organic medium, when this is magnetic. Intriguingly there is a vast class of molecules, generally known as spin crossover compounds, whose spin state can be changed from low spin to high spin by an external perturbation [74]. Since the crossover transition is entropy driven, it is most typically achieved by increasing the temperature, although also light, pressure and electro-chemical redox reactions can all produce it. Most recently the possibility of spin crossover driven by static electric fields has been proposed theoretically [75, 76, 77].

Even more interesting is the fact that spin crossover molecules can be prepared in a single crystal form in either one, two or three dimensions [81]. In these structures the active mononuclear spin crossover building blocks [usually Fe(II)] are connected via hydrogen bonding, π - π stacking or bridging ligands. As a consequence of such an interaction the spin crossover properties of the so-made polymers differ from that of the constituent single molecules. This class of materials then appears to be an excellent platform for constructing spin-devices, which incorporate an element of multi-functionality.

In the following subsection we shall provide the computational details used by us to model OSCs.

3.1 Computational methods

We consider a single-site tight binding model for a 1D lattice, including repulsive Hubbard interaction and both el-ph and hyperfine interaction. This is described by the following Hamiltonian

$$\begin{aligned} \hat{H} = & \sum_{i\sigma} \epsilon_{i\sigma} c_{i\sigma}^\dagger c_{i\sigma} + \sum_{ij} [t_{ij} + \alpha(q_i - q_j)] (c_{i\sigma}^\dagger c_{j\sigma} + c_{j\sigma}^\dagger c_{i\sigma}) + \\ & + U \sum_i \hat{n}_{i\uparrow} \hat{n}_{i\downarrow} + J_H \sum_{i\alpha\beta} \vec{S}_i^N \cdot [c_{i\alpha}^\dagger (\vec{\sigma}_{\alpha\beta}) c_{i\beta}] + \frac{1}{2} k \sum_{i,j} (q_i - q_j)^2, \end{aligned} \quad (3.1)$$

where $c_{i\sigma}^\dagger$ ($c_{i\sigma}$) denotes the creation (annihilation) operator for an electron at site i with spin σ , $\epsilon_{i\sigma} = \epsilon$ is the on-site energy and t_{ij} is the transfer integral for a uniform undistorted lattice. In this chapter we consider only nearest neighbor hopping, i.e. $t_{ij} = t$ for $i = j \pm 1$ and $t_{ij} = 0$ for any other (i, j) pair. The other microscopic parameters of the model are the el-ph coupling parameter, α , the Hubbard repulsion strength, U , the hyperfine exchange J_H , and the elastic constant, k . Thus, the second term of the Hamiltonian, in addition to electron hopping, describes the el-ph coupling, with q_i being a set of classical vectors representing the atomic displacement of site i (we consider 1D longitudinal motion only).

The third term is the standard on-site Hubbard repulsion, while the fourth one describes a Heisenberg-like interaction between the electron spins, $c_{i\alpha}^\dagger(\vec{\sigma}_{\alpha\beta})c_{i\beta}$, and a set of classical vectors, \vec{S}_i^N , representing the nuclear spins. Finally the last term is a classical elastic energy.

In what follows we will express all energy related quantities (including the temperature) as a function of t , which sets the energy scale of the problem. The on-site energy is taken to be zero and k is $5 t/\text{\AA}^2$. Note that for $t \sim 2.5$ eV this corresponds to $k = 12.5$ eV/ \AA^2 , which is in between the value for the H_2 molecule and that of Au monoatomic chains [85]. Also it is important to note that $k > 5t/\text{\AA}^2$ is a value commonly used in recent literature about transport in organic polymers [72, 86].

Please note that Eq. (3.1) is valid in the limit of fast moving electrons such that the nuclear kinetic energy is much smaller than the electronic kinetic energy t . This is the assumption in our approach and we will justify it with the speed of nuclear motions for realistic OSCs in Chapter 5. Furthermore, in Eq. (3.1) we have only considered the Peierl's (non-local) el-ph coupling and have ignored Holstein's (local) el-ph coupling. We will provide a quantitative estimation for these el-ph interaction strengths in Chapter 5 for rubrene and justify the exclusion of Holstein el-ph coupling in the model Hamiltonian.

We wish to put our work in this chapter in context with previously published literature for the Hubbard-Peierls model, which is that described by equation (3.1), when one excludes the hyperfine interaction. The ground state of such a model for the infinite 1D case, sometimes including a quantum description of the phonons (Holstein-Hubbard model), has been extensively investigated with either variational methods [87], density-matrix renormalization group [88, 89], quantum Monte Carlo [90] and exact diagonalization [91]. In all these studies the attention has been focussed on describing the various electronic phases at zero temperature and for selected filling factors (mostly half-filling and quarter-filling) in the thermodynamic limit ($L \rightarrow \infty$ and $N \rightarrow \infty$, with $N/L = n$). Finite temperature calculations are much less abundant and usually have looked only at a small region of the

parameter space [92]. This is mainly connected to the significant computational overheads associated to performing finite-temperature many-body calculations.

In general a "site" can be interpreted either as a real atom or as a molecular unit forming a conjugated compound. In both cases our description is limited only to valence electrons, which occupy either atomic or molecular orbitals. Organic magnets such as bis(benzene)vanadium-tetracyanoethylene $[V(\text{TCNE})_x]$ [16], polymeric spin crossover compounds [81], charge transfer complexes like tetrathiafulvalene (TTF) derivatives [72] and OSC single crystals like rubrene are among the few examples where our model can be applied.

In all the calculations presented in this chapter, we consider only the half-filling case (one electron per site) so that the model exhibits an insulating behavior at $T = 0$ for an undistorted infinite chain. Our interest, however, is in finite chains of different lengths, L , mimicking real finite molecules. In particular the simulations presented here will be for the cases $L = 10$ and $L = 20$. Our approach consists in replacing the Hubbard term with its unrestricted mean-field approximation [83] and then in solving the Hamiltonian self-consistently for different lattice displacements $\{q_i\}$ ¹. Energy minimization is performed by conjugate gradient over $\{q_i\}$ and further verified by additional simulated annealing [84]. The bond lengths, x_i , are calculated from the ground state displacements as $x_i = d + q_{i+1} - q_i$, where d is the equilibrium bond distance. The main observables calculated are the dimerization parameter, D , and the local magnetic moment per site, m_i . These are defined respectively in Eq. (3.2) and Eq. (3.3)

$$D = \sum_{i=1}^{N-2} |x_i - x_{i+1}| + |x_{i+1} - x_{i+2}|, \quad (3.2)$$

$$m_i = (n_i^\uparrow - n_i^\downarrow). \quad (3.3)$$

¹Thus the electron-electron interaction term in the Hamiltonian reduces to a quadratic problem instead of a quartic one, in respect to the particles' creation and annihilation operators. Please note that the number of states in the solution are $2L$, with the prefactor 2 coming from spins.

Note that in Eq. (3.3) n_i^σ is the electron spin density at site i , which is calculated as the diagonal matrix elements of the density matrix, $\hat{\rho} = \sum_{n=1}^{\text{occupied}} \{|\Psi_n\rangle\langle\Psi_n| \frac{1}{e^{\beta E_n} - 1}\}$, where E_n and $|\Psi_n\rangle$ are respectively n -th electronic eigenvalues and eigenvectors. Our results are then plotted in a phase-diagram like form, where the different phases are presented as a function of α and U .

For finite temperature simulations we consider the system described by the Hamiltonian of Eq. (3.1) and evolve the classical dynamical variables $\{q_i\}$ and $\{\vec{S}_i^N\}$ by using the standard Metropolis algorithm [15]. Note that since $J_H \ll t$ [93] the hyperfine interaction has little effect on the α - U phase diagram, so that in what follows in this chapter we will neglect it unless otherwise indicated. As such, the only classical dynamical variables are the atomic displacements $\{q_i\}$. In the Metropolis algorithm the acceptance probability of a new state is unity if the new configuration has an energy lower than that of the old configuration. Otherwise it is given by the Boltzmann factor $e^{-\frac{\Delta G}{k_B T}}$, where ΔG is the difference in the Gibbs free energy between the old and new configuration. By using the grand-canonical ensemble the Gibbs free energy G can be written as

$$G(\{q_i\}) = -\frac{1}{\beta} \sum_{n=1}^{N_o} \ln \left(1 + e^{-\beta[E_n(\{q_i, S_i^N\}) - \mu]} \right) + \frac{1}{2} k \sum_{i,j} (q_i - q_j)^2, \quad (3.4)$$

where the chemical potential μ is updated self-consistently from

$$N = \sum_n \frac{1}{e^{\beta[E_n(\{q_i\}) - \mu]} + 1}, \quad (3.5)$$

with $\beta = \frac{1}{k_B T}$ being the inverse temperature and N the total number of electrons ($N = 10$ and 20 respectively for $L = 10$ and $L = 20$). G and μ are computed at each MC step during the simulations. For every value of $(\alpha/t, U/t)$ and each temperature the system is allowed to reach equilibrium. Then both D and m_i are calculated over several million MC steps. Such a procedure is incorporated in all the MC simulations presented in the entire thesis.

Here we took a simplified approach, by solving the electronic part of the problem at a mean-field level. This allows us to explore conveniently the wide parameter space of the model at different temperatures. Importantly we expect that our main result, namely the spin-crossover transition occurring in a particular region of the parameter space, will be little affected by a more rigorous treatment of electron correlation. As we will demonstrate in the next section this is an entropy-driven transition and no significant changes in the entropy are forecasted as the result of including many-body corrections over our mean field electronic structure. Furthermore we wish to remark here that all calculations presented in this chapter are for relatively small (up to 20 sites) molecules, so that we do not expect to recover the results for the infinite systems. Such small molecules however are closer to real 1D spin crossover polymers so that our theoretical analysis applies directly only to that specific class of materials.

3.1.1 Tight binding Hamiltonian matrix: an example

Before we explore the phase diagram of the model, let us explicitly write down the Hamiltonian matrix for a chain of only two atoms ($L = 2$). This is intended to be a clarification to the reader, so as to better understand all the terms in the Hamiltonian Eq. (3.1). Each atom i is represented by a tight binding basis $|i^\sigma\rangle$, where i is the atom index, which ranges from 1 – 2 in this case and σ is the spin index, which can be \uparrow or \downarrow . Furthermore, ϵ , t , α and U are respectively the on-site energy, transfer integral, el-ph interaction constant and el-el interaction, which are assumed to be the same for all the atoms. Moreover, $\vec{q}_i = q_i$ (only longitudinal phonons) and $\vec{S}_i^N = (\vec{S}_{xi}^N, \vec{S}_{yi}^N, \vec{S}_{zi}^N)$ are the vectors representing respectively the displacement and nuclear spins of each atom i .

For the sake of simplicity, we will first write down the Hamiltonian matrix for the non-spin mixing (nsm) part of the tight binding Hamiltonian. This will include all the terms in Eq. (3.1) apart from the hyperfine interaction term. The Hamiltonian matrix written in the basis of $\{|1^\uparrow\rangle, |2^\uparrow\rangle, |1^\downarrow\rangle, |2^\downarrow\rangle\}$ is :

$$\hat{H}_{\text{nsm}} = \begin{pmatrix} \epsilon + U \cdot n_1^\downarrow & t + \alpha \cdot (q_1 - q_2) & 0 & 0 \\ t + \alpha \cdot (q_1 - q_2) & \epsilon + U \cdot n_2^\downarrow & 0 & 0 \\ 0 & 0 & \epsilon + U \cdot n_1^\uparrow & t + \alpha \cdot (q_1 - q_2) \\ 0 & 0 & t + \alpha \cdot (q_1 - q_2) & \epsilon + U \cdot n_2^\uparrow \end{pmatrix}.$$

Notice that the Hamiltonian matrix elements, which mix spins of different kinds are zero. Now, the spin mixing (sm) part of the Hamiltonian, which will be given only by the hyperfine interaction term in Eq. (3.1), written in the same basis set as above takes the following form

$$\hat{H}_{\text{sm}} = \begin{pmatrix} -J_H \cdot S_{z1}^N & 0 & J_H \cdot (S_{x1}^N + \iota S_{y1}^N) & 0 \\ 0 & -J_H \cdot S_{z2}^N & 0 & J_H \cdot (S_{x2}^N + \iota S_{y2}^N) \\ J_H \cdot (S_{x1}^N - \iota S_{y1}^N) & 0 & J_H \cdot S_{z1}^N & 0 \\ 0 & J_H \cdot (S_{x2}^N - \iota S_{y2}^N) & 0 & J_H \cdot S_{z2}^N \end{pmatrix}.$$

The full Hamiltonian matrix given by Eq. (3.1) is

$$\hat{H} = \hat{H}_{\text{nsm}} + \hat{H}_{\text{sm}}. \quad (3.6)$$

Thus the Hamiltonian matrix for our model can be generalized for all L .

3.2 Phase diagram of the model

3.2.1 Ground state

Let us begin our discussion by investigating the α - U phase diagram at $T = 0$ for a finite chain of length $L = 10$, which is presented in Fig. 3.1. This is populated by four different

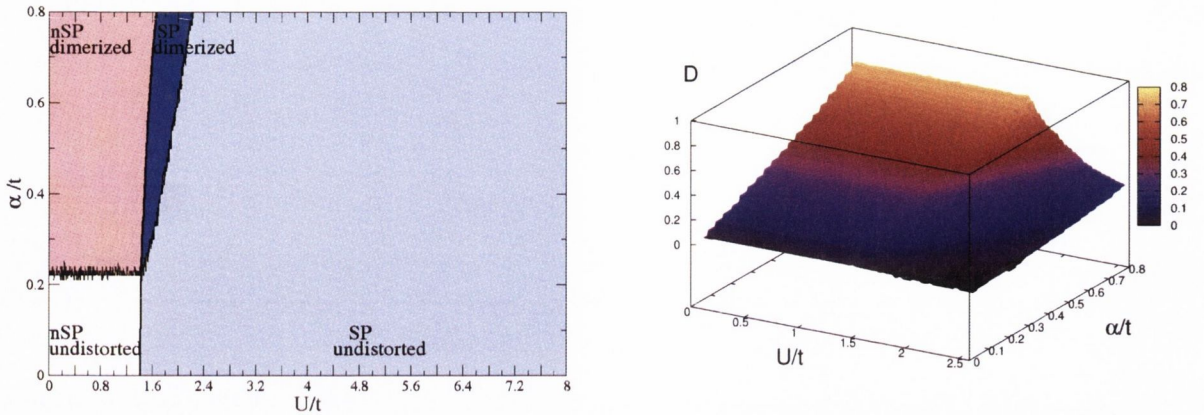


Figure 3.1: α - U phase diagram at $T = 0$ for a finite chain of length $L = 10$ for the 1D model polymer investigated. In the left panel we present the schematic phase diagram, while in the right panel the dimerization parameter, D , as a function of α/t and U/t .

phases characterized by the different combined structural and magnetic properties of the chain. In particular there are two magnetic states and two geometrical configurations. For small α/t and U/t the chains are undistorted (the atomic spacing is approximately uniform throughout the chain) and in a non-spin polarized (nSP) state. We denote this phase as nSP-undistorted. As U/t increases eventually a spin polarized solution develops. This is the one expected from the mean field Hubbard model at half-filling, where local moments form at each atomic site, but their orientation alternates along the chain. Such a spin polarized (SP) phase may or may not be accompanied by a structural distortion, depending on the value of α/t . In general however there is a vast region of the model parameter space, where no significant distortion appears for the SP spin state. We denote this phase as SP-undistorted.

As α/t increases for moderate U/t the system progressively developed a Peierls instability and makes a transition to a geometry where long bond distances alternate to short ones. This dimerized phase, expected for the non-interacting case, remains non-spin polarized (nSP-dimerized) for small U/t but can coexist with a SP solution for a significant range of parameter. In summary and as expected the phase diagram of the finite size molecule is characterized by a competition between the on-site repulsion, driving the magnetic instability, and the el-ph coupling, driving the Peierls distortion.

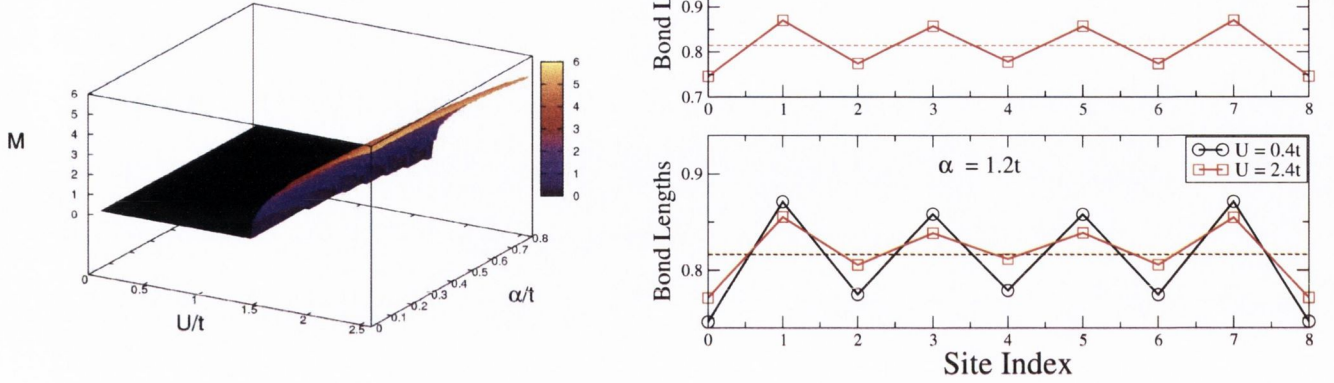


Figure 3.2: Detailed investigation of the $T = 0$ phase boundary. In the left-hand side panel we present the staggered magnetization parameter M vs $(U/t, \alpha/t)$. In right-hand side one we show the bond length as a function of site index for $U = 0.4t$ and two different values of α (top panel), and for $\alpha = 1.2t$ and two different values of U (bottom panel). All the calculations shown here are performed for a ten-site long chain and at $T = 0$.

In the discussion we have assigned the phase boundary of the magnetic transition to the condition $\sum |m_i| \neq 0$ [note that for this particular situation, where the local atomic spin polarization alternates in sign along the chain, the quantity $\sum |m_i|$ coincides with the more frequently used definition of staggered magnetization $M = \sum (-1)^i m_i$]. In contrast assigning the phase boundary to the Peierls transition is more complicated since D changes continuously upon increasing α . Thus we have used the operational definition of placing the phase boundaries at $D = 0.17$, which is interpreted as representative of strong dimerization. The complete evolution of D as a function of U/t and α/t is presented in the right hand side panel of Fig. 3.1. The figure clearly reveals the interplay between el-ph coupling and Coulomb repulsion. In fact D grows almost linearly with α/t for small U/t but then is drastically reduced as U/t grows.

Further evidence for the various phase transitions is provided in Fig. 3.2, where we show the staggered magnetization, M , as a function of U/t and α/t (left-hand side panel) and the bond length distribution for a few values of the parameter space (right-hand panel). In both cases the calculations are for a ten-site long chain. From the figure one can immediately note that the magnetic phase boundary appears very sharp. In fact,

at the phase boundary M departs abruptly from $M = 0$, the value that characterizes the nSP solution. In contrast the bond-length distribution changes gradually with U and α . For instance one can note that for the same $\alpha = 1.2t$ the distortion for $U = 0.4t$ is about twice as large as that for $U = 2.4t$ (see lower right panel of Fig. 3.2). Likewise for fixed $U = 0.4t$ the distortion is significant for $\alpha = 1.2t$ and decreases when α is reduced. However, even for the very small value of $\alpha = 0.04t$ a small distortion can still be detected (see top right panel of Fig. 3.2).

3.2.2 Finite temperature phase diagram

We now move to study the finite temperature properties of our model. These are summarized in Fig. 3.3, where we present the α - U phase diagram for $L = 10$ and $L = 20$ site long molecules, each at two representative temperatures, respectively $\beta = 200 \text{ eV}^{-1}$ and 400 eV^{-1} (these correspond respectively to $T = 0.002t$ and $0.001t$ or, $T = 58 \text{ K}$ and 29 K for $t = 2.5 \text{ eV}$).

The most important feature in each of the finite temperature plots is the complete absence of a structural phase transition. This means that in general the system does not dimerize any longer as the temperature is increased. The dimerization is instead replaced by a general increase in all the bond lengths and by a random distribution of the various bonds along the chain.

More details about the structure of the chains at finite temperature can be found in the right-hand side panel of Fig. 3.3, which show the quantity D [defined in Eq. (3.2)] as a function of U/t and α/t at $T = 0.001t$. Note that at finite temperature the quantity D is a measure of the disorder in the bond distances of the chain as the thermal vibrations onset. As such D is maximum at high values of the el-ph coupling and low U/t but falls rapidly as U/t increases.

The second most striking feature in both the finite temperature α - U phase diagrams is the movement of the nSP/SP phase boundary towards lower U/t as the temperature

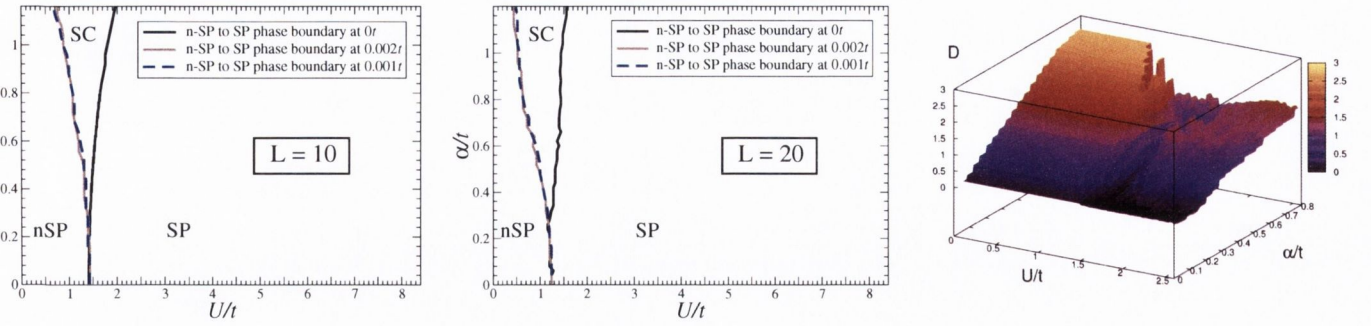


Figure 3.3: Finite temperature α - U phase diagram for the model 1D polymers investigated. In the left-hand side and middle panels we present the schematic phase diagrams for $L = 10$ and $L = 20$ chains respectively, each at two different temperatures, $T = 0.001t$ and $T = 0.002t$. Note that now there are only two phases (nSP and SP) and there is no longer a distorted (Peierls) geometrical configuration. In the picture we also report the nSP/SP phase boundary for the $T = 0$ case. Thus in both the finite temperature phase diagrams, the region comprised between the solid black line and either the solid red, or the dashed blue line is characterized by a nSP to SP phase transition (spin crossover - SC - region) as a function of temperature. In the right-hand side panel we present the parameter D as a function of α/t and U/t for the $L = 10$ site chain (at $T = 0.001t$), which indicates the degree of disorder in the bond distances at finite temperature.

increases. This essentially means that, as the temperature grows, it takes less on-site Coulomb interaction to drive the system towards a magnetic instability. A similar effect is also found as a function of the chain length. In fact we note a general expansion of the SP phase at the expenses of the others as the chain gets larger (from $L = 10$ to $L = 20$). We further explore the evolution of the phase boundary as a function of temperature in figure 3.4, where we present the critical U value, U_C , at which the spin polarized solution for $L = 10$ develops. This effectively represents the position of the nSP/SP phase boundary. In particular U_C is plotted as a function of the temperature, T , and for three different el-ph strengths α/t . In general we find that the nSP/SP phase boundary moves in response to the disappearing of the distorted phase. Thus for the lower value of α/t (0.12), for which there is no distorted phase even at $T = 0$, the phase boundary does not change as the temperature is increased and U_C remains constant at $\sim 1.4t$. For the larger values of the el-ph interaction strengths investigated the $T = 0$ phase diagram presents both a distorted and a homogeneous structural phase depending on U . In this

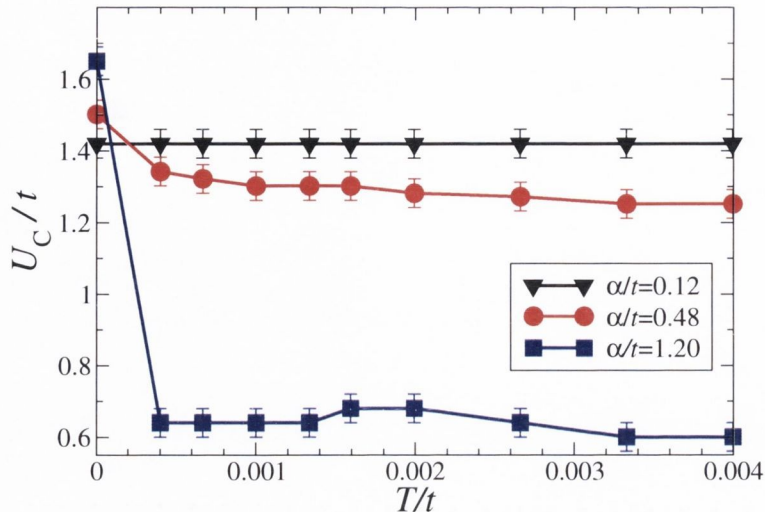


Figure 3.4: Critical on-site Coulomb repulsion, U_C , needed for a spin polarized solution as a function of temperature and evaluated at three different values of the el-ph coupling strength for a $L = 10$ chain. The error bars correspond to spacing of the interpolation grid used to extract U_C .

case the nSP/SP phase boundary (i.e. U_C) decreases fast at low temperatures in response to the melting of the distorted phase and then becomes essentially constant.

An important consequence of the movement of the nSP/SP phase boundary as the temperature increases is the fact that there is a vast region in the α - U diagram where the system makes a nSP to SP transition as the temperature increases. Such a region is the one enclosed between the two vertical lines marking respectively the phase boundary at finite temperature and at $T = 0$ in figure 3.3, left-hand side and middle panels. What is also of significance here is that we observe this transition in finite chains of different lengths. For the particular values of α and U found in such a region (called the spin crossover -SC- region) there is a temperature driven spin crossover.

We will now suggest an experimental setup based on our calculations, as to how one can build a spin crossover molecular wire. The el-ph coupling strengths, α , of such a molecular wire could be manipulated for example, by external pressure while the el-el interaction, U , could be altered by adding impurities and doping the wire. Thus, by controlling the experimental conditions, the values for α and U for such a 1D molecular chain could be made to lie in the spin crossover region thereby yielding the spin crossover

transitions (with temperature) in such wires. Next, we will analyze this spin crossover phase.

3.2.3 Spin crossover phase

We now explain the spin crossover transition by using the standard framework of spin crossover usually employed for magnetic molecules having a divalent transition metal ion center [74]. In general the thermodynamically stable phase at finite temperature of a system that can assume different competing configurations is the one with the lowest Gibbs free energy, G . For the present case, where the competition is among the nSP and the SP phases, the relevant quantity is the difference, $\Delta G = G_{\text{SP}} - G_{\text{nSP}}$, between their Gibbs energies,

$$\Delta G = \Delta H - T\Delta S \quad (3.7)$$

where $\Delta H = H_{\text{SP}} - H_{\text{nSP}}$ and $\Delta S = S_{\text{SP}} - S_{\text{nSP}}$ are respective the enthalpy and entropy differences.

For spin crossover in standard molecules with divalent magnetic ions $\Delta H > 0$, so that the most stable phase at low temperature is low spin (nSP here). However, since the crossover transition is associated with the softening of the phonon modes of the first coordination shell around the transition metal and to the formation of a local magnetic moment, we also have $\Delta S > 0$. Hence as the temperature increases the entropic contribution to the Gibbs energy may eventually dominate over the enthalpic one and drive a phase transition. We now want to establish that the same mechanism holds for the spin crossover region of the α - U diagram of Fig. 3.3.

We have already demonstrated (see figure 3.1) that for $T = 0$ the spin crossover region is occupied by the nSP phase, meaning that $\Delta H > 0$. Therefore one has only left to show that also $\Delta S > 0$. In general the entropy comprises two main contributions, an electronic, S^{el} , and a vibrational one, S^{vib} . Since the SP phase is characterized by local spins, which are absent for the nSP phase, we can immediately conclude that $\Delta S^{\text{el}} = S_{\text{SP}}^{\text{el}} - S_{\text{nSP}}^{\text{el}} > 0$.

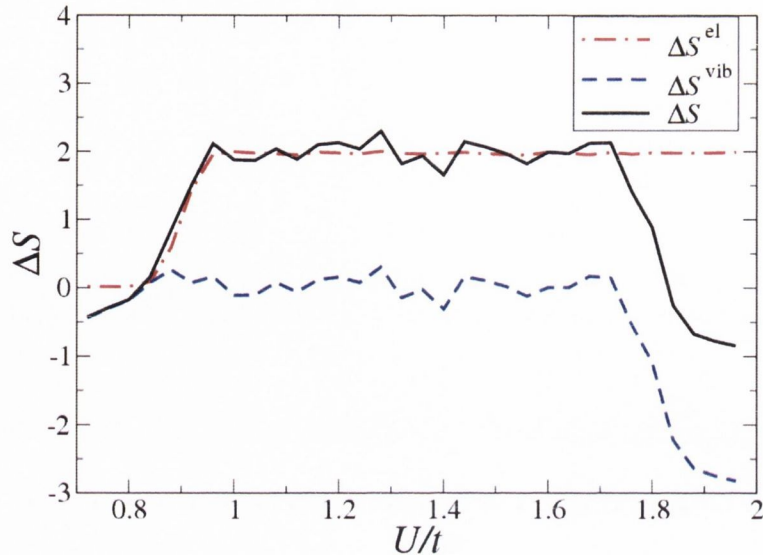


Figure 3.5: Entropy difference, ΔS , between the nSP and SP phases for a chain of $L = 10$ sites. The individual electronic, ΔS^{el} , and vibrational, ΔS^{vib} , contributions as well as their sum, ΔS , are presented as a function of U/t for $\alpha = 1t$. The entropy is presented in adimensional units where both the energy and the temperature are in units of the hopping integral t . Note that there is a large region $0.84t < U < 1.85t$, where $\Delta S > 0$. In this region the entropic contribution to the Gibbs free energy can drive a spin crossover transition.

A more precise evaluation of S^{el} can be obtained by computing

$$S^{\text{el}} = -k_{\text{B}} \text{Tr}[\hat{\rho} \ln \hat{\rho}], \quad (3.8)$$

where $\hat{\rho}$ is the system density matrix [96]. The calculated ΔS^{el} as a function of U/t of a $L = 10$ chain at the representative value of $\alpha/t = 1$, for which the spin crossover region is quite large, is presented in figure 3.5. The electron densities entering the evaluation of S^{el} have been obtained as follows. For the low temperature phase (nSP) ρ is calculated by fixing the occupation to $n_i = 1/2$ for every site and the geometry is that obtained from the $T = 0$ diagram. In contrast the entropy of the high-temperature phase is computed from a density matrix in which the occupation is fixed to the proper spin polarized state (the temperature is $T = 0.001t$) and the geometry is again that of the $T = 0$ solution. We have checked that the finite temperature geometry is rather similar to that obtained

at $T = 0$ for such a density-constrained solution.

The general trend can be understood as follows. For small values of U/t there is no local spin polarization forming, regardless of the chain geometry, so that $\Delta S^{\text{el}} = 0$. Then, as U/t gets larger a local magnetic moment gradually appears at each site, producing a linear increase of ΔS^{el} . Such an increase continues until the local moment reaches the maximum value compatible with the chosen electron filling, which is $1 \mu_{\text{B}}$ (μ_{B} is the Bohr magneton) for half-filling. At this point there is no further change in the electronic entropy and ΔS^{el} saturates to a positive value.

Similarly we can also estimate the vibrational contribution to the entropy. This is obtained from the molecule phonon spectrum, $\hbar\omega_i$, as

$$S^{\text{vib}} = k_{\text{B}} \sum_i^{N_v} \left\{ \beta \hbar \omega_i [e^{\beta \hbar \omega_i} - 1]^{-1} - \ln [1 - e^{-\beta \hbar \omega_i}] \right\}, \quad (3.9)$$

where ω_i is the vibration frequency of the i -th mode and N_v is the total number of modes. Note that the oscillator masses in computing S^{vib} were taken as 1 amu. Eq. (3.9) is a well-known formula for the vibronic contribution to the entropy of a collection of harmonic oscillators. It has been used in the past for estimating the vibrational entropy change associated to the low spin to high spin transition in spin crossover complexes [94, 95]. We calculate the phonon spectra of the SP and nSP configurations by diagonalizing the associated dynamical matrices. These are constructed by finite difference, i.e. by displacing the atomic sites by a small fraction of the equilibrium bond length (0.1 %) and then by numerically evaluating the energy gradient (the force) associated to such a displacement. The density matrices and the initial geometries used to construct the finite difference dynamical matrices are the same used for calculating the electronic contribution to the entropy. Also in this case ΔS^{vib} as a function of U/t evaluated at $\alpha/t = 1$ for the $L = 10$ site chain, is presented in figure 3.5.

In general the vibrational contribution to the entropy difference shows only a small dependence on the Coulomb on-site repulsion and is approximately $\Delta S^{\text{vib}} \sim 0$. However

we also report a relatively sharp decrease as U/t approaches 1.7. This is value close to U_C for $T = 0$, i.e. corresponds to a region in the parameter space where our Monte Carlo analysis does not find a nSP-SP transition and therefore the system remains in the SP state at any of the temperatures investigated.

In summary the picture emerging from figure 3.5 is that of a region, $0.84t < U < 1.85t$, in which ΔS is always positive. This is the only region of the parameter space where the entropy can drive the spin crossover and substantially matches the spin crossover region observed in our Monte Carlo simulations (see Fig. 3.3). We then conclude that in this case the spin-crossover is entropy driven. It is interesting to note that also in transition metal ion-based spin-crossover complexes, where the magnetic moment is associated with the d shell of the transition metal, the spin-crossover process is in fact entropy driven [78]. The low spin to high spin transition of the molecule causes $\Delta S^{\text{el}} > 0$. Furthermore, as the spin-crossover involves the transfer of one or more d electrons from a bonding state to a non-bonding one, the ligand field weakens and hence $\Delta S^{\text{vib}} > 0$ [78, 80].

Finally before summarizing, we wish to comment on the role played by the hyperfine interaction. In general we expect very little changes to the phase diagram obtained by neglecting the hyperfine contribution to the total energy, since this is rather small for realistic hyperfine coupling strengths. In particular we have verified that minor modifications to the $T = 0$ phase diagram start to appear for J_H in the region of $0.01 t$, which corresponds to local magnetic fields of 10^7 T (considering $|\vec{S}_i| = 1$ and t of the order of 1 eV).

3.3 Summary

In this chapter, we have explored the possibility of spin crossover transition in π -conjugated polymer chains with a simple tight binding model including a Hubbard on-site repulsive potential and both el-ph and hyperfine interactions. The model has been investigated both in its $T = 0$ ground state and at finite temperature for polymer molecules of finite

sizes by Monte Carlo methods combined with a mean field treatment of the Hubbard many-body interaction. At $T = 0$ we have found four different phases depending on the relative strength of the Coulomb on-site repulsion U/t and of the el-ph coupling strength α/t . The four phases are characterized either by a non-spin polarized or a spin polarized magnetic state and by the possible presence of a dimerized geometrical configuration. By increasing the temperature the structural distortion disappears and only the phase boundary between the nSP and the SP solution remains. Intriguingly the position in the $\alpha-U$ parameter space of such a phase boundary changes with temperature so that there is a region of parameters where a temperature driven nSP-SP spin crossover transition can be found. We have investigated the nature of the phase transition by calculating the relative entropy of the different magnetic phases and found that this is indeed entropy driven as in the most conventional case of divalent magnetic molecules. This suggests that π -type magnetism can be achieved in organic molecules and that this can be switched on and off by temperature.

The work presented in this chapter is also important for understanding the detailed response of the tight binding Hamiltonian elements, representing the essential interactions in OSCs. In particular, we now have a comprehensive knowledge of the effect of these terms in the tight binding Hamiltonian, on the model through its phase diagram. This will give us invaluable insights into understanding the transport properties of the microscopic model of Chapter 4 and in developing the entire *ab initio* computational framework to compute charge carrier mobility and spin properties of OSCs from first principles, in Chapter 5.

Chapter 4

Charge and Spin transport in Organic Semiconductors: a microscopic study

”Regardless of what form future electronic devices take, we will have to learn how to model and describe the electronic properties of device structures that are engineered on an atomic scale“ Supriyo Datta on reaching Moore’s law upper limit.

4.1 Introduction

The ease with which charge carriers traverse a semiconducting material characterizes its charge transport property. There are physical quantities which one can measure, and which throw light onto the charge transport properties of a system. For example, according to the Drude model for electrical conduction [97] proposed in 1900, one can obtain the conductivity of the material as $J = \sigma E$ ^[1], where J is the current density, E is the applied electric field and σ is the conductivity of the material. The conductivity is a material property of the conductor. Thus, higher the conductivity, better will be the

¹This is Ohm’s law.

charge transport characteristics of the macroscopic conductor.

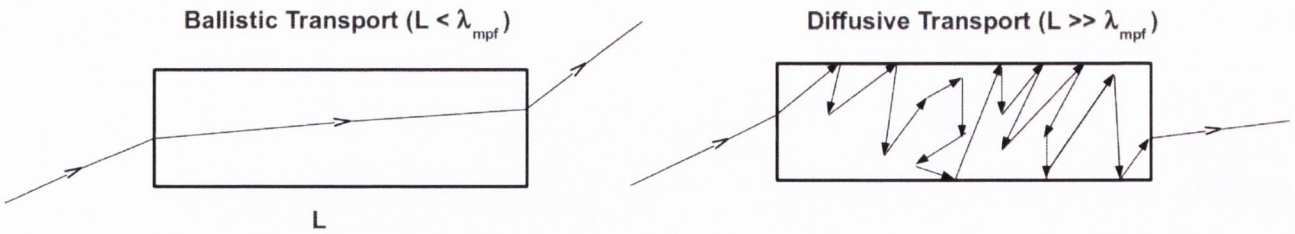


Figure 4.1: Schematic illustration of the path of a charge carrier through a conductor of length L , when the transport mechanism is ballistic (*left panel*) and diffusive (*right panel*). In this thesis we shall simulate carrier transport through nanoscale systems using the Landauer-Büttiker and Kubo formulae at low applied biases, describing both transport scenarios. Please note that the lateral length of the conductor illustrated above (in both transport scenarios) is comparable to the carrier mean free path, λ_{mfp} .

The exact nature of carrier transport through the macroscopic conductor (in Drude model) is diffusive in nature as illustrated in the right panel of Fig. 4.1 (right panel). In such a diffusive transport scenario the length of the conductor, L , is always larger than the charge carrier mean free path, λ_{mfp} . Therefore, the higher the number of scattering events, the lesser will be the conductivity through the macroscopic material. The mean free path λ_{mfp} is defined as the average distance travelled by a charge carrier before being scattered by other carriers or by impurities (either static or dynamic).

What happens if we begin to reduce the dimensions of the conductor, reaching the limit $L < \lambda_{mfp}$? Here one is interested in investigating the transport properties of small-sized conductor right upto the nanoscale level. In that scenario, as seen in the left panel of Fig. 4.1, due to the absence of scattering events (as $L < \lambda_{mfp}$) one cannot define the conductivity. However, the current passing through the device and also its conductance can be experimentally measured by connecting the channel to two large current-voltage probes in a manner similar to a macroscopic conductor. This regime of carrier transport is known as ballistic transport.

Theoretically, ballistic transport has been extensively explored by the pioneering works of Landauer and Büttiker [129]. In their approach one formulates the transport problem

in terms of incoming and outgoing single-electron wavefunctions, which propagate in the (ballistic) electrodes and are scattered elastically by the potential of the central region. In the simplest case of a one-dimensional wire and absence of any scattering, the conductance of such a system has the following constant value

$$G_0 = \frac{2e^2}{h}, \quad (4.1)$$

where G_0 is the quantum of conductance and has a value of $\frac{1}{12.9064} k\Omega^{-1}$. Note that Eq. (4.1) is the expression of conductance for spin polarized transport (hence multiplied by 2). This equation is quite powerful because it establishes that in a ballistic system at zero applied bias (linear response limit) the current through the device is zero, but the conductance has a constant value. This is a key feature of quantum transport.

In systems with higher dimensions one faces a "multi-channel" problem since several waves with the same energy can propagate in the electrodes. In this case, we have a quantity which is known as the total transmission probability $T(E)$ and is energy dependent. The total transmission probability denotes the probability for the wave to be transmitted, summed over all the available scattering channels in the left and in the right electrodes (of a two-probe transport device). Thus the expression for the conductance through the system at zero applied bias is given by

$$G = \frac{2e^2}{h} T(E). \quad (4.2)$$

The generic quantum transport setup to investigate the charge transport properties of OSCs is an organic field effect transistor (OFET), illustrated in Fig. 4.2. The charge transport observable which is of interest in such experiments is the intrinsic carrier mobility μ of the OSC. The carrier mobility is related to its conductivity as $\sigma = j e \mu$, where j is the current density and e is the electronic charge. In FET experiments intrinsic carrier mobility of OSCs can be estimated quite accurately. OFETs are constituted by a semi-

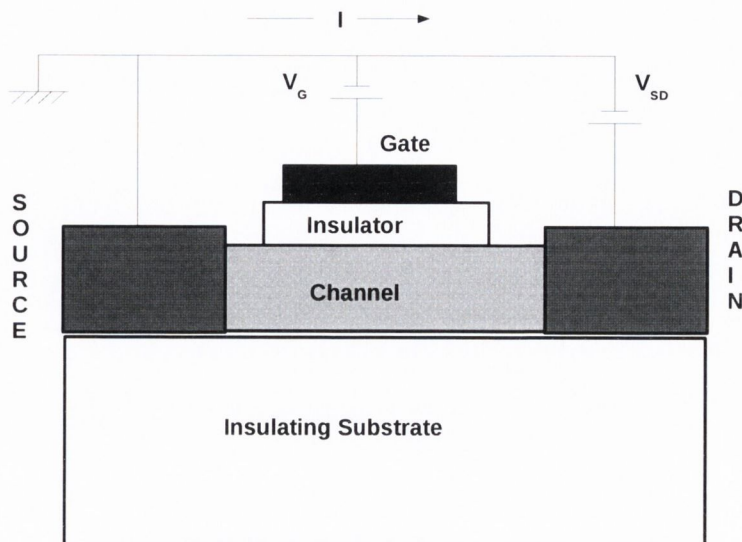


Figure 4.2: Illustration of an organic field effect transistor. In modern high performing OFETs the channel is made up of single crystal OSCs, like rubrene. The electrodes are usually made up of gold and the substrate can be poly-silicon or flexible organic polymers like poly methyl methacrylate (PMMA). Finally, there have been a large variety of high dielectric constant organic materials which have been used as the gate insulating material in OFETs [183].

conducting channel sandwiched between two metallic contact pads, which form the source and the drain electrodes and are highly conducting (good metals). The conductance of the device can be extracted by measuring the current flowing across the source and drain electrodes, I_{SD} , upon the application of a potential difference between them, V_{SD} . Moreover, the FET structure has a gate electrode separated from the semiconducting channel with an insulator (generally a material with high dielectric constant). The voltage on the gate V_G is crucial in the performance of the device since it controls the carrier density in the channel and therefore its conductance. We shall discuss the architecture of rubrene based OFETs and how experimental estimates for carrier mobility can be made, in some detail in the next chapter of this thesis.

Here we will introduce two approaches to investigate theoretically the charge transport characteristics of a device depicted in Fig. 4.2 in the linear response, i.e. at low applied bias. The theoretical approaches we use in this thesis comprises evaluating conductance

from the Landauer-Büttiker formula [129] and the charge carrier mobility from the Kubo Formula [194]. In principle, the former is applicable only to ballistic systems, while the latter holds true for both ballistic and diffusive transport scenario. However, both the methods are equivalent in the large wavelength or low frequency limit of the charge carrier.

4.2 Charge transport through OSCs

OFETs use π -conjugated OSC molecular crystals like polyacene, polyaniline, polypyrrole, metal-quinoline derivatives as the semiconducting channel material, in their single molecular crystalline form [100]. In particular single crystalline rubrene-based OFETs have mobilities even comparable to those traditionally made from amorphous and polysilicon [159, 114, 169]. The predominant interest in OSCs have soared due to the low-cost of such organic materials, their effective realization into large area devices and an increasing public sentiment towards biodegradable electronics. Solution processable OSC have also found widespread applications as polymer light-emitting diodes in high contrast optical display panels [101, 102]. This application integrates current modulation with light emission in OSC, a phenomenon coined as electroluminescence [103]. These display units can be commercially realized as fully colored all plastic flexible panels [102], therefore finding their place as key technological outputs of the optoelectronics industry.

Such applications of OSCs require a better understanding of their optoelectronic and electrical properties [104]. Investigating charge transport and understanding the factors, which limit charge carrier mobilities in such materials, are crucial first steps in order to design and synthesize better materials and further improve their device performances. OSCs have band gaps comparable to their inorganic counterparts [105], however their charge carrier mechanisms are completely different. Typical hydrocarbon based π -conjugated polymers have their valence electrons residing in sp^2 hybridized orbitals and p_z orbitals, which are orthogonal to the sigma bonds. While the valence electrons in the sp^2 hybridized orbitals are completely saturated, the ones in the p_z orbital are closer to the

fermi level and are also delocalized. Thus when an organic polymer is doped (oxidized), some of the delocalized p_z electrons are removed, and they become highly mobile along the direction of conjugation of the polymer chain. Such p -doping has been extensively demonstrated in a number of electronegative hole transport materials [106]. More often in organic light emitting diodes (OLEDs) hole injection into the HOMO levels of the OSC is achieved through an electrode with a very high workfunction material like Indium Tin Oxide (ITO) [107].

Also, n -doping in OSCs has been established [108]. This typically includes electron injection from an electrode (e.g. in an OLED device) material of a low work function metal, like Calcium or Magnesium, into the unoccupied LUMO states of the OSC. The subsequent charge transport within the organic material in both hole and electron transport scenarios, is generally facilitated by the $\pi - \pi$ stacking. The success of an efficient carrier injection and transport through OSCs as well as improved optical characterization, have resulted in the fabrication of OLEDs capable of producing white light with seriously improved device efficiency [109].

However, unlike inorganic materials, organic systems provide a very lively environment for carrier transport. Weak Van der Waals interactions, predominant $\pi - \pi$ stacking and interactions between electronic and nuclear degrees of freedom provide a phonon rich environment for charge transport [181, 62]. Needless to say, all these factors dominate charge transport through OSCs and must be accounted for in our theoretical methodology. While we are still in the subject of distinguishing between the electronic structures of organic and inorganic semiconductors there is one more point, which we want to mention. The band structures of inorganic semiconductors (e.g. Si) are generally quite dispersive, while that of an OSC (e.g. please see Fig. 5.8a) is relatively quite flat[62].

The charge transport mechanism in organic crystals is controlled by factors like temperature and charge carrier concentration. Historically with the advent of conducting polymers it was understood that the primary mechanism for carrier transport is thermally

assisted hopping [196]. By the virtue of defects prevalent in a semiconductor material, the charge carriers propagate through the localized states near the conduction and valance band edges in the band gap of the OSC. Subsequently with temperature, the carriers gain sufficient thermal energy to effectively hop across these localized states efficiently. This is usually reflected as an increase in charge carrier mobility with temperature which is the fingerprint of thermally assisted hopping mechanism [111].

As time progressed and with better experimental techniques, defect-free single crystalline semiconductors were synthesized. The reader is directed to the review in reference [117] for the history and development of organic single crystals. Such organic single crystals are grown under carefully controlled experimental conditions. Single crystalline semiconductors quickly became favored for applications in the optoelectronic industry. This is because of their physical characteristics by the virtue of which they are materials with a crystalline lattice that is continuous, with no grain boundaries and no defects or vacancies.

Charge transport mechanism in defect-free organic single crystals can be described by band transport. This transport mechanism is essentially characterized by delocalized charge carriers as in inorganic semiconductors or metals. Experimentally, evidence of band transport has been extensively reported in ultra pure naphthalene single crystals [111, 112, 113]. Apart from these a substantial Hall effect in OSCs at room temperature is an indication of delocalized (band) transport [160, 114]. The characteristic feature of band transport is that the charge carrier mobility rapidly decreases with temperature, as a result of increased scattering due to phonons at high temperature. We must also mention the theoretical work of Troisi *et al.* [218, 115, 219, 116] who proposed an interesting concept based on localization induced by the intrinsic dynamic disorder of the molecules in an organic crystal, as another explanation for the mechanism of charge transport in ultra-pure organic crystals.

Interestingly, the signature of dynamic disorder is the same as band transport, i.e. a

decrease in mobility with temperature as a result of increased localization due to disorder at high temperature. We shall discuss a system where dynamic disorder explanation is applicable in Chapter 6 of this thesis. Although in an ideal experiment defect free charge transport through the organic is desired, in a single crystalline OFET, gate dielectric always introduces some sort of localized defect states in the organic channel. A systematic study of charge transport properties as a function of gate insulators (with varying dielectric constants) provides valuable insights into this aspect [110].

In this section of the chapter, we will represent one-dimensional and two-dimensional OSC molecular networks using the Hamiltonian introduced by us in the previous chapter. We monitor the transport observable namely charge carrier mobility of different 1D and 2D networks as a function of the microscopic parameters of the Hamiltonian. We find strong evidence of band transport for the range of parameters taken into consideration in the calculations presented here. Also, we find an acute sensitivity of the charge transport properties to the morphology of the networks.

The work presented in this section of the thesis is intended to provide an understanding for the charge transport response of the basic Hamiltonian representing OSCs. Before we move onto investigating the transport properties of real systems from first principles in the next chapter, we would like to familiarize ourselves with the “charge transport phase diagram” of the model, i.e. the behavior of the charge transport as a function of model parameters and network morphology. Therefore, this would also enable us to understand the capacity and capability of our computational procedure.

4.2.1 Linear Response Kubo Formula

We consider a single-site tight binding model for a quasi two-dimensional lattice, which includes repulsive Hubbard and electron-phonon (el-ph) interactions. This is described by the following Hamiltonian, which is exactly the same as the one introduced by us in

the previous chapter

$$\begin{aligned} \hat{H} &= \sum_{i\sigma} \epsilon_{i\sigma} c_{i\sigma}^\dagger c_{i\sigma} + \sum_{ij} [\gamma_{ij} + \alpha(q_i - q_j)] (c_{i\sigma}^\dagger c_{j\sigma} + c_{j\sigma}^\dagger c_{i\sigma}) + \\ &+ U \sum_i \hat{n}_{i\uparrow} \hat{n}_{i\downarrow} + \frac{1}{2} k \sum_{i,j} (q_i - q_j)^2. \end{aligned} \quad (4.3)$$

The microscopic parameters of the model are the el-ph coupling parameter, α , the Hubbard repulsion strength, U , the elastic constant, k , the transfer integrals $\gamma_{ij} = t$ and ϵ the on-site energy. Moreover, q_i is the atomic displacement of site i and again we consider only 1D longitudinal motion. The magnitudes of ϵ , t and k are maintained the same as in the previous chapter.

In Eq. (4.3), it is assumed that the nuclear kinetic energy is quite small in comparison to the electronic kinetic energy, t . This assumption is valid according to the classical treatment of nuclear motions, q_i . Furthermore, the Holstein (non-local) electron phonon interaction term is ignored because the particular phonon modes which contribute to the Holstein term are excited at only very high temperature [118, 119, 116].

In this thesis we evaluate the charge carrier mobility from the linear response Kubo formula [194] in particular using the approach by Cataudella and co-workers [98]. The conductivity, σ , as a function of frequency ω , for each Monte Carlo configuration is given by the following expression

$$Re[\sigma(\omega; \{q_i\})] = \frac{(ea)^2}{\hbar} \frac{2\pi}{V\omega} \sum_{\lambda, \lambda'} (f_\lambda - f_{\lambda'}) |\langle \lambda | \hat{J} | \lambda' \rangle|^2 \times \delta(E_\lambda - E_{\lambda'} + \omega). \quad (4.4)$$

Here $|\lambda\rangle$ are the eigenstates of \hat{H} , J is the current density, a is the equilibrium distance between sites in the model and $V = L \cdot a$ is the system volume. Moreover in Eq. (4.4), f_λ is the Fermi function representing the thermal occupancy of the carrier eigenstates

$$f_\lambda = \frac{1}{\exp[\beta(E_\lambda - \mu)] + 1}. \quad (4.5)$$

The current density J enters in Eq. (4.4) through the matrix elements of the current-correlation operator. This can in turn be re-written in terms of the unitary matrix Ψ that diagonalizes \hat{H} [Eq. (4.3)], as:

$$\langle \lambda | J | \lambda' \rangle = \sum_{ij} \tau_{ij} [\Psi(i, \lambda) \Psi(j, \lambda') - \Psi(j, \lambda) \Psi(i, \lambda')] \quad (4.6)$$

where

$$\tau_{ij} = \gamma_{ij} + \alpha(q_i - q_j). \quad (4.7)$$

In order to use Eq. (4.4) for a finite lattice, the delta function, $\delta(E_\lambda - E_{\lambda'} + \omega)$, is replaced by a Lorentzian

$$\delta(E_\lambda - E_{\lambda'} + \omega) = \frac{\pi\eta}{(E_\lambda - E_{\lambda'} + \omega)^2 + \eta^2}. \quad (4.8)$$

Here η is an artificial broadening added to the discrete eigenvalues of the finite length lattice. Let us discuss in more detail the physical meaning of η . From solid state knowledge, in a uniform chain of H atoms of length L with on-site energy ϵ and transfer integral t the expression for energy eigenvalues is $E_m = \epsilon + 2t \cos(\frac{m\pi}{L+1})$. Here m is an integer taking values $m = 1, 2, \dots, L$. When $L \rightarrow \infty$ this reduces to the band dispersion for the infinite chain, with $\frac{m\pi}{L+1} \rightarrow k$ for $0 \leq k \leq \pi$. However for finite lengths the chain has a discrete energy spectrum. In our approach in computing the carrier mobility, η causes an artificial broadening of these discrete energy levels for finite lengths.

The charge carrier mobility μ is defined as :

$$\mu = \frac{1}{\rho e} \lim_{\omega \rightarrow 0} \text{Re}[\sigma(\omega)]. \quad (4.9)$$

The mobility μ is averaged over all the ionic displacements generated by the Monte Carlo simulations [180]. In principle, the above equations to compute the mobility in the linear response is only valid when $\omega \rightarrow 0^+$ (static limit) and $\eta \rightarrow 0^+$ (thermodynamic limit $L \rightarrow \infty$). Let us briefly discuss the values for ω and η used in our calculations.

In our results it turns out that for any combination of (η, L) and at every temperature T , the mobility depends only slightly on ω . Moreover, as we keep reducing the value of ω there is a particular threshold, beyond which mobility does not depend on further decreasing ω . Thus we take the value of $\omega = 0.00004t$ as a good approximation of the static limit. Next, we also monitor the values of the mobility as a function of system size L and η . It is argued that for a one-dimensional system if $\eta = 0$ the carrier mobility μ from Eq. (6.12) could be zero [98]. As such, in order to obtain a finite mobility in our model one needs to introduce an artificial broadening, η . For this purpose we monitored μ vs η at different L . At low values of η , μ is small and subsequently on increasing η the mobility reaches a plateau. We use the value of $\eta = 0.02t$ corresponding to the onset of this plateau to calculate the mobility. We also find that for larger values of L (closer to the thermodynamic limit in the model), we reach a constant μ . Our procedure to compute mobility from Kubo formula was inspired by the work of Clautadella and co-workers [98, 99]. Here we have investigated one-dimensional chains up to $L = 512$, but with no periodic boundary conditions. Thus in all the calculations of carrier mobility presented in this thesis, we also have rigorously analyzed μ vs different values of ω and η .

In the following section we shall investigate in detail the role of microscopic parameters on charge transport properties of OSC crystals with this approach. In particular we analyze the dependence of mobility on the charge carrier density, the el-el and the el-ph interactions. We also explore the charge trapping mechanisms in various one-dimensional (1-D) networks. In the final part of this section we shall examine the charge transport properties of two-dimensional (2-D) polymer networks, and in particular the role played by the various (inter and intra molecular) hopping constants in such networks.

4.2.2 Results and discussions

1-D Chains

The charge transport properties of the model can be understood by exploring the temperature dependence of the charge carrier mobility as a function of other microscopic parameters in the problem. Let us begin our discussions first by investigating the role played by charge carrier density. The left panel of Fig. 4.3 shows the temperature dependence of the mobility at different densities. The carrier densities investigated here correspond to the half filling situation ($\rho = 1.0$) similar to the previous chapter, a filling slightly less than half ($\rho = 0.85$) and finally at a very low filling ($\rho = 0.02$). The first aspect that is apparent from the left panel of Fig. 4.3, is that at half-filling, the temperature dependence of the mobility is extremely shallow. This can be understood by keeping in mind the fact that for a half-filled band the group velocity of the charge carriers is maximum. Therefore electrons are scattered little by phonons at finite temperatures. In contrast at low charge carrier concentration (corresponding to single electron filling, $\rho = 0.02$), the mobility decreases rapidly with temperature, following a (near) power law. This rapid decrease in mobility with temperature is attributed to an increased scattering due to phonons and to the small group velocities of the carriers at the edge of the Brillouin zone.

In the right panel of Fig. 4.3, we show the temperature dependence of the mobility at two different values of the el-el interaction $U = 0.02t$ and $2.4t$ at half filling. These two values of U correspond to the non-spin polarized (nSP) and spin polarized (SP) phases of the model explained in detail in the previous chapter. We notice that the absolute value of charge carrier mobility is smaller for $U = 2.4t$ in comparison to $U = 0.02t$ at low temperatures. This is a direct consequence of the charge localization as a result of SP phase at increased el-el interactions. The temperature dependence of the mobility at $U = 2.4t$ can be understood in the following manner. With increasing U and at low temperature, the charge carriers are more localized forming the SP phase. Therefore the carrier mobility is

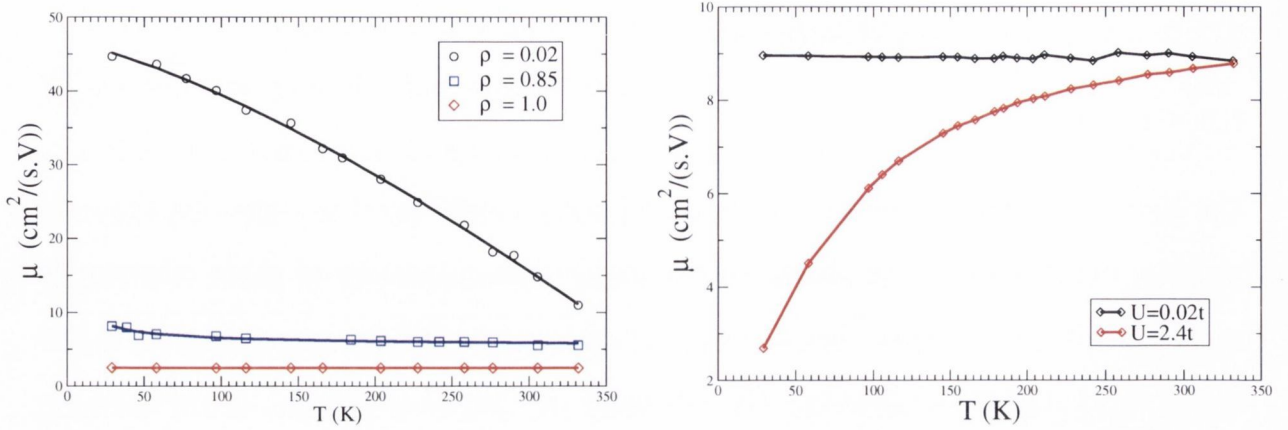


Figure 4.3: The temperature dependence of the charge carrier mobility as a function of the microscopic parameters in the problem: charge carrier density ρ in the *left panel* and el-el interaction U in the *right panel* is shown here. In the left panel the other microscopic parameters used are $U = 2.4t$, $\alpha = 0.01t$, $k = 4.2t$ and $t = 2.5$ eV. The other parameters used in the results presented in the right panel are $\rho = 1.0$, i.e. the half-filling scenario, $\alpha = 0.015t$, $k = 4.2t$ and $t = 2.5$ eV.

low. However with temperature, the itinerant electrons acquire sufficient thermal energy to overcome the trapping induced by localization, and thus the mobility increases with temperature. Here we would like to point out an important aspect in the functioning of OFETs, which is very pertinent to the discussions we just had on charge carrier concentration. The optimal performance in an OFET is at low voltages, which correspond to low carrier concentrations in the organic channel and therefore less localization [160]. Henceforth in all our calculations we shall use low charge carrier densities of $\rho = 1/L$ and $U = 0.0$.

In Fig. 4.4, we show the temperature dependence of the mobility plotted on a log-log scale for different values of the el-ph interaction strength, $\alpha = [0.004t - 0.08t]$, for a chain of $L = 256$ atoms. In our calculations we have observed that the discrepancies due to boundary conditions were negligible for a large enough size of the chain. We fit each of the plots to a power law expression $\mu = \mu_0 T^{-\delta}$. For all values of el-ph interaction strengths, we note that the mobility rapidly decreases as a function of temperature with $\delta = 1.25 - 1.30$. A large power law decay of the mobility is generally a fingerprint of band-transport as observed in single crystal organic materials. For weak el-ph interaction

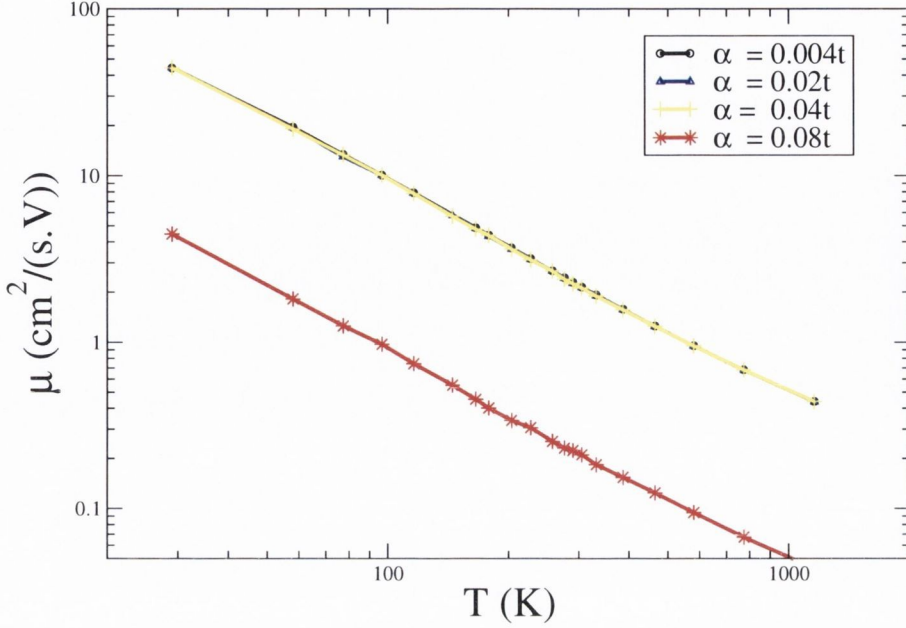


Figure 4.4: μ vs T for different values of the el-ph interaction strengths, α , for a chain of $L = 256$ atoms. At finite el-ph interactions the mobility decreases rapidly with T , signalling band transport. The other microscopic parameters used in obtaining the graph are $\rho = 1/256$, $U = 0$, $k = 4.2t$ and $t = 2.5$ eV.

($\alpha = 0.004t - 0.04t$) the power law exponent is $\delta = 1.25$. As the el-ph interaction strength is increased, the absolute value of the mobility decreases. This is attributed to an increased scattering of the itinerant charge carriers at all temperatures as a result of phonons, due to enhanced el-ph coupling also observed in previous works[218, 98]. However, interestingly the power law exponent, δ , slightly increases, $\delta = 1.30$ for $\alpha = 0.08t$ and $\delta = 1.40$ for $\alpha = 0.20t$. This means that even for a stronger el-ph interaction, when there is increased scattering of the charge carriers, i.e. the signature of μ vs T is still the same. This was also observed in previous theoretical work [219]. Finally, we must mention that when $\alpha > 0.1t$ for these range of parameters the μ vs T curves become increasingly noisy.

In the 1D polymer chain simulated here, we obtain a power law dependence of the mobility on temperature over the entire range of parameters. Thus the charge carrier mechanism is the well established band transport. Indeed, the wavefunctions of the system are delocalized in nature for $t = 2.5$ eV, $U = 0.0$ eV and α/t is relatively small. According to the band transport mechanism with temperature the delocalized carriers of the system

are increasingly scattered due to phonons and therefore the mobility decreases. We must stress here that the charge transport mechanism depends on the absolute magnitudes of α , t and k as we shall see in the results presented in the next chapters in this thesis.

1-D Segments (Molecular Chains)

The charge transport calculations reported so far were performed on a uniform 1-D chain (inter-atomic hopping parameter t is constant throughout the chain). We are now interested in investigating the length dependence and studying the effect of charge trapping on transport. This is because the principal objective of this thesis is to simulate carrier transport through organic molecular crystals. The results presented in this subsection are indeed a step forward in that direction, justifying the coarse graining procedure to model organic molecular crystals.

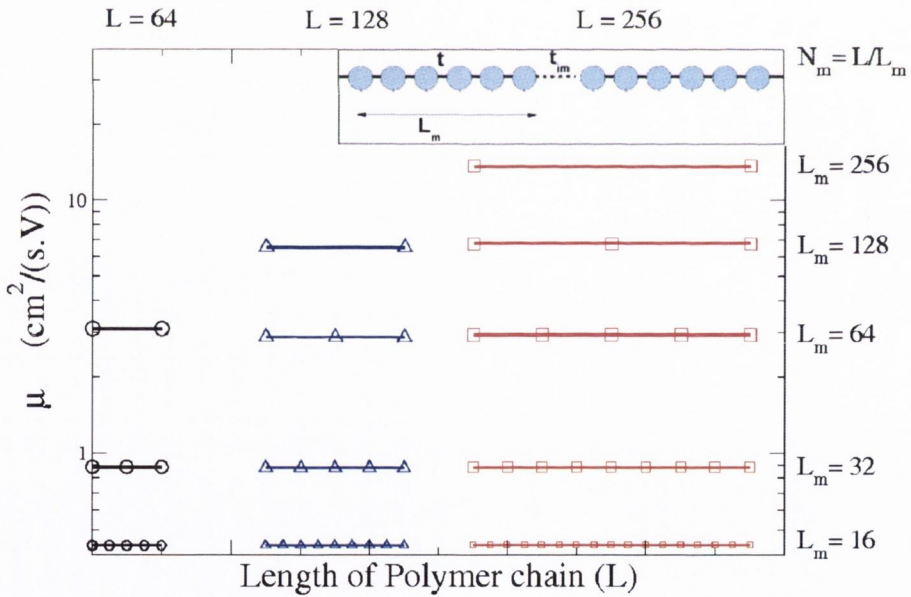


Figure 4.5: μ for different 1D segments; $L = 64$ (circles), $L = 128$ (triangles) and $L = 256$ (squares). The polymer networks comprise molecules of a given length, electronically coupled by the intermolecular hopping, $t_{im} \ll t$ as shown in inset diagram. The mobility of the smallest molecule (segment), determines the overall mobility as a consequence of percolation theory [125]. The other microscopic parameters used are $\rho = 1/L$, $U = 0$, $k = 4.2t$, $t = 2.5 \text{ eV}$, $t_{im} = 0.05 \text{ eV}$ and $T = 300\text{K}$.

Fig. 4.5, shows the absolute value of mobility for various 1D polymeric networks cor-

responding to chains of length (from left to right) $L = 64, 128$ and 256 atoms, each at a fixed temperature $T = 300\text{K}$. The polymer networks are chains of total length L , each comprising of N_m molecules of length L_m . Thus $L/L_m = N_m$. Moreover, the intermolecular hopping integral t_{im} is $t_{\text{im}} \ll t$, thereby creates an obstruction for charge transport. As an example, $L_m = 128$ for a chain $L = 256$ has $N_m = 2$ molecules and likewise $L_m = 32$ for a chain $L = 256$ has $N_m = 8$ molecules. Let us now analyze our results.

First of all in Fig. 4.5 for a chain with one molecule ($N_m = 1$, uniform hopping constant through-out) the mobility μ increases with L . This can be understood very conveniently by considering that as the 1D chain becomes longer, the number of terms in the current-correlation operator J in Eq. (4.6) increases and therefore the charge carrier mobility increases. However, for $L > 256$ the carrier mobility converges to a constant value. It can be said that the thermodynamic limit in the model is reached for $L \geq 256$.

The central message coming from Fig. 4.5 is that for a fragmented molecular chain the mobility of the smallest segment determines the overall mobility. This is a direct consequence of percolation theory [125], because the smallest unit forms a bottle neck ($t_{\text{im}} \ll t$) for transport in the entire chain.

The results presented in Fig. 4.5 will be quite significant in justifying the basic concept behind the coarse graining method which we employ for representing organic molecular crystals, in the coming chapters of this thesis. Indeed according to these discussions, when we want to simulate transport properties of molecules in a crystal, one only needs to worry about the transfer integrals between the molecules. This is provided that the carrier is "delocalized" within the molecule (e.g. in rubrene). In this manner one can coarse-grain out molecular details smaller than a particular segment.

2-D polymer networks

Here we investigate the charge transport properties of 2D networks. A 2D rectangular slab (see Fig. 4.6), containing five 1D chains, coupled by a interlayer hopping t_{il} and an

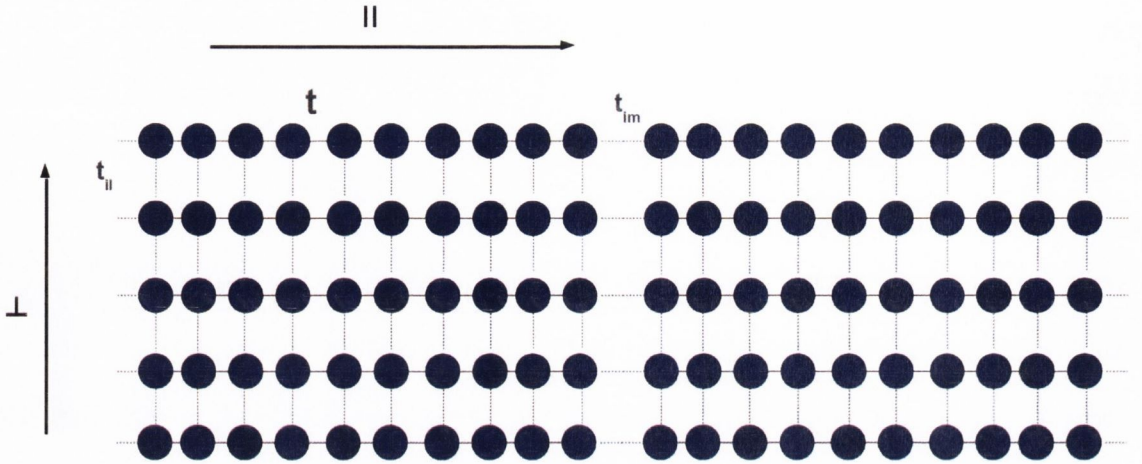


Figure 4.6: 2D rectangular slab containing five layers of 1D chain with a interlayer hopping t_{\parallel} . The 2D rectangular slab, which we have investigated here is 256×5 sites.

intermolecular hopping t_{im} (t_{\parallel} and t_{im} can be up to the same order as t) is used in our simulations. In general, the highest charge carrier mobility in oligomers is found when there is a co-facial π -stacking of the individual molecules. This arrangement forms the inspiration of the 2D polymer network simulated here. In our calculations we consider phonons only in the longitudinal direction assuming the effect of phonons in the perpendicular direction, \perp to be negligible. The charge carrier mobility in such a 2D network is anisotropic and we shall report the absolute values of mobility in the directions parallel, μ_{\parallel} , and perpendicular, μ_{\perp} , to the 1D segments (see Fig. 4.6).

The left panel of Fig. 4.7 illustrates the temperature dependence of μ_{\parallel} at a fixed $\alpha = 0.08t$ and $t_{im} = 1.0t$, but changing t_{\parallel} as $t_{\parallel} = [0.0000002t - 1.0t]$. We notice that for a minuscule value of $t_{\parallel} = 0.0000002t$, the 2D network is essentially five disjointed 1D chains, hence the temperature dependence of mobility should reflect the 1D charge transport characteristic. Indeed the charge carrier mobility decreases rapidly with temperature following a power law ($\delta = 1.2$) decay. Therefore the charge transport of the setup can be understood with the same explanation as in the previous section.

As t_{\parallel} is increased from $t_{\parallel} = 0.02t$ to $1.0t$, the absolute value of μ_{\parallel} increases. This is by the virtue of more conducting channels available for the charge carriers to move along

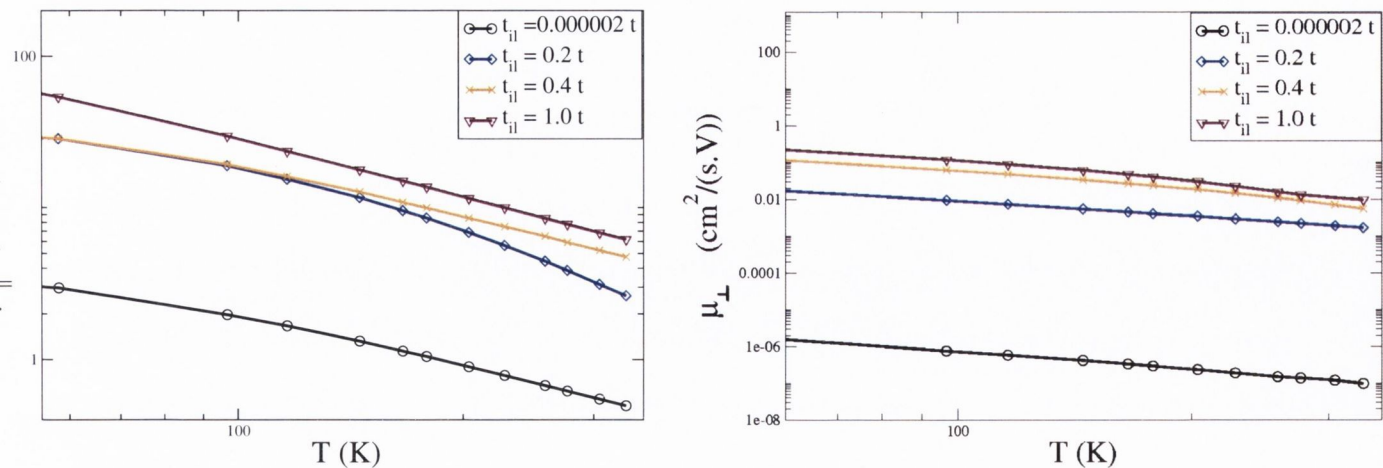


Figure 4.7: Charge transport in a quasi-2D network. The temperature dependence of the charge carrier mobilities evaluated for the 2D network (Fig. 4.6) in the directions parallel $\mu_{||}$ vs T (*left panel*) to the 1D chains and perpendicular to them μ_{\perp} vs T (*right panel*), both at fixed $\alpha = 0.08t$ and $t_{im} = 1.0t$, but varying t_{il} for $t_{il} = 0.0000002t - 1.0t$. This behavior is again an indicative of dynamic disorder in such 2D networks. Please note that here $t = 2.5$ eV.

the various 1D chains as a result of an increasing t_{il} . As a proof for this argument we also find that μ_{\perp} increases as t_{il} increases (see the right panel of Fig. 4.7). With increasing t_{il} , the $\mu_{||}$ vs T relation in the upper panel of Fig. 4.7 is a power law decay but with a smaller $\delta = 1.05$. These calculations show that in order to simulate real organic crystals, one must take into account the intermolecular interactions along all the crystallographic directions, as the charge transport characteristics of the system will depend on them.

The results presented in this subsection on 2D networks has enabled us to understand the behavior of μ vs T on the structural morphology of 2D networks. This work intends to be a first step and gives us an idea of what to expect when simulating full 3D rubrene single crystals in the next chapter.

To summarize the work in this section, we have investigated in detail the charge transport characteristics obtained from a microscopic approach for different OSC networks. These are described by a microscopic Hamiltonian, which includes all the essential interactions in an organic material. We have observed that for 1D and 2D networks,

typically emulating ultra-pure semiconductor materials used in OFETs, the charge carrier mechanism is band transport. We have also observed the effect of deliberate charge localization within a certain number of atoms (molecules) in the network and verified percolation theory for 1D polymer networks. Finally we have also studied the charge transport characteristics of different 2D polymer networks. The dependence of charge transport properties on the morphology of the polymer networks observed in this work suggests a significant need for a comprehensive investigation of the different intermolecular interactions along all the crystallographic directions. These are essential to understand the transport characteristics of a real OSC.

4.3 Spin transport

4.3.1 Spin relaxation mechanisms in organic materials

The spin transport properties of a material are characterized by how effectively electron spins maintain their polarization while travelling through it. In OSCs the loss of spin polarization due to the interaction of spins with defects or magnetic ions can be safely ignored because such events are quite rare in ultra pure single crystalline OSCs described by band transport².

As such, the two main interactions responsible for spin relaxation of the carriers in OSCs are hyperfine (HI) and spin-orbit coupling (SO) [66].

Hyperfine Interaction Hyperfine interaction is by the virtue of the electron's spin interacting with the nuclear spins of the atoms constituting the organic material. It is well established that in an OSC HI is mediated in two different ways. The itinerant carbon π -electrons can indirectly couple to proton spins in the organic material through exchange interactions with hydrogen s electrons [136]. Moreover, there is also dipole-

²There are very few spin-flipping impurities in organic single crystals.

dipole coupling of the π -electrons to the proton spins. A combination of these two effects can give rise to a hyperfine field of a few mT [93] in particular because H has a large nuclear spin.

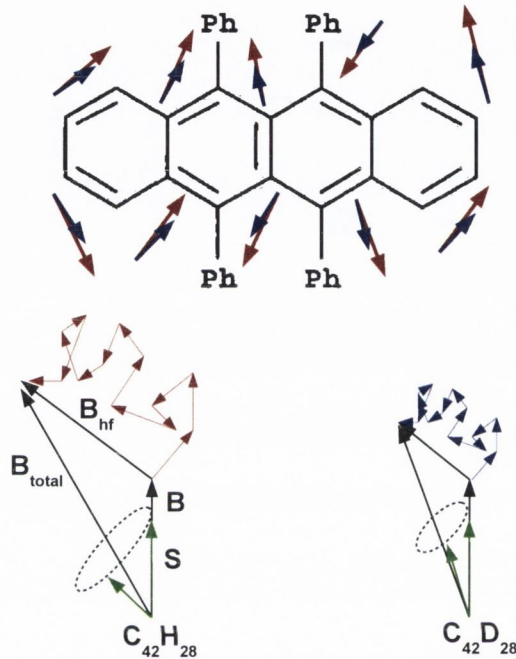


Figure 4.8: Semi-classical model [135] to explain the decoherence of carrier spins due to HI is illustrated here for the example case of a rubrene molecule. Due to a substantial nuclear magnetic moment of H atoms, the corresponding random hyperfine fields associated with the protons in rubrene will be significant. Vector summation of these random fields are illustrated as the total hyperfine field, B_{hf} (in red). Replacing H with D [132, 133] is an experimental technique to probe the effect of HI in controlling spin transport through organic materials, as D has nuclear spin a fourth of that of H. The corresponding hyperfine fields of D are indicated in blue and they are smaller than those associated with H. The carrier spins (shown as green arrows) precess around the total field, B_{total} , which will be the sum of external magnetic field B , and the total effective hyperfine field B_{hf} . According to this model, the random component of B_{total} is reduced upon deuteration and therefore spin relaxation is less for the deuterated polymer, as illustrated in the lower right panel. This model is derived from the work of Bobbert [135]

There is a semi-classical model based on the works of Schulten and Wolynes [134] and later Bobbert of [135], which explains the mechanism of HI in controlling spin relaxation through OSCs. According to the works, many proton spins in a material cause the itinerant electron's spin to precess around an effective classical random hyperfine field

which adds to an external magnetic field as illustrated in Fig. 4.8.

We explain the loss of spin polarization in the example case of rubrene molecule $C_{42}H_{28}$. In the top panel of Fig. 4.8 the molecular structure of rubrene is depicted, where Ph is a phenyl side group. In order to illustrate the concept of spin decoherence due to random proton spins we extend the explanation to hydrogenated rubrene ($C_{42}H_{28}$) as well as deuterated rubrene ($C_{42}D_{28}$). This is because the spin relaxation is expected to be less in the latter case as the nuclear spin of deuterium D is weaker than that of H.

The mobile π -electrons interact with the H and D nuclear spins, represented by red and blue arrows, respectively in Fig. 4.8. These are randomly aligned. In the semi-classical model, the π -electron spins (green vectors in the bottom panels of Fig. 4.8) precess around the effective magnetic field, $\mathbf{B}_{\text{total}}$, which is the sum of the applied magnetic field, \mathbf{B} and a cumulative total of the classical random hyperfine fields, \mathbf{B}_{hf} ($\mathbf{B}_{\text{total}} = \mathbf{B} + \mathbf{B}_{\text{hf}}$). \mathbf{B}_{hf} is proportional to the sum of all the randomly oriented quantum nuclear spins of the system. Since the nuclear magnetic moment of D is smaller than that of H, the magnitude of total effective \mathbf{B}_{hf} is reduced for the deuterated rubrene, therefore the loss of spin polarization is expected to be less in this case.

Another factor determining the effective efficiency of HI in producing spin-decoherence is that the wavefunctions of electrons and holes may be different, so that the resulting HI coupling will be different for the two carrier types [137]. Therefore, HI will be different in OSCs where the transport is hole dominated (e.g. in rubrene) and when it is electron dominated (e.g. in Alq₃).

Lets us now discuss the experiments which probe the role of HI in OSCs. Experimentally a crafty way to evaluate the effects of HI is by replacing H atoms in the OSCs with D atoms, which have a much smaller nuclear magnetic moment (D: 0.433×10^{-26} Joule T^{-1} ; H: 1.411×10^{-26} Joule T^{-1}). Replacing H with D does not significantly change the electronic structure or the geometry but it can change the spin relaxation. However, the results from such experiments have been quite controversial.

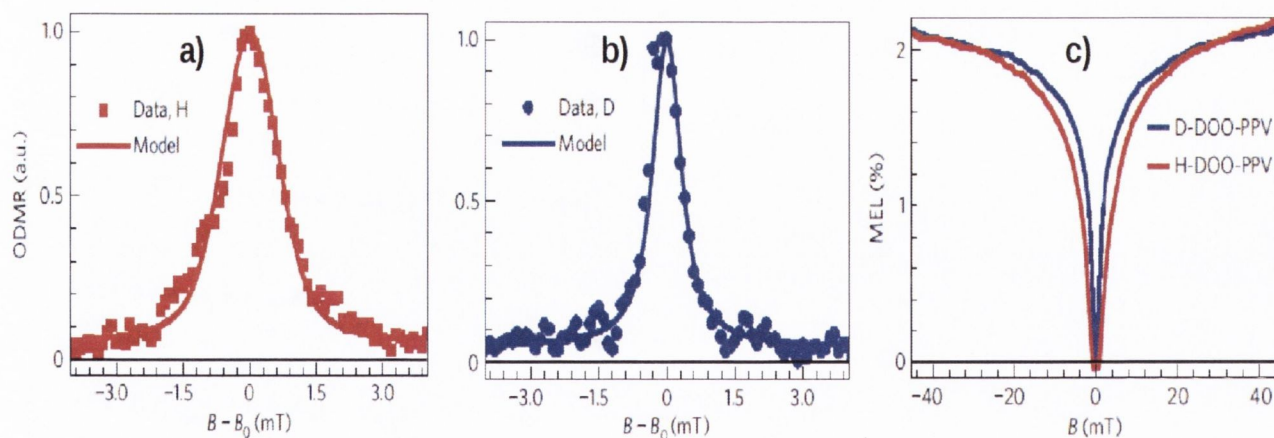


Figure 4.9: Experiments investigating the role played by HI in controlling spin transport through OSCs from Ref. [132]. The Optically Detected Magnetic Resonance (ODMR) in the left and middle panels and the Electroluminescence response in the right panel, as a function of magnetic field (lineshapes) are narrower for the deuterated polymer in comparison to the hydrogenated polymer. These results indicate that HI significantly influences spin transport through organic materials. Furthermore, an enhanced magnetoresistance was also observed for the deuterated polymer based spin valve as opposed to that measured for the hydrogenated polymer based spin valve (see Fig. 4.10a).

Nguyen *et al.* [132] found a significant effect upon deuteration. In the first of their experiments they monitored the photoluminescence spectra of a hydrogenated and deuterated π -conjugated polymer³ as a function of magnetic field⁴ (see Fig. 4.9a and Fig. 4.9b). Furthermore, they also monitored the electroluminescence of LED devices made up of those polymers as a function of magnetic field (Fig. 4.9c). In both these experiments a pronounced narrowing of the corresponding magnetic resonance peaks was observed, upon deuteration of the π -conjugated polymer. Moreover, the peak widths were all in the mT range corresponding to the hyperfine coupling of the charge carriers. They also evaluated the magnetoresistances (MR) of spin valves made from the hydrogenated and deuterated polymer (shown in Fig. 4.10a) and observed that the deuterated polymer spin valves had a larger MR than the hydrogenated one. This could be explained by low spin relaxation upon deuteration. Moreover, as shown in the inset of Fig. 4.10a they also observed that

³Poly(p-phenylene vinylene), i.e. a PPV based polymer.

⁴They monitored the magnetic resonance setup by a microwave field known as Optically Detected Magnetic Response (ODMR).

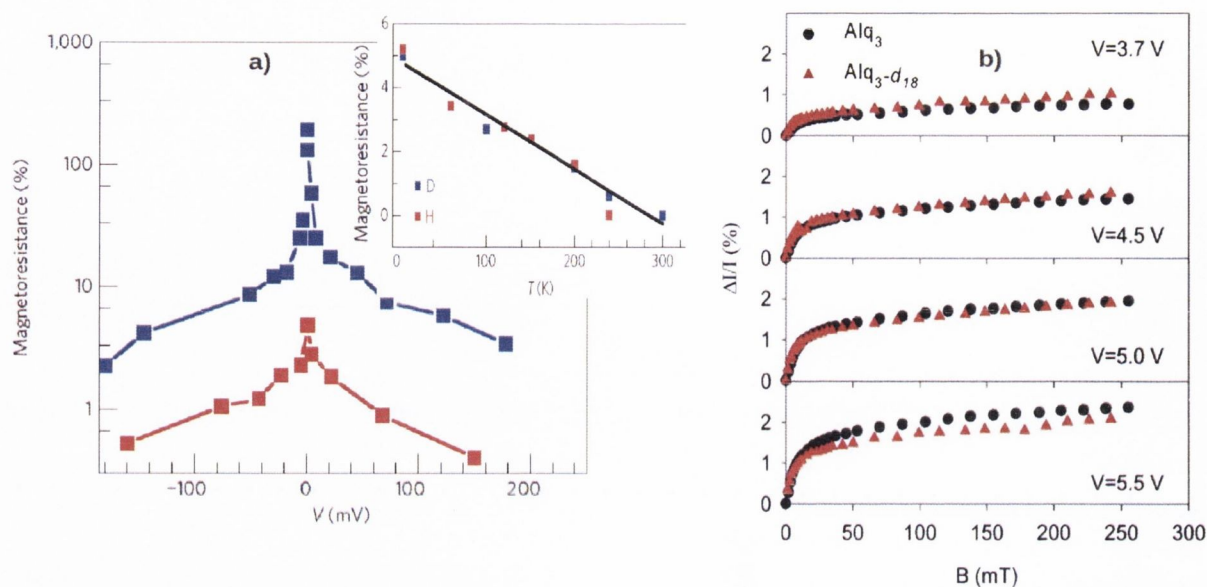


Figure 4.10: The magnetoresistance (MR) of a spin valve (shown in the left-hand panel) made from the deuterated polymer was an order of magnitude larger than that composed of the hydrogenated polymer. These results (from the work of Nguyen *et al.* [132]) together with an absence of a temperature dependence of MR for both polymers (inset) indicate that HI play an important role in governing spin transport. However, Rolfe *et al.* [133] in the right panel, did not find an appreciable change in the MR upon deuteration.

both the hydrogenated and deuterated polymer spin valves, followed a similar decrease in MR with temperature. This corroborated the fact that spin relaxation in their spin valves is indeed due to HIs. The latter is expected to be temperature independent because the energy scale for nuclear spins dynamics is tiny.

Meanwhile however, another experiment carried out by Rolfe *et al.* [133] reported no significant change (in MR) upon deuteration of the OSC (see Fig. 4.10b). Thus, they concluded that HI is irrelevant in controlling spin transport in OSCs. Apart from these experiments, there have also been a few theoretical works [93, 143] which advance HI as the principal spin scattering mechanism in organic materials.

A fair assignment of the current situation is that, whether or not HI controls spin transport through OSCs is still an open question.

Spin-orbit Coupling The other important spin relaxation mechanism in OSCs is due to SO interactions. As the name suggests spin relaxation due to SO occurs by the virtue of the interaction between the spin and orbital components of the angular momentum of the itinerant carriers. In principle, atomic SO in organic materials is quite small as its strength is inversely proportional to the fourth power of atomic number Z (for a spherical potential). Since the atoms constituting organic materials are from the first two of rows of the periodic table the corresponding atomic SO strength will be small. However, there have been interesting arguments, which make SO mechanisms sufficient to influence spin transport through organic materials, particularly because it is dependent on geometry.

In Fig. 4.11a we show the experimental results from Ref. [148]. Here a rapid decrease in spin diffusion length (l_s) of a NiFe/LiF/Alq₃/TPD/FeCo⁵ based spin valve, with temperature is shown. The inset of Fig. 4.11a illustrates the MR of the device as a function of temperature also following a similar trend. The fast decrease in l_s with temperature indicates that SO interactions are the main spin diffusion mechanism in OSCs. This is because the loss of spin polarization due to HI is not temperature dependent, as the energy scale corresponding to nuclear spin dynamics is tiny [181]. On the other hand spin relaxation due to SO coupling is controlled by temperature. Consequently with temperature, as the distance travelled by the spin polarized carriers (before losing their polarization) decreases the device MR also decreases. Please note that in these experiments l_s is obtained directly with muon spin resonance techniques.

The specific mechanism for spin relaxation in OSCs was identified as the Elliott-Yafet (EY) [141] one. According to the EY mechanism, whenever a charge carrier through a semiconductor scatters and loses (or gains) momentum, it relinquishes some of its spin polarization. Momentum scattering can occur due to phonons, which are ubiquitous in organic materials. The identification of the EY mechanism is based on another experi-

⁵Their device configuration is as follows: a few nanometers of LiF serves as a tunneling barrier, TPD: N,N'-diphenyl-N-N'-bis(3-methylphenyl)-1, 1'-biphenyl-4,4'-di amine is the hole transporting OSC and Alq₃ is the electron transporting OSC.

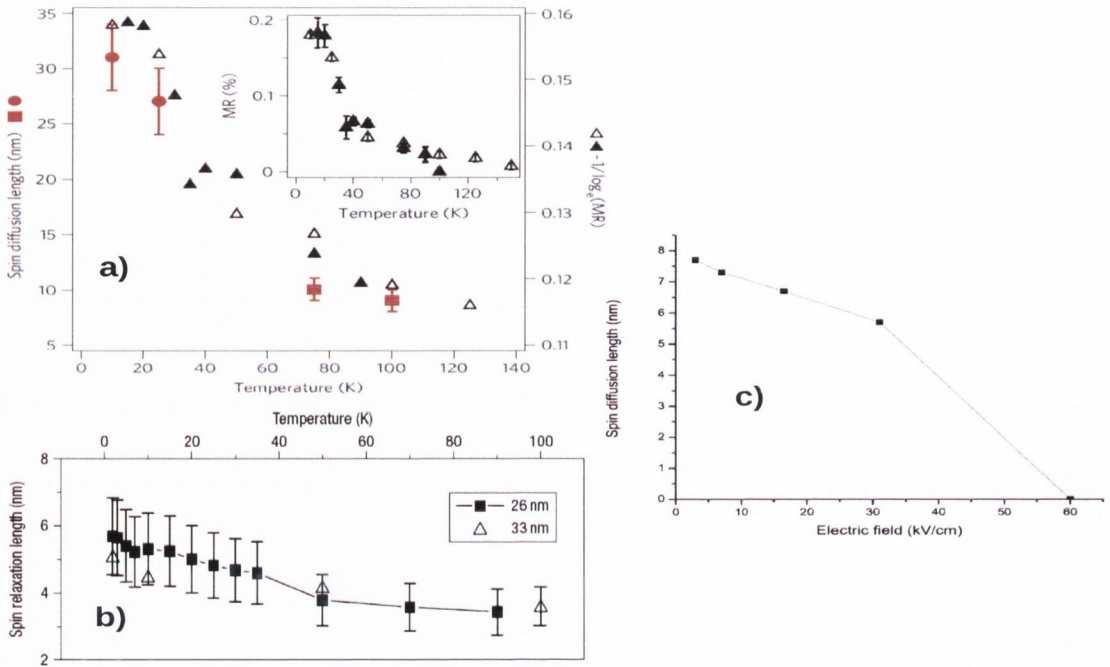


Figure 4.11: Experimental results, which support the evidence of SO coupling as the main carrier spin relaxation mechanism in organic materials, are shown here. Panels **a** and **b** respectively show a rapid and a slow decrease in spin diffusion length (l_s) of Alq₃-based organic spin valves with temperature, taken from references [65] and [148]. The inset of **b** shows a decrease in device magnetoresistance with temperature following a similar trend. Panel, **c** shows a decrease in the estimated l_s , as a function of an electric field [142]. The decrease in l_s with temperature (in **a** and **b**) and with electric field (in **c**) indicate spin relaxation due to spin-orbit coupling.

mental work [65], where they observed a decrease in l_s with system confinement. This is based on observation of an inverse dependence of l_s on mobility that is predicted by the EY mechanism of spin relaxation. Furthermore, the l_s of their Co/Alq₃ nanowires/Ni spin valves also showed a temperature dependence (see Fig. 4.11b). In the experiment, l_s was obtained by fitting the MR data to a modified Julliere's formula [138]. Another compelling evidence that SO interactions are responsible for spin relaxation in organic materials is based on the decrease in l_s with electric field observed by the same group (see Fig. 4.11c). For a detailed explanation please see the derivations in Ref. [142].

However, there have been experiments [139, 140] which have also observed a similar decrease in MR of Alq₃ based spin valves with temperature, as illustrated in Fig. 4.12.

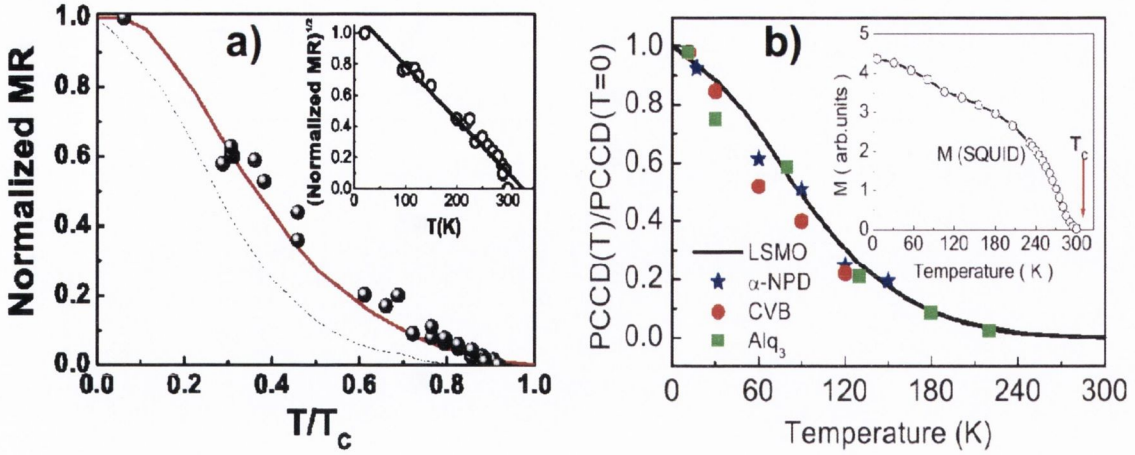


Figure 4.12: Steady decrease in MR in organic spin valves has also been observed in two other experiments. The results from reference [139] are shown in the left-hand side panel and those from reference [140] in the right-hand side panel. In both these experiments, the magnetoresistance decreases to zero around the Curie temperature of the ferromagnet (LSMO). In the inset of right-hand panel the magnetization of LSMO as measured in SQUID measurement is shown. These results show that the temperature dependence of MR curves observed is only controlled by the spin polarization of the injecting (bottom) electrode and has little to do with the intrinsic spin transport through the organic layer.

In this case curiously, the MR of the device decreases to zero at exactly the Curie temperature ($T = T_c$) of the LSMO ferromagnetic electrode. These results indicate that the temperature dependence of the spin valve effect is driven by the weakening of the spin polarization of the carrier injecting ferromagnetic electrode. In other words, the loss of spin polarization is likely to be controlled by the spin injection at the FM/OSC interface and not by the intrinsic spin transport through the organic layer. This argument is bolstered by the results of magnetization of the LSMO electrode plotted vs temperature measured using superconducting quantum interference device (SQUID) technique (see the inset of Fig. 4.12b), exhibiting a similar trend as MR vs T and decreasing to zero at $T = T_c$.

It is quite fair to say that the experiments, which probe spin transport through OSCs have been quite ambivalent in our opinion. It would be interesting to understand the reason as to why the experimental opinion on spin transport through OSCs is divided, as we have seen from the discussions in the preceding pages. Therefore, in this section we present a microscopic approach for investigating the spin transport properties in OSCs.

We can directly compare and understand the role of HI and SO coupling in controlling the spin transport properties of OSCs, by monitoring l_s .

4.3.2 Theoretical setup for spin transport

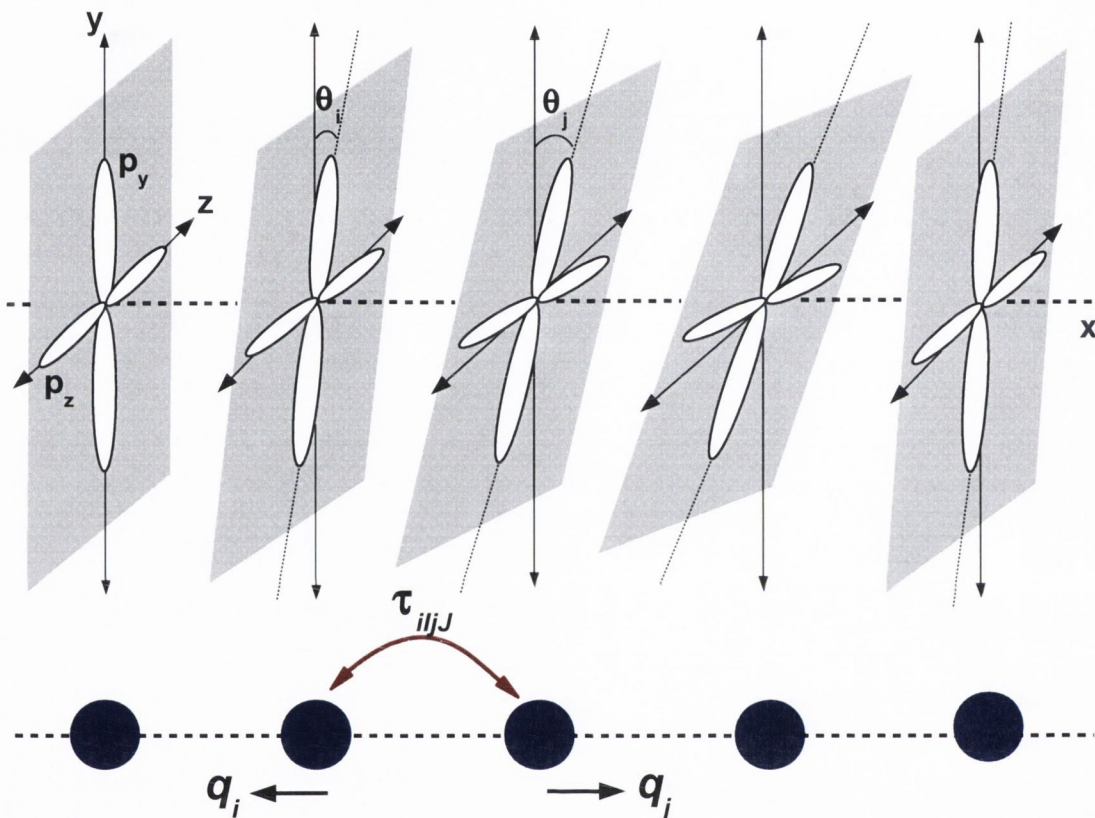


Figure 4.13: The model Hamiltonian of Eq. (4.10) captures the essential interactions in OSCs. The system we model includes a one-dimensional chain of atoms (bottom panel), containing two p (p_y and p_z) orbitals per atom (top panel). The carrier transport direction is along the \hat{x} axis and the p_y and p_z reside in the orthogonal yz plane. In order to account for spin-lattice fluctuations in our model, the atoms in the chain are rotated in the yz plane (e.g. atom i is rotated by an angle θ_i). Therefore the nearest neighboring transfer integrals [$\tau_{iIjJ} = \gamma_{iIjJ} + \alpha_{IJ} (q_i - q_j)$] will have an angular dependence. Furthermore, the atoms (i.e. both the p_y and p_z orbitals simultaneously) move along the \hat{x} axis due to phonons, with lattice displacements q_i for atom i .

We work on a one-dimensional chain of atoms representing an organic molecule, containing two p (p_y and p_z) orbitals per atom. The transport direction is along \hat{x} and the p_y and p_z orbitals reside in the yz plane. A schematic picture of our $\pi - \pi$ model system

is illustrated in the top and bottom panels of Fig. 4.13. The Hamiltonian describing this ensemble is given by Eq. (4.10) (below). This is an extension to the one which we have used in the previous section. Please be aware that we now introduce additional notations and have changed the names of few of the variables and their indices, as compared to the Hamiltonian discussed in the previous section. Here $c_{i\sigma I}$ ($c_{i\sigma I}^\dagger$) denotes the creation (annihilation) operator for an electron in an orbital I (p_y or p_z orbitals) at a site (atom) i with spin σ . Going through the constants in the Hamiltonian: ϵ is the on-site energy, k is the elastic constant and J_H and λ_{SO} are the strengths of the hyperfine and spin-orbit interactions respectively.

$$\begin{aligned} \hat{H}_M = & \sum_{i\sigma I} \epsilon c_{i\sigma I}^\dagger c_{i\sigma I} + \sum_{ijJ} [\gamma_{iIjJ} + \alpha_{IJ}(q_i - q_j)] (c_{i\sigma I}^\dagger c_{j\sigma J} + h.c.) + \frac{1}{2}k \sum_{i,j} (q_i - q_j)^2 + \\ & + J_H \sum_{i\alpha\beta I} \vec{S}_i^N \cdot [c_{i\alpha I}^\dagger (\vec{\sigma}_{\alpha\beta}) c_{i\beta I}] + \lambda_{SO} \sum_{iIJ\alpha\beta} \vec{L}_{iIJ} \cdot c_{i\alpha I}^\dagger (\vec{\sigma}_{\alpha\beta}) c_{i\beta J}. \end{aligned} \quad (4.10)$$

Let us systematically go through the Hamiltonian terms since H_M will form the basis of a large portion of the work presented in this thesis.

Transfer Integrals In the Hamiltonian in Eq. (4.10) the second term represents the transfer (hopping) integrals between each of the two p orbitals of nearest neighboring molecules ($j = i \pm 1$). In our model, we assume that the molecules (therefore the p_y and p_z orbitals) can rotate in the yz plane. For example the p_y and p_z orbitals of site i will make an angle θ_i with respect to (both) the original \hat{y} and \hat{z} axis. This is schematically illustrated in the top panel in Fig. 4.13.

We will now discuss the hopping terms between the individual p orbitals of the nearest neighbor atoms i and j . Assuming that the effective transfer integrals between two orbitals (I and J) is τ_{iIjJ} where $\tau_{iIjJ} = \gamma_{iIjJ} + \alpha_{IJ}(q_i - q_j)$, the hopping terms between similar kinds of p orbitals, i.e. when $I = J$ are $t_{ip_yjp_y} = \tau_{ip_yjp_y} \cos(\theta_i - \theta_j)$ and $t_{ip_zjp_z} = \tau_{ip_zjp_z} \cos(\theta_i - \theta_j)$. Furthermore, the hopping terms between dissimilar kinds of p orbitals,

when $I \neq J$, are $t_{ip_yjp_z} = -\tau_{ip_yjp_z} \sin(\theta_i - \theta_j)$ and $t_{ip_zjp_y} = \tau_{ip_zjp_y} \sin(\theta_i - \theta_j)$. Here θ_i and θ_j are the angles, which the molecules i and j are rotated, in the yz plane.

These expressions for the transfer integrals satisfy the limiting case, $\theta_i - \theta_j = 0$, i.e. the transfer integrals between dissimilar p orbitals are zero by symmetry. The angles in our model are classical vectors, which are evolved via Monte Carlo simulations [180]. Finally in our model, the electron-phonon interaction constants are taken as, $\alpha_{IJ} = \alpha$ and $\gamma_{IJJ} = t$.

Spin-orbit Coupling Next, the SO term in Eq. (4.10) can be decomposed for each site i in the chain as $\lambda_{SO} \vec{L}_{iIJ} \cdot \vec{S}_{iIJ} = \hat{H}_{SO}^{iIJ}$, where \hat{H}_{SO}^{iIJ} is the intra-atomic, on-site, SO Hamiltonian. L_{iIJ} and $S_{iIJ} = c_{i\alpha}^\dagger (\vec{\sigma}_{\alpha\beta}) c_{i\beta J}$ here are the orbital and spin angular momenta at site i . Also, $\vec{\sigma}_{\alpha\beta}$ is a vector of electron Pauli matrices and α and β represents the spin indices (\uparrow, \downarrow). \hat{H}_{SO}^{iIJ} can be expanded as

$$\hat{H}_{SO}^{iIJ} = \lambda_{SO} \vec{L}_{iIJ} \cdot \vec{S}_{iIJ} = \frac{\lambda_{SO}}{2} (L_{iIJ}^+ \sigma_{iIJ}^- + L_{iIJ}^- \sigma_{iIJ}^+) + \lambda_{SO} L_{iIJ}^z \sigma_{iIJ}^z, \quad (4.11)$$

where $L_{iIJ}^\pm (\sigma_{iIJ}^\pm)$ is the angular momentum (spin) ladder operators. In the spin-dependent orbital basis $\{|p_y^i \uparrow\rangle, |p_z^i \uparrow\rangle, |p_y^i \downarrow\rangle, |p_z^i \downarrow\rangle\}$, the resulting spin-orbit Hamiltonian matrix, $\langle I\sigma | \vec{L}_{iIJ} \cdot \vec{S}_{iIJ} | J\sigma' \rangle$, for an site i in the chain is

$$\hat{H}_{SO} = \frac{\lambda_{SO}}{2} \begin{pmatrix} 0 & 0 & 0 & -\iota \\ 0 & 0 & \iota & 0 \\ 0 & -\iota & 0 & 0 \\ \iota & 0 & 0 & 0 \end{pmatrix}.$$

Please refer to Appendix A where we derive all the non zero SO coupling matrix elements $\langle I\sigma | \vec{L}_{iIJ} \cdot \vec{S}_{iIJ} | J\sigma' \rangle$. As such, \hat{H}_{SO}^{iIJ} lifts the spin degeneracies of the eigenvalues of \hat{H}_M [Eq. (4.10)]. In OSCs, the strength of SO (λ_{SO}) is small, therefore this splitting is also small.

It is important to note that a minimal tight binding model which includes a non-zero SO, needs to have p_z and another p orbital (please refer to Appendix A). In our model this is the p_y orbital. It is for the sake of computational simplicity that we have dropped the p_x orbitals in our model. Furthermore, the justification to this is also based on the structure of organic molecular crystals. They are commonly characterized by a herringbone stacking (see Fig. 5.2c in the next chapter), with π electron density residing in the herringbone planes and minimal electron density between them. In our $\pi - \pi$ model, these herringbone planes can be the yz planes (in grey) shown in the top panel of Fig. 4.13.

Having described the incorporation of SO in our model let us go through the other terms in the Hamiltonian.

Hyperfine Interaction The hyperfine interaction term describes a Heisenberg-like interaction between the electron spins, $c_{i\alpha I}^\dagger (\vec{\sigma}_{\alpha\beta}) c_{i\beta I}$, and a set of classical vectors, \vec{S}_i^N , representing the nuclear spins. The hyperfine coupling strength for OSCs is $J_H = 10^{-5} - 10^{-6}$ eV [93]. The classical nuclear spins \vec{S}_i^N are also evolved in our simulations via Monte Carlo sampling.

Other Terms The first term of Eq. (4.10) accounts for the on-site energy and the third term is the classical elastic energy. For the spin transport calculations presented in this section, the values of the various constants in Eq. (4.10) are $\epsilon = 0$ eV, $t = 0.1 - 0.7$ eV, $\alpha = 0.05$ eV \AA^{-1} and $k = 12.5$ eV \AA^{-2} [180]. Finally, in all the calculations the half-filling scenario is considered.

Thus to epitomize, our $\pi - \pi$ model describes carrier transport across the herringbone structure in organic molecular crystals (like rubrene).

4.3.2.1 Extracting the spin diffusion length

Experimental approach Usually the spin diffusion length l_s , which is the figure of merit for spin transport in a semiconductor can be extracted by fitting the modified

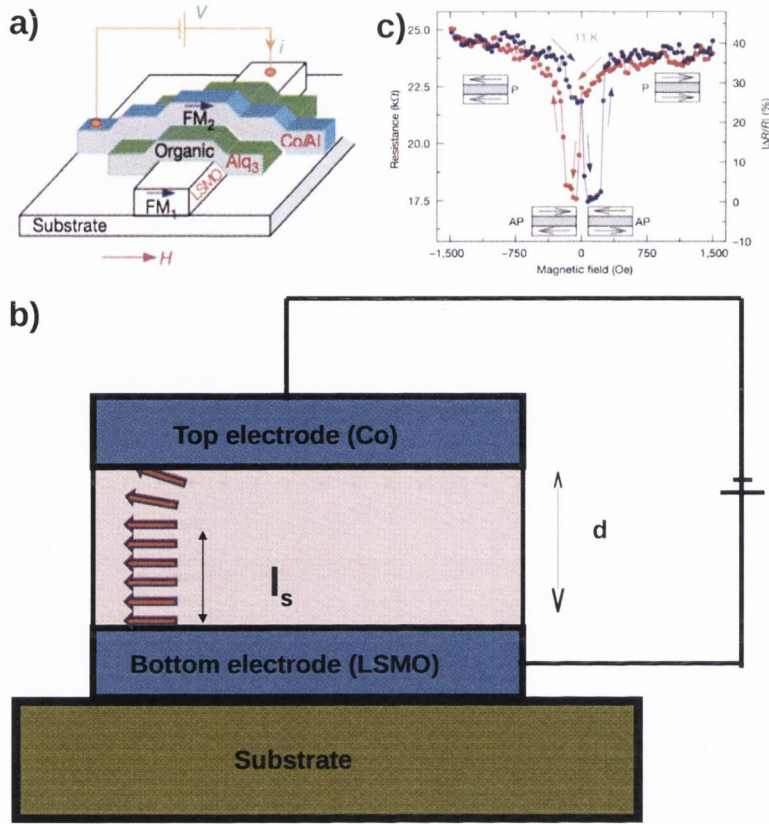


Figure 4.14: The device structure of a $\text{La}_{0.7}\text{Sr}_{0.3}\text{MnO}_3$ (LSMO)/ Alq_3 /Co spin valve is shown in **a**. A cartoon depicting the essential concept of spin diffusion length is illustrated in **b**. The characteristic magnetoresistance curve of the spin valve is shown in **c** from experimental work of reference [71]. Spin diffusion lengths (l_s) are usually estimated in experiments by fitting the magnetoresistance curve as a function of layer thickness, shown in **c** with modified Julliere's formula, Eq. (4.12). Panels **a** and **c** are from the experimental work of Xiong *et al.* [71].

Julliere's formula [138] to the experimental magnetoresistance curves as a function of layer thickness, for example the one shown in Fig. 4.14c. The modified Julliere's formula is

$$\text{MR} = \frac{\Delta R}{R} = \frac{2P_1P_2 e^{-(d-d_0)/l_s}}{1 - P_1P_2 e^{-(d-d_0)/l_s}}. \quad (4.12)$$

Here P_1 and P_2 are the spin polarization at the Fermi level of the two electrodes, d is the width of the organic layer and d_0 is the width of the tunneling barrier at the FM-OSC interface. Note that d_0 should be around 1 nm to produce spin polarized carrier injection into the organic. The argument for using Eq. (4.12) is the following: at the

first FM/OSC interface spin polarized carriers are injected into the organic layer from the FM. These carriers drift and diffuse through the rest of the organic layer, with an exponentially decaying spin polarization $P_1 e^{-(d-d_0)/l_s}$. Finally at the second FM/OSC interface the carriers tunnel into the FM (top) electrode causing the current flow through the external circuit. A cartoon illustrating the concept of l_s is shown in the Fig. 4.14b also depicting some of the parameters from Eq. (4.12). The device is a vertical spin valve of LSMO/Alq₃/Co taken from reference [71] illustrated in Fig. 4.14a and the corresponding magnetoresistance profile is shown in Fig. 4.14c.

Our theoretical approach The theoretical spin valve, which we simulate in this work is a two-terminal setup as illustrated in Fig. 4.15. It is comprised of three distinct regions, two semi-infinite leads (current-voltage probes) sandwiching a central scattering region. Our device's leads act as electron reservoirs pumping uncorrelated electrons into the central scattering region at energies corresponding to their respective chemical potentials, μ_L and μ_R for the left-hand side and right-hand side leads respectively. We evaluate the transport properties in the linear response regime, i.e. when $\mu_L - \mu_R \rightarrow 0$. The ballistic transport approach used in this work is based on the algorithm introduced by Rungger and Sanvito [13].

The leads are semi-infinite, and are modelled by a single site tight binding Hamiltonian. The diagonal terms of the Hamiltonian matrix (of the leads) are the on-site energies of the atoms comprising the lead, and the off diagonal terms are the hopping elements between nearest neighbor atoms of the leads. The corresponding Hamiltonian for the leads are: $H_L = \sum_{i\sigma} \epsilon_L C_{i\sigma}^\dagger C_{i\sigma} + \sum_{ij} \gamma_L (C_{i\sigma}^\dagger C_{j\sigma} + C_{j\sigma}^\dagger C_{i\sigma})$, such that $\epsilon_L \gg \epsilon$ and $\gamma_L \gg t$ (wide band limit). Here $C_{i\sigma}$ ($C_{i\sigma}^\dagger$) are the creation (annihilation) operator of the spin polarized carrier in the leads. Note that there is no spin mixing within the electrodes. Also the condition $\gamma_L \gg t$, is vital in this approach so as to ensure an almost constant density of states in the leads. Here the index i runs over the atoms constituting the leads. Also, there is a hopping integral, γ_{LM} , between the leads and both the p_y and p_z orbitals of the organic

molecule.

The scattering region of the problem is defined by the Hamiltonian of the OSC Eq. (4.10), and the left and right retarded self-energies (Σ_L and Σ_R respectively). The self-energies of the leads include the coupling between the OSC and the respective leads as well as the electronic structure of the semi-infinite leads themselves. Thus the Hamiltonian (H_{eff}) of the "effective" scattering region can be written down as :

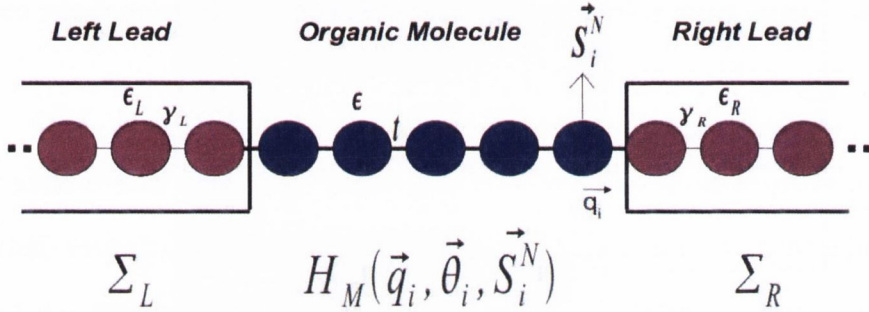


Figure 4.15: The spin-transport setup, containing the chain of atoms (organic molecule) described by Eq. (4.10), sandwiched between metallic leads.

$$H_{\text{eff}}(E) = H_M + \Sigma_L(E) + \Sigma_R(E). \quad (4.13)$$

The definition of the retarded Green's function G^R of the scattering region is

$$G^R(E) = \lim_{\eta \rightarrow 0} [(E - i\eta)I - H_{\text{eff}}(E)]^{-1}. \quad (4.14)$$

Furthermore, the left-hand side and right-hand side leads' retarded self-energies in Eq. (4.13) can be written in terms of the surface Green's function \hat{g}_L and \hat{g}_R and the coupling matrix between the leads and the OSC H_{LS} and H_{RS}

$$\Sigma_L(E) = H_{LS}^\dagger \hat{g}_L(E) H_{LS}, \quad (4.15)$$

$$\Sigma_R(E) = H_{RS} \hat{g}_R(E) H_{RS}^\dagger. \quad (4.16)$$

The technique [13] for obtaining the surface Green's function relies on first constructing the Green's function for an infinite system, then applying the relevant boundary conditions. The surface Green's function for a single site 1D tight binding model takes the following form

$$\hat{g}_L(E) = \hat{g}_R(E) = \frac{1}{\gamma_L} e^{ik(E)z}, \quad (4.17)$$

$$k(E) = \cos^{-1} \left(\frac{E - \epsilon_L}{2\gamma_L} \right). \quad (4.18)$$

where $k(E)$ is the dispersion relation for the itinerant electrons coming from the leads. The coupling to the left-hand side and right-hand side leads has the effect of broadening the discrete energy levels in the scattering region. This is characterized by the broadening functions $\Gamma_{L,R}(E)$

$$\Gamma_{L,R}(E) = i[\Sigma_{L,R}(E) - \Sigma_{L,R}^\dagger(E)]. \quad (4.19)$$

Finally the two-probe conductance is given by the Fischer-Lee relation

$$G(E) = \frac{e^2}{h} \text{Tr}[\Gamma_L(E)G^{R\dagger}(E)\Gamma_R(E)G^R(E)]. \quad (4.20)$$

The term $\text{Tr}[\Gamma_L(E)G^{R\dagger}(E)\Gamma_R(E)G^R(E)]$ is the energy dependent transmission coefficient $T(E)$ that can be calculated from scattering theory.

In the case of spin polarized transport which is of interest to us, the total transmission probability (and hence total conductance) is spin dependent. Thus the spin polarized conductance can be decomposed as follows

$$G(E) = \frac{e^2}{h} [T_{\uparrow\uparrow}(E) + T_{\downarrow\downarrow}(E) + T_{\uparrow\downarrow}(E) + T_{\downarrow\uparrow}(E)], \quad (4.21)$$

Here, $T_{\uparrow\uparrow}$ ($T_{\downarrow\downarrow}$) refers to the transmission probability that an electron with spin up (down) enters the organic layer and exits out as a spin up (down), thereby preserving its spin direction. In contrast, $T_{\uparrow\downarrow}$ ($T_{\downarrow\uparrow}$) refers to the transmission probability that an electron

with spin up (down) enters the OSC and leaves it, with its spin orientation down (up), after encountering spin mixing events (HI and SO) within the organic layer.

In our procedure, the transmission coefficient is integrated over the entire spectrum. At zero applied bias the integrated total transmission can be decomposed into its constituent spin-contributions using the Landauer-Büttiker formula for ballistic conductance G as

$$G = \frac{e^2}{h} [T_{\uparrow\uparrow} + T_{\downarrow\downarrow} + T_{\uparrow\downarrow} + T_{\downarrow\uparrow}]. \quad (4.22)$$

Here, G and T are the respective integrated conductance and transmissions and hence we have dropped the dependence on E . We may separate the integrated transmission coefficient in Eq. (5.17) into a spin-conserving part, $T_{sc} = T_{\uparrow\uparrow} + T_{\downarrow\downarrow}$ and a spin-mixing part, $T_{sm} = T_{\uparrow\downarrow} + T_{\downarrow\uparrow}$.

As discussed earlier to obtain l_s in experiments, the spin polarization, SP , at the first metal-organic interface⁶ is monitored as a function of the organic layer thickness. SP is defined as

$$SP = \frac{N^\uparrow - N^\downarrow}{N^\uparrow + N^\downarrow}, \quad (4.23)$$

where N^\uparrow and N^\downarrow are respectively the density of states of the \uparrow and \downarrow carrier spins. It can be very easily shown⁷ that Eq. (4.23) can be rewritten in terms of T_{sc} and T_{sm} as

$$SP = \frac{T_{sc} - T_{sm}}{T_{sc} + T_{sm}}. \quad (4.24)$$

Therefore, in our theoretical approach, l_s can be extracted by monitoring the length dependence of SP .

In this work we are interested in understanding from a microscopic viewpoint, what is responsible for the loss of spin polarization of the itinerant carrier in OSC molecular crystals? In particular we investigate and compare the role played by intrinsic effects, i.e.

⁶Bottom electrode-OSC interface, see Fig. 4.14b.

⁷ $SP = \frac{N^\uparrow - N^\downarrow}{N^\uparrow + N^\downarrow} = \frac{T_{sc} \cdot N^\uparrow - T_{sm} \cdot N^\uparrow}{T_{sc} \cdot N^\uparrow + T_{sm} \cdot N^\uparrow}$.

HI or SO coupling. Keeping this in mind, our approach to evaluate l_s from a ballistic approach to spin transport is justified. In such a limit we will be estimating l_s by measuring the spin relaxation only due the intrinsic spin relaxation effects of the OSC i.e. HI and SO coupling and excluding any scattering effects.

The classical variables \vec{q}_i , $\vec{\theta}_i$ and \vec{S}_i^N in Hamiltonian Eq. (4.10) are evolved via metropolis algorithm [180] and the transport observables are subsequently averaged over 50,000 Monte Carlo (MC) steps. Also, all the spin transport calculations have been performed at $\alpha = 0.2$ eV/Å.

4.3.3 Results and discussions

Hyperfine interactions

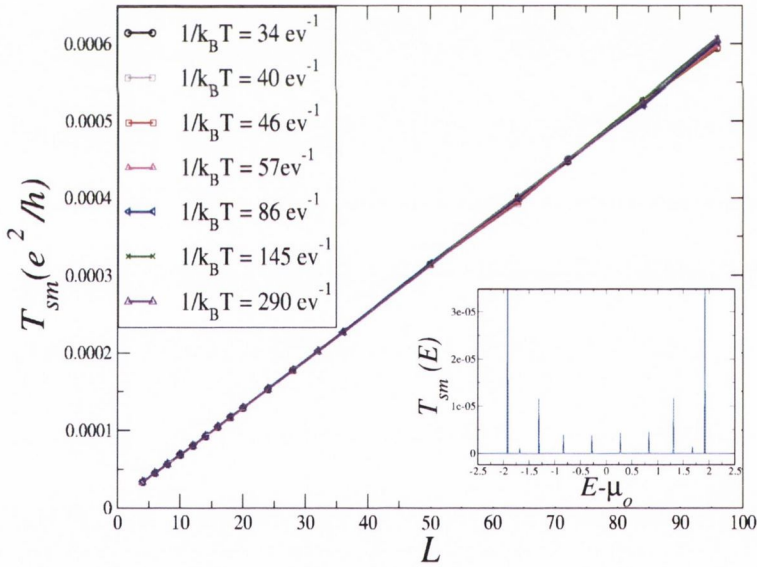


Figure 4.16: T_{sm} vs L evaluated at different temperatures ($\beta = 1/k_B T$), when only HI is the source of spin-scattering in the model, i.e. $\lambda_{SO} = 0$ and $J_H = 10^{-5}$ eV. Note that T_{sm} is independent of temperature at all lengths. The inset shows an example of $T_{sm}(E)$ vs E , where μ_o is the chemical potential and $E - \mu_o$ is in units of eV. In order to obtain T_{sm} the spin mixing transmissions, $T_{sm}(E)$, are integrated over the entire spectrum. Please note that to convert T in units of K the Boltzmann's constant is $k_B = 8.617 \times 10^5$ eV/ K .

We begin with presenting the spin transport results for the $\pi - \pi$ model when only HI is the source of spin scattering, i.e. $\lambda_{SO} = 0$. In Fig. 4.16 we report, T_{sm} evaluated at

$J_H = 10^{-5}$ eV and $\lambda = 0$ eV, as a function of length of the molecular chain (number of sites) L , each at different temperatures ranging from $1/k_B T = 34 - 290$ eV⁻¹[⁸]. Note that the temperature dependence of T_{sm} vs L is almost non-existent when the spin relaxation mechanism is only HI. This is because the energy scale for hyperfine coupling is too small for the spin dynamics to be affected by temperature. Since the strength of hyperfine coupling (J_H) in OSCs is very small, the itinerant electron sees a frozen configuration of nuclear spins (randomly aligned) in the time it takes to travel through the chain. This also explains why T_{sm} increases with L . Similar increase in T_{sm} with L was also observed when $J_H = 0$ and λ_{SO} is finite. In this scenario, it can be reasoned that with increasing L (number of sites), the spin scattering due to the on-site SO coupling increases and therefore T_{sm} increases. However, please note that the overall conductance (or $T_{sc} + T_{sm}$) decreases with length.

According to Ref. [93], the effective magnetic field created by HI in OSCs is in the mT range. This means that the lower bound of J_H in our model is 10^{-6} eV and the upper bound can be 10^{-4} eV. Please note that, it is quite difficult to establish the equivalency between our model and their theoretical work. Therefore, to understand the qualitative behavior of HI we have investigated the spin transport characteristics of the model for different strengths of J_H .

In Fig. 4.17 we illustrate the length dependence of SP for values of $J_H = 10^{-4}$, 10^{-5} and 10^{-6} eV. The SP vs L graphs when spin diffusion is only due to HI are independent of both T and t . Also $J_H > 10^{-4}$ eV is a rather large estimate for the HI strength. To extract the spin diffusion length, l_s , in our model, the SP vs L graphs can be fitted to an exponential function, $SP = SP_0 e^{-\eta L} \simeq SP_0 (1 - \eta \cdot L)$, where the second equality is for the limiting case of small L . l_s for the system is the reciprocal of the exponential constant, $l_s = 1/\eta$.

In Fig. 4.17 we observe that the rate of decay in SP with increasing L is quite small

⁸Where $k_B = 8.617 \times 10^5$ eV/K.

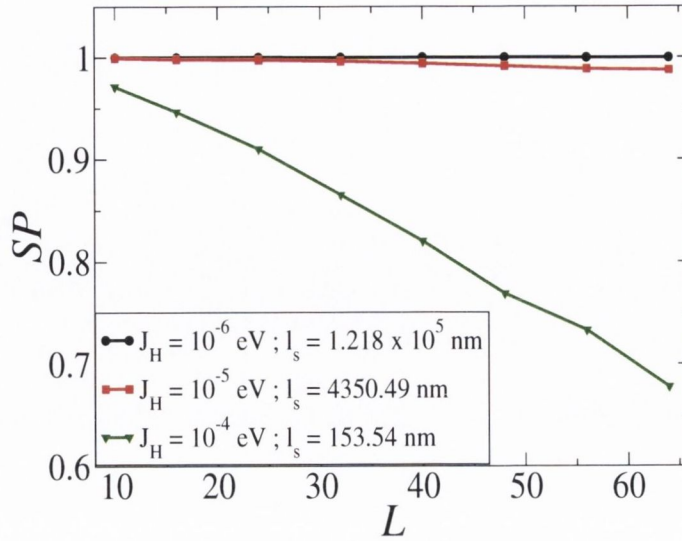


Figure 4.17: When the spin diffusion mechanism in the model is only controlled by HI, the spin transport is independent of temperature T and the transfer integral t . SP vs L evaluated for one such T and t but at different HI strengths, J_H , is shown here. The rate of decay in SP with L increases rapidly as the strength of HI is increased. The corresponding estimates for l_s (mentioned in the graph) also show a drastic decrease.

when $J_H = 10^{-6}$ eV and is rapid as the the strength of HI is increased (by a factor of 10), especially in the case when $J_H = 10^{-4}$ eV. Consequently, the estimate for l_s also decreases swiftly. This is due to an enhanced spin scattering with increasing HI strength. The estimates for spin diffusion lengths are the following, $l_s = 153.54$ nm for $J_H = 10^{-4}$ eV, $l_s = 4350.49$ nm for $J_H = 10^{-5}$ eV and $l_s = 1.218 \times 10^5$ nm for $J_H = 10^{-6}$ eV^[9]. We observe a stark increase in l_s on decreasing the magnitude of HI.

Let us now look into the effect of SO interactions on the spin transport properties of the model.

Spin-orbit interactions

We will begin by comparing the spin transport properties of the model as a function of HI and SO coupling strengths.

Please note that obtaining the magnitudes of both HI and SO coupling for organic

⁹Note that such large estimates of l_s for $J_H = 10^{-6}$ eV is expected from the nearly flat SP vs L behavior in Fig. 4.17.

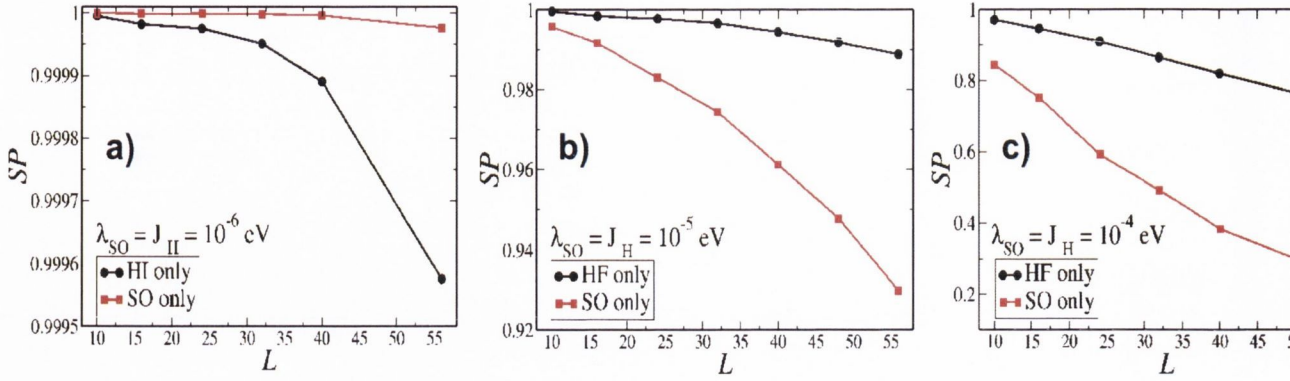


Figure 4.18: SP vs L graphs for equal strengths of HI (in black) and SO coupling (in red), each corresponding to spin relaxation magnitudes of : 10^{-6} eV (left panel), 10^{-5} eV (middle panel) and 10^{-4} eV (right panel). As evident from the graphs, when the spin relaxation strengths are minute (as in the left panel), the decay of SP with L is quicker in the scenario when spin relaxation is only due to HI as opposed to SO coupling alone. However, as the spin mixing interaction magnitudes are increased (middle and left panels), SP decays rapidly with L for the case of SO coupling as opposed to HI. The results shown here are for a fixed $t = 0.1$ eV and $\beta = 60$ eV $^{-1}$.

materials, proved to be not so straight-forward. There is lack of experimental insights in this respect because of the difficulties in measuring HI and SO couplings directly. The said complications arise because the magnitudes of these spin relaxation mechanisms are small in OSCs. Therefore experimentalists resort to indirect approaches to measure the effect of SO coupling and HI on spin transport as discussed earlier in section 4.3.1. Furthermore, theoretical attempts to quantify HI and SO coupling are also not conclusive. In our work we are interested in understanding the behavior of the spin relaxation mechanisms (HI vs SO coupling) through OSCs. For this purpose our approach is as follows.

Fig. 4.18 illustrates SP vs L for equal strengths of HI (in black) and SO coupling (in red) when each of the spin scattering mechanisms are acting alone; with spin relaxation strengths corresponding to 10^{-6} eV (left panel), 10^{-5} eV (middle panel) and 10^{-4} eV (right panel). Note that the amount of spin mixing (J_H and λ_{SO}), which we consider correspond to their upper and lower limits.

For small magnitudes of spin relaxation as in Fig. 4.18a, we observe that the decay in SP with L is small for both the cases (note the ordinate of the graph). However, the rate

of decay of SP with L is more for HI as opposed to SO coupling. This suggests that in the lower limit for the spin flip mechanisms HI plays a more dominant role in governing spin transport than SO coupling.

Interestingly, the reverse holds true when the strength of spin-flip mechanisms are increased (to 10^{-5} eV and 10^{-4} eV) in the $\pi - \pi$ model. For a given strength, SP decays more quickly with L when spin relaxation is controlled by SO coupling as opposed to HI (see Fig. 4.18b and Fig. 4.18c). This means that for stronger magnitudes of spin scattering, SO coupling plays a more crucial role in dictating the spin transport properties than HI. Please note that in both cases, as the spin relaxation strengths are increased from 10^{-5} eV to 10^{-4} eV, the magnitude of SP decreases more rapidly with L .

Let us now discuss the significance of the results presented in Fig. 4.18 with respect to spin transport characteristics in OSCs. In organic materials both J_H and λ_{SO} lie in the range between 10^{-4} eV and 10^{-6} eV. The magnitude of HI depends on the amount of nuclear spins coming from H (and also ^{13}C contaminations). Furthermore, the magnitude of SO coupling will depend on the geometry of the OSC molecular crystal, temperature and intermolecular interactions. Therefore, in OSC the magnitudes of HI and SO would be controlled by a number of different variables¹⁰. It may be suggested that in experiments, one of the two mechanism dominates over the other based on specific conditions like temperatures, concentration of defects and impurities etc (which will govern the strength of J_H and λ_{SO}).

Next, in Fig. 4.19 we show the dependence of l_s on T and t when $\lambda_{SO} = 10^{-4}$ eV and $J_H = 0$ eV, i.e. when spin relaxation is only governed by SO coupling. We show l_s vs $1/t$ for $T = 200$ K (in red) and $T = 58$ K (in black). We investigate the spin transport characteristics of the 1D model for values of t between, $0.1 - 0.5$ eV, corresponding to reasonable estimates for bandwidths in real OSCs¹¹ (please see the *ab initio* estimates for

¹⁰And they may not be equal, as assumed in the comparisons in the individual panels of Fig. 4.18. Therefore it is difficult to establish HI vs SO coupling without proper quantification of the spin relaxation strengths.

¹¹Note that for our 1D model the bandwidth is $4t$.

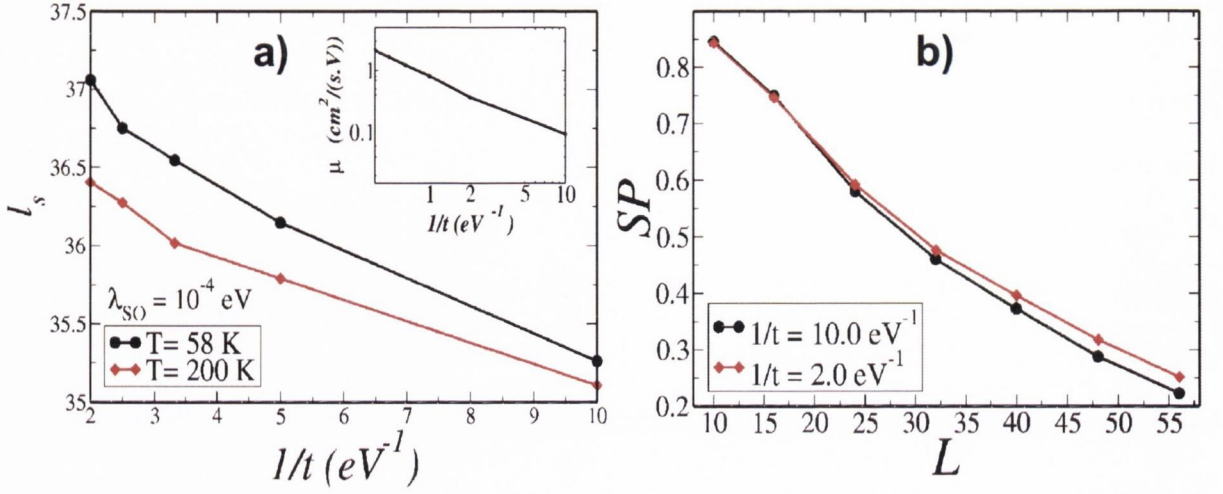


Figure 4.19: The left panel shows the dependence of l_s on T and t , when spin relaxation in the model is only controlled by SO ($\lambda_{SO} = 10^{-4} \text{ eV}$ and $J_H = 0$). We notice that l_s decreases only slightly with decreasing t (increasing $1/t$). Furthermore, the magnitude of l_s is marginally smaller at a higher temperature. The inset in the left panel shows a rapid (power law) decrease in charge carrier mobility with $1/t$. The right panel shows SP vs L for $t = 0.1 \text{ eV}$ [$1/t = 10.0 \text{ eV}^{-1}$] and $t = 0.5 \text{ eV}$ [$1/t = 2.0 \text{ eV}^{-1}$]. Note that at a lower t and at larger lengths, SP is slightly small.

the transfer integrals for OSCs in Chapter 5 and Chapter 6).

First and foremost, one can see in Fig. 4.19a that for every t , the magnitude of l_s is greater at $T = 58 \text{ K}$ in comparison to $T = 200 \text{ K}$, although only slightly. This is because of an enhanced spin scattering due to SO coupling at higher temperature due to increased modulation of the transfer integrals. Furthermore, we observe that with decreasing t (increasing $1/t$), l_s also decreases, but only marginally.

In Fig. 4.19b we illustrate SP vs L for $t = 0.1 \text{ eV}$ [$1/t = 10.0 \text{ eV}^{-1}$] and $t = 0.5 \text{ eV}$ [$1/t = 2.0 \text{ eV}^{-1}$]. Note that for large lengths, the absolute value of SP is slightly smaller at a lower temperature. This can be attributed to enhanced spin scattering¹² due to SO coupling.

What exactly does decreasing t (increasing $1/t$) mean in terms of describing the overall carrier transport properties of the system? To answer this question, in the inset of

¹²Since α is constant in our calculations, as t decreases, α/t increases and therefore the fluctuations in $t + \alpha \cdot (q_i - q_j)$ increases (which will govern SP).

Fig. 4.19a we illustrate the carrier mobility, μ ^[13] vs $1/t$ on a log-log scale at $T = 200$ K. Note that on decreasing the transfer integral t , i.e. decreasing the probability of hopping between neighboring sites in the model, μ decreases rapidly following a power law behavior. Please keep in mind that here we summarize the charge transport of the system in the diffusive limit while the spin transport observables throughout this section is evaluated in the ballistic limit. The graph shown in the inset of Fig. 4.19a is only intended to illustrate that the charge carrier becomes less itinerant on decreasing t (increasing $1/t$). Indeed the corresponding ballistic transport observable ($T_{sm} + T_{sc}$) also decreases on increasing $1/t$. From Fig. 4.19a we find that the distance travelled by the carrier spins before losing their spin polarization (l_s), only decreases slightly with decreasing t (and increasing $1/t$). Therefore in our spin transport calculations (for both HI and SO coupling) l_s is marginally dependent on the carrier mobility. This has also been documented in literature [146].

We will now recap the main conclusions based on the work presented in this section. We have understood the effect of HI and SO coupling on controlling spin relaxation of the itinerant carrier as it travels through the OSC. While the loss of spin polarization due to HI is temperature independent the same due to SO coupling increases with T and $1/t$. Finally, based on the absolute values of l_s , it is difficult to establish a comparison between HI and SO coupling, as which of the two mechanisms dominate spin transport. We have provided a microscopic explanation to this based on the strengths of HI and SO coupling.

From experiments, it is difficult to get an estimate of these spin relaxation strengths, in particular because their magnitudes are quite weak. For example, the nuclear hyperfine structure (in static case) can be obtained from Electron Paramagnetic Resonance (EPR) experiments [152]. However, the effect of the nuclear spins on an itinerant electrons (the scenario we are interested in to describe transport) is not straightforward to estimate. Furthermore, optical pump-probe techniques based on Kerr/Faraday rotation are the

¹³Evaluated from Kubo formula in the ballistic transport limit.

standard methods for estimating the spin transport characteristics of inorganic semiconductors [153], while for metals both electrical [154] and optical methods [155] can be used. Unfortunately, the same methods, i.e. spin-manipulation and optical spin-detection [151] cannot be utilized for investigating spin-dephasing through OSCs. This is because the weak magnitude of SO coupling in OSCs make polarized-light pump-probe optical techniques ineffective for organic materials and most of the standard optical characterization tools designed for inorganic semiconductors cannot be adopted for OSCs [59]. These factors make an accurate experimental estimation of J_H and λ_{SO} for OSCs challenging !

4.4 Summary

In this chapter we have established the computational methods to investigate the charge and spin transport properties of OSC represented by a tight binding Hamiltonian. We presented the method to evaluate charge carrier mobility using Kubo formula within the Monte Carlo scheme. Furthermore in the second part of this chapter we have introduced the spin polarized tight binding Hamiltonian to include the two main spin relaxation mechanisms in OSC: spin orbit coupling and hyperfine interactions. We outlined in detail the method by which we can evaluate the spin polarized transmission coefficients from Landauer-Büttiker formula and thereafter a scheme to calculate spin diffusion length which is a figure of merit for spin transport.

In an organic spintronic device (e.g. one outlined in Fig. 2.1), both charge transport and the corresponding loss of its spin polarization takes place simultaneously. However, in this work to specifically understand the microscopic origins of both, we have adopted the ballistic approach to study the spin relaxation of the itinerant carriers due to intrinsic effects of the OSC (HI and SO coupling) and the diffusive transport approach to estimate the carrier mobility. In other words, in this chapter we have explored in detail the spin and charge transport phase diagram in terms of the microscopic model Hamiltonian parameters. However, what is missing from this analysis, is a first principle's description of the

OSC itself and therefore an *ab initio* estimation of the transport observables. This would enable us to compare the estimated transport observables directly with experiments. In fact, this is exactly what we wish to achieve in the next chapters of the thesis.

Chapter 5

Charge and spin transport properties of Rubrene from first principles

In this chapter we will provide a systematic approach to investigate the charge and spin transport characteristics of rubrene from first principles. Our technique involves obtaining the *ab initio* tight binding Hamiltonian for rubrene by computing the maximally localized Wannier functions of the system. The material specific tight binding Hamiltonian of the system investigated provides a comprehensive information of the essential interactions in the crystal. This is then used to compute carrier mobility from the Kubo formula and the spin diffusion length from the algorithm introduced in the previous section. Before we embark upon a detailed description of the procedure to estimate the transport properties, let us spend the introductory section of this chapter on the motivation behind our choice of rubrene as the OSC to address in this work. Furthermore, let us also provide our perspective on the state of the art experiments which study transport through rubrene based nanodevices. These will form the experimental benchmark for the *ab initio* simulations presented in the chapter.

5.1 Charge transport experiments on single crystalline rubrene based OFETs

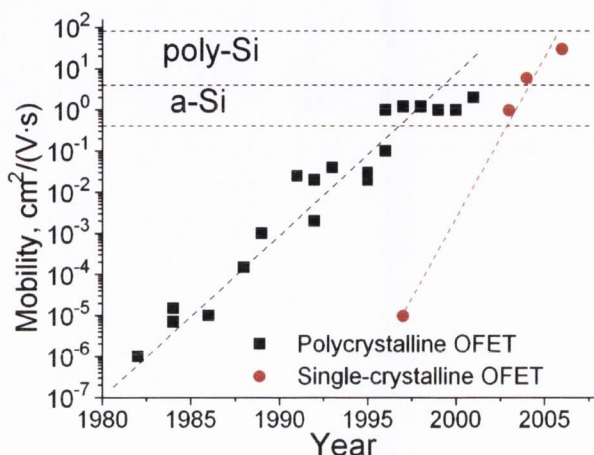


Figure 5.1: The evolution of carrier mobility in single-crystalline OFETs over the years is shown. This graph is borrowed from the review of Hasegawa and Takeya [159]. In recent years rubrene based single-crystalline OFETs have exhibited highest mobilities of about 20–40 cm²/V·sec, thereby performing better than amorphous (α -Si) and polycrystalline Silicon (poly-Si).

In the previous chapters we have already discussed in some detail Organic Spin Valves and the experimental methods to extract the spin properties of OSCs. We will again come back to those in the latter part of this chapter, but for now we shift our focus on the experiments which probe charge transport in organic materials. OFETs (Organic Field Effect Transistors) are the prototypical devices to investigate the charge transport characteristics of OSCs. The semi-conducting channel material in such devices comprises a single crystal OSC like rubrene, which has been known to deliver improved performance in terms of its intrinsic charge carrier mobility. Indeed one of the figures of merit for OFET characterization is its carrier mobility. Fig. 5.1 shows how within the last few years the mobilities of single-crystalline rubrene based OFETs have surpassed that of FETs made from amorphous as well as polycrystalline silicon. This is partly due to advancements in experimental techniques, the use of better and cleaner substrates, as well as of better gate insulating materials in fabricating high-performance FETs.

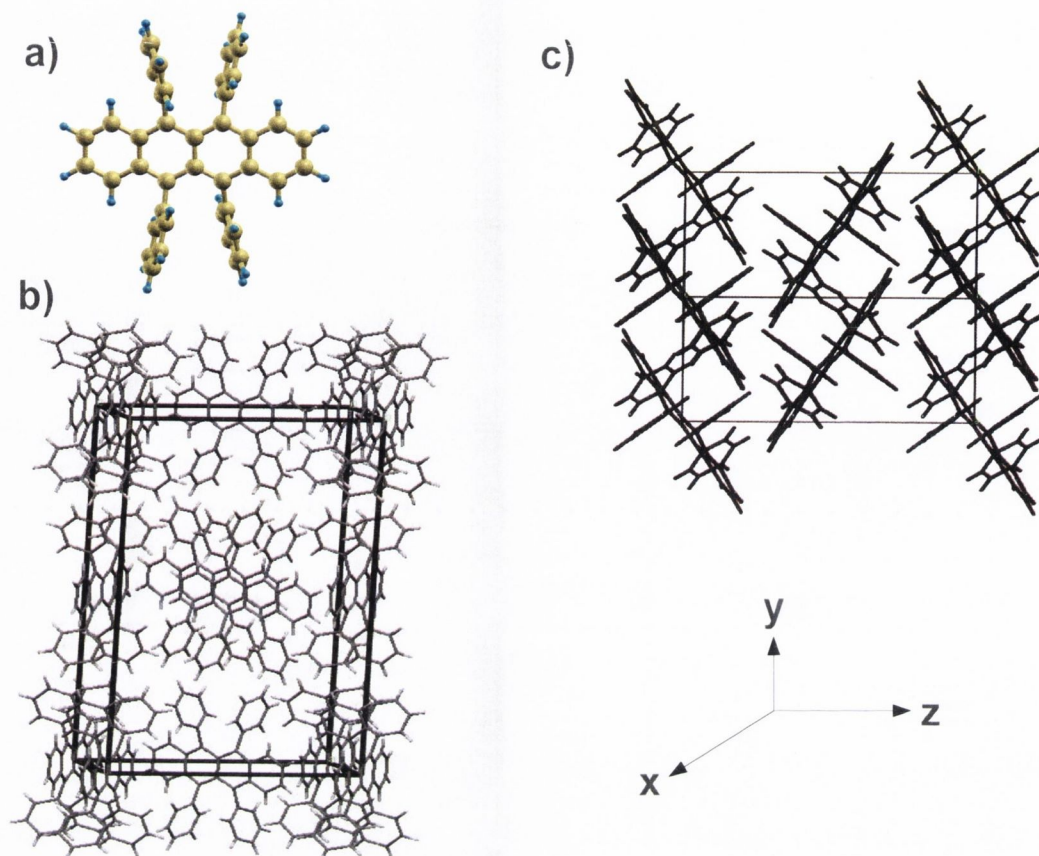


Figure 5.2: The structure of rubrene molecule in the gas phase and in an orthorhombic crystal [179] is shown respectively in (a) and (b). Rubrene molecule consists of a π -electron rich central tetracene backbone which contributes to much of intermolecular interactions, and bulky phenyl side groups. We show the orientation of its unit cell along the shortest crystallographic axis \hat{y} , illustrating the famous herringbone motif, which many polyacene OSCs are associated with. Moreover, as one can predict, there will be a strong π - π overlap along the \hat{y} direction which will therefore dictate the charge transport properties in the crystal.

Another reason why rubrene based OFETs have superior charge carrier mobilities is because of the inherent structure of rubrene molecular crystals. Let us discuss this in detail. First we depict the structure of the rubrene molecule in Fig. 5.2a. The molecule consists a π -electron rich central tetracene backbone and heavy phenyl side groups. Next, we show the orthorhombic crystallographic structure of rubrene crystal in Fig. 5.2b. The unit cell parameters are $a = 26.92 \text{ \AA}$, $b = 7.17 \text{ \AA}$ and $c = 14.35 \text{ \AA}$ [179]. In Fig. 5.2c we show the orientation of the crystal along the shortest crystallographic direction, i.e. along the \hat{y} direction. As is clearly evident from the right panel of Fig. 5.2 there is a

strong $\pi - \pi$ overlap along the \hat{y} direction thereby forming a herringbone motif along that direction. Furthermore, we expect that there will be little intermolecular interaction along the other crystallographic directions. Hence, if the rubrene single crystals are aligned in the channel of an OFET such that the \hat{y} direction of the crystal is along the source-drain of the transistor, one can expect exceptional charge transport characteristics in such OFETs. Such an anisotropy in rubrene crystal based OFETs was also observed in experiments [156].

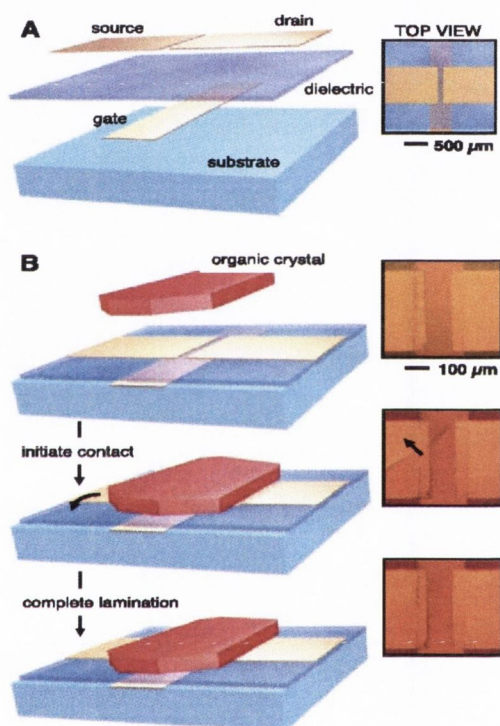


Figure 5.3: The method to fabricate high performing OFETs is schematically illustrated here from the work of Sundar *et al.* [156]. They used a flexible elastomeric polydimethylsiloxane (PDMS) substrate on top of which the gate, dielectric and the transistor source and drain electrodes are deposited as shown in panel A. The corresponding top view of the device is shown in the right frame. This is the first step in the fabrication process. Next, the organic crystal is laminated on the transistor stamp as shown in panel B. Here at first the initial contact is achieved (first and second frame) which creates a wetting area between the two surfaces. Thereafter, the organic is held together in the architecture by Van der Waals forces with the elastomeric substrate.

Here we would also like to draw the attention of the reader to the key difference between molecular crystals and inorganic solids. As we shall see in this chapter, the mor-

phology of rubrene molecular crystals play an important role in dictating its electronic properties. Indeed, the main problem with fabricating any organic based device lies in its inherent fragile nature. For example, due to chemical bonds between the organic material and the substrate the molecular ordering in the organic layer can be severely disrupted. Furthermore, these may also generate interfacial trapping sites creating barriers to charge injection and subsequent transport, and thereby causing many unwanted changes to these fragile organic molecular systems. Therefore the main goal in experiments to fabricate high performing OFETs is for the fragile OSC to be maintained relatively untouched. Current experimental techniques to obtain high quality rubrene based OFETs are based on the pioneering work of Sundar *et al.* [156]. The authors demonstrated that Polydimethylsiloxane (PDMS) can be used as a substrate on top of which the OFET architecture can be fabricated effectively.

This is systematically illustrated in Fig. 5.3. Before we address the detailed experimental procedure employed to fabricate OFETs we must mention that in their procedure, the entire transistor circuitry is fabricated on a flexible elastomeric substrate and in the final stage is bonded to the surface of the organic layer with Van der Waals forces. An alternative popular method is to laminate the organic material against a Silicon (Si) wafer with pre-deposited electrodes [157, 158]. Both the methods eliminate the need to deposit any metal or gate dielectrics directly onto the fragile structure of the organic material. However, there are particular advantages which the method of Sundar *et al.* has over that of laminating the OSC onto a Si wafer. The first advantage lies in the fact that the elastomeric technique is compatible with thicker and rigid structures (in comparison to the Si stamp technique) because the flexible elastomeric PDMS substrate and the ductile gold electrodes can adjust themselves easily to different crystal shapes. Secondly, the elastomeric approach is non destructive and reversible. For a detailed perspective of the other different fabrication methods for OFETs the reader is directed to the nice review by Hasegawa and Takeya [159].

The relatively simple OFET fabrication technique employed by Sundar *et al.* [156] is schematically illustrated in Fig. 5.3. Firstly the gate, dielectric, and source-drain electrodes are sequentially deposited onto a PDMS substrate as shown in Fig. 5.3A. The right panel is the top view of the device. The next step is to laminate the OSC single crystal onto the transistor stamp as depicted in Fig. 5.3B. The lamination process is as follows: firstly an initial contact (first frame) is created between the two surface producing a wetting front that progresses across the semiconductor stamp (second frame) and finally the entire organic crystal has an intimate contact with the transistor stamp due to Van der Waals interactions between the two surfaces (third frame). The right panels show the corresponding optical micrographs. In modern high performing OFETs, the source, drain and gate electrodes are made up of gold. The gate insulator is made up of a material with a high dielectric constant (parlyene, air gap, flouropolymer, etc.) which acts as a capacitor in preventing a direct ohmic contact between the gate and the OSC. We must also mention that Sundar *et al.* [156] reported the highest mobility of $15 \text{ cm}^2/\text{V}\cdot\text{sec}$ which indicates a superior performance of their OFET devices.

At this point, a crucial question may be proposed, i.e. how exactly does carrier transport take place in an OFET? Let us try to deliver an answer to this question without going into much detail of the electronic structure of the underlying organic, which will be addressed in this chapter. Rubrene is a hole transport dominated OSC ($\mu_h \gg \mu_e$). Under ideal circumstances carrier transport through the device can be described by the situation illustrated in the top panel of Fig. 5.4. According to this, holes are injected from the electrodes into the Highest Occupied Molecular Orbitals (HOMO) of rubrene, where they subsequently travel across the HOMO levels (that are broadened) of the organic to reach the opposite electrode. The carrier transport mechanism is therefore band transport. In such an ideal circumstance carrier transport across the HOMO of the OSC can be understood from a delocalized nature of the charge carrier in the band transport limit. The fingerprint of band transport is therefore a steady (power law) decrease in carrier

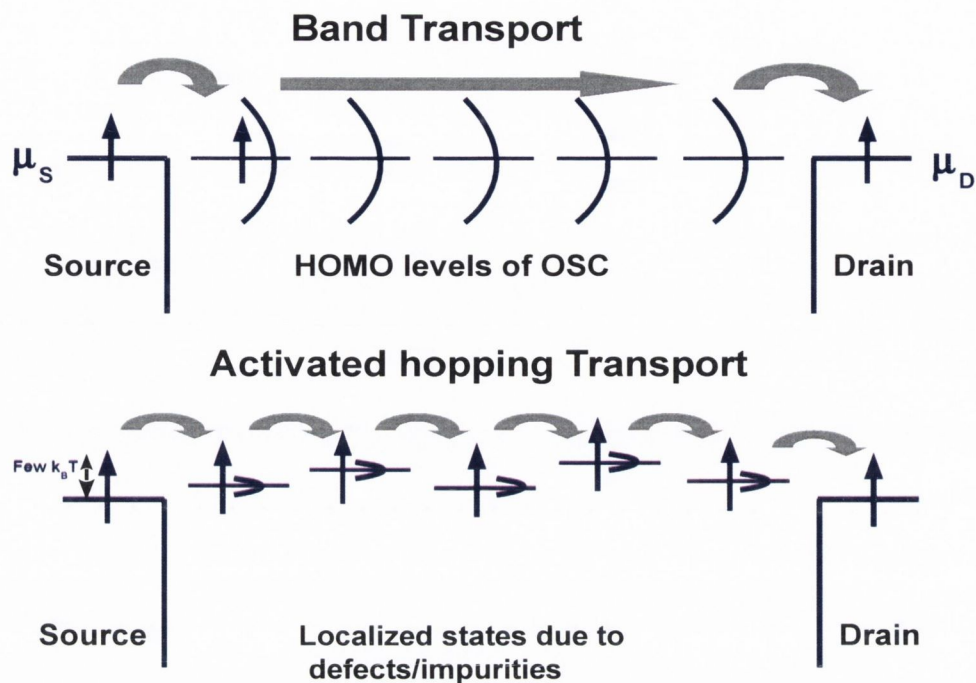


Figure 5.4: The hole transport mechanisms through an OSC (e.g. rubrene) in an OFET device is illustrated with the help of two cartoons. When the OSC is completely defect-free, the carriers travel through the OSC via a band transport mechanism. According to this the charge carrier's wavefunctions are delocalized across the molecules constituting the OSC (due to strong $\pi-\pi$ interactions) and this charge transport scenario is illustrated in the top panel. There is a substantial broadening in the individual levels constituting the organic which facilitates the delocalized transport. The bottom panel depicts the carrier transport mechanism when there are localized defect states (shown here) present close (within a few $k_B T$) to the HOMO of the OSC. As a result of the localization, carrier mobility is reduced. Furthermore, with temperature this localization is overcome by the carriers and hence the transport mechanism is activated in nature.

mobility due to temperature.

In actual experiments, intermediate trap states are located close to the HOMO and within the band gap of the OSC. These trap states can shift the HOMO energies by a few $k_B T$ as illustrated in the bottom panel of Fig. 5.4. These defect states could exist due to a structural mismatch or chemical bonding between organic and substrate and/or gate dielectric. Occasionally deep trap states within the band gap of the organic may also form due to water contamination or oxidation of the organic material induced by gate dielectrics or severe structural imperfections. Thus, any sort of trap states causes localized levels and reduces the carrier mobility through the OSC. So, what is the influence of these

localized trap states on the charge transport through the device?

At low temperatures carrier transport through the device now takes place via these localized states as shown in bottom panel of Fig. 5.4. As the energy levels of these shallow (localized) trap states are randomly distributed, carrier transport will be activated in nature. Therefore carrier mobility, which is itself low due to trapping effects increases with temperature according to the following expression for activated transport, $\mu = \mu_0 e^{\frac{-E}{k_B T}}$. For obvious reasons in a high performing OFET the number of such localized defect states must be as little as possible. Moreover, beyond a particular temperature when the thermal energy is sufficient to overcome the localization due to these states, carrier transport becomes again band like. Usually in experiments both types of transport behavior are observed in OFET's mobility (see the top panel of Fig. 5.6C) [160]. Finally, we must also mention that the existence of deep trap states within the band gap of the organic severely impedes the performance of the device by lowering the mobility dramatically and it is therefore undesired.

5.1.1 Experimental estimation of carrier mobilities in OFETs

It is crucial to spend a few pages of the introductory section of this chapter to learn the experimental techniques to estimate the charge transport properties in organic materials, which will form a benchmark for our *ab initio* calculations later on in this chapter.

Two-terminal measurements

In a FET architecture, commonly estimated two-terminal mobility (μ_{2T}) can be obtained from the following expression:

$$\mu_{2T} = \frac{1}{C_i} \times \frac{dI_D}{dV_G} \times \frac{1}{V_D} \times \frac{L}{W}, \quad (5.1)$$

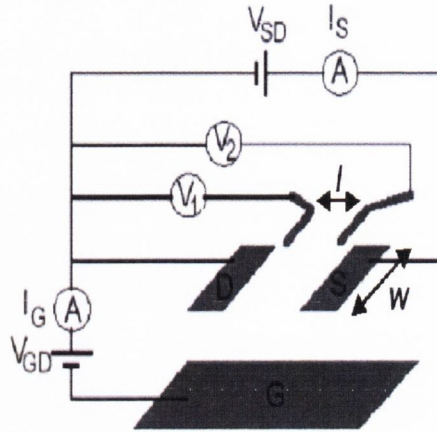


Figure 5.5: Schematic circuit diagram for a four-terminal conductivity measurement with applied gate voltage to measure the intrinsic charge carrier mobilities of an OSC in an OFET device. The diagram is taken from the review of Hasegawa and Takeya [159]. Here, S, D and G are source, drain and gate electrodes respectively ; I_G and I_D are the gate and source-drain current respectively; V_{GD} and V_{SD} are the gate drain and source drain voltages respectively and finally W is the width of the organic channel and l is the distance between the voltage probes.

where L is the distance between the source and the drain electrodes and W is the width of the channel. Also, I_D is the drain current between the two electrodes (source and drain), V_D and V_G are the drain and gate voltages respectively and C_i is the capacitance of the gate insulator per unit area.

Fig. 5.5 shows the electrical circuit used for measuring the drain current I_D and the gate leakage current I_G on applying V_G and V_D . In the transistor operation V_{th} is the threshold gate voltage and only when $V_G > V_{th}$, I_D is finite. Additionally, the charge transport characteristics of the device is estimated when the measurement reaches a saturation regime. The saturation regime is achieved for a value of V_D beyond which I_D stays constant. In this scenario, the excess carriers are accommodated at the depletion layer formed near the gate electrode. The saturation regime is reached when V_D larger than $V_G - V_{th}$ and the saturation mobility (μ_{sat}) can be estimated according to the following formula:

$$I_D^{sat} = C_i \mu^{sat} (V_G - V_{th})^2 / 2, \quad (5.2)$$

where I_D^{sat} is the saturation drain current.

Four-terminal setup in an OFET architecture

Two terminal measurements always include parasitic influences due to the contacts. Therefore in order to probe the intrinsic carrier transport property of single crystalline OFETs, a four-terminal setup is incorporated. This is schematically illustrated in Fig. 5.5. By detecting the voltages V_1 and V_2 at two positions on the crystal (as illustrated in Fig. 5.5), the longitudinal sheet conductivity can be obtained as:

$$\sigma = \frac{I_D}{(V_2 - V_1)} \frac{L_{12}}{W}, \quad (5.3)$$

where $L_{12} = l$ is the distance between the additional two voltage probes in the direction of the current. The four-terminal mobility μ^{4T} which gives insights into the intrinsic charge transport characteristics of the organic material can be obtained using the following formula:

$$\mu^{4T} = \frac{1}{C_i} \times \frac{d\sigma}{dV_G}, \quad (5.4)$$

and

$$\sigma = je\mu^{4T} = C_i(V_G - V_{th})\mu^{4T}. \quad (5.5)$$

Here j denotes the density of carriers and e is the electronic charge. Fig. 5.6A shows a typical I_D and σ vs V_G graphs in a four-terminal measurement from which the mobility can be extracted using Eq. (5.4).

Hall Effect to probe intrinsic transport of field induced carriers in OFETs

An important step towards understanding the charge carrier mechanisms and therefore fabricating high quality single-crystalline OFETs was in the realization of Hall effect in such devices [160, 161, 162]. The primary conclusion from these experiments were that, (indeed) band transport is realized for charge carriers generated in single crystalline OSC

with highly overlapped orbitals between adjacent molecules.

Hall measurements are done using a "six-probe Hall-bar" [163] which is illustrated in the inset of Fig. 5.6B. The transverse Hall voltage V_H is estimated. This requires the evaluation of three voltages V_1 , V_2 and V_3 (by additional source measure units) as shown in the inset of Fig. 5.6B. In Hall experiments the sheet conductivity and $V_H = V_3 - V_1$, as a function of external magnetic field perpendicular to the channel are monitored. Succinctly, Hall measurements give a direct indication of the fate of the injected charge carriers within the OSC.

Fig. 5.6 shows some of the experimental [160, 161] results of Hall effect on single crystalline rubrene based OFETs. Prior to the Hall measurements in zero applied magnetic field the longitudinal conductivity and therefore mobility was monitored from a four-terminal setup. The results are illustrated in Fig. 5.6A. The upper bound of the mobilities [estimated from the slope of the graph and Eq. (5.3)] were reported to be 25 $\text{cm}^2/\text{V}\cdot\text{sec}$ at low gate voltage and 2 $\text{cm}^2/\text{V}\cdot\text{sec}$ at high gate voltages.

For the Hall-effect measurements, a magnetic field is swept between B T to $-B$ T (B can be in the order of 10) back and forth and the transverse voltage is obtained. From this the Hall coefficient R_H is derived as $R_H = \Delta V_H / I_D \Delta B$. For rubrene OFETs the sign for R_H is positive which is consistent with hole injection. In Fig. 5.6B the inverse Hall coefficient, $1/R_H$, and sheet conductivity, σ , as a function of gate voltage is illustrated. These results show that $1/R_H$ decreases linearly with decreasing the negative gate voltage, which is an indication of the absence of any unwanted polarization effects of the carriers due to the gate dielectric and therefore a text book Hall effect. $1/R_H$ is directly proportional¹ to the number of carriers (n) in the rubrene crystal responsible for charge transport.

Hall mobility measured as $\mu_H = R_H \sigma$ therefore gives the average intrinsic carrier mobility. True Hall effect ($1/R_H$ proportional to V_G) demonstrates the absence of charge

¹ $1/R_H = ne$, where e is the electronic charge.

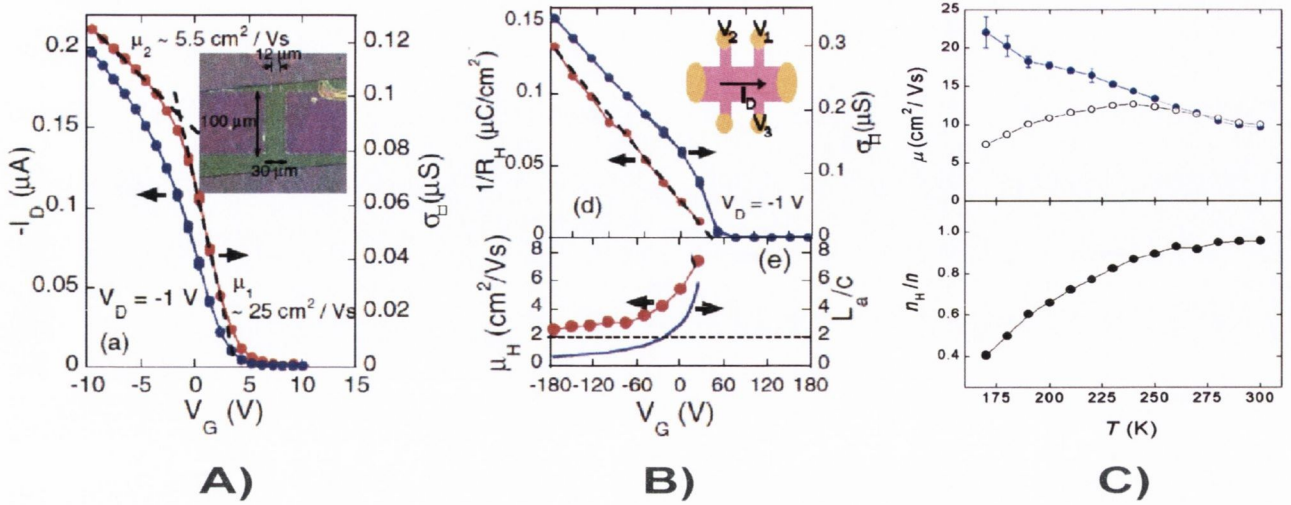


Figure 5.6: Experimental results [160, 161] on the Hall-effect on rubrene are illustrated. Demonstration of Hall-effect is crucial as it implies that the experimentally measured mobility is indeed the intrinsic mobility of carriers. A) The I_D vs V_G relationship from a four-terminal measurement is shown here and the corresponding mobilities are also indicated. B) Hall measurement setup is shown in the inset of the upper panel of B. Moreover in the upper panel of B, the inverse of the Hall coefficient (which is an estimate for intrinsic carrier density) is plotted as a function of V_G . The bottom panel illustrates the dependence of Hall mobility and carrier distribution depth (solid curve) again as a function of V_G . These results are from the work of Takeya *et al.*[160]. C) Mobility (Hall mobility in *blue* and OFET four-terminal mobility in *black*) as a function of temperature are shown in the upper panel. The ratio of Hall carrier density to the carrier density is shown again as a function of temperature in the bottom panel. These results are from the work of Podzorov *et al.* [161].

trapping effects especially at low V_G . Fig. 5.6B (bottom panel) shows the variation of μ_H and the carrier distribution depth L_a ² within the organic crystal. At low gate voltages V_G , the carrier mobility is $8 \text{ cm}^2/\text{V}\cdot\text{sec}$. Also L_a , which is an indication of the carrier mean free path and therefore the extent of carrier wavefunction in the organic crystal, is sufficiently long (6 lattice spacings). These demonstrate that the carriers upon injection have thermally diffused into the crystal via a band transport mechanism. This is because the wavefunction of the injected carriers is quite delocalized throughout the bulk of the

²In terms of lattice units.

crystal. Moreover, at low gate voltages since the charge carriers are less, which can be deduced from the low $1/R_H$ value in the upper panel of Fig. 5.6B (at low V_G), carrier correlation effects can be safely ignored. As the negative gate voltage is increased, the authors found that the carrier mobility drops to $2 \text{ cm}^2/\text{V}\cdot\text{sec}$ and so does L_a to almost zero lattice spacings. These results indicate that at higher negative V_G , the injected charge carriers are confined to the interface (hence negligible L_a) because of larger electrostatic force and therefore a shorter screening length.

Similar demonstration of band transport was also shown by Podzorov *et al.* [161]. We show in Fig. 5.6 C the μ vs T relationship for their OFET four-terminal measurements and Hall measurements. Notice the almost power law decrease of the hall mobility (in blue) with temperature which is an indication of band transport mechanism for the charge carriers within the rubrene organic layer. Furthermore, the four-terminal OFET mobility (in black) is also shown as a function of temperature, indicated by activated transport at low temperatures (due to localization originating from traps) and band transport at high temperatures. Moreover, at room temperature the Hall mobility and the four-terminal mobility match clearly. In the bottom panel of Fig. 5.6C the ratio of the Hall carrier density to the overall carrier density is shown which reaches unity at room temperature. These results indicate that the estimates for charge carrier mobilities from these experiments are indeed a good measure of the intrinsic carrier transport through the organic layer (rubrene).

Having provided an overview of charge transport experiments in rubrene-based single crystalline OFETs and also of spin transport experiments (previous chapter), let us now begin to discuss some of our results. In the following section of this chapter we provide a detailed DFT characterization of the electronic structure and the geometry of rubrene.

5.2 Electronic and structural characterization of rubrene from DFT

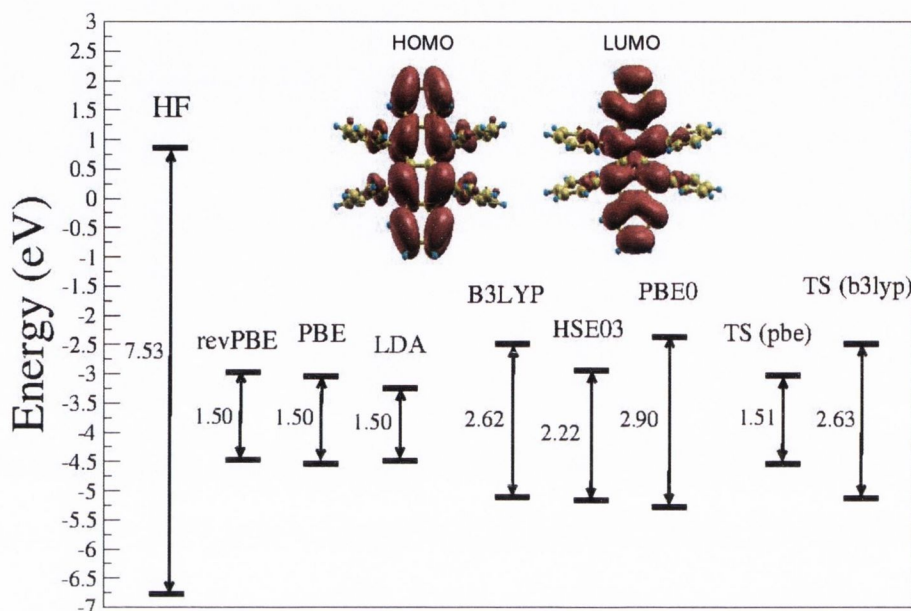


Figure 5.7: The Kohn-Sham HOMO-LUMO gap for the rubrene molecule in the gas phase is shown here for the different DFT functionals which we have tested. Also shown are the shape of the HOMO and LUMO molecular orbitals, which are identical for all the DFT functionals. Note that the Ionization Potentials and Electron Affinities calculated using the Δ SCF method which can be compared with the corresponding experimental values, are reported in Table. 5.1.

Before we embark upon our journey into investigating the transport properties of rubrene single crystals, it is vitally important to perform a detailed DFT study of the electronic structure and geometry of rubrene molecule in the gas phase and also rubrene crystals. Here we report our results on these studies, in particular a discussion regarding the performance of different DFT functionals and atomistic simulation codes. We explore the effect of standard DFT functionals, Van der Waals functionals and hybrid functionals. The calculations reported in this section have been performed using the FHI-aims code [168]. This is an all-electron code. In particular, we found that the implementation of hybrid functionals in FHI-aims is computationally less expensive than in Quantum

Espresso [201]³ especially for rubrene crystal which has 280 atoms and has a large unit cell volume. Also within FHI-aims, there is an accurate implementation of Van der Waal's functional by Tkachenko and Scheffler (TS) [47, 48], which was also a motivation to use the code. We have also performed the DFT calculations using SIESTA [55], Quantum Espresso [201] and Gaussian [199] throughout the course of the work presented in this thesis, and in this section (wherever possible) we will try to comment on the results of using different atomistic simulation packages. The functionals used here are standard LDA (Perdew and Zunger) [34], GGA (PBE) [35] and revPBE [49]; Hybrid functionals including B3LYP [37, 38, 39], HSE03 [42] and PBE0 [41]; vdW functionals [43, 46] including and TS functionals [47, 48].

5.2.1 Gas phase rubrene molecule

We performed the DFT calculations using FHI-aims on rubrene molecule in the gas phase as follows: the experimental structure [179] was relaxed till the forces on all the atoms were less than $0.01 \text{ eV}/\text{\AA}$. Furthermore, the convergence criteria for density and total energy were set to be 10^{-4} and 10^{-6} eV, respectively.

Electronic Structure

In Fig. 5.7 we illustrate the Kohn-Sham HOMO-LUMO gaps for rubrene molecule in gas phase as calculated using different DFT functionals. Firstly the shape of the HOMO and LUMO orbitals, which are constituted by the C π electrons (also illustrated in the figure), for all the DFT functionals investigated here are identical. Next let us look into the energetics predicted by the various DFT functionals. According to Koopmans' theorem if a DFT functional gives the correct electron-electron interaction energy functional (including the exchange-correlation part), the negative of the HOMO eigenvalue will be equal to the Ionization Potential (I.P.) of a system. The experimental estimate for I.P.

³Which is used for the results presented in the second part of this chapter.

DFT Functional	I.P. (in eV)	E.A. (in eV)	Band Gap $\Delta_g = \text{I.P.} - \text{E.A.}$ (in eV)
HF	7.002	1.149	5.853
revPBE	6.087	1.377	4.709
PBE	6.163	1.438	4.726
LDA	6.378	1.624	4.754
B3LYP	6.533	1.113	5.421
HSE03	6.693	1.460	5.234
PBE0	6.637	1.047	5.590
TS (PBE) vdW	6.209	1.432	4.778
TS (B3LYP) vdW	6.575	1.123	5.452
GW [164]	6.300	1.880	4.420
Diffusion QMC [164]	6.220 ± 0.140	0.960 ± 0.140	5.260 ± 0.140

Table 5.1: The Ionization Potentials (I.P.), Electron Affinity (E.A.) and the band gap ($\Delta = \text{I.P.} - \text{E.A.}$) of rubrene molecule in the gas phase is tabulated here, for different DFT functionals as well as those from GW [164] and diffusion Quantum Monte Carlo (QMC) [164] calculations. The main message from the calculations shown here is that the standard PBE functional is able to accurately capture the energetics of rubrene.

from Ultraviolet Photoemission Spectroscopy (UPS) is 6.4 eV. The standard DFT functionals and hybrid functionals in Fig. 5.7 are off from the UPS estimate by about 2 eV and 1 eV respectively. This discrepancy from the experimental value is due to approximations in the exchange-correlation in the various DFT functionals, causing a self-interaction error. Furthermore, hybrid functionals performs better than standard DFT functionals (LDA/GGA) because of a partial error cancellation of the self-interaction error, in them. However it is interesting to note that even the hybrid functionals in this case are off by 1 eV.

The simplest and reliable DFT scheme to estimate the excitation energies (in particular electron addition or removal energies), is evaluating the total energy difference between the initial and final states. This is known as the ΔSCF method and is a reliable procedure to extract excited state properties like I.P. provided that the initial and the final state are within the reach of DFT, that is, when both states have the lowest energy for a given symmetry or a given number of electrons. For all the functionals we have obtained the I.P. and E.A. with the ΔSCF method, and then the corresponding band gaps as $\Delta = \text{I.P.} - \text{E.A.}$

These results are tabulated in Table. 5.1, along with those obtained from many-body GW calculations [164] and diffusion QMC [164] calculations using the CASINO code [165]. The latter approach is assumed to be an accurate calculation because it treats electron-electron interaction effects exactly, as a many-body problem.

Notice, that apart from HF the I.P.'s estimated by all the other DFT functionals are quite close to those obtained from GW and QMC calculations, as well as to the experimental estimate from UPS experiments [166] which is $I.P._{UPS} = 6.4$ eV. This is particularly because the Δ SCF procedure using total energy differences is quite accurate since all the functionals are based on the Hohenberg-Kohn theorems and therefore as long as our calculations are well converged⁴, the total energy from the DFT calculations will be accurate. HF does not agree with experiments because it completely ignores the correlation energy. Furthermore because HF energy functional is exact, the Kohn-Sham eigenvalues (in Fig. 5.7) correspond to the I.P. and E.A. (in Table. 5.1) as Koopmans' theorem is valid.

Unfortunately, experimental estimates of E.A. for rubrene were not available from literature⁵. Since our estimation of the I.P. from Δ SCF were remarkably close to experiment we could also expect the estimates for E.A. to be reasonably accurate. Indeed, the E.A.s are all (for the different DFT functionals) roughly within a range of 0.5 eV of each other and also from QMC calculation. Interestingly, the E.A. estimated from GW is overestimated.

In the last column of Table. 5.1, the band gap $\Delta_g = I.P. - E.A.$ is shown. These also follow a similar trend in terms of proximity to QMC estimate for E.A. and each of the DFT functionals perform better than GW calculations. Finally, to the best of our knowledge there have been no experimental estimation of the transport band gap of rubrene (with which Δ_g can be compared).

⁴We have the true ground state density.

⁵Perhaps because rubrene is a hole transport based OSC.

Geometry

DFT Functional	C-C Bond (% error)	C-H Bond (% error)	C-C-C Angle (% error)	C-C-H Angle (% error)
HF	0.98	11.48	0.20	-0.74
revPBE	0.63	13.76	-0.00	-0.81
PBE	0.35	13.65	0.05	-0.81
LDA	-0.33	13.94	0.14	-0.80
B3LYP	0.19	12.60	0.06	-0.80
HSE03	-0.07	12.59	0.10	-0.80
PBE0	0.02	12.76	0.10	-0.81
TS (PBE) vdW	0.28	12.59	0.16	-0.75
TS (B3LYP) vdW	0.28	12.59	0.16	-0.75

Table 5.2: For gas phase rubrene molecule the percentage error in the C-C, C-H bond lengths as well as in C-C-C and C-C-H bond angles with respect to the experimental geometry [179], for different DFT functionals are reported in this table.

Moving on, we have also investigated the relaxed geometries of rubrene molecule obtained using the different DFT functionals. The results are tabulated in Table. 5.2. Here we report the percentage error⁶ for a C-C and an outer C-H bond length (the one with the highest error). Furthermore, we also report the percentage error in the C-C-C and C-C-H bond angles for the different functionals investigated. The central message coming from Table. 5.2 is that, all the functionals can produce accurate geometries with little discrepancies and perform more or less equally in terms of the relative error in the bond lengths and bond angles.

To summarize the results of the previous few pages, we have explored in detail the energetics and the relaxed geometry of gas phase rubrene molecule using different DFT functionals. While the different XC functionals return different Kohn-Sham HOMO-LUMO energies and the corresponding gap, the symmetry of the HOMO and LUMO wavefunctions are the identical. This point is quite crucial because it implies that the transfer integral between two rubrene molecules will not be dependent on the choice of XC functional. Furthermore, the IPs estimated by the different XC functionals (except HF)

⁶With respect to experimental value.

agree quite well with experiments. This is also very significant especially because rubrene is a hole transport OSC. Furthermore, we have also shown that the relaxed geometries predicted by the different DFT functionals are similar.

Finally, before moving to the next section, we report our results on the effect of spin-orbit coupling (SO) on the energy levels of rubrene. For this we used SIESTA and Quantum Espresso, which have SO implemented with an on-site approximation [53]. We found that on switching on SO, the energy levels of rubrene are only split by 10^{-4} eV. This is a confirmation that atomic SO in rubrene will be small as the molecule is constituted by light elements, C and H. Moreover, as expected, the relaxed geometries is altered very little on switching on SO.

5.2.2 Rubrene crystal

Effect of vdW DFT functionals on the geometry of rubrene crystal

In this section we explore the energy levels (bands) and the relaxed unit cell parameters of rubrene crystals calculated using different DFT functionals. We are interested in testing standard DFT functionals (LDA/GGA) and Van der Waal's (vdW) functionals namely TS (PBE), TS (LDA), Grimme vdW [43] and vdW-DF [46] functionals. Since the structure of organic molecular crystals is determined by vdW dispersive forces, we are particularly interested in exploring the relaxed geometries using different vdW's functionals within DFT. We must point out that performing a relaxed DFT calculation on rubrene crystal is computationally quite demanding because of its large crystal volume and also the fact that the unit cell of rubrene contains 280 atoms. Due to hardware limitations, investigations of HF and hybrid functionals for rubrene crystals are not possible.

The DFT calculations are performed using Quantum Espresso except for the TS functionals, which are implemented only in FHI-aims. For all the calculations the experimental structure of rubrene [179] (including the unit cell) is relaxed to a tolerance of 0.01 eV/Å and the overall stress on the unit cell is negligible. For the Quantum Espresso calculations

convergence is tested in total energy for an accuracy better than 1 mRy for a plane-wave cut-off of 30 Ry and a $5 \times 5 \times 5$ Monkhorst-Pack grid using a Gaussian broadening of 0.01 Ry. For the FHI-aims calculation, the convergence in the electronic density and total energy has been checked as a function of Monkhorst-Pack grid. In the final calculations reported here a $5 \times 5 \times 5$ Monkhorst-Pack grid is used with a density and energy convergence of 10^{-4} and 10^{-6} eV, respectively.

DFT Functional	HOMO-LUMO Gap (in eV)	a (% error)	b (% error)	c (% error)
PBE	1.175	0.243	1.713	2.247
Grimme vdW	1.144	-1.679	-1.994	-4.605
vdW-DF	1.156	-0.079	0.114	0.537
TS (PBE)	1.088	-0.117	-1.426	-0.653
TS (LDA)	1.051	-0.552	-4.256	-2.175

Table 5.3: The HOMO-LUMO gap and the percentage deviation from the experimental value of the relaxed rubrene unit cell axes are reported here. The percentage deviation (error) is evaluated as $(\text{DFT} - \text{Exp.})/\text{Exp.} \times 100$. For every DFT functional reported here, unit cell relaxations are performed till atomic forces are less than $0.01 \text{ eV}/\text{\AA}$ and the stress on the unit cell is negligible.

The Kohn-Sham band gap of rubrene for the various DFT functionals are shown in the second column of Table. 5.3. These compare quite accurately with the gap obtained for previous GGA calculations on rubrene crystal published in literature [164]. We must also mention that the band gap of rubrene obtained from optical experiments is 2.3 eV [167] and that calculated from Bethe-Salpeter equation⁷ is 2.8 eV [164]. Again, the symmetry of the HOMO and LUMO bands are exactly identical for all the DFT functionals investigated here.

The other columns in Table. 5.3 contain the percentage deviation of the relaxed unit cell lattice parameters of rubrene molecular crystal for different DFT functionals. This percentage deviation (error) is evaluated as $(\text{DFT value} - \text{Exp.Value})/\text{Exp.Value} \times 100$. The main motivation for the calculation performed in this subsection is to explore the effect of different vdW DFT functionals on the crystal structure. Overall, all the DFT

⁷Which produces the correct quasi-partial states.

functionals accurately reproduce the experimental crystal structure of rubrene with less than 5% error.

Let us now try to understand how each of the different vdW DFT functionals perform with respect to each other and also with respect to a standard PBE calculation. We must keep in mind that the b lattice parameter is also the distance between the rubrene molecules in adjacent herringbones. The accuracy with which b is reproduced will determine the accurateness of the intermolecular interactions in rubrene molecular crystal. Standard PBE functionals overestimate the experimental rubrene lattice constants while all the other vdW functionals except for vdW-DF underestimate them (hence all the vdW DFT functionals bind molecules in the crystal). Grimme's vdW functional gives the maximum relative error while vdW-DF reproduces the experimental structure with remarkable accuracy.

In the next subsection we will explore the band structure and the Partial Density of States (PDOS) of rubrene crystals obtained from DFT.

Band structure

Firstly, we would like to mention that for all the DFT functionals investigated in this subsection the band structures of rubrene crystal are very similar⁸. In Fig. 5.8a we illustrate the band structure of a rubrene crystal obtained from DFT along the high symmetry points in its orthorhombic Brillouin Zone, which is shown in Fig. 5.8b. Also in Fig. 5.8b we plot the partial Density of States (PDOS), which illustrate that the HOMO and LUMO levels of rubrene are entirely constituted by carbon $2p$ electrons (the contribution from H is little).

We interpret the band structure as follows. The HOMO and the LUMO levels are each comprised of four bands, each from the individual rubrene molecules (there are four molecules per unit cell). Moreover, if we look at the band structures carefully we

⁸Each plotted for the corresponding relaxed geometries.

notice that two of the HOMO (LUMO) levels are separated from the other two levels, by about 0.1 eV. This is because the two distinct rubrene molecules which constitute the herringbone motif (Fig. 5.2c) in a crystal are not equivalent in the cell.

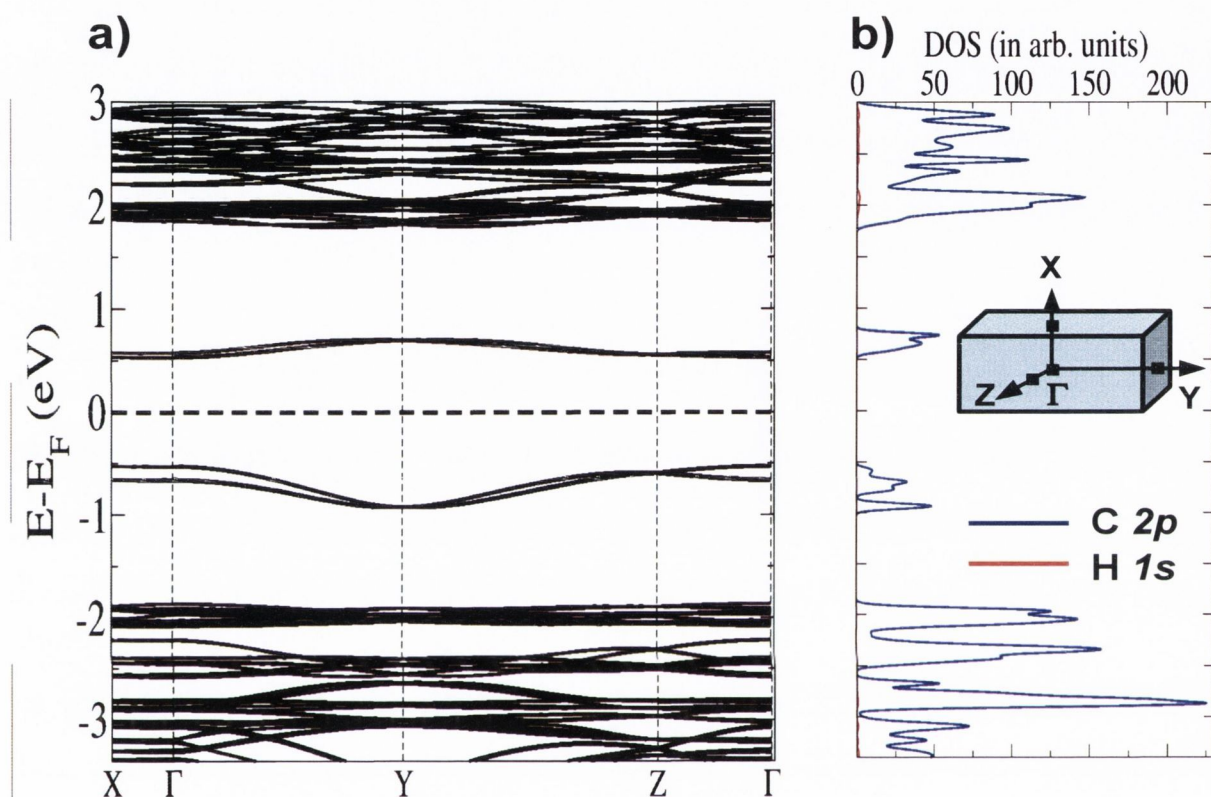


Figure 5.8: The DFT band structure of rubrene obtained is plotted in (a) along with the high symmetry points in the Brillouin Zone of an orthorhombic rubrene crystal which is illustrated in the inset of (b). Also the DFT partial density of states (PDOS) is shown in (b), which illustrates that HOMO and LUMO levels are entirely constituted by C 2p electrons.

Furthermore, one sees that the HOMO and LUMO levels are very well separated from the other bands, which is a characteristic feature of the polyacene family of OSCs (unlike the bands of Si crystals, for instance). Also, if one looks carefully at the HOMO and LUMO levels, one can decipher that there is minimal dispersion of these bands along the $\Gamma - X$ direction, while the maximum dispersion is along the $\Gamma - Y$ direction. Correspondingly, in the orthorhombic rubrene unit cell the \hat{x} crystallographic axis is the longest while the \hat{y} axis is the shortest. Infact, the characteristic features of the HOMO

levels from the DFT bandstructure exactly corresponds to their dispersions from Angle Resolved Ultraviolet Photoemission Spectroscopy (ARUPS) [73]. Also according to the experimental work, the dispersion of the HOMO levels along the $\Gamma - X$ direction is negligible and that along the $\Gamma - Y$ direction is the largest. Furthermore the bandwidth of the HOMO levels along the $\Gamma - Y$ direction is 0.4 eV, which is the same for the DFT HOMO bands of Fig. 5.8a. Thus the bandstructure results strongly indicate that rubrene crystal is a quasi one-dimensional solid with important intermolecular interactions predominantly along the \hat{y} direction. Indeed in reality the rubrene molecular crystal has a herringbone packing structure (see Fig. 5.2c) with a strong $\pi - \pi$ stacking and vdW interactions along the \hat{y} direction. This discussion will be very relevant when we will compute the transfer integrals along the different crystallographic axis in the following section.

We will discuss further the band structure of rubrene crystals in the next section of this chapter. For now, let us begin with introducing the central achievement of the work presented in this thesis. In the next section, we shall elaborate in detail our procedure to obtain the *ab initio* tight binding Hamiltonian for rubrene using Wannier functions and thereafter compute its charge and spin transport properties from first principles.

5.3 First principles estimation of charge and spin transport in rubrene molecular crystals

Introduction

In the last few years, a body of work in the organic spintronics community has shifted in attempting to investigate the spin transport characteristics of crystalline OSCs. Rubrene single crystals are strong candidates, as they possess the highest mobility of 20–40 cm²/Vs [169] among the OSC family. Therefore one can expect spin polarized carriers to travel

over large distances and hence a large spin diffusion length l_s . Indeed recent spin tunneling and spin transport measurements through rubrene tunnel barriers show evidence of very long spin diffusion lengths, $l_s = 13.3$ nm [170].

Theoretical understanding of charge carrier transport through OSCs is often based on simple tight binding (TB) models including electron-lattice coupling such as the Su-Schrieffer-Heeger (SSH) model [218, 219]. Indeed the work presented in the previous chapter addresses this perspective. Such models describe the electronic structure of a material in a certain energy window in terms of the localized "hydrogen-like" orbitals. To solve the problem one has to write the Hamiltonian in the basis of the localized molecular orbitals of the characteristic system. For example, in the case of rubrene (illustrated in Fig. 5.2) provided we know the true molecular wavefunctions of the system we simply have to write down the Hamiltonian which we have worked on in the previous two chapters, in the basis set of those wavefunctions. In this procedure one can obtain the "material-specific" TB Hamiltonian which provides an accurate first principles representation of all the interactions in rubrene.

Indeed such a "material-specific" estimation of the TB Hamiltonian parameters is quintessential for understanding carrier transport through organic systems at a quantitative level. In the past this has been done by fitting the TB band structure to angle-resolved photoemission data [171] and to *ab initio* band structures. In this chapter we will describe an alternative, efficient and a reliable way to extract the model Hamiltonian parameters of crystalline rubrene using localized Wannier functions (WFs). This is indeed the central part of this thesis and more importantly the main contribution which the work presented here intends to make to the field of Organic Spintronics. Once we obtain the *ab initio* Hamiltonian for rubrene, we compute the carrier mobility from Kubo formula and the spin diffusion length (l_s) from the algorithm introduced in the previous section. The *ab initio* transport observables that we obtain can be directly compared with their experimental counterparts.

Localized WFs computed from the Kohn-Sham states obtained from DFT provide a systematic and dependable route for extracting the TB parameters from first principles for a specific system. This procedure ensures a rigorous downfolding of the DFT Kohn-Sham states into localized WFs and in the process captures the *ab initio* information of the system. Furthermore the WFs in our work are intended to represent the real space localized molecular wavefunctions of the system. However, the procedure to extract the correct WF is actually not straightforward. This is because WFs are not uniquely defined since they are not invariant to gauge transformation of the original Bloch function. For example, for each k -point one can perform an arbitrary unitary transformation of the Bloch states such as the one shown below,

$$|\tilde{\psi}_{nk}\rangle = e^{i\phi_n(k)}|\psi_{nk}\rangle. \quad (5.6)$$

Here $\phi_n(k)$ is a generic real function periodic in the reciprocal space. Indeed, $|\tilde{\psi}_{nk}\rangle$ and $|\psi_{nk}\rangle$ describe the same Bloch function but generate different WFs. Therefore in this respect the main predicament is, which Bloch states does one need to use in order to compute the localized WFs? The answer to this problem was addressed by the seminal work of Marzari and Vanderbilt [173], where they postulated a maximally localized paradigm to generate a unique set of WFs for the particular system in consideration. Their method produces a unique set of Maximally Localized Wannier Functions (MLWFs) and also yields the *ab initio* TB model of the system. We will discuss these in detail in the coming section.

Apart from reproducing accurately the *ab initio* (material specific) band structure of the system, MLWFs have found significant importance in modern electronic structure theory. Since WFs are localized functions they provide intuitive information regarding the nature of the chemical bonds in real solids. MLWFs also allow one a systematic estimate of bulk polarization of a system from the microscopic modern theory of polarization. This is because of a one to one correspondence between charge centers of WFs and the Berry

phases of Bloch functions as one moves through the Brillouin zone. Alternatively WFs are also used to define the basis sets in methods like DMFT (dynamical mean field theory), etc. which provide a detailed and accurate description of many-body effects for strongly correlated systems. Furthermore MLWFs are also used to study ballistic transport properties of systems from first principles, where the Green's functions and self-energies can be constructed in a WF basis. Comprehensive reviews on the broad applications of MLWFs in modern electronic structure theory can be found in the literature [174, 175].

In this work we compute the MLWFs corresponding to the HOMO and LUMO levels of rubrene molecular crystals. We then evaluate the real space, direction dependent Hamiltonian matrix elements in the MLWFs basis for the different HOMO and LUMO levels, also in the spin polarized case. Our results indicate a strong anisotropy in rubrene crystal, which will reflect in the transport characteristics. Furthermore we compute the charge carrier mobility using Kubo formula [194] and the spin diffusion length from the scaling of the spin polarized conductance, which in turn is obtained using the Landauer formula. Both the carrier mobility and the spin diffusion length are estimated at a finite temperature using MC sampling. We find quite good agreement between the experimental and *ab initio* estimates for the spin and charge transport observables. To the best of our knowledge this method to extract *ab initio* based TB Hamiltonian for a molecular crystal has never been used so far. In the next section we provide a brief background on Wannier functions which is another important tool in our multiscale modelling technique.

5.4 Wannier Functions

Electronic structure (DFT) calculations performed on perfect periodic solids yield eigenfunctions that are described by a system of extended Bloch waves. The Bloch vectors of the solid $|\Psi_{nk}\rangle$, can be identified by a wave-vector quantum number \mathbf{k} and a band index n . As an example, in our case of rubrene they represent the true molecular wavefunctions. Furthermore, these Bloch waves can also be expressed in terms of localized atomic-like

TB basis functions, for example Wannier Functions.

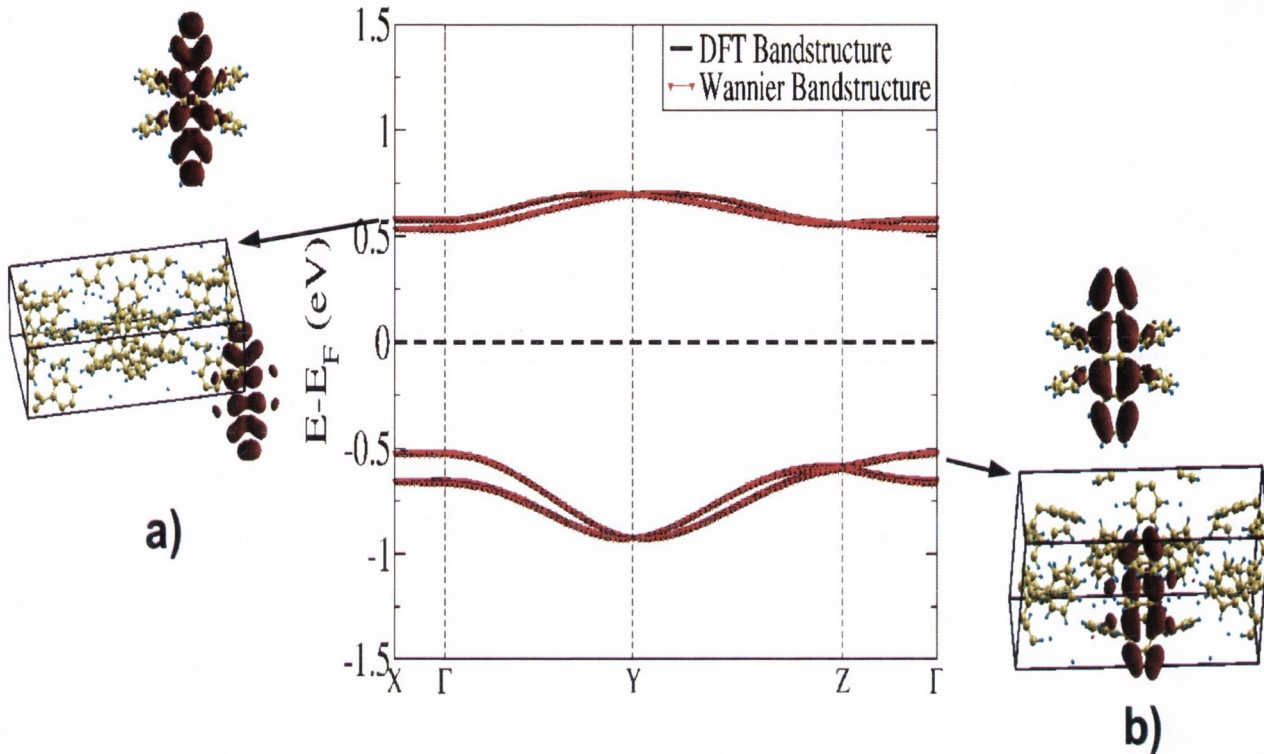


Figure 5.9: The DFT band structure of rubrene molecular crystal is shown in black. MLWFs obtained for the bands corresponding to the HOMO and LUMO energy levels are illustrated in red triangles. Note that there is a one-to-one resemblance between the DFT and the Wannier band structures across the entire Brillouin Zone. a) The wavefunction corresponding to the LUMO band of a rubrene molecule *top panel* and a real space representation of a MLWF corresponding to a LUMO level in rubrene crystal *bottom panel*. b) The wavefunction corresponding to the HOMO level of a rubrene molecule *top panel* and a real space representation of a MLWF corresponding to a HOMO band *bottom panel*. The symmetry of the molecular wavefunctions and the MLWFs for both the HOMO and the LUMO bands are essentially identical.

Fig. 5.9 shows the DFT band structure of rubrene focussed on the energy window corresponding to the HOMO and LUMO bands, i.e. those responsible for transport in the crystal. As discussed earlier in this chapter the HOMO (LUMO) bands form a four band manifold corresponding to the four rubrene molecules included in the unit cell. The HOMO and LUMO energy levels are very well separated with respect to any higher or lower bands outside this manifold across the entire Brillouin zone (BZ). For such an isolated group of J bands with $J = 4$, a set of J localized Wannier functions $|w_{nR}\rangle$, can

be obtained according to the following transformation

$$|w_{nR}\rangle = \frac{V}{(2\pi)^3} \int_{\text{BZ}} \sum_{m=1}^J U_{mn}^k |\psi_{mk}\rangle e^{-ik \cdot R} dk. \quad (5.7)$$

Here U_{mn}^k is a unitary matrix mixing the Bloch states with wave-vector k and V is the volume of the unit cell. Note that the indices of the WFs $|w_{nR}\rangle$, are n which is the band index and R which is a quantum number associated with the real space representation of the WFs.

Without the unitary matrix U_{mn}^k , Eq. (5.7) is essentially a Fourier transformation of the extended Bloch bands which generates localized functions. There are two main issues that are associated with this Fourier transformation. Firstly as evident from Fig. 5.9, there are degeneracies among the bands constituting the HOMO (LUMO) levels at certain locations in the BZ. The bands in question become non-analytic in k at those points and hence the Fourier transform would result in a poorly localized WFs. Thus, to obtain well localized WFs one usually starts with a selected number of Hamiltonian eigenstates $|\psi_{nk}\rangle$ that may not be smooth in the k space, and then introduces a set of unitary transformations U_{mn}^k that cancels out any such discontinuities so that the smoothness is restored.

The second issue associated with the Wannier transformation in Eq. (5.7), is that the WFs are non-unique. This non-uniqueness in the WFs comes from the presence of gauge freedom that exists in the definition of Bloch functions, $|\Psi_{nk}\rangle$ as mentioned earlier in Eq. (5.6). Therefore, different sets of U_{mn}^k yield different WFs which have distinct shapes and spreads. Marzari and Vanderbilt [173] showed that a unique set of MLWFs for a crystal can be obtained by minimizing the quadratic spread of the J WFs about their centers,

$$\Omega = \sum_n [\langle r^2 \rangle_n - \mathbf{r}_n^2], \quad (5.8)$$

where \mathbf{r} is the expectation value of the position operator between WFs and $\langle r^2 \rangle$ is the expectation value of the square of the position operator. To express Ω in terms of the

Bloch functions, the expectation values of the position operators are defined in the Bloch representation based on the separate works by Blount [184] and Vanderbilt and King-Smith [185]. The MLWFs are then obtained by minimizing Ω with respect to U_{mn}^k . This minimization is done in an iterative manner [173].

Once we have obtained the MLWFs we can use the corresponding U_{mn}^k to construct the Hamiltonian matrix $H^w(k)$ expressed in the basis of the MLWFs as:

$$H_{mn}^w(k) = (U_{mn}^k)^\dagger H^B U_{mn}^k, \quad (5.9)$$

where $H^B = \epsilon_{nk} \delta_{mn}$ is the Bloch Hamiltonian matrix with ϵ_{nk} being the Bloch eigenvalues. In order to obtain this Hamiltonian in real space we can simply take its Fourier transform yielding

$$h_{mn}^R = \frac{1}{N_k} \sum_k e^{-ik \cdot R} H_{mn}^w(k). \quad (5.10)$$

Here h_{mn}^R are essentially the matrix elements of the Hamiltonian in the basis of the MLWFs, hence in real space. Thus, this procedure of obtaining the MLWFs yields the *ab initio* TB Hamiltonian of the system in real space as a simple by-product. Finally, the main advantage especially in the case of rubrene is that, no disentanglement procedures [176] are required to obtain the MLWFs corresponding to HOMO (LUMO) levels as they are well separated from the bulk bands as seen in Fig. 5.9. Therefore the TB Hamiltonian obtained for rubrene is exact, it reproduces the DFT one at an arbitrary accuracy and it is constructed with molecular orbitals of minimal extension.

We have performed spin polarized DFT calculations using the Quantum Espresso package [201] with the same specifications as in the band structure calculations of the previous sections. The DFT calculations were done for GGA, Grimme's vdW DFT and vdW-DF, and we observed that even though the relaxed geometries were only slightly different, the TB Hamiltonian parameters did not change a lot.

After obtaining the DFT Bloch bands we perform the Wannier post-processing using

the Wannier90 code [178] embedded into Quantum Espresso. Indeed, the principal reason for using the Quantum Espresso simulation package in the work presented in this section is that there is an efficient and well tested implementation of a post-processing subroutine to compute the MLWFs (Wannier90 code). We found the implementation of Wannier post-processing (Wannier 90) using the Quantum Espresso DFT output most convenient (in comparison to VASP or SIESTA).

We obtain four sets of MLWFs for the HOMO (LUMO) bands of rubrene. The spread functional, Eq. (5.8) (both gauge invariant and non-gauge invariant parts) are converged if the corresponding fractional change between two successive iterations is smaller than 10^{-10} . This ensures that we have truly obtained "maximally localized" Wannier functions for our system.

5.5 TB Hamiltonian parameters

Fig. 5.9 shows the DFT band structure (in black) along with the high symmetry points of the BZ, calculated for the orthorhombic crystal of rubrene in the energy window including only the HOMO and LUMO levels. MLWFs corresponding to the four HOMO (LUMO) bands are also illustrated, in red in Fig. 5.9. Notice an exact correspondence between the Wannier and the DFT band structure across the entire BZ for those bands. Moreover even the symmetry of MLWFs and the corresponding molecular wavefunctions are identical as we shall show next. One such MLWF (*bottom panel*) and the corresponding molecular orbital in the gas phase (*top panel*) are shown in Fig. 5.9a and Fig. 5.9b respectively, for the LUMO and HOMO bands. All the MLWFs of the HOMO and LUMO bands are identical to their corresponding molecular orbital wavefunctions (for the molecule in the gas phase) obtained from DFT.

Therefore, we can assert that the real space representation of the Hamiltonian in the MLWFs basis in Eq. (5.10) will be exactly equivalent to a realistic TB description in the basis of the molecular orbitals of rubrene. In other words, the TB model constructed

from the WFs exactly reproduces the *ab initio* band dispersion for the HOMO and LUMO bands without the need of employing any additional fitting procedures. Thus Eq. (5.10) can be re-arranged to write the full TB Hamiltonian for rubrene in terms of its molecular orbitals as:

$$\hat{H} = \sum_{R, \Delta R} h_{mm'}(\Delta R) [c_{mR+\Delta R}^\dagger c_{m'R} + h.c.] \quad (5.11)$$

Here the indices of the Hamiltonian matrix elements $h_{mm'}(\Delta R)$ correspond to Wannier orbitals of the HOMO (LUMO) levels. Moreover due to the equivalency between Wannier and molecular orbitals established previously, indices m, m' can also label the rubrene molecules in the crystal. Therefore from now on we shall follow the definition where m, m' represents rubrene molecules (i.e. their molecular wavefunctions) 1 to 4 per unit cell. We schematically represent the four molecules in a unit cell of rubrene corresponding to the real-space position of the MLWFs in Fig. 5.10 *i – b*. For the sake of clarity in Fig. 5.10 and in the following discussions, we shall only depict a straight line along the central tetracene backbone (Fig. 5.10 *i – a*) of each rubrene molecule as the real space notation of the molecule itself. Finally, in Eq. (5.11) $c_{m'R}$ ($c_{m'R}^\dagger$) are the creation (annihilation) operator of a charge carrier in the specific HOMO (LUMO) band of a particular rubrene molecule.

In the case of rubrene, the TB Hamiltonian in Eq. (5.11) can be decomposed into a local part and a non-local part, based upon identifying the nature of real space MLWF TB matrix elements $h_{mm'}(\Delta R)$ as

$$\hat{H}' = \hat{H}_{local} + \hat{H}_{non-local} \quad (5.12)$$

$$\hat{H}_{local} = \sum_{mR} \epsilon_m c_{mR}^\dagger c_{mR} + \sum_{\substack{mm'R \\ \Delta R=0}} t_{mm'} (c_{mR}^\dagger c_{m'R} + h.c.) \quad (5.13)$$

$$\hat{H}_{non-local} = \sum_{\substack{mm'R \\ \Delta R=1,2\dots}} t_{mm'\hat{r}}(\Delta R) (c_{mR+\Delta R}^\dagger c_{m'R} + h.c.) \quad (5.14)$$

Eq. (5.13) represents the local TB Hamiltonian with ϵ_m being the on-site energy for the itinerant carrier in the orbital (HOMO/LUMO) of molecule m and $t_{mm'}$ is the hopping integral between the corresponding bands of molecule m and m' within the same unit cell, i.e. $\Delta R = 0$. Eq. (5.14) represents the non-local TB Hamiltonian with $t_{mm'\hat{r}}(\Delta R)$ being the hopping integral between the particular bands of molecule m and m' along a direction \hat{r} in the crystal, belonging to neighboring unit cells, which are determined by the value of ΔR . For example, when $\Delta R = 1$, $t_{mm'\hat{r}}(\Delta R = 1)$ are the nearest neighbor hopping terms and for $\Delta R = 2$, $t_{mm'\hat{r}}(\Delta R = 2)$ are the next-nearest neighbor hopping terms and so on so forth.

5.5.1 On-site energies and transfer integrals

The *ab initio* TB Hamiltonian parameters for the HOMO and LUMO bands of rubrene are listed in Table. 5.4. Let us systematically go through the parameters one by one. The on-site energy for the HOMO bands is $\epsilon = 1.873(3)$ eV and for the LUMO bands is $\epsilon = 3.333(3)$ eV. The absolute values of the on-site energies are the same up to the third decimal place for each of the four rubrene molecule per unit cell. We find that $\epsilon_m(\text{LUMO}) - \epsilon_m(\text{HOMO}) = 1.14$ eV which is also the HOMO-LUMO gap estimated from DFT in Table. 5.3.

Furthermore, when spin-orbit coupling for the system is taken into consideration the splitting of the energy bands on an average is less than 10^{-4} eV. This tiny difference can be attributed to the fact that rubrene is made up of light elements, i.e. C and H, for which spin-orbit interaction is small. We also observed that when including spin-orbit coupling the average forces on the individual atoms fluctuate only by 0.01%. Hence we can safely rule out the role of spin-orbit coupling on affecting the Hamiltonian matrix elements in the case of rubrene.

Moving to the *ab initio* estimate of the hopping terms, the largest of the hopping integrals is the one between similar molecules on the herringbone structure along the \hat{y}

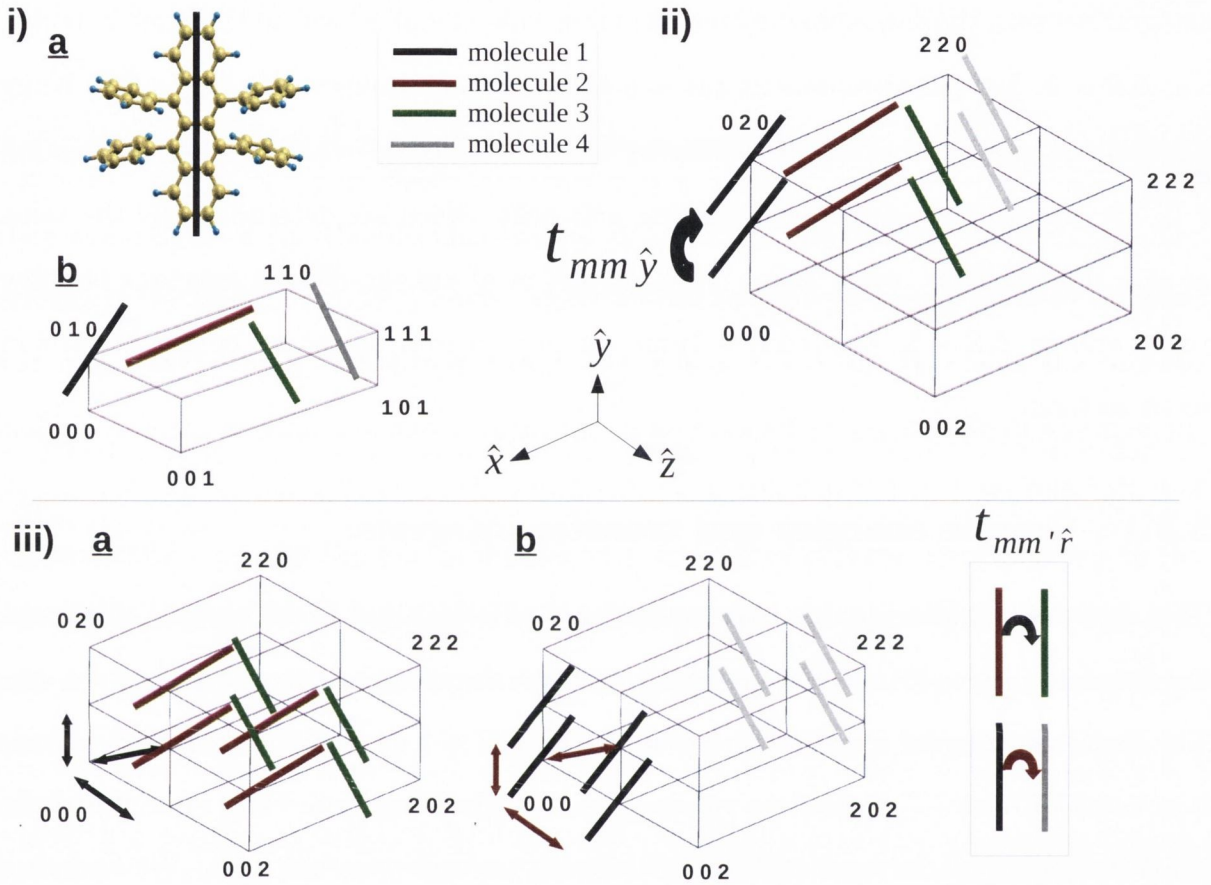


Figure 5.10: *i*–a) Ball and stick representation of a rubrene molecule is illustrated here. A bold vertical line is shown along the axis of symmetry of the molecule⁹. Since the MLWFs are exactly equivalent to the corresponding molecular wavefunctions the bold lines in *i*–b) are used to represent the real space position of the molecules in the crystal. The four rubrene molecules per unit cell are indicated by four different colors and the herringbone molecular structure can be clearly identified. The inter-unit cell, nearest neighbor hopping between similar color rubrene molecules, $t_{mm}(\Delta R = 1) = t$ is illustrated in (ii) with $m \in$ rubrene molecules $[1 \rightarrow 4]$. This hopping is the largest in rubrene crystal and is along the \hat{y} direction. Finally, the inter-unit cell hopping between dissimilar color rubrene molecules, $t_{mm'}(\Delta R = 1) = t'$ along the \hat{y} , \hat{z} and $\hat{y} + \hat{z}$ directions of rubrene crystal with m, m' being molecules 1, 4 is shown in *iii*–a) and those between molecules 2, 3 are shown in *iii*–b). All other hoppings are very small and hence can be safely ignored. For the sake of clarity in these illustrations describing the various TB hopping elements, the atoms and bonds constituting the rubrene unit cells are stripped off.

direction, $t_{mm\hat{y}}$ ($\Delta R = 1$) as depicted in Fig.5.2c. As illustrated, this is between similar rubrene molecules of nearest neighboring unit cells along the \hat{y} direction for both the HOMO and LUMO levels. Indeed, the \hat{y} direction is also the shortest crystallographic axis of the orthorhombic cell. The transfer integrals are, $t_{mm\hat{y}}(\Delta R = 1) = 0.0976(2)$ eV for HOMO levels and $t_{mm\hat{y}}(\Delta R = 1) = 0.0535(0)$ eV for LUMO levels, note $m \in$ molecule $[1 \rightarrow 4]$. The hopping integrals $t_{mm\hat{y}}(\Delta R = 1) = t$ are schematically illustrated in Fig. 5.10 (ii). They are between identical rubrene molecules of the same color. Note that this large hopping value in rubrene along the \hat{y} direction was also inferred from the DFT bandstructure as discussed earlier, since the maximum dispersion for HOMO (LUMO) bands in is along the $\Gamma - Y - \Gamma$ direction.

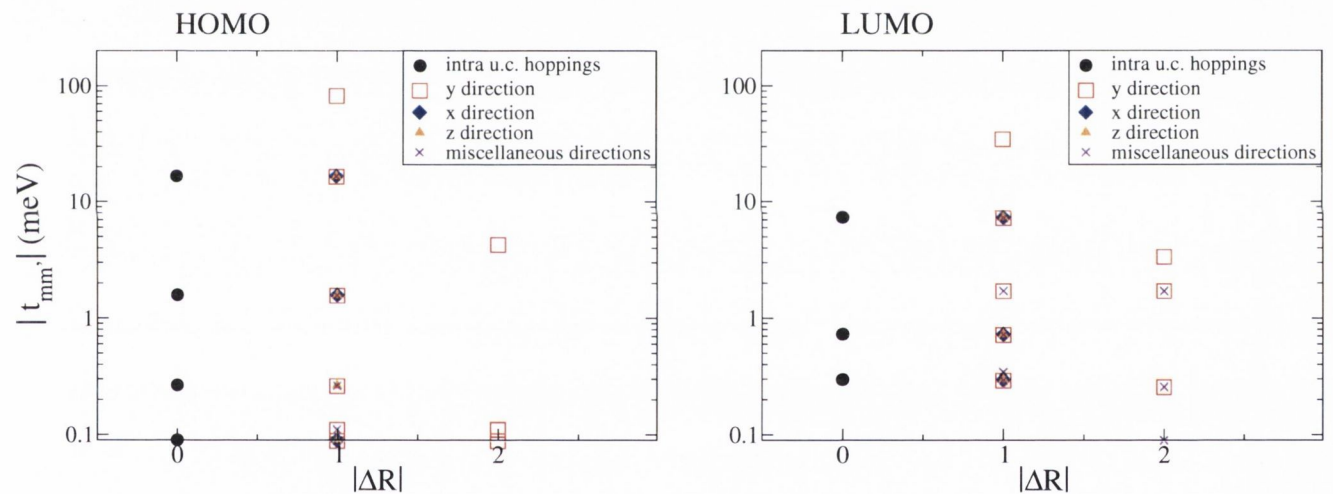


Figure 5.11: The magnitudes of all the transfer integrals in rubrene for the HOMO (*left panel*) and LUMO (*right panel*) bands along the different crystallographic directions are illustrated here. Note that the ordinates of the graphs are in a logarithmic scale. One can distinguish quite conveniently the largest transfer integral [$t_{mm\hat{r}}(\Delta R = 1) = t$] from all the other transfer integrals. The largest transfer integral corresponds to nearest neighboring hopping ($\Delta R = 1$) along the herringbone structure.

The other hopping integrals in rubrene crystal, $t_{mm'\hat{r}}(\Delta R = 0, 1) = t'$ are quite small in comparison to the nearest neighbor hopping. These are between the dissimilar rubrene molecules constituting the herringbone structure with the combination (mm') being molecules (1, 4) and (2, 3) along the \hat{y} , \hat{z} and the $\hat{y} + \hat{z}$ directions as shown in Fig.5.10 *iii - a* and *iii - b*. Thus, $t_{mm'\hat{r}}(\Delta R = 0, 1) = 0.0112(8)$ eV for the HOMO levels and

$t_{mm'\hat{r}}(\Delta R = 0, 1) = 0.0109(3)$ eV for the LUMO levels. Hopping terms along all the other directions between all the different combinations of rubrene molecules for $\Delta R = 0, 1, 2, \dots$ are minute and are henceforward neglected in this work.

The magnitudes of all the transfer integrals along the different crystallographic axis in rubrene (upto $\Delta R = 2$) are summarized in a pictorial form in Fig. 5.11 for the HOMO (*left panel*) and LUMO (*right panel*) bands. Fig. 5.11 is designed to give the reader a feeling of the different direction depended transfer integrals, in particular how their magnitudes compare with each other. Notice that the ordinate of the graphs (in Fig. 5.11) is in a logarithmic scale. Furthermore, $t_{mm\hat{y}}(\Delta R = 1) = t$, the largest of the transfer integrals between similar rubrene molecules in the herringbone (Fig. 5.2c) along the \hat{y} direction for both the HOMO and LUMO levels, is quite distinct from the other transfer integrals.

Let us now compare our estimates of the transfer integrals for the HOMO electrons with previous theoretical approaches in rubrene molecular crystals. The computational technique used by Troisi includes representing all the essential interactions in the crystal with a SSH Hamiltonian and thereafter the transfer integrals are evaluated via a combination of quantum chemistry computation (ZINDO overlap technique) and molecular dynamics [219]. Thus a distribution of transfer integrals were obtained. Troisi's results for the two main transfer integrals in rubrene are 0.1426 ± 0.0508 eV and 0.0229 ± 0.0099 eV. Furthermore, other theoretical works which have probed charge transport in rubrene molecular crystals include that of Coropceanu and co-workers [216]. They estimated the two predominant transfer integrals as 0.083 eV and 0.015 eV from Koopman's theorem¹⁰ for a rubrene dimer system. Please note that each of the theoretical methods discussed above are different from our multiscale computational approach. However it is interesting to note that our *ab initio* estimate of the transfer integrals are close to previous theoretical works and infact also those obtained by fitting the experimental band structures [73].

The results for the TB Hamiltonian elements in Table. 5.4 are for GGA (PBE) bands.

¹⁰We will use this method in Chapter 6, where we will descibe the details of this method.

TB Parameter	HOMO	LUMO
ϵ_m (eV)	1.873(3)	3.333(2)
$t_{mm'\hat{r}}(\Delta R = 1)$ (eV)	$t_{mm\hat{y}} = 0.0976(2)$ $t_{mm'\hat{y}} = 0.01128$ $t_{mm'\hat{z}} = 0.01128$ $t_{mm'\hat{y}+\hat{z}} = 0.01127$	$t_{mm\hat{y}} = 0.0535(0)$ $t_{mm'\hat{y}} = 0.01092$ $t_{mm'\hat{z}} = 0.01092$ $t_{mm'\hat{y}+\hat{z}} = 0.01093$
$t_{mm'}(\Delta R = 0)$ (eV)	$t_{mm'} = 0.01127$	$t_{mm'} = 0.01093$
$\alpha_{mm'\hat{r}}$ (eV/Å)	$\alpha_{mm\hat{y}} = 0.0106$ $\alpha_{mm'\hat{y}} = 0.003$ $\alpha_{mm'\hat{z}} = 0.0001$ $\alpha_{mm'\hat{y}+\hat{z}} = 0.0004$	$\alpha_{mm\hat{y}} = 0.0048$ $\alpha_{mm'\hat{y}} = 0.001$ $\alpha_{mm'\hat{z}} = 0.0003$ $\alpha_{mm'\hat{y}+\hat{z}} = 0.001$
K (eV/Å ²)	0.06612	0.06612

Table 5.4: The *ab initio* TB parameters for the rubrene molecular crystal are summarized in this table. The TB Hamiltonian representing the essential interactions in rubrene responsible for charge transport is described by Eq. (5.15). For computing the charge and spin transport observables in the later portion in this section, only the TB Hamiltonian parameters corresponding to HOMO bands are used. This is because rubrene is a hole transport OSC with the itinerant carriers residing in the HOMO bands.

We also repeated the procedure for Van der Waals functionals: Grimme [43] and vdW-DF [46] and we found that the different TB Hamiltonian parameters for rubrene differs by only 1% in comparison with the same estimated from PBE.

5.5.2 Electron-phonon and stiffness constants

We elaborate upon Eq. (5.12) to include all the physical processes that describe charge dynamics in an OSCs. These are summed up in Eq. (5.15) below

$$\hat{H}' = \sum_{\substack{mm'R \\ \Delta R=1,2\dots}} [t_{mm'\hat{r}}(\Delta R) + \alpha_{mm'\hat{r}}(q_m - q_{m'})](c_{mR+\Delta R}^\dagger c_{m'R} + h.c.) + \sum_{mm'} \frac{1}{2} K_{\hat{r}}(q_m - q_{m'})^2. \quad (5.15)$$

Here $\alpha_{mm'\hat{r}}$ is the carrier-phonon interaction constant, corresponding to a molecular displacement direction \hat{r}' ^[11] and modulates the transfer integrals between the rubrene molecules m and m' . In the equation, q_m is the displacement (from the equilibrium position) of the rubrene molecule m in the crystal along that particular direction (\hat{r}') and finally $K_{\hat{r}'}$ is the elastic constant also calculated along the particular direction (\hat{r}'). In principle, a comprehensive charge transport theory should take into account all the phonon modes of the crystal. However, computing the phonon band structure for rubrene (which has 280 atoms in a unit cell) in our experience proved to be computationally very expensive, exhaustive and therefore not possible with our computational hardware constraints. In our charge transport procedure we have therefore employed the following steps.

Firstly, since rubrene is a hole transport based OSC, in all our simulations from this moment on we only consider the TB Hamiltonian matrix elements for the HOMO levels. This is because the itinerant carrier (hole) in a rubrene crystal resides in the HOMO levels. Next, since rubrene has an almost quasi one-dimensional crystal structure with only one dominant transfer integral, we expect that there will be just one particular phonon mode along which the values of α as well as K will be significant and will therefore govern transport. The displacement due to this particular phonon mode, which we considered in our simulations, corresponds to a co-facial sliding motion of similar (colored) rubrene molecule (Fig. 5.12) in adjacent unit cells along its tetracene backbone; with respect to one another. We shall discuss further in the coming paragraphs on our justification of this particular phonon mode for rubrene, which is chosen in our simulations.

An estimate of the elastic constant K per rubrene molecule is made from, $K = \frac{1}{q_m} \left(\frac{\delta E'}{\delta q_m} \right)$. Here E' is the total energy of the Hamiltonian, Eq. (5.15). We obtain $K = 0.06612$ eV/Å² per rubrene molecule, which corresponds to a frequency $\omega = \sqrt{\frac{K}{M}}$, 36.53 cm⁻¹, of the corresponding optical phonon mode. Here M is the mass of rubrene molecule,

¹¹This corresponds to the particular phonon mode in the crystal.

which is 532 a.m.u. The value for ω obtained agrees quite well with the lowest frequency phonon mode calculated previously for the rubrene crystals in the works of Troisi [219] and Girlando and co-workers [182]. Note that this frequency, $\omega = 36.53 \text{ cm}^{-1}$, justifies the classical treatment of the phonons via MC sampling. Indeed the corresponding nuclear motions (ω) are slow and as a result the nuclear kinetic energy can be ignored.

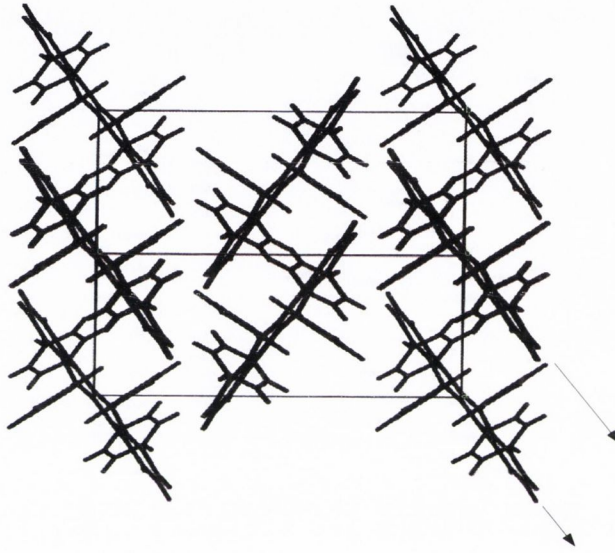


Figure 5.12: The herringbone crystal structure of rubrene along the \hat{y} direction is shown here. The arrows shown in this figure depict a sliding displacement of one set of molecules corresponding to the nearest neighboring transfer integrals. All the molecules in the crystal are displaced along such a sliding mode to estimate α and K (from finite differences) in our simulations.

To obtain $\alpha_{\hat{r}'} = \frac{\delta t_{\hat{r}'}}{\delta q_m}$, again we make a small displacement of a molecule m along the sliding mode (\hat{r}') shown in Fig. 5.12 and evaluate the change in the TB hopping parameters obtained upon recalculating the MLWFs. For the HOMO levels we obtain $\alpha_{mm\hat{y}} = 0.0106 \text{ eV/\AA}^{[12]}$ for $t_{mm\hat{y}}(\Delta R = 1) = t$. Next, the el-ph interactions corresponding to the other transfer integrals (of smaller magnitudes) between dissimilar kind of rubrene molecules m and m' are $\alpha_{mm'\hat{y}} = 0.003$, $\alpha_{mm'\hat{z}} = 0.0001$ and $\alpha_{mm'\hat{y}+\hat{z}} = 0.0004 \text{ eV/\AA}$. The el-ph interactions (α) for the LUMO levels are also tabulated in Table. 5.4. Our estimates for non-local el-ph interactions are smaller than those obtained by Troisi [219].

¹²Note that $\alpha_{mm\hat{r}}$ follows the corresponding transfer integrals $t_{mm\hat{r}}$.

For the sake of completeness we have computed the el-ph interactions corresponding to Holstein phonon modes. These correspond to local (on-site) electron-phonon coupling, which can be calculated as $\alpha_{\text{local}} = \frac{\delta \epsilon_{\tilde{r}}}{\delta q_m}$. We find the calculated α_{local} for the Holstein phonons to be minute and the frequencies corresponding to such modes exceed 1000 cm^{-1} in agreement with previous works of Troisi [219] and Bredas [126]. Therefore the contribution of local electron-phonon interactions in determining the charge transport characteristics in rubrene crystals can be safely neglected, as these modes will be excited only at very high temperatures.

We also evaluated α and K along another set of phonon modes corresponding to motion of the rubrene molecules along the \hat{y} direction, since it is the shortest crystallographic axis and has the maximum amount of intermolecular interactions in the crystal. We found that the magnitude of all the el-ph interaction constants are $\alpha < 10^{-4} \text{ eV}/\text{\AA}$. Therefore in this case $\alpha \ll t$ and hence would make little contribution to the carrier mobility. Let us leave the discussions on the particular phonon mode chosen, upto here and again come back to it in the next section.

5.6 *Ab initio* transport observables

5.6.1 Charge carrier mobility

After obtaining the TB parameters for rubrene, we evolve the classical lattice displacements in Eq. (5.15) via MC sampling according to our previous work [180]. In Fig. 5.13 *a* and Fig. 5.13 *b* we show the statistical distribution of the (two main) hopping integrals t and t' in rubrene crystal (discussed previously), respectively at $T = 96 \text{ K}$ and at $T = 387 \text{ K}$ arising from the MC simulations. For each temperature the distributions are fitted to a Gaussian function and the corresponding Full Width at Half Maxima (FWHM) are reported. Firstly we notice that for all temperatures the fluctuations in t and t' are of the order of $\pm 10 \text{ meV}$. Indeed the small magnitudes of lattice displacements are a direct

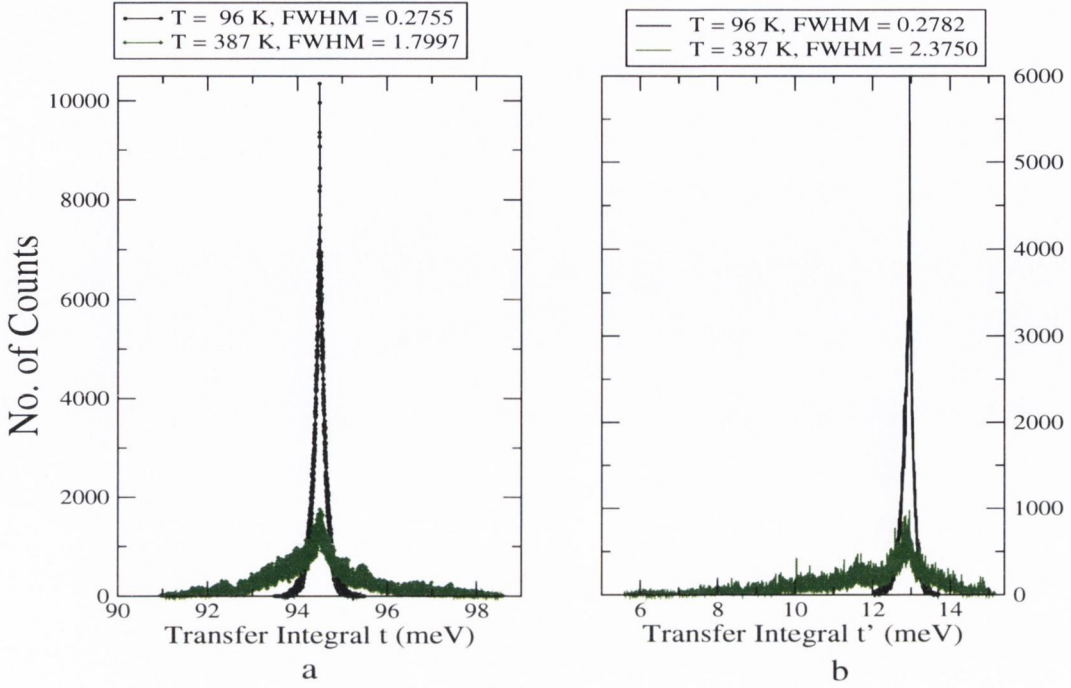


Figure 5.13: *a*) and *b*) show the statistical distribution of the two main hopping integrals t and t' in rubrene crystal (respectively) at a small and large value of temperature, each evaluated from the full Hamiltonian. The distributions are fitted to a Gaussian function and the full width at half maxima (FWHM) are also reported. Note that for all temperatures the fluctuation in the transfer integrals (t and t') are small, i.e. at maximum ± 10 meV.

fallout of the estimates for electron-phonon interaction strengths $\alpha_{mm'\vec{r}}$ and stiffness constant $K_{\vec{r}}$. Moreover the statistical distribution is narrow at low temperature and broad at high temperature, which can be confirmed from the values of FWHM reported in the graphs. Also because $\left(\frac{t}{\alpha_{mm'\vec{r}}}\right) \gg \left(\frac{t'}{\alpha_{mm'\vec{r}}}\right)$, at higher temperatures the fluctuation in the effective t' (Fig. 5.14 *b*) is slightly larger. The main message coming from the statistical distribution plots of Fig. 5.13 is that, because the fluctuation in the transfer integrals are not large, for the system represented by Eq. (5.15), at any time (and at any temperature) carriers will occupy delocalized wavefunctions¹³. In this particular aspect, even at high temperatures our results indicate pure band transport, as in inorganic semiconductors (or metals). Interestingly, this high temperature behavior is different from that reported

¹³This is because the value of the transfer integral t will be relatively unaffected by temperature (phonons). Furthermore, the estimate for t is quite significant among the OSC family.

by Troisi [219] and Hannewald [236] for organic molecular crystals, each of whom have proposed different charge transport theories.

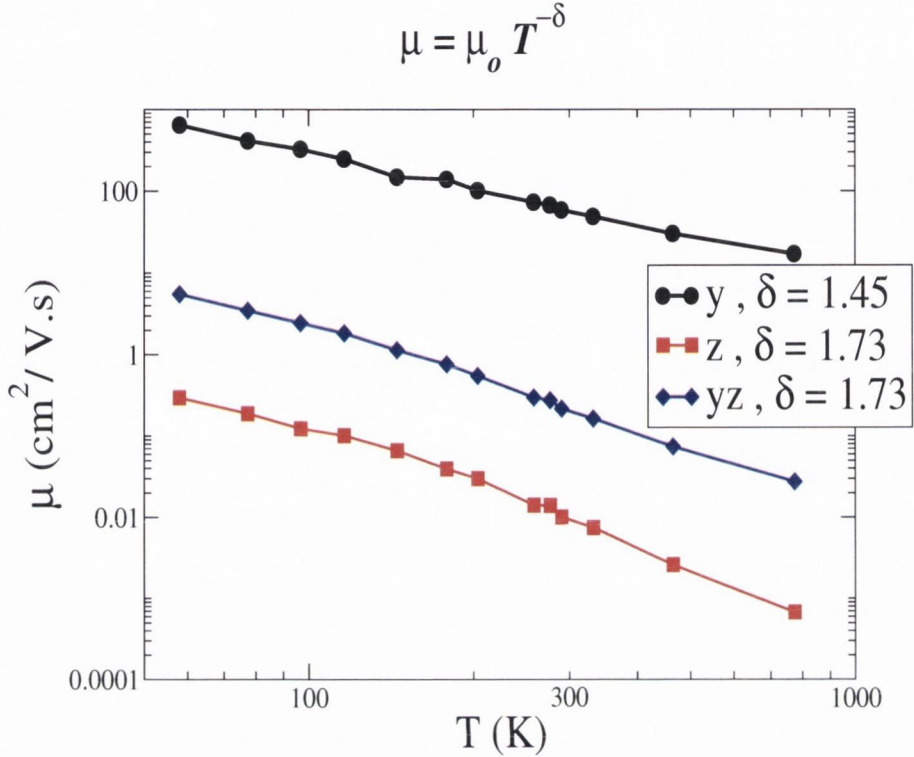


Figure 5.14: The temperature dependence of the *ab initio* charge carrier mobility, μ , of rubrene evaluated along the \hat{y} , \hat{z} and $\hat{y} + \hat{z}$ directions plotted on a log-log scale are illustrated here. Our estimates shows that the crystal is highly anisotropic exactly as found in experiments [156]. Furthermore the carrier mobility decreases with temperature according to a power law, $\mu = \mu_0 T^{-\delta}$. The corresponding power law coefficients, δ , are reported. At $T = 300$ K the estimate for *ab initio* mobility in rubrene is, $\mu = 58 \text{ cm}^2/\text{V}\cdot\text{s}$, which agrees with the highest experimental estimate from a four-terminal setup for single crystalline rubrene based OFETs. [169]

Next we evaluate the charge carrier mobility from the linear response Kubo formula [194]. The procedure is similar to the one used to evaluate mobility in the previous chapter. After the MC simulations have reached equilibrium for every MC configuration the charge carrier mobility is evaluated and averaged over 100,000 MC steps. Fig. 5.14 illustrates the mobility of rubrene along \hat{y} , \hat{z} and $\hat{y} + \hat{z}$ directions of the crystal, as a function of temperature, on a log-log scale¹⁴. From the figure we can clearly understand that the

¹⁴Note that the results in Fig. 5.14 are for $L = 128$ unit cells. The length dependence of mobility has been verified to be non-existent for $L > 64$ unit cells.

charge carrier mobility is strongly anisotropic as also observed in experiments [156]. This is expected from our work as the predominant transfer integrals in the rubrene crystal are along the \hat{y} direction. Therefore the highest mobility in rubrene is also along the \hat{y} direction. Furthermore, we notice that the charge carrier mobility decreases according to a power law as the temperature is increased. The corresponding power law coefficients are indicated in Fig. 5.14 which are quite large and indicate a "band-like" transport. Further evidence of a band-like transport can be based on the small magnitude of carrier-phonon coupling which we estimate and also the fact that the thermal fluctuations of the transfer integrals are little (due to small lattice displacements), as observed in Fig. 5.13a and Fig. 5.13b. Therefore, in rubrene molecular crystals (described by band transport), on increasing the temperature the charge carriers are increasingly scattered due to phonons and the mobility decreases.

We find our estimate for *ab initio* mobility of rubrene at room temperature ($T = 300$ K) to be $\mu = 58 \text{ cm}^2/\text{V}\cdot\text{s}$. This is slightly larger than the value for contact-free intrinsic mobility observed experimentally from four-terminal measurements conducted on single crystal rubrene based OFETs [169]. Our result for charge carrier mobility also agrees quite well with previous theoretical predictions for rubrene based on sliding phonon modes [218, 219] as well as that calculated from the full phonon band structure [182]. This reaffirms that, in order to obtain the mobility of rubrene crystal, one does not need to include the contributions of all the phonon modes of the entire phonon spectra.

5.6.2 Spin diffusion length

In the final section of this chapter we shall explore the spin transport properties of rubrene from first principles. In order to achieve such goal we add the spin Hamiltonian \hat{H}_{spin} as defined below, to Eq. (5.15). The spin Hamiltonian describes the two main sources of spin scattering in OSCs namely hyperfine (HI) and spin-orbit (SO) interactions.

Hyperfine interaction

In order to include the effect of HI in our problem we add the following spin Hamiltonian to the *ab initio* Hamiltonian of rubrene [in Eq. (5.15)]

$$\hat{H}_{\text{HI}} = J_H \sum_{\alpha\beta m} \vec{S}_m^N \cdot [c_{\alpha m}^\dagger (\vec{\sigma}_{\alpha\beta}) c_{\beta m}]. \quad (5.16)$$

Eq. (5.16) includes HI in a manner similar to the approach we have followed in the previous two chapters of this thesis. Therefore \vec{S}_m^N are a set of classical vectors representing the collective nuclear spins of all the hydrogen atom in the m -th rubrene molecule. The itinerant carrier's spin in every rubrene molecule m is described by a vector of Pauli matrices, $[c_{\alpha m}^\dagger (\vec{\sigma}_{\alpha\beta}) c_{\beta m}]$, where α and β are the spin indices (\uparrow, \downarrow). Finally J_H is the hyperfine coupling strength, which for organic materials is estimated to be $J_H = 10^{-4} - 10^{-6}$ eV. Please note that the value for J_H taken from the theoretical work of Bobbert [93] is a close estimate for the parameter. Our two models are not equivalent in representing HI in OSCs and in particular \vec{S}_m^N (in our model) is the collective nuclear spins of all the hydrogen atom of a rubrene molecule.

Our spin transport setup comprises the rubrene molecular crystal described by the corresponding full TB Hamiltonian $\hat{H} = \hat{H}' + \hat{H}_{\text{HI}}$, sandwiched between two semi-infinite metallic electrodes. The Hamiltonian of the electrodes and the ballistic transport approach that we use here are the same as the one introduced in the previous chapter. The spin polarized ballistic conductance is evaluated according to the Fisher-Lee equation as

$$G = \frac{e^2}{h} [T_{\uparrow\uparrow} + T_{\downarrow\downarrow} + T_{\uparrow\downarrow} + T_{\downarrow\uparrow}], \quad (5.17)$$

where $T_{\uparrow\uparrow} + T_{\downarrow\downarrow} = T_{sc}$ is the spin-conserving (*sc*) transmission coefficient and $T_{\uparrow\downarrow} + T_{\downarrow\uparrow} = T_{sm}$ is the spin-mixing (*sm*) transmission coefficient. Please note that each of the transmission coefficient constituents appearing in Eq. (5.17) are integrated over only the HOMO energy levels where the charge transport occurs. Furthermore, the reciprocal of the slope

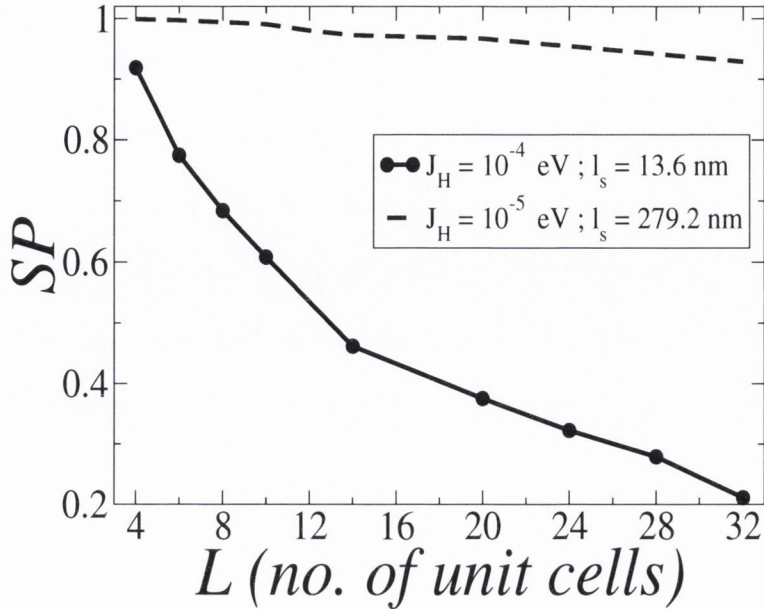


Figure 5.15: SP vs L graphs for $J_H = 10^{-4}$ eV (solid line) and at $J_H = 10^{-5}$ eV (dashed line without the data points for clarity) is shown here. The corresponding values for l_s are also mentioned. The lower bound estimate for l_s (when only HIs are taken into account), i.e. $l_s = 13.6$ nm matches quite well with the experimental value of Ref. [170]. Note that $L = 1$ rubrene unit cell corresponds to 7.17\AA which is the b axis length of a rubrene crystal (orthorhombic).

of the length dependence of SP [see Eq. (4.24)] gives us the spin diffusion length (l_s) of the spin valve setup in a manner exactly the same as discussed in the previous chapter. We compute the *ab initio* estimate for l_s by evolving the classical variables (\vec{q}_i and \vec{S}_m^N) in the Hamiltonian, $\hat{H} = \hat{H}' + \hat{H}_{\text{HI}}$ via MC sampling. Once the MC simulation reaches equilibrium, l_s is averaged over 10,000 MC steps.

Before we present our results for the first principles estimate of l_s , we first discuss the validity of the ballistic limit (Fig. 4.1b) used to investigate the spin transport properties. The reason why we consider the ballistic approach to spin transport are two folds. Firstly, we have a convenient algorithm (introduced in the previous chapter) that can be used to estimate l_s based on the length dependence of SP , a parameter which can be directly related to the corresponding experimental value. In other words, l_s that we estimate from the procedure discussed above can be actually compared directly with experiments. Furthermore the second point is that, by considering a ballistic limit for carrier transport

we will estimate the value of l_s by measuring the spin relaxation only due the intrinsic spin scattering effects of the OSC i.e. HI and SO coupling. As such, our approach is closer to an ideal experimental scenario in a TMR device (ignoring scattering and other spurious effects). Our estimate of l_s can be thus considered to be the upper limit.

In Fig. 5.15 we illustrate SP vs L (number of rubrene unit cells) for $J_H = 10^{-4}$ eV (solid line) and $J_H = 10^{-5}$ eV (dashed line). We observe that the SP vs L graphs are independent of temperature when spin relaxation is only due to HI. The estimates for spin diffusion length are the following, $l_s = 279.2$ nm for $J_H = 10^{-5}$ eV and $l_s = 13.6$ nm for $J_H = 10^{-4}$ eV. Since in organic materials $J_H > 10^{-4}$ eV is a rather large magnitude for HI [93], we may take $l_s = 13.6$ nm to be the lower bound estimate when only HI is taken into account.

The experimental measure [170] for l_s for amorphous rubrene bases spin valves is $l_s = 13.3$ nm. Thus, the close proximity of the *ab initio* and the experimental results suggests that our multiscale procedure for modelling spin transport in rubrene is quite accurate.

Spin-orbit coupling

In order to include the effect of spin scattering due to SO coupling we use the following spin Hamiltonian

$$\hat{H}_{\text{SO}} = \lambda \sum_{\alpha\beta m} \vec{L}_{mm} \cdot [c_{\alpha m}^\dagger (\vec{\sigma}_{\alpha\beta}) c_{\beta m}]. \quad (5.18)$$

Here \vec{L}_{mm} and $\vec{S}_{mm} = [c_{\alpha m}^\dagger (\vec{\sigma}_{\alpha\beta}) c_{\beta m}]$ are the orbital and spin components of the angular momentum. Let us discuss in more detail how we incorporate SO into our simulations.

We start with pictorially representing the largest transfer integral $t_{mmj}(\Delta R = 1) = t$ along the herringbone motif of a rubrene crystal, in the left panel of Fig. 5.16. Here four such molecules (m, m, m' and m'), belonging to nearest neighboring unit cells, constituting the herringbone structure are shown. In order to demonstrate how SO is incorporated

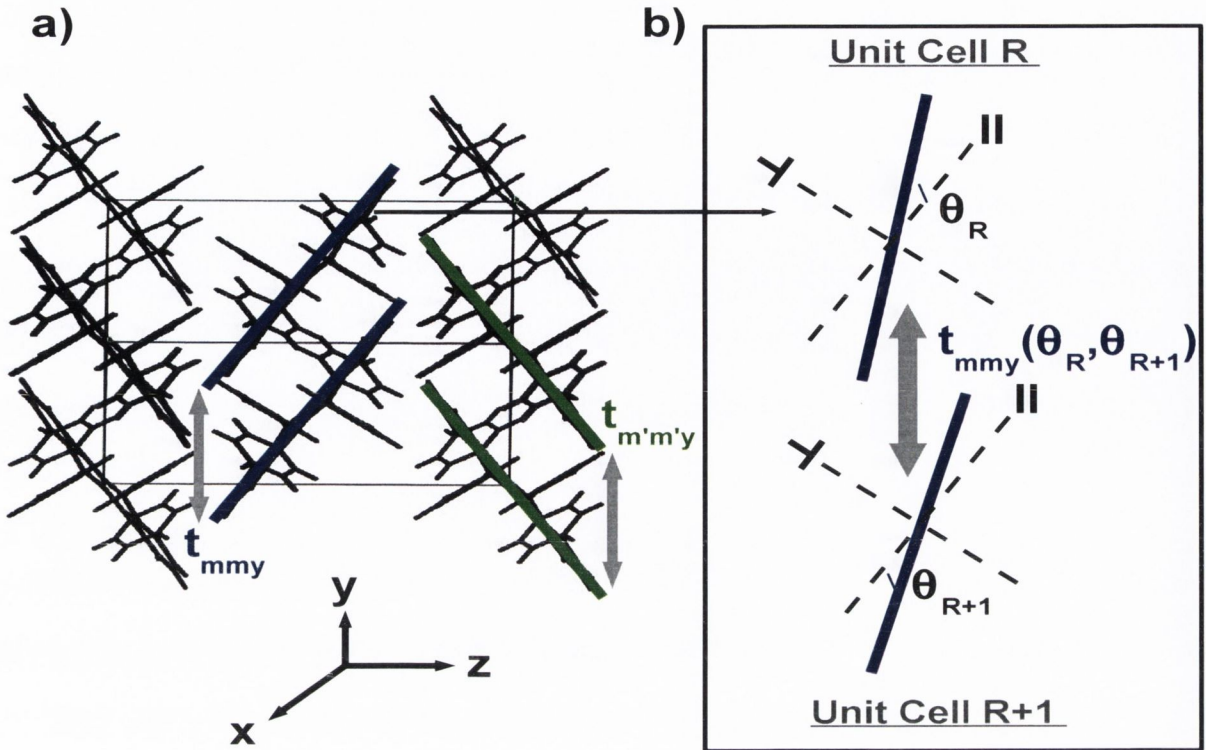


Figure 5.16: In the left panel (a), the crystal structure of rubrene oriented along the \hat{y} direction is illustrated, showing the characteristic herringbone motif. Also depicted are a set of rubrene molecules (m , m , m' and m') between which there is the largest transfer integrals in the crystal, $t_{mmy}(\Delta R = 1) = t$ (along the herringbone motif). In order to incorporate a trajectory-dependent spin mixing due to SO, in our model we assume an angular dependence (with respect to the original parallel axis) of the molecules as depicted in (b). An example is shown here for generic molecules m and m belonging to the nearest neighboring unit cells R and $R + 1$, corresponding to transfer integral $t_{mmy}(\Delta R = 1)$. Therefore the transfer integral will have an angular dependence and together with an on-site $\vec{L}_{mm'} \cdot \vec{S}_{mm'}$ matrix, this induces spin mixing.

in our simulations let us consider one such set of molecules m , m , belonging to nearest neighboring unit cells labelled by their unit cell index, R and $R + \Delta R$ with $\Delta R = 1$ and henceforth referred to as $R + 1$.

The inclusion of SO in our model is in the following manner: the rubrene molecules R and $R + 1$ are assumed to be at an angle θ_R and θ_{R+1} with respect to a parallel axis (\parallel) as shown in Fig. 5.16 (right panel). Ideally, the angles must also have an m index to represent the corresponding molecule, but in this explanation we drop it for the sake of simplicity. The parallel axis is along the plane containing the central tetracene backbone

of rubrene molecule when $\theta_R = \theta_{R+1} = 0^\circ$. Similarly we may define a perpendicular axis (\perp) when $\theta_R = \theta_{R+1} = 90^\circ$. These axes are schematically illustrated in the right panel of Fig. 5.16. Since in our model, the rubrene molecules are at an angle θ_R , we may decompose the molecular wavefunction w into a parallel w_{\parallel} and perpendicular w_{\perp} component. Furthermore, we now express Eq. (5.18) as well as Eq. (5.15) in terms of the parallel and perpendicular molecular wavefunction components by introducing an extra index, $O = \parallel, \perp$.

Therefore Eq. (5.15) will have an additional index O and O' , added only to the transfer integrals. The system wavefunctions can be written down in the following basis: $|\eta\rangle = |R\zeta\sigma\rangle$, where $\zeta = w_O^m$, σ is the spin index and the other indices are the same as in the previous section. The original transfer integral between nearest neighboring unit cells R and $R + 1$, $t_{mm\hat{y}}(\Delta R = 1) = t$ which is pictorially represented in the right panel of Fig. 5.16 can be written down as the following four components: $t_{m\parallel m\parallel} = t \cos(\theta_R - \theta_{R+1})$, $t_{m\perp m\perp} = t \cos(\theta_R - \theta_{R+1})$, $t_{m\parallel m\perp} = -t \sin(\theta_R - \theta_{R+1})$ and $t_{m\perp m\parallel} = t \sin(\theta_R - \theta_{R+1})$. Also all the other transfer integrals ($t_{mm'\hat{r}}$) in the problem can be expressed with an analogous angular dependence. Note that when $\theta_R = \theta_{R+1} = 0$ and $\theta_R - \theta_{R+1} = 0$, there is no hopping between the \parallel and \perp components of the molecular wavefunctions of adjacent rubrene molecules and $t_{m\perp m\parallel} = t_{m\parallel m\perp} = 0$.

We finally need to evaluate the SO matrix elements $\langle \eta | \vec{L}_{mm} \cdot \vec{S}_{mm} | \eta' \rangle$, which lift the spin degeneracy. For every $|\eta\rangle = |R\zeta\sigma\rangle$ with $\zeta = w_O^m$ and $|\eta\rangle = |R\zeta'\sigma'\rangle$ with $\zeta' = w_{O'}^m$, the SO Hamiltonian, $\langle \eta | \vec{L}_{mm} \cdot \vec{S}_{mm} | \eta' \rangle$ when expressed in the ket notation of $\{|w_{\parallel}^m \uparrow\rangle, |w_{\perp}^m \uparrow\rangle, |w_{\parallel}^m \downarrow\rangle, |w_{\perp}^m \downarrow\rangle\}$ is the following

$$\hat{H}_{SO} = \frac{\lambda_{SO}}{2} \begin{pmatrix} 0 & 0 & 0 & -\iota \\ 0 & 0 & \iota & 0 \\ 0 & -\iota & 0 & 0 \\ \iota & 0 & 0 & 0 \end{pmatrix},$$

where λ_{SO} is the SO coupling strength. The above $\langle \eta | \vec{L}_{mm} \cdot \vec{S}_{mm} | \eta' \rangle$ matrix is the SO coupling matrix between p orbitals similar to the one used in the previous chapter. Therefore the approximation made in this part of the work is that the \parallel and \perp components of the wavefunctions of rubrene w , i.e. w_{\parallel}^m and w_{\perp}^m correspond approximately to p_y and p_z wavefunctions. The justification for using such approximation, is based on the fact that the rubrene molecular orbitals are entirely constituted by C $2p$ electrons¹⁵. Furthermore, due to the nature of the herringbone stacking of its molecular crystal (see Fig. 5.2c), the molecular wavefunctions reside in those herringbone planes. Therefore the inclusion of only two orthogonal coordinate systems, i.e. w_{\perp}^m and w_{\parallel}^m mimicking the basis of p_y and p_z orbitals respectively (representing each molecule), can be the minimal model to describe SO coupling.

The spin transport setup is exactly the same as in the previous section (when estimating l_s for HI alone) except that now the MC simulations are performed also over an additional set of classical vectors representing the angles θ_R 's.

In Fig. 5.17 we illustrate SP vs L for the following cases, $J_H = 10^{-5}$ eV and $\lambda_{SO} = 10^{-4}$ eV (shown in dashed lines) and $J_H = 10^{-4}$ eV and $\lambda_{SO} = 10^{-4}$ (shown in bold lines) each at a high temperature of $T = 300$ K (in red) and a low temperature of $T = 58$ K (in black). Please note that this magnitude for SO coupling strength is based on the SO splitting of the rubrene crystal eigenvalues (from a DFT calculation) and also from Ref. [146]. For spin relaxation strengths corresponding to $J_H = 10^{-5}$ eV and $\lambda_{SO} = 10^{-4}$ eV, we obtain $l_s = 165.6$ nm at $T = 58$ K and $l_s = 153.9$ nm at $T = 300$ K. Note that when both HI and SO interaction are taken into account, the magnitude of l_s decreases in comparison to when there is only HI (for $J_H = 10^{-5}$ eV). Furthermore, for $J_H = 10^{-4}$ eV and $\lambda_{SO} = 10^{-4}$ eV, we obtain $l_s = 13.8$ nm at $T = 58$ K and $l_s = 10.4$ nm at $T = 300$ K. Also note that the spin transport properties of the system is now temperature dependent due to SO coupling and l_s is higher at a lower temperature. Finally, the lower bound estimates for

¹⁵See the PDOS in Fig. 5.8b and the molecular wavefunctions of the HOMO bands in Fig. 5.9.

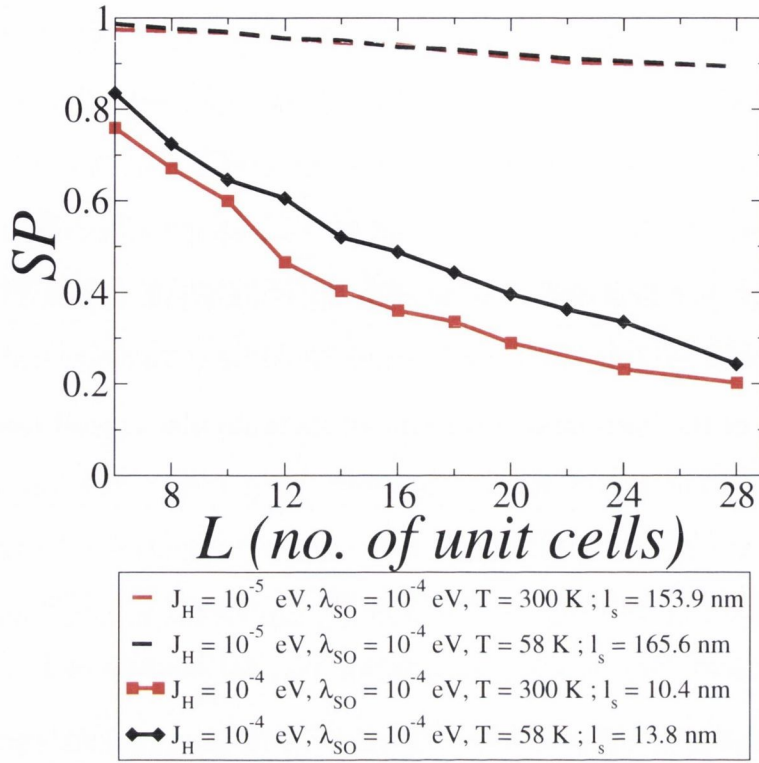


Figure 5.17: SP vs L graphs for $J_H = 10^{-5}$ eV and $\lambda_{SO} = 10^{-4}$ eV (shown in dashed lines without the data points) and $J_H = 10^{-4}$ eV and $\lambda_{SO} = 10^{-4}$ (shown in bold lines) each at a high temperature, $T = 300$ K (in red) and a low temperature, $T = 58$ K (in black). The corresponding estimates for l_s are also mentioned. We observe that the lower bound estimates for l_s (when spin relaxation is the maximum) matched really well with the experimental value in Ref. [170], i.e. $l_s(\text{exp.}) = 13.3$ nm at room temperature.

l_s agrees remarkably well with the experimental value of $l_s(\text{exp.}) = 13.3$ nm in Ref. [170] at room temperature.

We would like to point out that the spin diffusion length in our approach obtained is for crystalline rubrene. For an amorphous rubrene barrier as in the case of the experiment of Ref. [170], we may calculate l_s by assuming t , α and K to be 10% its crystalline value. However we do not find a significant change in l_s for the amorphous rubrene barrier even though the charge carrier mobility (at $T = 300$ K) decreases to 11 $\text{cm}^2/\text{V s}$ (from 58 $\text{cm}^2/\text{V s}$).

5.7 Summary

In conclusion, in this chapter we have successfully implemented a systematic method to extract the basic *ab initio* TB Hamiltonian for rubrene using MLWFs. The magnitudes of the transport observables obtained for rubrene crystal, namely the charge carrier mobility, μ , and the spin diffusion length, l_s , agree remarkably well with their experimental estimates. Thus, our procedure has the potential to be a systematic and a reliable method for obtaining the spin and charge transport properties of OSCs, in general. This may also turn out to be a very helpful tool for predicting new OSCs materials with improved spin and charge transport properties.

In the next chapter, we shall show a similar multiscale approach to compute the spin and charge transport properties for a family of triarylamine based organic nanowires, which have been recently grown through a self-assembly process.

Chapter 6

First principles study of Organic Nanowires synthesized from light sensitive triarylamine derivatives

In previous chapters we have described in detail our procedure to extract the charge and spin transport properties of rubrene molecular crystals from a multiscale theory. We have shown that the *ab initio* estimates for carrier mobility and spin diffusion length obtained for rubrene agrees quite well with their corresponding experimental estimates. A perfect test for any comprehensive theory is its transferability, i.e. can the theory be applied to other systems? We would wish to convince the readers with the work presented in this chapter, that indeed we have a affirmative answer to this question.

Let us now describe the particular system we will be investigating in this chapter. In order to motivate this we want to raise the following question: What should be the characteristics of an ideal OSC in terms of maximum performance of the corresponding solid state device? We answer this crucial question with the help of the following discussions.

An ideal OSC for optimum device performance must have exceptional charge transport characteristics. In terms of a measurable quantity this means that the carrier mobility

should be as high as possible. This situation could be achieved in an OSC, if under certain operating conditions it has a metallic type transport behavior. An experimental fingerprint of this scenario could be a linear current voltage profile for a two-probe transport device or a gapless density of states. Under these circumstances, another important issue associated with organic based device is circumvented, which is the "infamous" resistance mismatch problem. Let us explain this in a little more detail.

The skeleton of any organic photovoltaic or nanoelectronic device is an OSC material placed between metallic electrodes. A convenient way to create mobile charge carriers within the organic layer is upon charge injection (from electrodes) into the conducting molecular orbitals of the OSC. Herein, lies a very crucial problem.

When mobile charge carriers in the device travel through the metallic electrodes they face very little resistance. However once they enter into the organic layer the resistance increases massively due to the poor transport characteristics generally associated with conventional organic materials. This effect is known as the infamous resistance mismatch problem, which can entirely impede transport between the metallic electrodes and the OSC, as it creates large contact resistances. Thus the obvious solution to overcome this problem is to use organic materials with exceptional charge transport characteristics. This actually gives us a very narrow range of potential candidates, in fact just carbon nanotubes. However, in practice it is extremely difficult to isolate and process such carbon nanotubes which is quintessential to incorporate them into a device geometry.

This brings us to the second characteristic which an ideal OSC material should have. It is concerned with the fabrication of an organic solid state device like an OFET or an organic spin valve. We have seen in the beginning of the previous chapter how the different deposition techniques in the device architecture results in a contact between the organic and substrate material. The deposition technique is crucial because any irregular contacts between the organic and substrate material has a tendency to disrupt the fragile geometry of the OSC or cause chemical reactions, which can severely affect device performances. A

key development in this respect was to use flexible elastomeric PDMS substrates based on the work of Sundar *et al.* [156] which preserves the integrity of the OSC.

Another alternative would be if the organic material can be effectively grown in a self-assembled manner on top of a particular substrate material (e.g. metallic electrodes) [187, 188]. Self-assembly is an equilibrium process by which individual entities come together to form a structure, with the lowest free energy and the highest possible entropy. Thus the need of any physical deposition techniques can be entirely eliminated in a self-assembled process. The biggest advantage in any self-assembled process is that the structure of the organic material is preserved and in particular it will not be affected by the substrate.

Finally from a spintronics point of view, when a carrier travels through a particular semiconductor material there must be minimal spin relaxation events within the semiconductor. This is a point, which we also addressed previously and is the third characteristic of an ideal OSC material for spintronic application.

Presently the main drawback of OSCs which is hindering their ability to revamp the entire electronics industry is their not so improved transport characteristics, which are related to the discussions above. Recent experiments [189, 190] suggested triarylamine derivatives as a promising candidate that seems to be a solution to these issues. We will now describe these experiments in detail.

6.1 Light triggered self-assembly of supramolecular organic nanowires: the experiments

Triarylamine derivatives are well known to be an excellent hole transporting component used in organic light-emitting diodes (OLEDs) [186]. Hence, understanding the behavior of their radical-cation is crucial for designing efficient materials to be incorporated in optoelectronic devices. Over the past decades, these derivatives have continuously stimulated exciting research both theoretically and experimentally. This is primarily because of

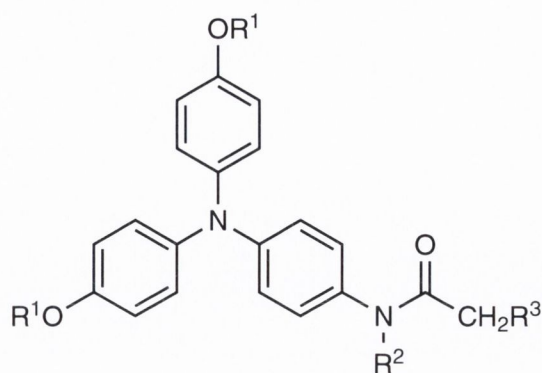


Figure 6.1: Structure of the triarylamine derivatives synthesized in Ref. [189] and investigated in this work. R¹, R² and R³ denote the position of three radicals. A list of all the molecules synthesized is provided in Table 6.1.

the general widespread drive towards incorporating OSCs into modern electronic devices, due to their low cost, low weight and mechanical flexibility. Two additional advantages of triarylamine derivatives are that they are generally also chemically inert and that their optical and transport properties can be chemically tuned.

Recently a chemistry group from Strasbourg [190, 189] showed that when certain triarylamine derivatives in chloroform solution are exposed to light, one-dimensional supramolecular (and self-assembled) nanowire structures were obtained. The particular triarylamine derivatives synthesized by the experimentalists are shown in Fig. 6.1. The key difference between the various derivatives is the possibility of choosing the three radicals, R¹, R² and R³. In particular eight different molecules have been synthesized in Ref. [189] (the same will be investigated by us). These are listed in Table 6.1. Note that the various molecules are labelled as "precursors" since they are the precursors for the synthesis of the 1D nanowires. The table also indicates whether a particular precursor leads to the actual formation of the nanowire, a process whose unique fingerprint is the disappearance of the NMR signals of the aromatic protons upon exposure to light [189].

It was suggested that the self-assembly process involves cooperative phenomena, which begin with the formation of cationic radicals induced by light and then proceed with neutralization upon charge hopping across other molecules. This leads to a supra-molecular

Precursor	R ¹	R ²	R ³	Photoactive
P1	C ₈ H ₁₇	H	Cl	yes
P2	C ₈ H ₁₇	H	H	yes
P3	C ₈ H ₁₇	CH ₃	H	no
P4	C ₈ H ₁₇	H	C ₆ H ₁₃	yes
P5	Bn	H	Cl	yes
P6	Bn	H	H	yes
P7	H	H	Cl	no
P8	CH ₃	H	Cl	no

Table 6.1: List of the nanowires precursors synthesized in Ref. [189] and investigated here. The photoactivity is established from the disappearance of the NMR signals of the aromatic protons upon exposure to light. Photo-active precursors lead to the formation of the 1D nanowires. P1 has been highlighted since P1-based nanowires have been employed in the transport experiments of Ref. [190].

polymerization of units that contain a delocalized cationic radical. More recently, the same group used one of those triarylamine-based nanowires as a channel in a two-terminal device setup [190]. They showed that such device exhibits a combination of metal-like transport characteristics and also low interface resistance, although the intrinsic transport properties of the organic nanowires, such as the mobility, were not measured.

In their setup nanotrenches were dug out on a gold substrate and filled with triarylamine (P1 derivative in Fig. 6.1) plus chloroform solution. A cartoon illustrating their device structure is shown in the upper panel of Fig. 6.2. On the left-hand side of the figure the situation in the absence of light is shown, while on the right-hand side the same is illustrated when light is switched on. The corresponding images from AFM topography and phase images are shown in the middle and lower panels respectively (Fig. 6.2), with light switched on and off. As clearly seen from the experimental results illustrated in Fig. 6.2, on exposure to light astonishing one-dimensional nanowire bundles were observed in the nanotrenches between the gold electrodes.

Furthermore, the authors also measured the conductance of their device under the two situations. Their results are summarized in Fig. 6.3. We can see in Fig. 6.3a that on exposure to light a substantial increase in conductance of the device was observed,

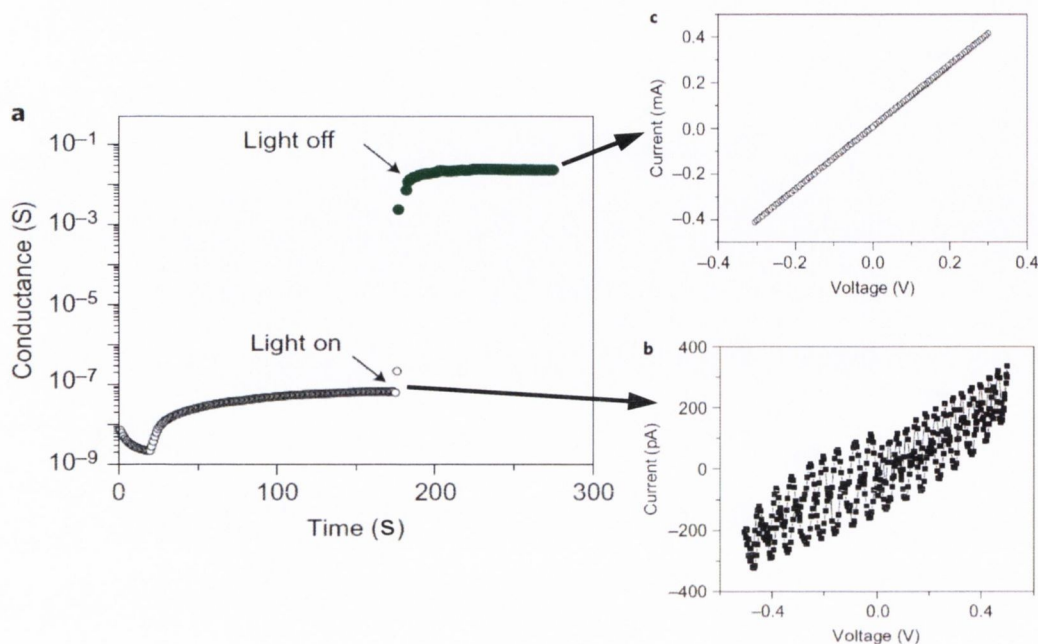


Figure 6.2: The nanodevice architecture constructed in the experimental work of Ref. [190] is shown here. The top panel shows the cartoon of the device structure which is a nanotrench dug in gold substrate. These nanotrenches are filled with triarylamine dispersed in a chloroform solution. The situation when light is switched off and when it is switched on is shown in the left and right panels respectively. The corresponding AFM topography and phase images are shown in the middle and bottom panel respectively. As clearly evident from the experimental figures when light is switched on, one-dimensional nanowire structures are formed in the nanotrenches connecting the gold platform. This now serves as electrodes in the device.

by almost six orders of magnitude. Moreover, the device exhibited Ohmic type (linear) current-voltage (IV) characteristics, which is shown in Fig. 6.3c. The corresponding non-linear IV of the device when light is switched off is illustrated in Fig. 6.3b¹. Clearly the self-assembled organic nanowire structures obtained from triarylamine solution were responsible for such enticing transport characteristics of the device.

In this chapter we report on state of the art DFT calculations on the structural, elec-

¹Notice that the actual current through the device when light is switched on, also increases by six orders of magnitude.

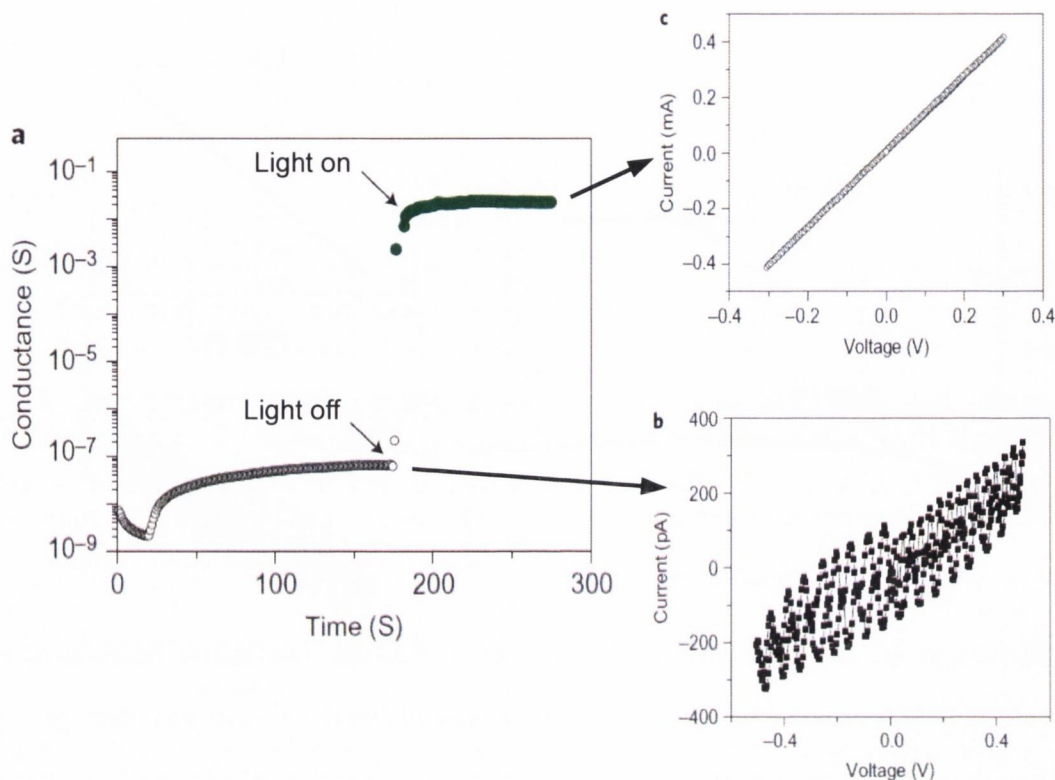


Figure 6.3: The conductance of the nanodevice fabricated from triarylamine derivative is shown in a), in the situation when light is switched on and when it is off. The corresponding IV characteristics are shown in b) and c) (note the different current scales). As clearly seen from the above figures, when light is switched on both the conductance and the current through the device increases six folds. Moreover, the device exhibits a linear (metallic like) IV characteristic (light switched on). The figure is reproduced from the experimental work of Faramarzi *et al.* [190].

tronic and transport properties of such triarylamine-based nanowires, with the aim of relating the electronic characteristics of the triarylamine precursors to the self-assembly process and to the nanowires mobility. We begin by looking at the derivatives proposed in Ref. [189] in their gas phase and provide a detailed analysis of the electronic structure of these precursors and their intramolecular interactions. As reference material we also include calculations for the basic triphenylamine (TPA) molecule, for which both theoretical and experimental data are available.

We then move to investigating the intermolecular interactions and the transport char-

acteristics of the nanowires. Unfortunately, no crystallographic information were available for these triarylamine based organic nanowires. Therefore we adopted two different approaches. The first is the semi-classical Marcus theory [191] to investigate the transport properties of defective nanowires. This procedure relies on the internal reorganization energy and on the transfer integrals between molecules dimers. The Marcus theory approach has been used to calculate hole mobility in oligothiophenes [192] and pentacene [193], yielding reasonable values in agreement with experimental trends. The second approach, used only for the case of ultrapure nanowires, is based on the linear response Kubo Formula [194] and Monte Carlo sampling to extract the charge carrier mobility. In this case a few non-local phonons modes, treated at the classical level are introduced. For both the approaches all the parameters of the theory are extracted from DFT, so that our estimates for the mobility are those obtained by taking into account the detailed electronic structure of the nanowires. It is important to note here that Marcus theory and the linear response Kubo approach have two different limits of validity. The first is constructed for hopping conductance while the second performs best for band-like transport. Here we used both, since we do not have any direct experimental evidence of the actual transport mechanism or the concentration of defects in the nanowires. Finally in the last section of this chapter we will investigate the spin transport characteristics for the organic nanowires using a procedure similar to the one we have used in the previous two chapters. It is actually the mechanism of carrier transport through these organic nanowires which led us to propose to use them as spin transporting media.

6.2 Charge transport properties

System and computational methods

First principles calculations are performed for all the derivatives in the gas phase and for TPA, chosen as a reference system. Since our interest is in hole transport, we restrict

the discussion to that of the positively charged derivatives. Their molecular geometry (in the ground and single cationic state), the energy level of the Highest Occupied Molecular Orbital (HOMO) and the Lowest Unoccupied Molecular Orbital (LUMO), the HOMO-LUMO gap, the ionization potential (IP), the total density of states (DOS) and the reorganization energy are computed by using DFT [20, 21]. The B3LYP hybrid functional [195], which is known to be suitable for most molecular systems is adopted together with a 6-31G* basis set [221].

In order to evaluate the intermolecular interactions to be input in Marcus theory, we construct molecules dimers from the B3LYP optimized monomers, we calculate their binding energies (BE) and then estimate the transfer integral (TI) as a function of the intermolecular distance along the nanowire axis (z -axis). The mobilities are then computed at the optimum dimer distance (the nanowire lattice parameter), which is at the BE minimum. While B3LYP-DFT usually describes well electronic properties like the IP, the HOMO-LUMO gap, and molecular geometries, it does not describe in a satisfactory way weak interactions, in particular those of dispersive nature. These include van der Waals (vdW) and π - π interactions, which in turn play an important role in determining the structure of organic materials [192]. As a test, we calculate the BE and TI for the TPA dimer model system by using three additional DFT functionals: the long-range-corrected version of B3LYP (CAM-B3LYP) [197], the meta-hybrid generalized gradient approximation (GGA) M06-2X functional [198] and the Grimme's functional including vdW dispersion [43]. Then, by using the functional that returns the lowest BE for TPA, we calculate the BE and TI for all the precursors and estimate the values of their mobilities at the optimal intermolecular distance.

Finally, we move to investigate in detail the charge transport characteristics of such organic nanowires as a function of temperature. DFT calculations are first performed on a one-dimensional nanowire geometry, by using the optimized B3LYP monomer structure and maintaining the distance between the monomers at that of the BE minimum for the

dimer. We then obtain a complete band structure for the organic nanowires and from the dispersion of its valence band we extract an elementary tight binding (TB) Hamiltonian. This includes a static term and a Su-Schrieffer-Heeger-type interaction [196], which relates the hopping integrals with the molecular displacements in the nanowire, i.e. it introduces carrier-lattice coupling. The parameters for such an interaction term are evaluated with a simple finite difference method (see Section 6.2.3). The charge carrier mobility as a function of temperatures is then calculated by using the linear response Kubo formula, evaluated with Monte Carlo sampling.

Ending this section we report the technical details of the DFT calculations performed in this work. All the simulations for the single molecules in the gas phase are performed with the Gaussian09 suit [199], using the 6-31G* basis set. The same package is also employed to evaluate the electronic structure of the dimers, then used for the semi-classical Marcus theory. Relaxation with Gaussian09 is carried out with the Bery algorithm [200] until the forces are smaller than 2×10^{-5} Hartrees/Bohr. After relaxation the phonon spectrum is computed and the vibrational frequencies are inspected. The absence of imaginary frequencies confirms that the energy minimum is reached.

The Quantum Espresso [201] code is used for the electronic structure of the organic nanowires. Spin polarized DFT calculations are performed at the GGA level as implemented by Perdew, Burke and Ernzerhof [35] and with the semi-empirical implementation of vdW interactions by Grimme [43]. In all calculations we employ Vanderbilt ultra-soft pseudopotentials [202]. Convergence is tested over the total energy and an accuracy lower than 1 mRy is achieved by a plane-wave cut-off 30 Ry. A $5 \times 5 \times 5$ Monkhorst-Pack grid with a Gaussian broadening of 0.01 Ry is used for sampling the reciprocal space. Additional details about our calculations will be provided later on whenever necessary. Also in this case geometrical relaxation is performed by standard conjugate gradient method.

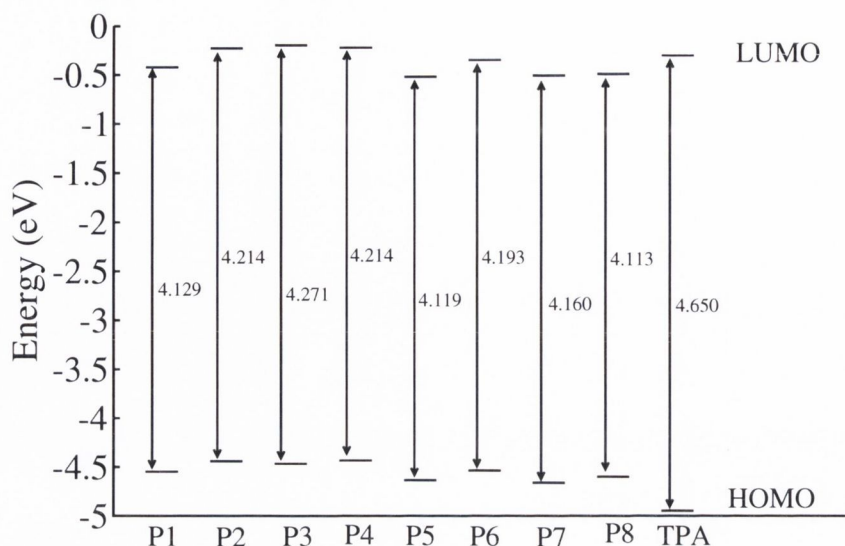


Figure 6.4: Energy level diagram of the frontier molecular orbitals for all the precursors and the TPA. Here we report the Kohn-Sham eigenvalues calculated for the neutral molecules with the B3LYP hybrid functional.

6.2.1 Single molecules in the gas phase

All the precursors and the TPA molecule have been optimized in their neutral and cationic states using the B3LYP hybrid functional. We start our analysis by examining the energy levels of the precursors' frontier molecular orbitals. Fig. 6.4 shows the Kohn-Sham HOMO and LUMO energy levels as well as the HOMO-LUMO gap for all the precursors and TPA. It is clear from the figure that, whether light active or not, there is no remarkable difference in the position of the energy levels of the frontier molecular orbitals, meaning that the different radicals that uniquely characterize a given precursor (R^1 , R^2 and R^3) have little effect on that region of the quasi-particle spectrum. Note that our calculated values for the TPA (our reference) agree well with existing literature, for instance with those reported in Ref. [203].

Next we calculate the IP and the hole extraction potential (HEP) of all the precursors. These are important parameters to characterize the molecules hole-transport ability. Both IP and HEP are well defined quantities obtainable by DFT in terms of total energies differences for the molecule in different charging states and positions over the potential

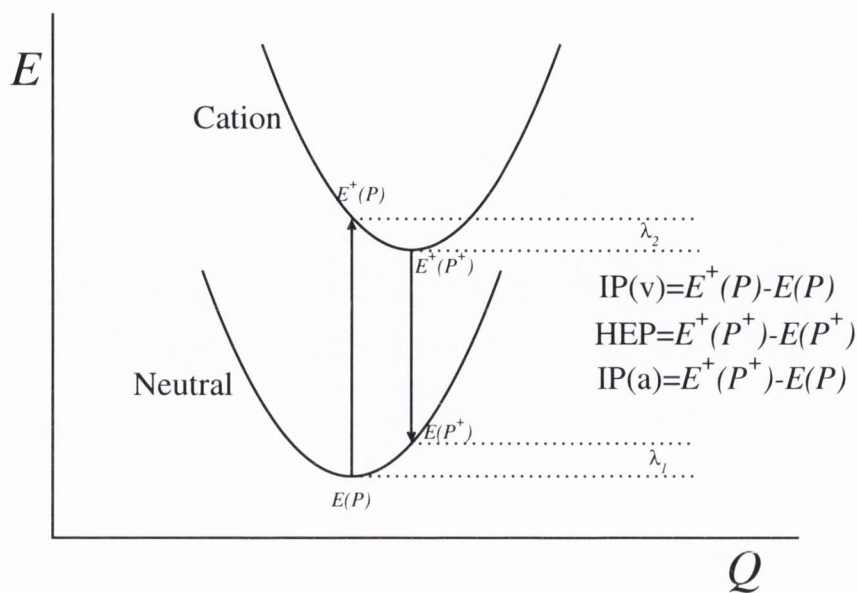


Figure 6.5: Schematic diagram of the potential energy surface, E , of a neutral and cationic radical precursor as a function of reaction coordinate, Q . $E^+(P^+)$ and $E(P)$ are the energies of the cationic radical and the neutral precursor in their lowest energy geometries, respectively. In contrast $E^+(P)$ [$E(P^+)$] denotes that of the cationic radical [of the neutral precursor] obtained at the geometries of the neutral precursor [cationic radical]. The definitions of the various IP's and of the HEP are also introduced.

energy surface (see diagram in Fig. 6.5). Thus, the vertical IP, $IP(v)$, is calculated as the energy difference between the neutral molecule and the cationic radical at the geometry of the neutral configuration. Likewise the HEP is the same energy difference, but now calculated at the geometry of the cationic state. Finally, the adiabatic IP, $IP(a)$, is obtained as the energy difference between the neutral and single positively charged state, both calculated at their equilibrium geometries.

The calculated IP's and HEP for all the precursors are shown in Table 6.2. We find the vertical IP's in the range 5.69-6.01 eV, the adiabatic ones in the range 5.54-5.88 eV, while the HEP's distribute over the interval 5.40-5.75 eV. In the case of $IP(v)$, as expected, we find good consistency between our total energy calculations and the Kohn-Sham HOMO levels reported in Fig. 6.4, i.e. we find that those precursors showing deep HOMO energies also display a deep $IP(v)$. In particular the energy order of the various Kohn-Sham HOMO's is the same as that of the $IP(v)$'s. Note that the calculated $IP(v)$'s

are not exactly matching the HOMO levels and that the two differ by about 1 eV, with the quasi-particle energies being systematically more shallow.

In general in DFT one expects the Kohn-Sham HOMO energy to correspond to the system vertical IP [31, 23]. This condition however is not satisfied by approximated exchange and correlation functionals because of the self-interaction error, and the HOMO levels are usually much more shallow than the true IP's. The B3LYP functional partially removes the self-interaction error. This removal however is not complete and the residual self-interaction is probably responsible for the differences. In any case, the overwhelming result is that there is almost no dependence of the charge extraction energies (IP's and HEP) on the nature of the precursors, meaning that the different radicals have little effect on the ability of a molecule to transfer electrons/holes. Further support to this conclusion is the fact that the IP's for TPA are within 0.5 eV from that of any precursors, indicating that the TPA unit is the molecular block responsible for the charge transfer. Finally, note that our calculated IP value for TPA is not only consistent with other theoretical works [203, 204, 205] but also close to the experimental data [206].

Precursors	Photoactive	IP(v) (eV)	IP(a) (eV)	HEP (eV)	λ_{int} (eV)	d_0 (Å)
P1	yes	5.81	5.66	5.52	0.30	0.39
P2	yes	5.71	5.57	5.42	0.30	0.38
P3	no	5.73	5.57	5.42	0.32	—
P4	yes	5.69	5.54	5.40	0.29	0.44
P5	yes	5.88	5.69	5.52	0.36	0.45
P6	yes	5.79	5.60	5.42	0.37	0.51
P7	no	6.01	5.88	5.75	0.26	—
P8	no	5.80	5.67	5.53	0.28	0.47
TPA	—	6.41(6.88)	6.35	—	0.12	0.60

Table 6.2: DFT-B3LYP estimates of the ionization potentials, IP(v) and IP(a), the hole extraction potential, HEP, the internal reorganization energy, λ_{int} , and the localization radius, d_0 , for all the precursors and for TPA. In the case of TPA the value reported in brackets is the experimental IP from Ref. [206]. Note that we report d_0 only for those precursors for which a good exponential fit of the transfer integral as a function of the dimer distance is obtained. We remind here that P3, P7 and P8 are not photo-sensitive, i.e. they do not form the nanowires.

We then examine the DOS of the precursors in their gas phase. Interestingly the main characteristics of the DOS are qualitatively similar for all the precursors, so that here in Fig. 6.6 we report only the illustrative case of the P1 molecule². The figure reports the DOS for both the neutral state (top panel) and the cation radical (bottom panel), together with the isosurface plots of the charge density of the different molecular orbitals. Note that the results reported here are for GGA, whose only difference from B3LYP for this molecule is in the quantitative position of the energy levels (the order and the symmetry is the same). Note also that in the figure the molecular DOS has been artificially broadened for visualization purposes.

From the DOS it is clear that the HOMO's of both the neutral molecule and the cationic radical are highly localized on the N atom of the TPA central unit. This means that the ionization process simply involves the extraction of an electron from such double occupied state, without affecting the rest of the molecule. Indeed a close analysis reveals that the symmetry of the HOMO-1 and of the LUMO is somehow different for the two charging states, indicating level reorganization upon ionization. The same, however, is not true for the HOMO, whose only difference in the two charging states lies in the occupation. In fact we find that the HOMO of all the precursors investigated here is essentially the same of that of the widely studied TPA isolated molecules [207, 203, 204], namely it is formed by the $2p$ orbitals of the central N ion.

In closing this section we wish to put our results in the context of the photo-induced self-assembly formation of the nanowires. The mechanism for the nanowires formation proposed in Ref. [189] is that, under exposure to light, initially a small amount of positively charged radical (6 over 1000 molecules) is formed. Our local DOS calculations point out that the positive charge in the radical is localized on the central N atom, as speculated in the original experimental work. According to the mechanism proposed, the positively

²The one for which transport has been measured.

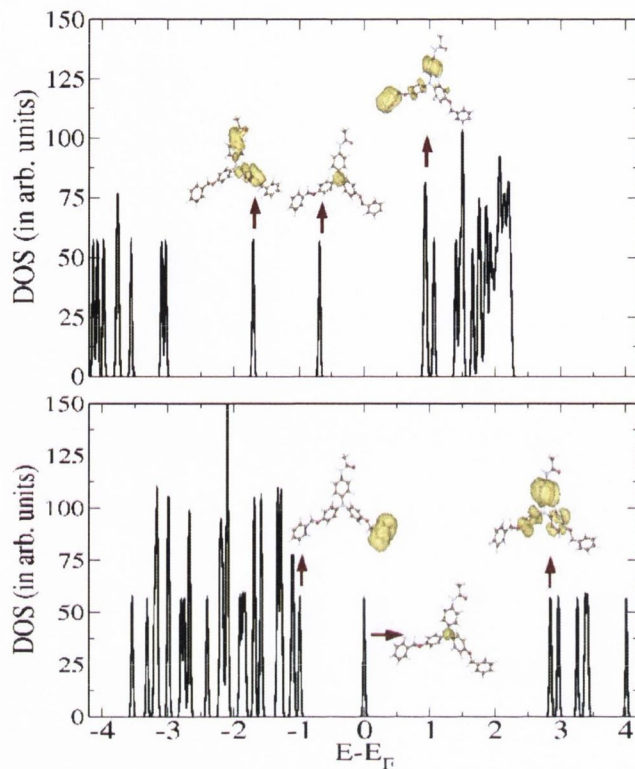


Figure 6.6: The DOS of the P1 molecule and the P1⁺ radical in the gas phase, as calculated from DFT-GGA, are shown in the top and bottom panels, respectively. Charge density isosurfaces (local DOS) for the HOMO−1, HOMO and LUMO levels are also displayed. The DOS has been artificially broadened for visualization purposes. Note that the HOMO of both the neutral molecule and the cation radical have identical symmetry with charge density distribution strongly localized over the central N atom of the central TPA unit. The qualitative features of the DOS and the orbitals symmetry of all precursors are very similar.

charged radical comes into contact with a neutral molecule and transfers its charge. This process continues until 1D triarylamine-based bundles of nanowires are formed. Our first principles analysis of the energy levels and of the nature of the frontier molecular orbitals for all the triarylamine derivatives, does not provide any evidence that may distinguish the light active precursors (which self-assemble into supra-molecular organic nanowires) from those, which are not light active. In other words we do not find any fingerprint in the electronic structure of the precursors, which can help us to identify the conditions for the self-assembly. Thus we conclude that the self-assembly process may be initiated by factors not completely intrinsic to the molecular precursors. For example it may be

affected by the strength of the oxidizing agent used in the solvent, i.e. by the interaction of the different precursors with the solvent.

6.2.2 Charge transport properties from Marcus theory

In the weak coupling limit, charge transfer between molecules is described by Marcus theory [191], and the calculated charge transfer rates can be used for evaluating the mobility of molecular crystals. Under the assumption that the temperature is sufficiently high so that vibrational relaxation is fast, Marcus' formula for the hole transfer rate, k_{CT} , reads [191]

$$k_{\text{CT}} = \left(\frac{\pi}{\lambda k_{\text{B}} T} \right)^{1/2} \frac{J^2}{\hbar} \exp \left(-\frac{\lambda}{4k_{\text{B}} T} \right), \quad (6.1)$$

where T is the temperature and k_{B} the Boltzmann constant. In equation (6.1) the two materials-specific quantities are the charge reorganization energy, λ , and the transfer integral, J . Various approaches have been put forward in literature to estimate these parameters (see for instance Ref. [208]).

The most popular method for evaluating the transfer integrals for a hole transporting pair of identical molecules (of equivalent symmetry) is rooted in Koopmans' theorem [24], which establishes that the HOMO of the neutral molecule is the negative of the ionization potential. This, together with the assumption that the geometry of the ground state of the neutral molecule is a good approximation of the geometry at the point of charge transfer [209], allows one to evaluate the absolute value of the transfer integral, $|J|$, as half of the energy difference between the HOMO and HOMO-1 levels of a dimer of molecules in its closed-shell configuration. In practice the idea is that, in the weak coupling limit, the energy separation between the HOMO and HOMO-1 levels of the dimer is simply the energy split between the bonding and anti-bonding orbitals derived from the HOMO of the individual molecule. This quantity is largely kinetic and as such it is relatively independent from the actual position of the HOMO level, i.e. from how the specific exchange and correlation functional reproduces a correct quasi-particle spectrum. In

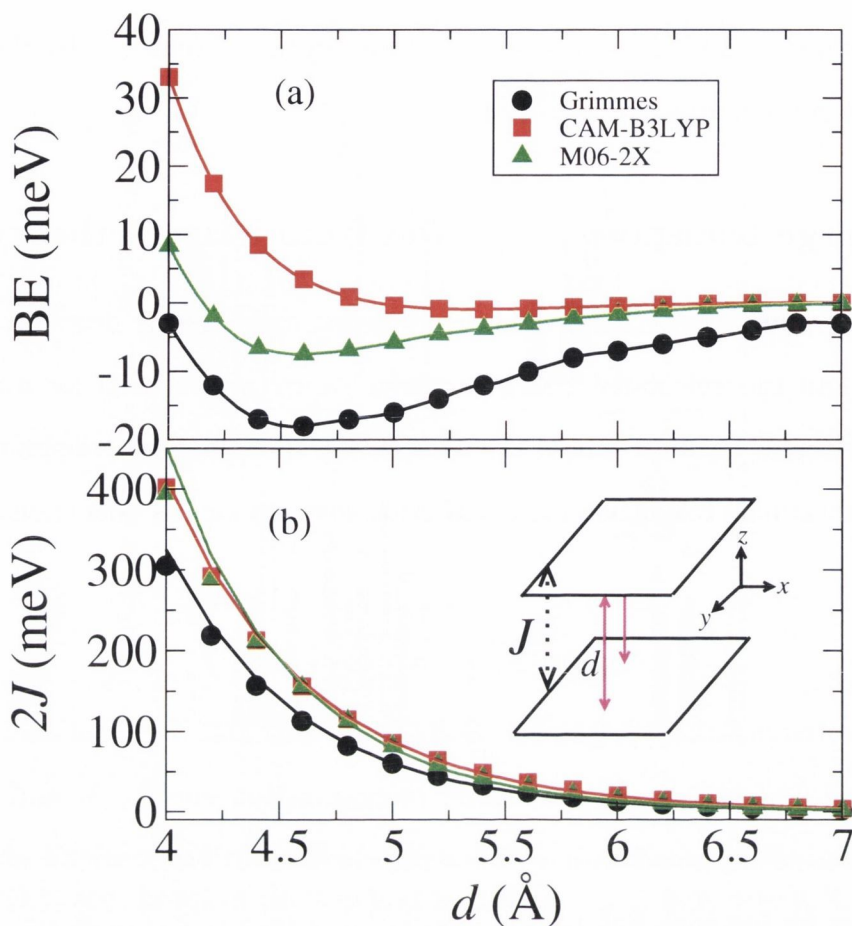


Figure 6.7: Variation of the (a) binding energy, BE and of the (b) charge transfer integral of TPA calculated by using different DFT functionals. The solid line in (b) are exponential fits of the data.

other words, one expects that it should not be important how a particular exchange and correlation functional quantitatively satisfies Koopmans' theorem as long as the HOMO has the correct symmetry. Because of its simplicity this approach has been widely used in literature to estimate J for organic molecules [209, 210, 192, 211, 212], although caution should be taken when the dimer is not co-facially stacked [213] and corrections should be included [214].

The reorganization energy deserves additional discussion. This contains two parts, namely an internal, λ_{int} , and an external, λ_{ext} , one. The internal contribution is intrinsic of the two molecules exchanging charge and accounts for the change in molecular geometry

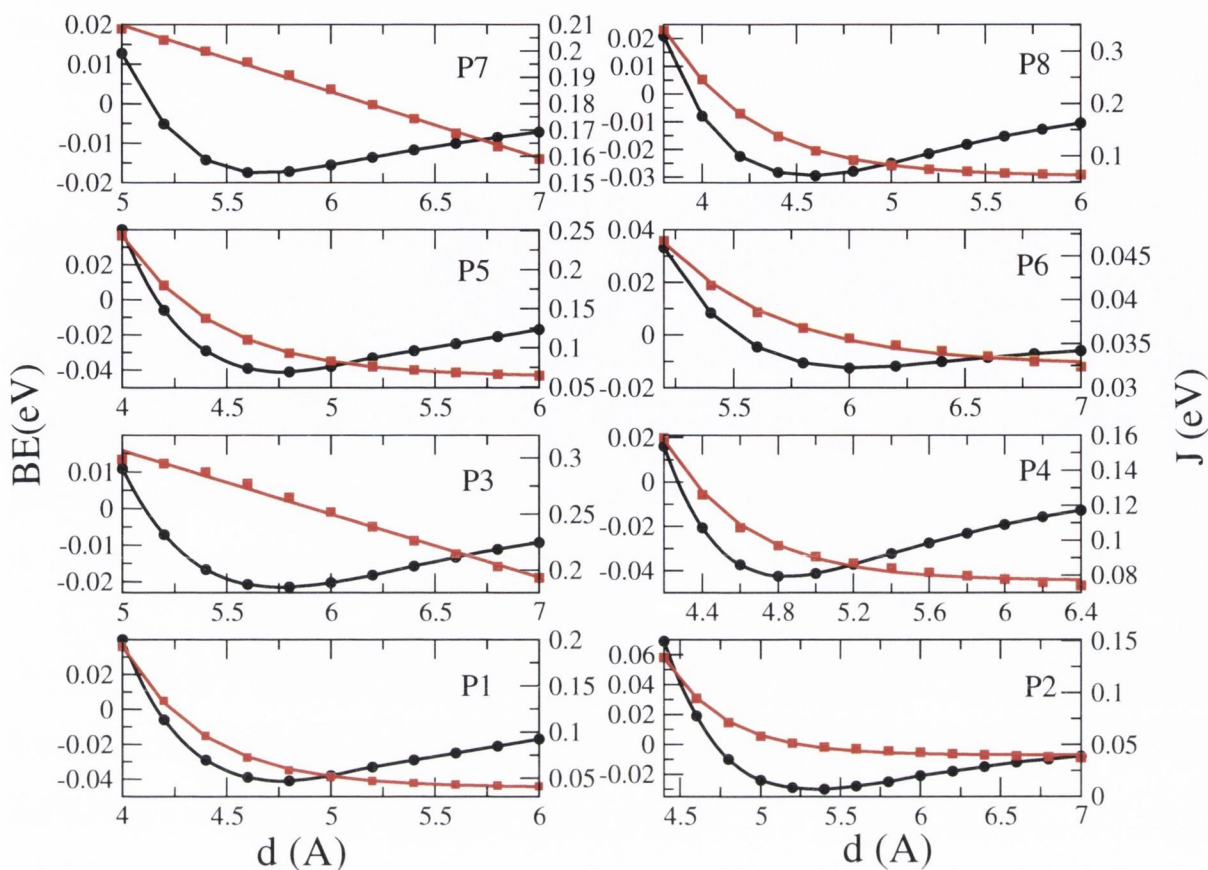


Figure 6.8: Binding energy (solid circles and left-hand side vertical axis) and charge transfer integrals (open squares and right-hand side vertical axis) for all the precursors calculated at the geometry provided by the Grimme’s functional. The solid black lines interpolate the binding energies while the red dashed lines are an exponential fit of the transfer integrals.

corresponding to the charge transfer, i.e. it accounts for the different geometries of the molecule in different charging states. In contrast, λ_{ext} describes the change in electronic polarization of the surrounding molecules associated to the charge transfer process. Such external contribution is not straightforward to calculate [208]. However for molecular crystals λ_{ext} is usually neglected since it is considerably smaller than λ_{int} [212]. The internal reorganization energy can then be written as the sum of two terms [214]: (1) the difference between the total energy of the neutral precursor at its equilibrium geometry and that at the geometry of the radical ion, and (2) the difference between the energy of the radical ion at its equilibrium geometry and that at the geometry of the neutral

configuration. By taking the definitions introduced in the diagram of Fig. 6.5 we can write

$$\lambda_{\text{int}} = \text{IP}(\text{v}) - \text{HEP} . \quad (6.2)$$

Since both IP and HEP for all the precursors are similar, we do not expect λ_{int} to differ much across the various precursors, as demonstrated in Table 6.2. Also for this quantity our calculated value for TPA compares well with those reported in previous works [203, 204, 205].

Let us now move to computing the J 's. First we need to calculate the equilibrium separation, d_{eq} , of the various dimers, i.e. to compute the dimer BE as a function of the separation, d , between two identical monomers. The geometry of each molecule in the dimer is optimized by using the B3LYP hybrid functional and the 6-31G* basis set, with the dimer considered in this work having a co-facial orientation. This means that the planes defined by the three bonds proceeding from the central N atom on each molecule are parallel to each other, with the two N atoms situated on a vector normal to their planes. This simulates a wire in which the central N atoms of the TPA unit are co-axial. Even though J may strongly depend on the type of crystal packing, the co-facial orientation is usually considered as a geometry of interest, having a high symmetry reference point and being an upper limit for the electronic coupling [216]. Furthermore a geometry of this type has been suggested for the nanowires under investigation by our reference experiments [189, 190].

Note that, in the weak coupling limit, one expects the J 's to vary exponentially with d [209]

$$|J| \sim \exp(-d/d_0) , \quad (6.3)$$

where d_0 is a constant called the localization radius. This decay is well understood and attributed to the exponential decay of the intermolecular overlap between the orbitals when the two monomers are pulled apart. In our analysis we will test such property, by

starting with the case of TPA.

The BE and the transfer integral of TPA calculated by using different DFT functionals are presented in Fig. 6.7. We note here that the BE is obtained by neglecting the basis set superposition error, since it has a negligible contribution [215]. We first determine the dimer optimum distance and then we examine J around this region. As expected J decays exponentially with d and the values of d_0 are 0.60 Å, 0.64 Å and 0.57 Å, when the BE is evaluated respectively with the Grimme, the CAM-B3LYP and the M06-2X functionals. The figure shows that only Grimme and M06-2X bind the dimer, while for CAM-B3LYP the binding energy does not present a minimum with d . Furthermore, we notice that although the equilibrium intermolecular distance is predicted rather consistently for the two functionals, Grimme displays a significantly larger binding energy than M06-2X. This is by the virtue of explicit inclusion (in Grimme) of pairwise van der Waals interactions. With these considerations at hand we have decided to optimize the dimer intermolecular distance for all the precursors by using the Grimme functional. However, we then calculate the TI's by using both Grimme and B3LYP (at the geometry obtained with Grimme), so that we can compare results from functionals that satisfy the Koopmans' theorem at a different level of accuracy.

As for the TPA, also for all the nanowires precursors we consider a co-facial arrangement of the dimers. We note that performing a rotation of one of the two molecules in the dimer around the axis joining the two N atoms gives approximately the same binding energy as that of a perfectly co-facial geometry. This further supports the idea that the co-facial geometry is indeed representative for the charge transfer, which interests by large the N atoms only. In Fig. 6.8 we present the BE and J 's as a function of the N-N distance for all the precursors. Clearly in all cases the dimer can form and one can identify an equilibrium intermolecular distance. This is true also for P3, P7 and P8, that experimentally are found not to be photo-sensitive, i.e. they do not lead to the nanowires formation.

Precursors	d_{eq} (Å)	J_{Grimme} (meV)	J_{B3LYP} (meV)	μ (cm ² /Vs)
P1	4.8	29.54	34.03	0.13
P2	5.4	24.18	24.61	0.11
P3	5.8	132.68	134.25	3.10
P4	4.8	48.72	51.88	0.40
P5	4.8	46.99	53.92	0.17
P6	6.0	17.86	18.14	0.04
P7	5.6	97.93	99.06	3.11
P8	4.6	55.05	64.31	0.53

Table 6.3: Table comparing the estimated J values at the minimum of the BE calculated by using the Grimme and the B3LYP functional for all the precursors. Note that in both cases the dimer optimal geometry and d_{eq} are that obtained with Grimme, since B3LYP does not bind the dimer.

Moving to the J 's we notice that for all photo-sensitive precursors (P1, P2, P4, P5 and P6) there is a clear exponential decay of J as a function of the dimer intermolecular separation, while this is not the case for the non-photo-sensitive ones (P3 and P7), for which the decay is linear. The precursor P8 remains outside this picture, since it is not photo-sensitive and yet the decay of J is exponential. As such, also the transfer integrals do not seem to provide a clear way to differentiate photo-sensitive from non-photo-sensitive precursors. Finally, in Table 6.3, our estimated J values calculated at the minimum of the BE (Grimme) are tabulated for all the precursors using the Kohn-Sham spectrum obtained either with the Grimme or the B3LYP functional. Notably there is a rather good agreement between the two functionals, strengthening the argument made before about the kinetic nature of the transfer integrals. Intriguingly we find the largest three transfer integrals for the three precursors known not to form nanowires, while the values for all the others are rather similar ranging from ~ 18 meV to ~ 50 meV. Importantly we do not find any particular correlation between the equilibrium dimer intermolecular separation, d_{eq} , and the magnitude of the transfer integral, apart for P6, which has the smallest J and the largest d_{eq} . This indicates that the fine details of the electronic structure of the precursors determine the molecule ability to exchange charges.

Finally, we are now in the position to evaluate the mobilities of the impure (defective) nanowires⁷. The charge carrier mobility, μ , can be estimated by using the following expression [208, 217]

$$\mu = \frac{e}{k_B T} d_{\text{eq}}^2 k_{\text{CT}}, \quad (6.4)$$

where e is electron charge. Having calculated both the λ_{int} 's (Table 6.2) and the J 's (Table 6.3) for all the precursors, the estimated mobilities at room temperature (300 K) are reported in Table 6.3. Notably, with the exception of P3 and P7, which anyway do not self-assemble, the mobilities are all around some fraction of cm^2/Vs , with the maximum value being for P4 ($0.40 \text{ cm}^2/\text{Vs}$) and the minimum for P6 ($0.04 \text{ cm}^2/\text{Vs}$). Such similarity between the mobilities is expected in the light of the fact that the transport occurs through the central N atom of the TPA unit, i.e. through a molecular orbital common to all precursors and largely independent from the particular radicals which characterize the precursors. This reflects in similar reorganization energies and, although to a smaller degree, transfer integrals, and therefore in similar mobilities. These estimates for charge carrier mobility are within the general limit beyond which charge transport in a particular semiconductor material cannot be described by a hopping mechanism [220]. It is because of the presence of defects or impurities in the nanowires that the charge carrier is localized and therefore the speed of sequential charge hopping is reduced. In general, the use of Marcus formula to describe the carrier transport mechanism in (pure) OSC must be utilized with a great deal of caution [220, 116].

6.2.3 Charge transport properties from linear response theory

As an alternative to Marcus theory we now reevaluate the mobility of P1 by linear response theory with parameters extracted from DFT. This approach is valid for ultrapure organic nanowires. The first task consists of writing an adequate TB Hamiltonian for the nanowires including electron-phonon coupling to a few relevant vibrational modes. We begin by calculating the electronic structure of the nanowires. This is obtained by placing

a single molecule, whose geometry has been optimized by DFT-B3LYP (the same of the previous section), in an orthorhombic unit cell with lattice parameters a , b and c . In particular we take c as the intermolecular separation for the dimer calculated in the previous section and $a, b \gg c$ (see Table 6.3). We verify that further crystal relaxation does not change significantly the value of c (the exchange and correlation functionals used to optimized the dimers and the 1D nanowires are the same), while considering $a = b = 63.5 \text{ \AA}$ ensures that there is no interaction between the image cells in the plane, i.e. that there is no interaction between adjacent nanowires. The spin polarized DFT calculations are performed with Quantum Espresso and the Grimme's exchange correlation functional [43] and the internal coordinates of the atoms inside the unit cell are relaxed until the forces are smaller than 10^{-4} Ry/\AA .

Fig. 6.9 displays the band structure of the nanowire constructed from the P1 molecules (henceforth referred to as the nanowire P1) plotted along the 1D Brillouin zone, $\Gamma - Z$. In the figure we report data for c being the equilibrium lattice constant, $d_{\text{eq}} = 4.8 \text{ \AA}$, and for an extremely compressed configuration, where $c = 3.18 \text{ \AA}$. This allows us to trace the band structure as the lattice parameter changes. Importantly we find that the band relative to the HOMO is always well separated from the rest of the valence manifold even at the compressed lattice parameter. This means that there is little interaction among the HOMO-derived band and the rest of the valence, so that a single-site TB effective Hamiltonian appears appropriate for the problem of hole conduction. A different situation appears for the conduction part of the band structure, which is characterized by a number of closely spaced bands presenting crossing.

In any case, we map the HOMO-related band onto the following TB Hamiltonian

$$\hat{H}_{\text{HOMO}} = \sum_{ij} [t_{ij} + \alpha(q_i - q_j)](c_i^\dagger c_j + h.c.) + \sum_{ij} \frac{1}{2} K (q_i - q_j)^2, \quad (6.5)$$

where $t_{ij} = t$ denotes the hopping integral between the molecules in the wire and extends only to nearest-neighbor molecules, α is the carrier-phonon coupling and K the stiffness

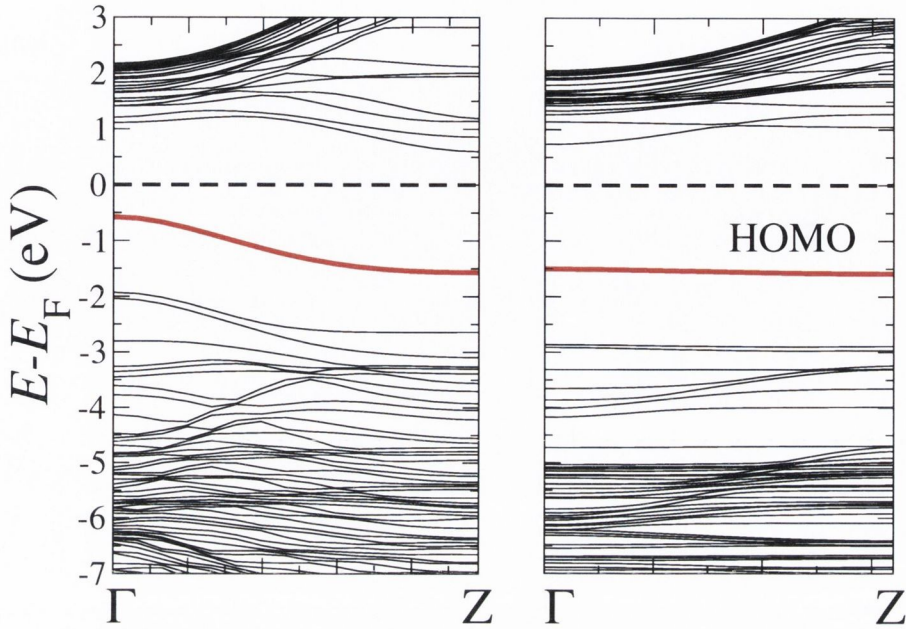


Figure 6.9: Band structure of a nanowire obtained by repeating periodically the P1 unit, plotted over the 1D Brillouin zone. Here we present data for the equilibrium lattice parameter $c = d_{\text{eq}} = 4.8 \text{ \AA}$ (right panel) and for a strongly compressed structure $c = 3.18 \text{ \AA}$ (left panel). The nanowire geometry keeps the molecules in a co-facial arrangement and the distance between the N centers is the same equilibrium distance found for the corresponding dimer (see Table 6.3). A single-orbital per site TB Hamiltonian, where the relevant orbital is the HOMO, can be extracted from the band structure by fitting the HOMO-derived band (in red). The dashed horizontal line denotes the Fermi level, which is simply placed in the HOMO-LUMO gap.

constant. Here c_i^\dagger (c_i) is the creation (annihilation) operator for a charge carrier at the i -th site (molecule), while q_i is a classical vector describing the displacement of the i -th molecule of the nanowire from its equilibrium position.

The magnitudes of the hopping integrals, t , can be simply obtained from the dispersion of the HOMO-derived band (Fig. 6.9) as $t = \Delta/4$, where Δ is the bandwidth. For the P1 nanowire at $c = d_{\text{eq}}$ (right panel Fig. 6.9) we extract $t = 25.0 \text{ meV}$, which is in close agreement with the value calculated for the corresponding dimer (29.5 meV from Table. 6.3).

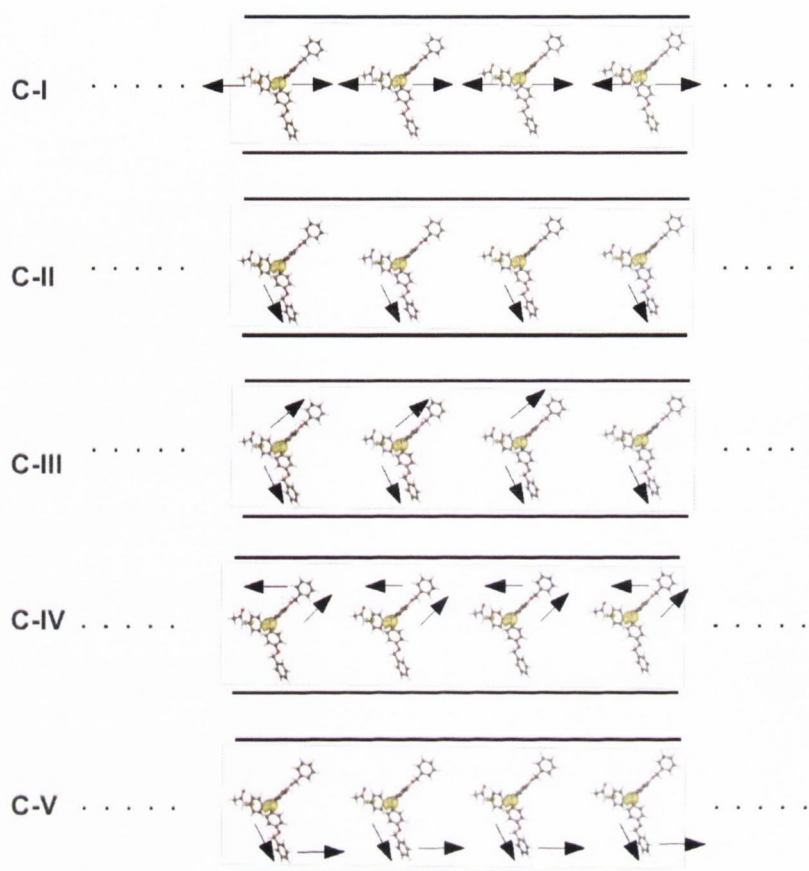


Figure 6.10: Schematic illustration of the molecular displacement of the different phonon modes for which the carrier-phonon coupling, α , and the stiffness constants, K , have been calculated. The picture is for the P1 nanowire. The various modes are labelled as C-I to C-V and only the C-I mode is considered when estimating the charge carrier mobility.

The parameters of \hat{H}_{HOMO} related to the coupling to the vibrations, namely α and K , can be evaluated from finite difference. In practice we displace the molecule along a particular direction \mathbf{r} (the phonon mode displacement vector) and then compute $\alpha_{\hat{\mathbf{r}}} = \frac{\delta t}{\delta \mathbf{r}}$ and $K = \frac{1}{\mathbf{r}} \frac{\delta E}{\delta \mathbf{r}}$, where E is the DFT total energy. In order to estimate the mobility we consider a single acoustic phonon mode constructed by displacing the molecules along the nanowire axis with respect to each other. This is illustrated in Fig. 6.10 and referred to as the C-I mode. We expect such particular phonon mode to be the most significant in governing charge transport through the organic nanowire because the motion of the molecules along the nanowire axis facilitates the overlap between the density of the local-

ized carriers thereby enhancing the charge transfer, a mechanism proposed in the original experimental work [189] to justify the excellent transport properties measured. For the P1 nanowire and the C-I mode we obtain $\alpha/t = 1.585 \text{ 1/\AA}$ and $K/t = 1.530 \text{ 1/\AA}^2$.

Mode	$\alpha/t \text{ (1/\AA)}$
C-I	1.585
C-II	0.000
C-III	0.067
C-IV	0.501
C-V	0.370
Rubrene	0.109

Table 6.4: Table showing the calculated values for α/t along the various phonon modes for the P1 nanowire. The labels for the phonons are those introduced in Fig. 6.10. In the table we also report the result for the rubrene crystal as reference.

Together with the C-I mode we have also evaluated α/t for other relative molecular displacements, as depicted in Fig. 6.10 (C-II to C-V). The results are listed in Table 6.4. In the same table we report as a comparison also α/t for the mode most relevant to the longitudinal transport in rubrene, the organic crystal displaying the overall highest mobility (previous chapter). In general we find the electron-lattice coupling along the C-I displacement to be significantly larger than that of all the others, and also of the analogous longitudinal mode in rubrene. This justifies our approximation of considering only the C-I mode when evaluating the mobility. It also tells us that the electron-lattice coupling in such nanowires is strong so that the mobility should display a rather strong temperature dependence.

We finally turn our attention to the mobility. This is calculated as a function of temperature using the linear response Kubo formula evaluated over a Monte Carlo sampling of the molecular displacements [in Eq. (6.5)]. The dynamical quantities entering the Monte Carlo scheme are the longitudinal displacements of the molecules (TB sites), which are treated as a continuous variable [180]. After equilibration the charge carrier mobility is evaluated using the Kubo formula [194] averaged over 100,000 Monte Carlo configurations.

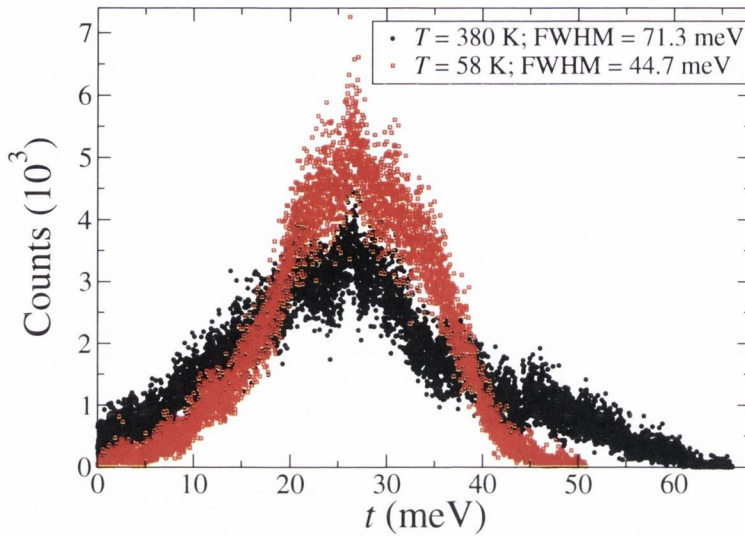


Figure 6.11: The statistical distributions of the transfer integral $t + \alpha(q_i - q_j)$ are shown at two different temperatures. The distributions are obtained from Monte Carlo simulations. For both temperatures the transfer integral fluctuates by about 100% of its magnitude as a result of the large value of α obtained for the phonon mode C-I.

Fig. 6.11 shows the statistical distributions of the transfer integral $t + \alpha(q_i - q_j)$ evaluated both at low and high temperature. As expected the fluctuations in the transfer integrals are larger at a higher temperature. This can be quantitatively observed in the full width at half maxima (FWHM, fitted to a Gaussian) of the distribution, which is 71.3 meV and 44.7 meV, respectively at 380 K and 58 K. Also it is important to note that based on the statistics, the fluctuation in the hopping integral is almost 100% of the static value at both temperatures. Such large fluctuations observed in the hopping integral are also fingerprint of the fact that the transport in these nanowires is dominated by dynamic disorder [218, 219]. Let us now explain this mechanism for charge transport.

The organic nanowire [modelled by Eq. (6.5)] has a number of different hopping integrals between nearest neighboring molecules, each fluctuating by 100% at any instant of time. Therefore, charge transport would be limited by those transfer integrals that fall in the tail of this distribution ($[t + \alpha(q_i - q_j)] \rightarrow 0$ in Fig. 6.11) at a given instant of time.

In practice, this would result in charge localization accross those few molecules. This is the concept behind the dynamic disorder explanation of charge transport [218, 219].

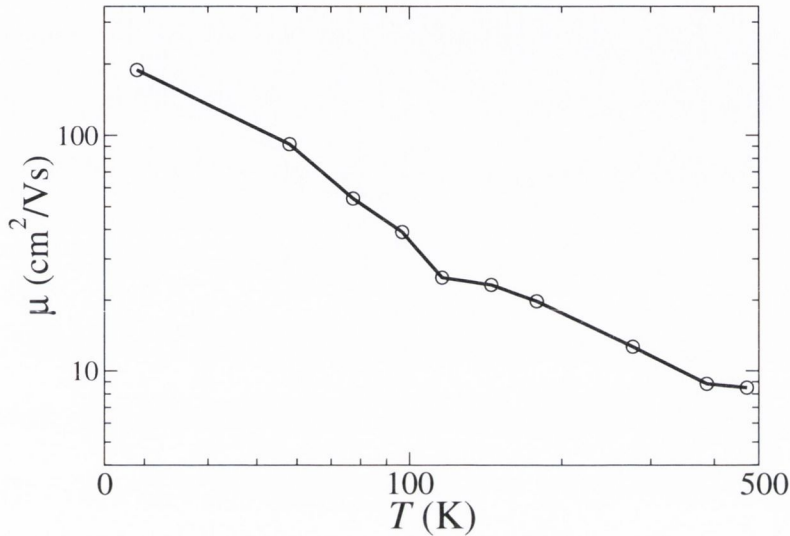


Figure 6.12: Our *ab initio* estimate for charge carrier mobility, μ , as a function of temperature for the P1 nanowire. The mobility drops drastically with temperature (note the double logarithmic scale) as a consequence of the very large value of carrier-phonon coupling calculated. At room temperature ($T = 300$ K) the mobility is found to be $11.6 \text{ cm}^2/\text{Vs}$.

Finally Fig. 6.12 shows the calculated mobility, μ , of the P1 nanowire as a function of temperature. We find an extremely severe dependence of μ over T , which is evident in its reduction by almost two orders of magnitude when T goes from 10 K to 500 K (note the double logarithmic scale). This is due to the rather strong carrier-phonon coupling, together with a general softness of the nanowires. Note in fact that here $K = 0.03825 \text{ eV}/\text{\AA}^2$, while for the longitudinal mode of rubrene one has $K = 0.06612 \text{ eV}/\text{\AA}^2$. Therefore it appears that, along the most relevant vibrational modes, the P1 nanowire is significantly softer than rubrene. Our results thus point to a transport mechanism dominated at high temperature by dynamic disorder [218, 219], where the degree of charge localization increases with temperature, as expected by an increasing spread of the statistical distri-

bution of the hopping parameters. At $T = 300$ K we estimate a charge carrier mobility of $11.6 \text{ cm}^2/\text{Vs}$. This is a rather large value for any one-dimensional object³. Thus our theoretical analysis confirms the experimental results, which attribute to the nanowires' exceptional charge transport properties.

In concluding this section it is important to note that for the P1 nanowire the room temperature mobility evaluated from Marcus theory and that calculated from linear response differ by two orders of magnitude, with the former being the smaller. This is not surprising since the two theories are applicable in rather different limits. It is reasonable to believe that our linear response value constitutes an upper limit to the actual mobility, since our calculation neglects effects such as static disorder (defective or reacted molecules in the wires), electrostatic charging, and it is constructed by considering only a single type of vibration. Instead probably the result from Marcus theory can be taken as a lower bound (unless in the actual nanowires the concentration of static defects is very high).

Thus, in this section we have explored in detail the electronic structure and the charge transport characteristics of organic nanowires obtained from triarylamine derivatives. Also we have confirmed the superior charge transport observed in experiments [190] based on the estimates for *ab initio* carrier mobility using two transport approaches. Next we will explore spin transport in these triarylamine-based organic nanowires. In particular, we think that spin transport through such nanowire structures may be noteworthy, particularly because carrier transport through the organic nanowire structure takes place through the central nitrogen atoms of each of the triarylamines. We will elaborate upon this in the next section.

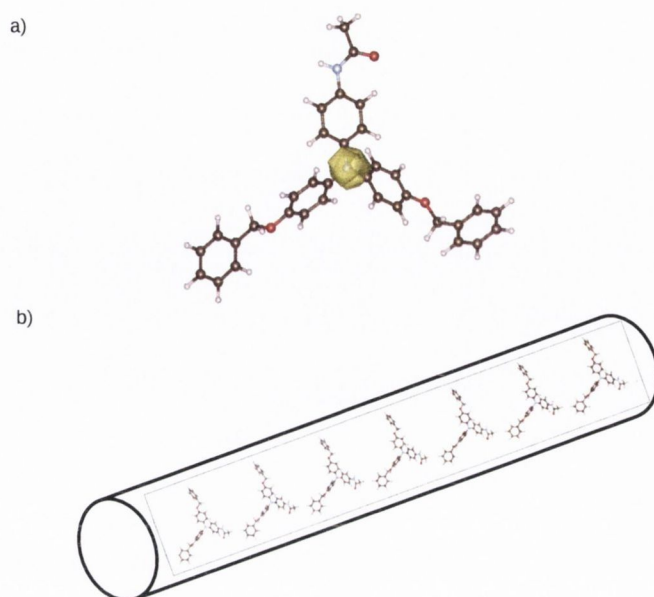


Figure 6.13: a) An illustration of triarylamine radical depicting the positive charge localized on the central N atom, which forms the itinerant hole across the nanowire. There are 6 such radicals every 1000 triarylamine molecules in the organic nanowires, self-assembled under exposure to light [189]. b) The sketch of one such organic nanowire P1, with a co-facial stacking of triarylamines, is simulated in this work.

6.3 Spin transport properties

When a semiconductor material is incorporated into a spintronic device, there are two principle paradigms that must be met in order to make an efficient device. Firstly, the spins must travel rapidly through the semiconductor material. This condition is automatically ensured in organic nanowires developed from triarylamines, as evident from their metallic I-V characteristics [190] and also from our theoretical calculations of their mobilities. The second criterion is that there must be minimal spin scattering occurring within the semiconductor material, when the charge carrier is travelling through it. In any material, the key mechanisms responsible for the loss of spin polarization of the itinerant charge carrier are spin-orbit (SO) coupling and hyperfine interaction (HI), as we have discussed in the previous chapters.

³Except for carbon nanotubes.

As established previously charge carriers are holes localized on the central nitrogen atom of the triarylamine molecule (see Fig. 6.13a). The charge transport pathway along the nanowire is through the nitrogen centers across each of the triarylamine molecules constituting the nanowire. Therefore, the HIs causing spin relaxation of the itinerant hole will be proportional to the nuclear magnetic moment of nitrogen, which has a magnitude of $\mu_N = 0.4037$ nuclear Bohr magnetons. This value is quite small, to put it in perspective $\mu_N = 0.14 \mu_H$, where μ_H is the nuclear magnetic moment of H, which is known to be quite substantial (as discussed in Chapter 4 and Chapter 5). Therefore spin relaxation due to hyperfine interaction in triarylamine-based organic nanowires will actually be quite meager. In principle, such organic nanowires could be ideal candidates for organic spintronics⁴ and therefore they could have the potential to revolutionize the field due to their exceptional charge and spin transport properties. How much of this is true in practice? We will try to address this question with our multiscale spin polarized transport approach.

Fig. 6.13a shows the essential backbone of the positively charged triarylamine radical used in the experimental work [190]. As speculated in the experiments there are about six such radicals every 1000 triarylamine molecules in the nanowire. The hole responsible for carrier transport across the nanowire is localized on the central N atom as illustrated by the space resolved local density of states of Fig. 6.13a. Fig. 6.13b depicts the organic nanowire formed by the individual triarylamine molecules in a co-facial arrangement, that we model.

***Ab initio* spin diffusion length l_s : $sp^2 - p_z$ model**

We will now focus our attention to describe the spin transport properties of such organic nanowires. We have carefully analyzed the structure of the triarylamines molecules and deduced that the central N atom and the three C atoms to which it is bonded (in Fig. 6.1)

⁴As one of the two spin scattering mechanism is negligible.

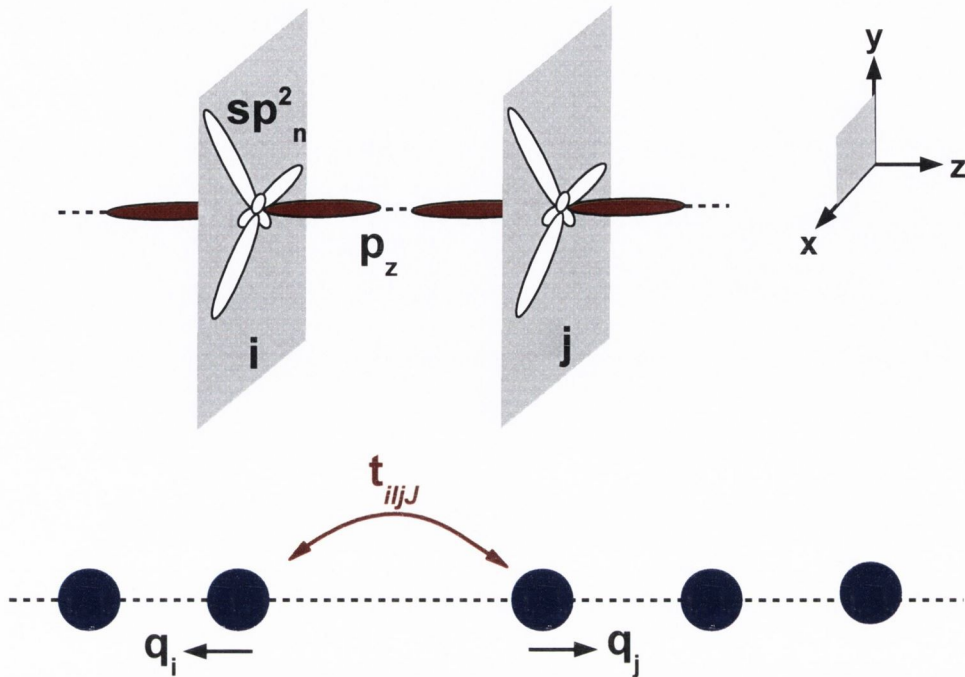


Figure 6.14: Schematic cartoon of a $sp^2 - p_z$ model which we use to represent spin transport through the organic nanowires. The bottom panel shows the chain of triarylamine molecules represented as coarse-grained spheres. The top panel illustrates the three sp^2 hybrid orbitals and the remaining p_z orbital (comprising each sphere), for nearest neighboring molecules i and j in the nanowire.

are in the same plane. Therefore, to describe the spin transport properties we can use a four band $sp^2 - p_z$ model (see Fig. 6.14). Please refer to Appendix B where we have discussed in detail, how one can construct the three degenerate hybrid orbitals: sp_a^2 , sp_b^2 and sp_c^2 .

The spin polarized Hamiltonian, $\hat{H}_{\text{nanowire}}$, representing hole transport through the central N atoms of the organic nanowire, with an additional SO coupling term can be written as

$$\hat{H}_{\text{nanowire}} = \hat{H}_{\text{HOMO}} + \lambda_{\text{SO}} \sum_{iIJ\alpha\beta} \vec{L}_{iIJ} \cdot c_{i\alpha I}^\dagger (\vec{\sigma}_{\alpha\beta}) c_{i\beta J}. \quad (6.6)$$

The index i represents the particular triarylamine molecule (site index) in the nanowire and $I(J)$ is the specific orbital (p_z , sp_a^2 , sp_b^2 , sp_c^2) in our model. Furthermore, \vec{L}_{iIJ} and

$\vec{S}_{iIJ} = c_{i\alpha I}^\dagger (\vec{\sigma}_{\alpha\beta}) c_{i\beta J}$ ^[5] are the orbital and spin angular momentum of the charge carrier, and λ_{SO} is the strength of the SO coupling. Hence a good spintronic material represented by Eq. (6.6) must have $\lambda_{SO} \rightarrow 0$.

The $\langle I\sigma | \hat{H}_{SO} | J\sigma' \rangle$ SO matrix elements for a particular triarylamine molecule i in the nanowire when expressed in the spin polarized basis set of $\{|p_z \uparrow\rangle, |sp_a^2 \uparrow\rangle, |sp_b^2 \uparrow\rangle, |sp_c^2 \uparrow\rangle, |p_z \downarrow\rangle, |sp_a^2 \downarrow\rangle, |sp_b^2 \downarrow\rangle, |sp_c^2 \downarrow\rangle\}$ is

$$\hat{H}_{SO}^i = \frac{\lambda_{SO}}{2} \begin{pmatrix} 0 & 0 & 0 & 0 & 0 & -\sqrt{\frac{2}{3}} & \frac{1}{\sqrt{6}} - \frac{\ell}{\sqrt{2}} & \frac{1}{\sqrt{6}} + \frac{\ell}{\sqrt{2}} \\ 0 & 0 & \frac{\ell}{\sqrt{3}} & -\frac{\ell}{\sqrt{3}} & \sqrt{\frac{2}{3}} & 0 & 0 & 0 \\ 0 & -\frac{\ell}{\sqrt{3}} & \frac{\ell}{\sqrt{3}} & 0 & -\frac{1}{\sqrt{6}} + \frac{\ell}{\sqrt{2}} & 0 & 0 & 0 \\ 0 & \frac{\ell}{\sqrt{3}} & 0 & -\frac{\ell}{\sqrt{3}} & -\frac{1}{\sqrt{6}} - \frac{\ell}{\sqrt{2}} & 0 & 0 & 0 \\ 0 & \sqrt{\frac{2}{3}} & -\frac{1}{\sqrt{6}} - \frac{\ell}{\sqrt{2}} & -\frac{1}{\sqrt{6}} + \frac{\ell}{\sqrt{2}} & 0 & 0 & 0 & 0 \\ -\sqrt{\frac{2}{3}} & 0 & 0 & 0 & 0 & 0 & -\frac{\ell}{\sqrt{3}} & \frac{\ell}{\sqrt{3}} \\ \frac{1}{\sqrt{6}} + \frac{\ell}{\sqrt{2}} & 0 & 0 & 0 & 0 & \frac{\ell}{\sqrt{3}} & -\frac{\ell}{\sqrt{3}} & 0 \\ \frac{1}{\sqrt{6}} - \frac{\ell}{\sqrt{2}} & 0 & 0 & 0 & 0 & -\frac{\ell}{\sqrt{3}} & 0 & \frac{\ell}{\sqrt{3}} \end{pmatrix}$$

The reader is again directed to Appendix B where we have explained the derivation of the SO Hamiltonian for the $sp^2 - p_z$ model. The matrix elements above lifts the degeneracies of the spin eigenvalues. Now, as a result of incorporating the orbitals into the problem we modify Eq. (6.5) to include the orbital indices I and J as

$$\hat{H}_{HOMO} = \sum_{iI} \epsilon_{iI} c_{iI}^\dagger c_{iI} + \sum_{ijIJ} [t_{ijJ} + \alpha_z (q_i - q_j)] (c_{iI}^\dagger c_{jJ} + h.c.) + \sum_{ij} \frac{1}{2} K (q_i - q_j)^2. \quad (6.7)$$

Please note that additionally we now have an on-site energy term in Eq. (6.7) (the first

⁵ $\vec{\sigma}_{\alpha\beta}$ are the vector of Pauli matrices.

term) to account for the fact that the sp^2 hybrid orbitals are lower in energy in comparison to the p_z orbital. In our calculations, we take the following values for the constants appearing in Eq. (6.7), on-site energies: $\epsilon_{sp^2} = -5.0$ eV and $\epsilon_{p_z} = -7.8$ eV, nearest-neighboring transfer integrals: $t_{sp^2sp^2} = -0.00038$ eV, $t_{p_zsp^2} = 0.00202$ eV^[6] and $t_{p_zp_z} = 0.025$ eV. Please refer to Appendix B where we have provided the detailed procedure by which one can obtain these parameters. Finally, $\alpha = 0.03963$ eV/Å and $K = 0.03825$ eV/Å²[7], were respectively taken to be the same for all the orbitals. This is the only approximation in our approach. We could not come up with a convenient way to obtain orbital specific el-ph constants for our system.

The source of spin relaxation as a result of SO coupling in triarylaminines is due to N and O atoms. In fact, in what follows we take $\lambda_{SO} = 10^{-2}$ eV which is an approximate upper bound estimate for the SO coupling (based on atomic SO strengths in organic materials [146]).

The spin valve arrangement which we model is schematically illustrated in Fig. 6.15 where the organic nanowire is sandwiched between two metallic electrodes. The metallic leads are modelled by a simple TB Hamiltonian, $H_L = \sum_{ij} \gamma_L (C_i^\dagger C_j + C_j^\dagger C_i)$, such that $\gamma_L \gg t$. Zero bias spin polarized conductance of the setup can be computed from Landauer-Büttiker formula. We integrate the spin polarized conductance over only the p_z levels, as they are the carriers responsible for transport. Finally from the length dependence of the integrated spin polarization, SP , the spin diffusion length, l_s , of the organic nanowire can be evaluated, as in the previous chapters.

Fig. 6.16 shows the length dependence of SP for the triarylamine P1 nanowire at room temperature ($T = 300$ K). The reciprocal of the slope of graph yields the spin diffusion length (l_s) for the nanowire.

In principle, if there is no spin relaxation of the itinerant carrier, i.e. if $\lambda_{SO} = 0$ then $l_s = \infty$. This would be an ideal situation desired for a perfect spintronic device. However

⁶Note that $t_{sp^2p_z} = -0.00202$ eV.

⁷ α and K values are the same as in the previous section.

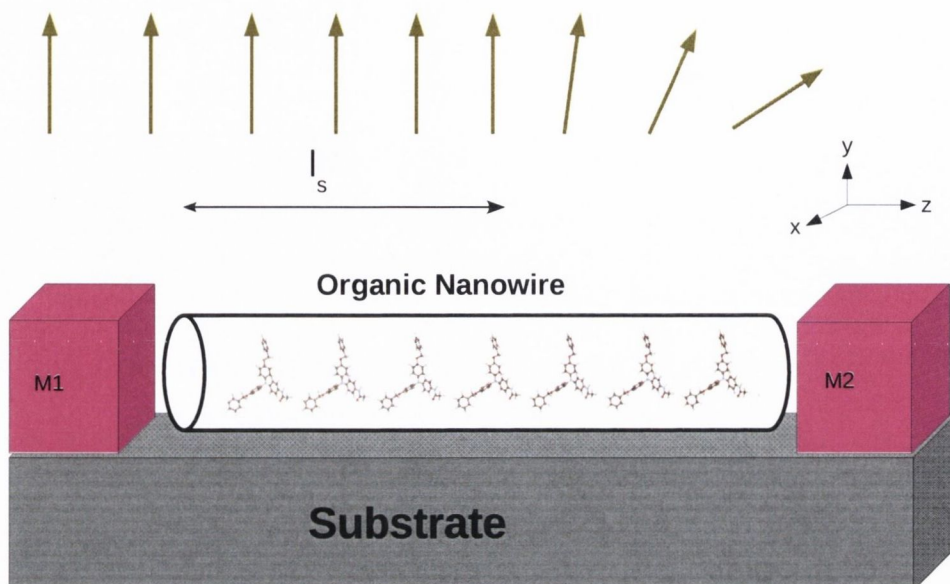


Figure 6.15: Schematic cartoon of a spin valve comprising a triarylamine based organic nanowire sandwiched between ferromagnetic leads, M1 and M2. In our simulations the *ab initio* Hamiltonian for carrier transport across the HOMO of triarylamine organic nanowires is illustrated by Eq. (6.6), while the metallic electrodes are represented by a simple TB model. We then compute the spin diffusion length, l_s , of the charge carriers, which is the distance travelled within the organic nanowire before the spin polarization is lost (see top panel), based on the procedure similar to the previous chapters.

in the case of triarylamine-based organic nanowires, the spin polarization of the carrier will be lost through the nanowire due to spin-orbit coupling, as included in Eq. (6.6). The *ab initio* estimate for spin diffusion length in triarylamine based organic spin valve is $l_s = 23.73$ nm at $T = 300$ K. The room temperature magnitude for spin diffusion length that we obtain is actually quite superior in comparison to common OSCs [60].

Overall our estimates for both the charge and spin transport observables are quite decent and strongly indicate such nanowires as promising candidates for spintronic devices. The principal reason, which can account for such superior spin and charge transport properties in these systems can only be attributed to their one-dimensional self-assembled nanowire structure, which is obtained upon irradiation with visible light of the triaryl-

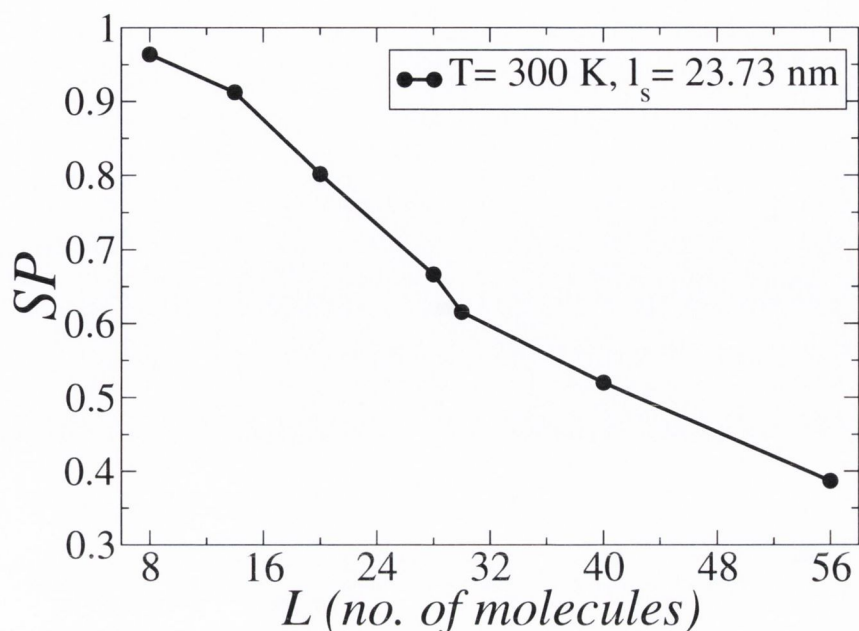


Figure 6.16: We show the length dependence of room temperature SP for the $sp^2 - p_z$ model which describes spin transport through the triarylamine nanowire. The spin diffusion lengths (l_s) of the nanowire are obtained from the reciprocal of the slope of the graph. We obtain $l_s = 23.73$ nm at $T = 300$ K. Please note that $L = 1$ corresponds to a length of 4.8\AA , which is the distance between two triarylamine molecules in the nanowire.

lamine solution. In such one-dimensional nanowire structures the charge carrier (hole) is localized on the central N atom. At finite temperatures due to excitation of phonons, when the individual triarylamine molecules come closer with respect to one another, the overlap of the HOMO of adjacent molecules in the nanowire is facilitated which ultimately results in an efficient hole transport across the entire organic nanowire. This also ensures that the itinerant carrier transport is along the central N atoms of the triarylaminines. Moreover it establishes that there is a negligible spin relaxation of the carrier through the organic nanowire due to hyperfine interactions. To the best of our knowledge, this is the first comprehensive work that provides the first principles estimate for charge and spin transport observables of organic nanowires synthesized from triarylaminines. We hope that these estimates can be confirmed by the experimental community.

6.4 Summary

We have reported on a detailed first principles study of the structural, electronic and transport properties of a class of triarylamine derivatives recently synthesized [189]. Our aim was that of gaining insights into the self-assembly process leading to 1D nanowires and into the charge transport characteristics of such nanowires. The basic electronic structure of the molecules in the gas phase is rather similar for all the precursors with a HOMO mainly localized around the N atom of the triarylamine unit. As a consequence all the precursors appear to have rather similar ionization potentials. These first calculations suggest that the criterion for the formation of supramolecular self-assembled organic nanowires in triarylamine derivatives is independent of the precursor chemistry.

Next the electron transport properties of the nanowire were explored. Firstly, we evaluated the hole mobilities of all the precursors by using Marcus theory, with the transfer integrals evaluated from the electronic structure of molecular dimers and the reorganization energy from the ionization potential of the single molecules. Then, for the P1 precursors, we also perform linear response mobility calculations by considering the most relevant phonon mode. As expected we find the mobility calculated from Marcus theory to be about two orders of magnitude smaller than that extracted from linear response, which reaches $12 \text{ cm}^2/\text{Vs}$ at room temperature. These two values can be realistically taken as the lower and upper bound for the nanowire mobility.

We also computed the *ab initio* estimate for spin diffusion length in such organic nanowires synthesized from triarylamine. The estimate for spin diffusion length from first principles is $l_s = 23.73 \text{ nm}$ at $T = 300 \text{ K}$, which is a very superior value for the distance which carrier's spins travel in a semiconductor before losing their spin polarizations. Our results thus prove that triarylamine-based nanowires are indeed good hole conductors and are also capable for spin polarized transport through them. Their ability to self-assemble in-situ in a device geometry [190] makes them interesting candidates for organic electronics and organic spintronics.

Finally, the procedure to estimate the charge and spin transport characteristics employed in this chapter is quite similar to the one we have used in the previous chapters. Therefore this is a successful test of transferability of the multiscale method to compute carrier mobility and spin diffusion length for OSCs.

Chapter 7

Current projects, Conclusions and Future works

7.1 Project in progress: investigating the organic magnetoresistance effect

After the spin valve effect was demonstrated in hybrid inorganic-organic devices [70] a very interesting phenomenon was observed in thin film OSCs by Francis *et al.* [228]. According to their work the intrinsic resistance through an OSC thin film can be altered when a small magnetic field is applied. This effect was termed as Organic Magneto Resistance (OMAR). The device structure designed to investigate this effect is illustrated in Fig. 7.1a and is the same as an OLED, i.e. a cathode/OSC/anode, simple two-probe architecture. The cathode is comprised of a hole injecting compound like Indium Tin Oxide while the anode can be an electron injecting material like an alkali metal (Ca, Mg, etc.).

Experiments to observe the OMAR effect were performed on Alq₃ films [228] but subsequently the effect was also observed in other OSCs namely: pentacene [231], regio polymers [231], PCBM (Phenyl-C61-butyric acid methyl ester) [230] and C₆₀ [229].

The salient features associated with the OMAR effect can be summarized as follows:

1. OMAR is a phenomenon due to the change in the bulk resistance of the OSC and is assumed to be unaffected by any semiconductor-metal interface effects. The latter is not conclusive at this moment and there are ongoing experiments to control OMAR by manipulating semiconductor-metal interface effects.
2. This effect is independent of the magnetic field direction.
3. The magnitude of the OMAR can be positive or negative depending on the OSC, device configuration and device operating conditions.

In experiments, the resistance through the device, R , is monitored as a function of magnetic field, B . OMAR is then defined by the following expression

$$\text{OMAR} = \frac{R(B) - R(0)}{R(0)} \times 100. \quad (7.1)$$

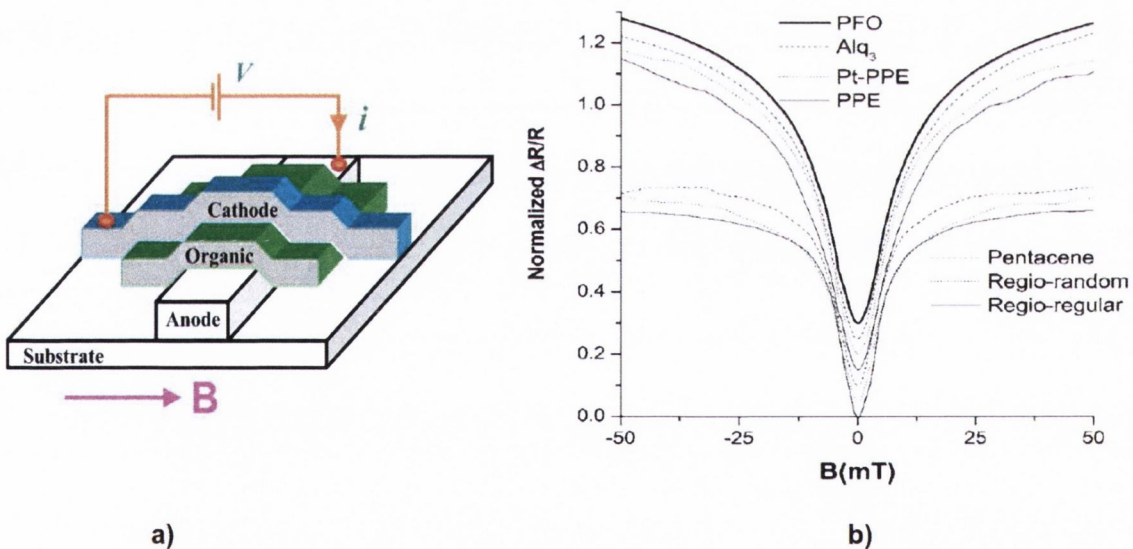


Figure 7.1: The left panel shows the characteristic device structure for investigating the OMAR effect, also resembling an OLED. In experiments the normalized resistance, $\Delta R/R$, is monitored as a function of magnetic field, B and OMAR is quantified according to Eq. (7.1). The right panel shows the OMAR from one such experiment [231] for different OSCs at room temperature.

Characteristic experimental results demonstrating the OMAR effect are shown in

Fig. 7.1b¹ where $\Delta R/R$ is plotted as a function of the applied magnetic field for different OSCs.

Typically the OMAR effect is observed at low applied magnetic fields of magnitude less than 100 mT. Furthermore, the maximum OMAR measured in experiments is about 20%. The OMAR effect generally decreases on increasing the electric field and the temperature. The field and temperature dependence of the OMAR have been both well documented in literature and for a detailed reading please refer to the review in Ref. [232]. Very recently OMAR effects of around 400% at 200 mT magnetic fields have also been reported in Alq₃ based devices [233].

The most interesting and enticing aspect of the OMAR effect is that it is observed even at room temperatures. In principle, this experimental observation could imply that the organic materials themselves can be used as resistive switches for data storage applications. However, this effect is still in its early days of research and more experimental and theoretical research is necessary in order to fully understand it. Furthermore, the OMAR effect has been observed only by a few research groups and the validity of the effect itself is still controversial.

One of the applications of the OMAR effect proposed by the authors who had first observed it, was in touch-screen devices. The idea was to couple an OLED-based display with a magnetic pen, which can generate a small magnetic field. When the pen approaches a specific pixel, the OSC detects the magnetic field through a change in its resistance (the OMAR effect), which can then be converted into pixel illumination [227].

Our *ab initio* estimation of OMAR in rubrene We are quite curious to explore the change in charge transport characteristics of OSCs as a function of magnetic field and investigate the microscopic origins of OMAR. We can include an external magnetic field

¹Taken from work of O. Mermer *et al.* [231].

in our model by adding the following Hamiltonian

$$\hat{H}_B = \sum_{iI\alpha\beta} \mu_B g \vec{B} \cdot c_{i\alpha I}^\dagger (\vec{\sigma}_{\alpha\beta}) c_{i\beta I}, \quad (7.2)$$

where μ_B is the Bohr magneton, g is the Landae g -factor and \vec{B} the magnetic field vector. Finally, $\vec{S}_{iI} = c_{i\alpha I}^\dagger (\vec{\sigma}_{\alpha\beta}) c_{i\beta I}$ are the carrier spin for holes belonging to the the i th rubrene molecule's I th orbital.

The OSC can be described through the coarse-graining procedure we employed in Chapter 5. Therefore, we already have the entire apparatus for representing the essential interactions in rubrene in the form of its *ab initio* tight binding Hamiltonian. The resultant Hamiltonian including the effect of an external magnetic field is

$$\hat{H} = \hat{H}_{\text{rubrene}} + \hat{H}_B. \quad (7.3)$$

Furthermore, the transport observable monitored as a function of magnetic field is the charge carrier mobility. Therefore we may define the OMAR as

$$\text{OMAR} = \frac{\frac{1}{\mu^{(B)}} - \frac{1}{\mu^{(0)}}}{\frac{1}{\mu^{(0)}}} \times 100 \quad (7.4)$$

Fig. 7.2 shows the OMAR for rubrene calculated using the definition in Eq. (7.4) as a function of applied magnetic field B , at three different temperatures. Let us systematically analyze our results.

Firstly, the *ab initio* estimate for OMAR at room temperature (300 K) is between 10-15%, which is quite close to that obtained also in experiments [230]. Secondly, we also find that the OMAR effect is independent of the direction of magnetic field. Moreover, it decreases on increasing temperature particularly because the carrier mobility decreases on increasing temperature (band transport limit). However, we find that our *ab initio*

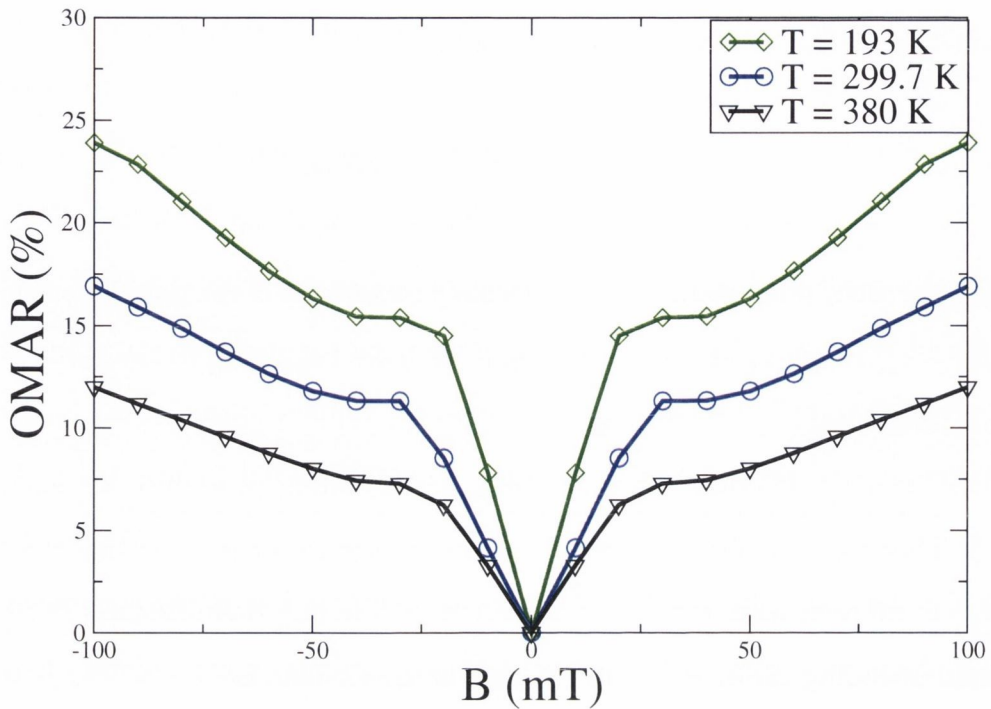


Figure 7.2: We can make an *ab initio* estimate of the OMAR using Eq. (7.4) by evaluating the carrier mobility of rubrene as a function of magnetic field (B). This is shown here for three different temperatures.

estimates for OMAR made using Eq. (7.4) has a much broader shape (vs B) in comparison to the same obtained by experiments. In experiments, OMAR vs B plot can be fitted with a Lorentzian [232].

In a model such as ours, used to investigate OMAR based on the definition in Eq. (7.4), with increasing B we will always observe a change in the carrier mobility. One can understand this very easily based on the description of how carrier mobility is estimated by using Kubo formula. How exactly we can relate our estimation of OMAR with that in experiments, is a question that we want to ponder about a little more. Moreover, another question is whether from our model we could explain the microscopic origins of the change in intrinsic resistance of an OSC due to magnetic field? This is a project currently in progress.

7.2 General conclusions and achievements of this thesis

The prospect of using OSC-based spintronic devices for high density data storage applications is quite enticing. Although, the foundations of the fields have already been laid based on the experience from the field of organic electronics, an actual understanding of how charge carriers and especially their associated spins travel through an OSC is not comprehensively achieved. Throughout the work presented in this thesis we have provided a microscopic understanding of both the charge and spin transport properties of OSCs.

One of the central problems in this respect was that the Hamiltonian used in modelling OSCs have a number of different terms representing a broad range of interactions and a large number of degrees of freedom. Throughout our work we have been successful in optimizing these degrees of freedom and simultaneously understanding the temperature dependent properties of the microscopic system as a function of these variables.

In this thesis we have developed an *ab initio* theory with which we can estimate the charge carrier mobility and spin diffusion length of particular OSCs. We have looked into the problem in different transport regimes, including ballistic and the diffusive limit. Most importantly, the transport observables were evaluated as a function of temperature with a Monte Carlo sampling procedure. Moreover, our multiscale procedure proved to be robust, self-contained and accurate. The work presented here is the first and a very crucial step towards achieving a full *ab initio* modelling of an organic spintronics device. This is indeed one of the central accomplishment of this thesis.

Furthermore, we have also carefully optimized the structure of triarylamine based organic nanowires without the access of its crystallographic information. We envisage that such a method can also be used for optimizing the structure of amorphous thin films of Alq₃ (whose crystalline structure is not known) in order to compute the transport properties through our multiscale process. The interests in Alq₃ films are plenty because

it is being extensively explored by the experimental organic spintronics community.

Based on what we have learned in this thesis we envisage a number of possible novel research projects on organic spintronics.

7.3 Future works

Organic-metal interface

Spinterface The premise of the work presented in this thesis is to understand charge and spin transport through the bulk of the OSC layer in a device. While the work presented in this thesis is indeed a significant achievement in describing the bulk transport properties of OSC, the organic-metal interface effects are neglected. However, in reality this is not at all the scenario. Therefore if one wants to model an entire organic device, incorporating and understanding the effects occurring at the metal-organic interface is absolutely quintessential. As we had mentioned previously, the problem of organic molecule on a metallic substrate has been widely studied in the last half decade. We will now share our perspective on modelling organic-metal interface in this subsection. In many ways the processes occurring at the metal-organic interface have similar effects on the electronic structure and transport properties of the entire device than those we have discussed already in this thesis to some extent. We will now summarize them.

Firstly from an experimental point of view, the contact between the fragile OSC material and the metal electrode must be as clean as possible. This means that the geometry and electronic structure of the OSC must be preserved in the device. Imperfect organic-inorganic contacts may cause metal inclusions into the OSC layer. This may short the device and cause spurious transport measurements. Moreover, it is absolutely crucial for an optimum device performance that there must not be any kind of complications arising due to chemical reactions between the metal and the organic.

The second issue that will always plague an OSC based device is associated with the

infamous resistance mismatch problem between the organic material and metal electrodes. There are two solutions to this. The first is to use an organic material with superior transport characteristics. The work presented in the previous chapter is quite promising in this respect. Generally, in experiments the resistance mismatch problem is circumvented by introducing a small tunneling barrier (1-2 nm of Al_2O_3) between the organic material and the metallic electrode.

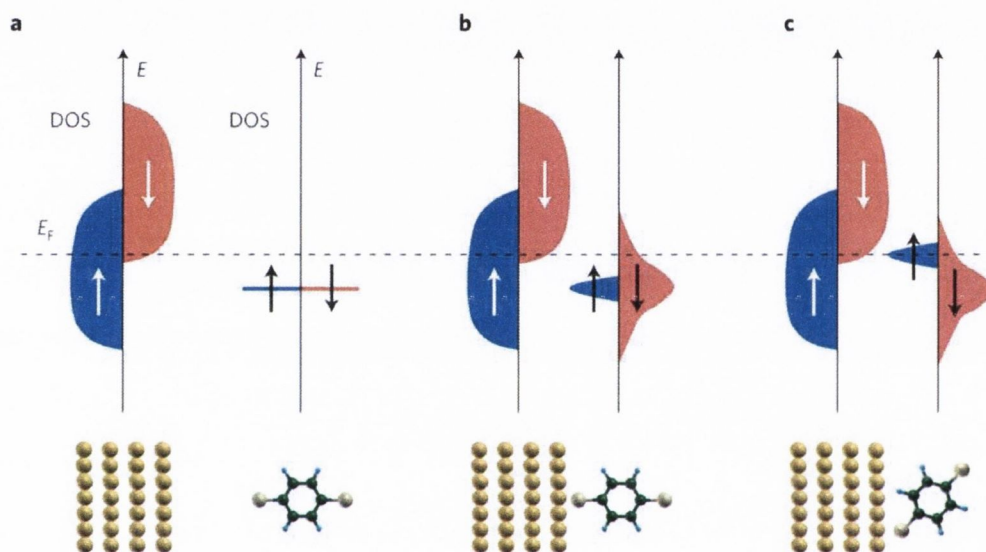


Figure 7.3: The concept behind spin dependent interface effects known as *spinterface* is illustrated. When the organic molecule is far away from the metallic electrode, it is characterized by a single discrete energy level as shown in a). However, as the molecule is brought closer to the metallic surface due to an increased metal-molecule interaction the energy level of the organic molecule broadens. This broadening depends on the nature of the interaction between the metal and the organic molecule. The importance of the exact nature of this broadening (therefore the organic molecule metal interaction) is illustrated in b) and c). The exact characteristic of this broadening, which will be controlled by spin dependent interaction (*spinterface*) between the organic molecule and the electrode will govern spin transport through the device.

The third issue is connected with a very fundamental property of a metal-organic molecule interface and is prevalent regardless of how clean is the metal organic interface. In Fig. 7.3a we show the energetics of such a metal-molecule interface, when the organic molecule is relatively far away from the metal. The organic molecule is characterized by a single discrete energy level while the ferromagnetic metal is represented by a continuous

spin polarized density of state. However, the situation is different when the organic molecule is brought closer to the metallic electrode and two possible scenarios can arise which are schematically illustrated in Fig. 7.3b and Fig. 7.3c.

When the organic molecule is gradually brought closer to the metallic electrode, the discrete energy levels will broaden due to increased organic-metal interactions (for example chemical bonding). The broadening of the organic molecule will entirely depend on the nature of interaction between the organic molecule and the metal at the interface and can be spin dependent. Indeed, such a spin polarized broadening can lead to two possible scenarios which are depicted in Fig. 7.3b and Fig. 7.3c. As we can clearly see from these two figures, the exact nature of the spin polarized carrier transport through the organic molecule are different in the two cases, since hybrid molecular orbitals with different spin polarization can appear at the electrode's Fermi level. This phenomenon of spin depended broadening due to metal organic interface effects, was coined as *spinterface* [7].

Needless to say that a proper systematic study of hybrid organic-inorganic interfaces is absolutely crucial to complete the modelling of an organic spintronic device. At the metal-organic interface the length scale is about 0 – 2 nm. At this length scale, DFT is a very powerful tool for investigating quite accurately the metal-organic interface effects. We suggest the following projects on investigating systematically the properties of hybrid organic-inorganic interface effects.

Possible projects

1. As we have seen, obtaining the correct interactions between the organic medium and a metal is crucial in describing hybrid organic-inorganic systems. The first step would be to obtain an accurate binding distance between the organic molecule and the metal. We propose investigating organic molecules such as rubrene or Alq₃ on Co substrates. In order to describe the correct binding properties we propose the use of state of the art vdW-DFT codes [47, 48]. The calculation, which we have

- in mind is quite simple: make a supercell out of the system under investigation, i.e. organic molecule on a metallic substrate and then relax the supercell till atomic forces are less than $0.01 \text{ eV}/\text{\AA}$, for different vdW DFT functionals.
2. Assuming we have the relaxed geometries and the correct organic-metal distances, the next step would be that of investigating the energetics and the energy alignment between the organic molecule and the metal. In order to describe the electronic structure of the ferromagnetic metal accurately we will however require more involved DFT functionals in order to treat strongly correlated systems, namely self-interaction error corrected functionals or hybrid functionals. An option could be to use the constraint DFT approach.
 3. Assuming we have the correct geometry and electronic structure of the hybrid organic-inorganic system, it would be worth investigating the transport properties of the ensemble. This will also give us an idea of the hybrid interface states involved in carrier transport at the interface of an organic device. One could also evaluate the IV characteristics as a function of the magnetization of the leads and therefore evaluate the TMR of the device. We suggest the use of the SMEAGOL atomistic quantum transport, a code developed by our group, for this project.

Charge and spin transport properties of Alq_3

The majority of the experiments on organic spintronics demonstrate substantial spin valve effect in Alq_3 -based devices. This is because Alq_3 thin films can be extensively grown on a range of different substrates. Furthermore, Alq_3 thin films have been widely employed for making OLEDs. A very exciting research project would be that of computing the electron mobility and spin diffusion length of Alq_3 from our multiscale procedure.

However, to the best of our knowledge crystalline Alq_3 has never been produced. Due to the lack of any crystalline data for Alq_3 one cannot use the approach we have used for

rubrene, to compute the corresponding *ab initio* tight binding Hamiltonian as in Chapter 5 of this thesis. Possible solution would be to optimize the structure using the coarse-grained method that we have employed for the organic nanowires work in Chapter 6. Another possible project could be that of estimating the change in mobility and spin diffusion lengths for Alq₃ with system confinement, i.e. for Alq₃ nanowires and compare them with experiments [65]. The change in mobility and spin diffusion lengths with system confinement would also give us information on the role of spin-orbit coupling in governing spin relaxation in such systems.

Detailed phonon bandstructure calculation

In both Chapter 5 and Chapter 6 we have estimated the electron-phonon coupling, α , and the stiffness constants, K , of the tight binding Hamiltonian for OSCs, along a particular direction, based on physical arguments for the respective systems. However, any system is characterized by many phonon modes having different energies (frequencies). Depending on the temperature, a set of phonon modes will be excited and will contribute to different magnitudes of α and K . Therefore, a systematic computation of these parameters (α and K) for all the phonon modes of the system is necessary in a comprehensive *ab initio* procedure to compute the transport properties of OSCs. The most severe hindrance in this respect is the fact that phonon bandstructure calculations for systems like rubrene (280 atoms) and triarylamine (70 atoms) is rather computationally intense.

On this very aspect I oversaw a project of a colleague. In the project the detailed phonon bandstructure of a much smaller OSC, Durene (C₁₀H₁₄) was calculated. Moreover, α and K from the procedure mentioned in this thesis were estimated for all the phonon modes of the system.

Organic charge transfer salts

κ -BEDT-(TTF)₂X [bis(ethylene-dithio) tetrathiafulvalene] organic charge transfer salts, which have been a subject of intense research by experimentalists and many-body physicists. This is because their anisotropic triangular lattice has a very rich phase diagram including superconducting, Mott insulating and spin liquid phases [222]. Recently, an *ab initio* study [234] found that these charge transfer salts may not be that frustrated. Such work was based on Car-Parrinello molecular dynamics simulations (CPMD) to evolve the crystalline structures of the charge transfer salts and then fitting the *ab initio* bandstructures of the system to a Hubbard model.

We have also explored the problem at the *ab initio* level, using Wannier functions to obtain the transfer integrals in the triangular lattice of such salts and therefore provide a more systematic procedure to estimate t and U in such systems. However, we could not reproduce the bandstructure of such salts in particular because we did not have access to the crystal structures of such salts. In fact we found that the bandstructures were quite sensitive to relaxation coordinates. Perhaps, a MD evolution of the structures is required for this project.

Self-assembly of organic nanowires: incorporating solvent effects

In Chapter 6, based on exploring the electronic structures of triarylamine precursors (in their dry states), we have concluded that their self-assemblies is not governed by their precursor chemistry but rather may be controlled by solvent induced effects. A possible project stemming out from this work can be to incorporate the solvent (chloroform) and study the dynamics of the nanowire plus solvent system, in order to investigate if we could achieve the same self-assemblies as in the experiments [189]. The dynamics of the system can be studied using classical molecular dynamics simulations. This project could be important to explore candidates for similar self-assembled nanowire structures with exceptional transport characteristics.

Appendix A

Derivation of the spin-orbit

Hamiltonian for the $\pi - \pi$ model

Throughout the course of this work we have used the spin-orbit coupling Hamiltonian

$$H_{SO}^{iIJ} = \sum_{iIJ} \lambda_{SO} \vec{L}_{iIJ} \cdot \vec{S}_{iIJ} = \lambda_{SO} \sum_{iIJ} \frac{1}{2} (L_{iIJ}^+ S_{iIJ}^- + L_{iIJ}^- S_{iIJ}^+) + L_{iIJ}^z S_{iIJ}^z. \quad (\text{A.1})$$

Here i is the atom index and I, J are the orbital index. The nature of spin-orbit coupling Hamiltonian used in this work is on-site as evident from Eq. (A.1). Therefore for every site i let us derive the spin-orbit matrix elements

$$\langle I\sigma | \lambda_{SO} \vec{L}_{IJ} \cdot \vec{S}_{IJ} | J\sigma' \rangle = \langle I\sigma | \frac{\lambda_{SO}}{2} (L_{IJ}^+ \sigma_{IJ}^- + L_{IJ}^- S_{IJ}^+) + \lambda_{SO} L_{IJ}^z S_{IJ}^z | J\sigma' \rangle \quad (\text{A.2})$$

Here $L_{IJ}^+(L_{IJ}^-)$ and $S_{IJ}^+(S_{IJ}^-)$ are respectively the angular momentum and spin ladder operators; L_z and S_z are the z components of the orbital angular momentum and spin angular momentum respectively. In order to obtain the on-site spin-orbit matrix elements we adopt the following procedure.

The orbitals I, J in our case are p_x, p_y and p_z . These can be written in terms of the complex spherical harmonics Y_l^m according to the following expressions, where l and m

are respectively the more familiar angular momentum and magnetic quantum numbers:

$$p_x = \frac{1}{\sqrt{2}}(Y^{-1} - Y^1), \quad (\text{A.3})$$

$$p_y = \frac{i}{\sqrt{2}}(Y^{-1} + Y^1), \quad (\text{A.4})$$

$$p_z = Y^0. \quad (\text{A.5})$$

In the above definitions, we have dropped the l subscript associated with the spherical harmonics, as for all p orbitals $l = 1$ and hence it is the same. Finally, we define the operators appearing in Eq. (A.2) as

$$L^z|Y^m; \sigma\rangle = m |Y^m; \sigma\rangle, \quad (\text{A.6})$$

$$L^+|Y^m; \sigma\rangle = \sqrt{l(l+1) - m(m+1)}|Y^{m+1}; \sigma\rangle, \quad (\text{A.7})$$

$$L^-|Y^m; \sigma\rangle = \sqrt{l(l+1) - m(m-1)}|Y^{m-1}; \sigma\rangle, \quad (\text{A.8})$$

and the corresponding spin operators as

$$S^z|Y^m; \sigma\rangle = \sigma |Y^m; \sigma\rangle, \quad (\text{A.9})$$

$$S^+|Y^m; \sigma\rangle = |Y^m; \sigma + 1\rangle, \quad (\text{A.10})$$

$$S^-|Y^m; \sigma\rangle = |Y^m; \sigma - 1\rangle. \quad (\text{A.11})$$

In the above definitions the index $\sigma = \pm \frac{1}{2}$ describes the spin quantum number associated with each of the spherical harmonics Y_l^m and \hbar is taken to be unity. Also, spin $\uparrow = \sigma$ and spin $\downarrow = -\sigma$, the corresponding spin quantum numbers for the two spin states. Finally there is one identity which will form the basis of the derivations presented in this appendix which is,

$$\langle Y_l^m; \sigma | Y_{l'}^{m'}; \sigma' \rangle = \delta_{l,l'} \cdot \delta_{m,m'} \cdot \delta_{\sigma,\sigma'}. \quad (\text{A.12})$$

Let us work out the spin-orbit matrix element for each atom i (on-site SO):

$$\begin{aligned} \langle p_y^\dagger | \frac{1}{2} (L^+ S^- + L^- S^+) + L^z S^z | p_z^\dagger \rangle &= \frac{-\hbar}{\sqrt{2}} \langle (Y^{-1} + Y^1); \sigma | \frac{1}{2} (L^+ S^- + L^- S^+) + L^z S^z | Y^0; -\sigma \rangle \\ \langle (Y^{-1} + Y^1); \sigma | \frac{1}{2} L^+ S^- | Y^0; -\sigma \rangle &= 0 \\ \langle (Y^{-1} + Y^1); \sigma | \frac{1}{2} L^- S^+ | Y^0; -\sigma \rangle &= \sqrt{2} \cdot \frac{1}{2} (\langle Y^{-1}; \sigma | Y^{-1}; \sigma \rangle + \langle Y^1; \sigma | Y^{-1}; \sigma \rangle) = \frac{\sqrt{2}}{2} \\ \langle (Y^{-1} + Y^1); \sigma | L^z S^z | Y^0; -\sigma \rangle &= 0. \quad -\sigma (\langle Y^{-1}; \sigma | Y^0; -\sigma \rangle + \langle Y^1; \sigma | Y^0; -\sigma \rangle) = 0 \end{aligned}$$

$$\therefore \langle p_y^\dagger | L \cdot S | p_z^\dagger \rangle = -\frac{\hbar}{2} \text{ and } \langle p_z^\dagger | L \cdot S | p_y^\dagger \rangle = \frac{\hbar}{2}.$$

$$\begin{aligned} \langle p_y^\dagger | \frac{1}{2} (L^+ S^- + L^- S^+) + L^z S^z | p_z^\dagger \rangle &= \frac{-\hbar}{\sqrt{2}} \langle (Y^{-1} + Y^1); -\sigma | \frac{1}{2} (L^+ S^- + L^- S^+) + L^z S^z | Y^0; \sigma \rangle \\ \langle (Y^{-1} + Y^1); -\sigma | \frac{1}{2} L^+ S^- | Y^0; \sigma \rangle &= \sqrt{2} \cdot \frac{1}{2} (\langle Y^{-1}; -\sigma | Y^1; -\sigma \rangle + \langle Y^1; -\sigma | Y^1; -\sigma \rangle) = \frac{\sqrt{2}}{2} \\ \langle (Y^{-1} + Y^1); -\sigma | \frac{1}{2} L^- S^+ | Y^0; \sigma \rangle &= 0 \\ \langle (Y^{-1} + Y^1); -\sigma | L^z S^z | Y^0; \sigma \rangle &= 0. \quad \sigma (\langle Y^{-1}; -\sigma | Y^0; \sigma \rangle + \langle Y^1; -\sigma | Y^0; \sigma \rangle) = 0 \end{aligned}$$

$$\therefore \langle p_y^\dagger | L \cdot S | p_z^\dagger \rangle = -\frac{\hbar}{2} \text{ and } \langle p_z^\dagger | L \cdot S | p_y^\dagger \rangle = \frac{\hbar}{2}.$$

$$\begin{aligned} \langle p_x^\dagger | \frac{1}{2} (L^+ S^- + L^- S^+) + L^z S^z | p_y^\dagger \rangle &= \frac{\hbar}{2} \langle Y^{-1} - Y^1; \sigma | \frac{1}{2} (L^+ S^- + L^- S^+) + L^z S^z | (Y^{-1} + Y^1); \sigma \rangle \\ \langle (Y^{-1} - Y^1); \sigma | \frac{1}{2} L^+ S^- | (Y^{-1} + Y^1); \sigma \rangle &= \frac{\sqrt{2}}{2} \langle Y^{-1}; \sigma | Y^0; \sigma \rangle + \langle Y^1; \sigma | Y^0; \sigma \rangle = 0 \\ \langle (Y^{-1} - Y^1); \sigma | \frac{1}{2} L^- S^+ | (Y^{-1} + Y^1); \sigma \rangle &= 0 \\ \langle (Y^{-1} - Y^1); \sigma | L^z S^z | (Y^{-1} + Y^1); \sigma \rangle &= \sigma \cdot (-1 \langle Y^{-1}; \sigma | Y^{-1}; \sigma \rangle + 1 \langle Y^{-1}; \sigma | Y^1; \sigma \rangle + \\ &+ 1 \langle Y^1; \sigma | Y^{-1}; \sigma \rangle - 1 \langle Y^1; \sigma | Y^1; \sigma \rangle) = -1 \end{aligned}$$

$$\therefore \langle p_x^\dagger | L \cdot S | p_y^\dagger \rangle = -\frac{\hbar}{2} \text{ and } \langle p_y^\dagger | L \cdot S | p_x^\dagger \rangle = \frac{\hbar}{2}.$$

$$\langle p_x^\dagger | \frac{1}{2} (L^+ S^- + L^- S^+) + L^z S^z | p_y^\dagger \rangle = \frac{\iota}{2} \langle Y^{-1} - Y^1; -\sigma | \frac{1}{2} (L^+ S^- + L^- S^+) + L^z S^z | (Y^{-1} + Y^1); -\sigma \rangle$$

$$\langle (Y^{-1} - Y^1); -\sigma | \frac{1}{2} L^+ S^- | (Y^{-1} + Y^1); -\sigma \rangle = 0$$

$$\langle (Y^{-1} - Y^1); -\sigma | \frac{1}{2} L^- S^+ | (Y^{-1} + Y^1); -\sigma \rangle = \frac{\sqrt{2}}{2} \langle Y^{-1}; -\sigma | Y^0; -\sigma \rangle + \langle Y^1; -\sigma | Y^0; -\sigma \rangle = 0$$

$$\langle (Y^{-1} - Y^1); -\sigma | L^z S^z | (Y^{-1} + Y^1); -\sigma \rangle = -\sigma (-1 \langle Y^{-1}; -\sigma | Y^{-1}; -\sigma \rangle + 1 \langle Y^{-1}; -\sigma | Y^1; -\sigma \rangle + 1 \langle Y^1; -\sigma | Y^{-1}; -\sigma \rangle - 1 \langle Y^1; -\sigma | Y^1; -\sigma \rangle) = 1$$

$$\therefore \langle p_x^\dagger | L \cdot S | p_y^\dagger \rangle = \frac{\iota}{2} \text{ and } \langle p_y^\dagger | L \cdot S | p_x^\dagger \rangle = -\frac{\iota}{2}.$$

$$\langle p_x^\dagger | \frac{1}{2} (L^+ S^- + L^- S^+) + L^z S^z | p_z^\dagger \rangle = \frac{1}{\sqrt{2}} \langle (Y^{-1} - Y^1); \sigma | \frac{1}{2} (L^+ S^- + L^- S^+) + L^z S^z | Y^0; -\sigma \rangle$$

$$\langle (Y^{-1} - Y^1); \sigma | \frac{1}{2} L^+ S^- | Y^0; -\sigma \rangle = 0$$

$$\langle (Y^{-1} - Y^1); \sigma | \frac{1}{2} L^- S^+ | Y^0; -\sigma \rangle = \frac{\sqrt{2}}{2} (\langle Y^{-1}; \sigma | Y^{-1}; \sigma \rangle - \langle Y^1; \sigma | Y^{-1}; \sigma \rangle) = \frac{\sqrt{2}}{2}$$

$$\langle (Y^{-1} - Y^1); \sigma | L^z S^z | Y^0; -\sigma \rangle = 0. -\sigma (\langle Y^{-1}; \sigma | Y^0; -\sigma \rangle - \langle Y^1; \sigma | Y^0; -\sigma \rangle) = 0$$

$$\therefore \langle p_x^\dagger | L \cdot S | p_z^\dagger \rangle = \frac{1}{2} \text{ and } \langle p_z^\dagger | L \cdot S | p_x^\dagger \rangle = \frac{1}{2}.$$

$$\langle p_x^\dagger | \frac{1}{2} (L^+ S^- + L^- S^+) + L^z S^z | p_x^\dagger \rangle = \frac{1}{\sqrt{2}} \langle (Y^{-1} - Y^1); \sigma | \frac{1}{2} (L^+ S^- + L^- S^+) + L^z S^z | Y^0; -\sigma \rangle$$

$$\langle (Y^{-1} - Y^1); -\sigma | \frac{1}{2} L^+ S^- | Y^0; \sigma \rangle = \frac{\sqrt{2}}{2} (\langle Y^{-1}; -\sigma | Y^1; -\sigma \rangle - \langle Y^1; -\sigma | Y^1; -\sigma \rangle) = -\frac{\sqrt{2}}{2}$$

$$\langle (Y^{-1} - Y^1); -\sigma | \frac{1}{2} L^- S^+ | Y^0; \sigma \rangle = 0$$

$$\langle (Y^{-1} - Y^1); -\sigma | L^z S^z | Y^0; \sigma \rangle = 0. \sigma (\langle Y^{-1}; -\sigma | Y^0; \sigma \rangle - \langle Y^1; -\sigma | Y^0; \sigma \rangle) = 0$$

$$\therefore \langle p_x^\dagger | L \cdot S | p_x^\dagger \rangle = -\frac{1}{2} \text{ and } \langle p_z^\dagger | L \cdot S | p_x^\dagger \rangle = -\frac{1}{2}.$$

Thus, the spin-orbit coupling matrix (for every site i) obtained by expanding Eq. (A.2) over the following basis $\{|p_x^i \uparrow\rangle, |p_y^i \uparrow\rangle, |p_z^i \uparrow\rangle, |p_x^i \downarrow\rangle, |p_y^i \downarrow\rangle, |p_z^i \downarrow\rangle\}$ is

$$\hat{H}_{SO}^i = \frac{\lambda_{SO}}{2} \begin{pmatrix} 0 & -\iota & 0 & 0 & 0 & 1 \\ \iota & 0 & 0 & 0 & 0 & -\iota \\ 0 & 0 & 0 & -1 & \iota & 0 \\ 0 & 0 & -1 & 0 & \iota & 0 \\ 0 & 0 & -\iota & -\iota & 0 & 0 \\ 1 & \iota & 0 & 0 & 0 & 0 \end{pmatrix}.$$

Appendix B

$sp^2 - p_z$ model

The discussions in this appendix section pertains to the $sp^2 - p_z$ model, which has been used to extract the spin diffusion length (l_s) in the second part of Chapter 6.

Construction of sp_2 hybrid orbitals

The three sp_n^2 ($n = a, b, c$) hybrid orbitals can be constructed based on the following equations

$$|sp_a^2\rangle = \left(|s\rangle + \sqrt{2}|p_x\rangle \right) / \sqrt{3}, \quad (\text{B.1})$$

$$|sp_b^2\rangle = \left(|s\rangle - \frac{|p_x\rangle}{\sqrt{2}} + \sqrt{\frac{3}{2}}|p_y\rangle \right) / \sqrt{3}, \quad (\text{B.2})$$

$$|sp_c^2\rangle = \left(|s\rangle - \frac{|p_x\rangle}{\sqrt{2}} - \sqrt{\frac{3}{2}}|p_y\rangle \right) / \sqrt{3}, \quad (\text{B.3})$$

here $|s\rangle$, $|p_x\rangle$ and $|p_y\rangle$ are the usual ket notations of the corresponding (real) wavefunctions for N $2s$ and $2p_x$ and $2p_y$ levels respectively.

These sp_n^2 hybrid orbitals together with the remaining $2p_z$ orbital form our four band $sp^2 - p_z$ model.

The SO matrix for the $sp^2 - p_z$ model

In order to obtain the SO matrix, $\langle I\sigma | \lambda_{SO} \vec{L}_{IJ} \cdot \vec{S}_{IJ} | J\sigma' \rangle$, we will have to write the wavefunctions of the orbitals (from the definitions above) in terms of their real spherical harmonics¹ and repeat the same procedure described in Appendix A.

The on-site SO matrix for the $sp_n^2 - p_z$ model (for every site i) written in the following basis $\{|p_z \uparrow\rangle, |sp_a^2 \uparrow\rangle, |sp_b^2 \uparrow\rangle, |sp_c^2 \uparrow\rangle, |p_z \downarrow\rangle, |sp_a^2 \downarrow\rangle, |sp_b^2 \downarrow\rangle, |sp_c^2 \downarrow\rangle\}$ is

$$\hat{H}_{SO}^i = \frac{\lambda_{SO}}{2} \begin{pmatrix} 0 & 0 & 0 & 0 & 0 & -\sqrt{\frac{2}{3}} & \frac{1}{\sqrt{6}} - \frac{\ell}{\sqrt{2}} & \frac{1}{\sqrt{6}} + \frac{\ell}{\sqrt{2}} \\ 0 & 0 & \frac{\ell}{\sqrt{3}} & -\frac{\ell}{\sqrt{3}} & \sqrt{\frac{2}{3}} & 0 & 0 & 0 \\ 0 & -\frac{\ell}{\sqrt{3}} & \frac{\ell}{\sqrt{3}} & 0 & -\frac{1}{\sqrt{6}} + \frac{\ell}{\sqrt{2}} & 0 & 0 & 0 \\ 0 & \frac{\ell}{\sqrt{3}} & 0 & -\frac{\ell}{\sqrt{3}} & -\frac{1}{\sqrt{6}} - \frac{\ell}{\sqrt{2}} & 0 & 0 & 0 \\ 0 & \sqrt{\frac{2}{3}} & -\frac{1}{\sqrt{6}} - \frac{\ell}{\sqrt{2}} & -\frac{1}{\sqrt{6}} + \frac{\ell}{\sqrt{2}} & 0 & 0 & 0 & 0 \\ -\sqrt{\frac{2}{3}} & 0 & 0 & 0 & 0 & 0 & -\frac{\ell}{\sqrt{3}} & \frac{\ell}{\sqrt{3}} \\ \frac{1}{\sqrt{6}} + \frac{\ell}{\sqrt{2}} & 0 & 0 & 0 & 0 & \frac{\ell}{\sqrt{3}} & -\frac{\ell}{\sqrt{3}} & 0 \\ \frac{1}{\sqrt{6}} - \frac{\ell}{\sqrt{2}} & 0 & 0 & 0 & 0 & -\frac{\ell}{\sqrt{3}} & 0 & \frac{\ell}{\sqrt{3}} \end{pmatrix}$$

Hamiltonian parameters for the $sp^2 - p_z$ model

The on-site energies for N 2s and 2p levels are $\epsilon_s = -13$ eV and $\epsilon_p = -5.0$ eV respectively [6] and hence $\epsilon_{sp^2} = (\epsilon_s + 2 \cdot \epsilon_p)/3 = -7.7$ eV. The various nearest-neighboring transfer integrals (t_{IJ}) in the model can be obtained from the following procedure:

$$t_{p_z p_z} = \langle p_z | \hat{H}_t | p_z \rangle = \gamma_{p_z p_z \sigma}, \quad (\text{B.4})$$

$$t_{p_z p_z} = \gamma_{p_z p_z \sigma} = 0.025 \text{ eV}^{[2]}.$$

¹ $|s\rangle = Y_0^0$ and the other bands are the same as in Appendix A.

²Evaluated from the dispersion of the HOMO band in Fig. 6.9.

$$t_{sp_n^2 sp_n^2} = \langle sp_n^2 | \hat{H}_t | p_z \rangle = \frac{1}{3}(\gamma_{ss\sigma} + 2 \cdot \gamma_{pp\pi}), \quad (\text{B.5})$$

$$t_{sp_n^2 sp_{n'}^2} = \langle sp_n^2 | \hat{H}_t | sp_{n'}^2 \rangle = \frac{1}{3}(\gamma_{ss\sigma} - 2 \cdot \gamma_{pp\pi}), \quad (\text{B.6})$$

$$t_{p_z sp_n^2} = \langle p_z | \hat{H}_t | sp_n^2 \rangle = \frac{1}{\sqrt{3}}\gamma_{sp\sigma}. \quad (\text{B.7})$$

In the above equations \hat{H}_t is the transfer integral Hamiltonian, i.e. the second term in Eq. (6.7) and $n(n') = a, b, c$. Furthermore, we obtain $\gamma_{ss\sigma} = -0.00115$ eV, $\gamma_{sp\sigma} = -0.00351$ eV and $\gamma_{pp\pi} \simeq 0.0$ eV. These are based on the dispersion of the corresponding bands in the band structure of a 1D N chain (calculated within DFT) with a N-N separation distance of 4.9 \AA , which gives $\gamma_{p_z p_z \sigma} = 0.025$ eV. Note that the latter clearly means that the HOMO of the organic nanowire is constituted by p_z electrons.

Appendix C

Publications stemming from this work

1. *The search for a spin crossover transition in small sized π -conjugated molecules: a Monte Carlo study*, **S Bhattacharya**, M S Ferreira and S Sanvito, **Journal of Physics.: Condensed. Matter** 23, 316001 (2011).
2. *What causes spin-flip in organic crystals?*, **S Bhattacharya** and S Sanvito, *in preparation*.
3. *Ab-initio estimation of charge and spin transport properties of rubrene using maximally localized Wannier functions*, **S Bhattacharya** and S Sanvito, *in preparation*.
4. *First Principles Study of the Structural, Electronic and Transport properties of triarylamine-based nanowires*, A Akande¹, **S Bhattacharya**¹, T Cathcart and S Sanvito, accepted in **Journal of Chemical Physics** (2013).
5. *Spin transport properties of Organic Nanowires synthesized from Triarylamine derivatives*, **S Bhattacharya**, A Akande and S Sanvito, submitted to **ChemComm** as an invited article (2013).

¹ These authors contributed equally in the work and are co-first authors in this paper.

Bibliography

- [1] G. Binasch, P. Grünberg, F. Saurenbach, and W. Zinn Phys. Rev. B **39**, 4828-4830 (1989).
- [2] A. Barthelemy, A. Fert, M.N. Baibich, S. Hadjoudj, F. Petroff, P. Etienne, R. Cabanel, S. Lequien, F. Nguyen Van Dau and G. Creuzet, J. Appl. Phys. **67**, 5908 (1990) and M.N. Baibich, J.M. Broto, A. Fert, F. Nguyen Van Dau, F. Petroff, P. Etienne, G. Creuzet, A. Friederich and J. Chazelas, Phys. Rev. Lett. **61**, 2472-2475 (1988).
- [3] J.B. Neaton, M.S. Hybertsen, and S.G. Louie, Phys. Rev. Lett. **97**, 216405 (2006).
- [4] S. Grimme, J. Antony, S. Ehrlich and H. Krieg, J. Chem. Phys. **132**, 154104 (2010).
- [5] K. Stokbroa, J. Taylora, M. Brandbyge, J.-L. Mozos, P. Ordejn, Computational Materials Science, **27**, 1-2, 151160 (2003).
- [6] A. Sutton, Electronic Structure of Materials (Oxford Science Publications) (1993).
- [7] S. Sanvito, Nature Physics, **6**, 562 (2010).
- [8] S. Sanvito, Nature Materials, **10**, 484-485 (2011).
- [9] A. Riminucci1, M. Prezioso, C. Pernechele, P. Graziosi1, I. Bergenti, R. Cecchini, M. Calbucci, M. Solzi and V.A. Dediu, Appl. Phys. Lett. **102**, 092407 (2013).
- [10] F.G. Monzon, H.X. Tang, and M.L. Roukes, Phys. Rev. Lett. **84**(21), 5022 (2000).
- [11] M.E.J. Newmann and G.T. Barkema, *Monte Carlo in Statistical Physics*, Oxford University Press (1999).
- [12] T. Valet and A. Fert, Phys. Rev. B, 48, 10 (1993).

- [13] I. Rungger and S. Sanvito, *Phys. Rev. B*, **78**, 035407 (2008).
- [14] K. Blum, *Density Matrix Theory and Applications*, Plenum Press, New York, (1996).
- [15] N. Metropolis, A.W. Rosenbluth, M.N. Rosenbluth, A.H. Teller, E. Teller, *J. Chem. Phys.*, **21**, 1087 (1953).
- [16] J.M. Manriquez, G.T. Yee, S. Mclean, A.J. Epstein and J.S. Miller, *Science*, 252 ,1415-1417 (1991).
- [17] V.N. Prigodin, N.P. Raju, K.I. Pokhodnya, J.S. Miller, A.J. Epstein, *Adv. Mater.*, **14**,17 (2002).
- [18] M. Born and J.R. Oppenheimer, *Annalen der Physik (Leipzig)*, **84**, 457 (1927).
- [19] A. Messiah, *Quantum Mechanics*, Courier Dover Publications, New York, USA (1999).
- [20] P. Hohenberg and W. Kohn, *Phys. Rev.*, **136**, B864-B871 (1964).
- [21] W. Kohn and L. Sham, *Physical Review*, **140** (4A): A1133-A1138 (1965).
- [22] H. Hellmann, *Einführung in die Quantenchemie*. Leipzig: Franz Deuticke. p. 285. (1937) and R.P. Feynmann, *Phys. Rev.* **56** (4): 340 (1939).
- [23] Janak, *Phys. Rev. B*, **18**, 7165 (1978).
- [24] T. Koopmans, *Physica* **1**, 104 (1934).
- [25] R.G. Parr, W. Yang, *Density-Functional Theory of Atoms and Molecules*, vol.16 of The International Series of Monographs on Chemistry, Oxford University Press, Oxford, UK (1989).
- [26] U. Von Barth, L. Hedin, *J. Phys. C*, **5**, 1629 (1972).
- [27] O. Gunnarsson and B.I. Lundqvist, *Phys. Rev. B* **13**, 42744298 (1976).
- [28] V.I. Anisimov, J. Zaanen, O.K. Andersen, *Phys. Rev. B*, **44**, 943 (1991).
- [29] S.L. Dudarev, G.A. Botton, S.Y. Savrasov, C.J. Humphreys, A.P. Sutton, *Phys. Rev. B*, **57**, 1505 (1998).

- [30] M. Cococcioni, S. de Gironcoli, *Phys. Rev. B*, **71**, 035105 (2005).
- [31] L.J. Sham, M. Schlünter, *Phys. Rev. Lett.*, **51**, 1888 (1983).
- [32] J.P. Perdew, M. Levy, *Phys. Rev. Lett* **51**, 1884-1887 (1983).
- [33] J.P. Perdew, R.G. Parr, M. Levy, J.L. Balduz, Jr, *Phys. Rev. Lett*, **49**, 1691-1684 (1982).
- [34] J.P. Perdew and A. Zunger, *Phys. Rev. B* **23**, 5048-5079 (1981).
- [35] J.P. Perdew, K. Burke and M. Ernzerhof, *Phys. Rev. Lett.* **77**, 3865 (1996).
- [36] C.J. Cramer, *Essentials of Computational Chemistry*. 2nd Edition-Wiley and Sons (2004).
- [37] A.D. Becke, *Phys. Rev. A*, **38**, 3098 (1988).
- [38] S.H. Vosko, L. Wilk, M. Nusair, *Can. J. Phys* **58** (8) : 1200-1211 (1980).
- [39] C. Lee, W. Yang, R.G. Parr, *Phys. Rev. B*, **37** (2): 785-789 (1988).
- [40] J. Heyd, G. E. Scuseria, and M. Ernzerhof, *J. Chem. Phys.* **118**, 8207 (2003).
- [41] J. Paier, R. Hirsch, M. Marsam, G. Kresse, *J. Chem. Phys*, **122**, 234102 (2005).
- [42] J. Heyd, G.E. Scuseria, and M. Ernzerhof, *J. Chem. Phys.* **118** (18): 8207 (2003).
- [43] S. Grimme, *J. Comput. Chem* **25**, 1463 (2004) and S. Grimme, *J. Comp. Chem.* **27**, 1787 (2006).
- [44] J. E. Lennard-Jones, "On the Determination of Molecular Fields", *Proc. R. Soc. Lond. A*, 106 (738): 463-477 (1924).
- [45] S. Grimme, J. Antony, S. Ehrlich and H. Kreig, *J. Chem. Phys.* **132**, 154104 (2010).
- [46] M. Dion, H. Rydberg, E. Schröder, D.C. Langreth, and B.I. Lundqvist, *Phys. Rev. Lett.* **92**, 246401 (2004).
- [47] A. Tkatchenko and M. Scheffler, *Phys. Rev. Lett.* **102**, 073005 (2009).
- [48] A. Tkatchenko, R.A. DiStasio Jr, R. Car, and M. Scheffler, *Phys. Rev. Lett.* **108**, 236402 (2012).

- [49] Y. Zhang and W. Yang, Phys. Rev. Lett. **80**, 890 (1998).
- [50] D.E. woon and J.H. Dunning, J. Chem. Phys, **98**, 1358 (1993).
- [51] N. Troullier and J.L. Martins, Phys. Rev. B **43**, 1993 (1991).
- [52] L. Kleinman and D.M. Bylander, Phys. Rev. Lett **48** (20), 1425 (1982).
- [53] L. Fernandez-Seivane, M.A. Oliveira, S. Sanvito and J. Ferrer, J. Phys.: Condens. Matter, **18**, 7999 (2006).
- [54] L. Kleinman, Phys. Rev. B, **21**, 26301 (1980) and G.B. Bachelet and M. Schter, Phys. Rev. B, **25**, 21038 (1982).
- [55] J.M. Soler, E. Artacho, J.D. Gale, A. Garca, J. Junquera, P. Ordejn, and D. Snchez-Portal, J. Phys.: Condens. Matt. **14**, 2745-2779 (2002).
- [56] H.J. Monkhorst and J.D. Pack, Phys. Rev. B, **13**, 5188 (1976).
- [57] A.R. Rocha, V. M. Garcia-Suarez, S.W. Bailey, C.J. Lambert, J. Ferrer and S. Sanvito, Nature Materials **4**, 335 (2005).
- [58] S. Sanvito, J. Mat. Chem. **17**, 4455 (2007).
- [59] S. Sanvito, Nature Materials, **6**, 803 (2007).
- [60] V.A. Dediu , L.E. Hueso, I. Bergenti and C. Taliani, Nature Materials, **8**, 707 (2009).
- [61] L. Bogani and W. Wernsdorfer, Nature Materials, **7**, 179 (2008).
- [62] G. Szulczewski, S. Sanvito and J.M.D. Coey, Nature Materials, **8**, 693 (2009).
- [63] C.B. Harris, R.L. Schlupp and H. Schuch, Phys. Rev. Lett. **30**, 1019 (1973).
- [64] V.I. Krinichnyi , S.D. Chemerisov and Y.S. Lebedev, Phys. Rev. B, **55**, 16233 (1997).
- [65] S. Pramanik, C.G. Stefanita, S. Patibandla, S. Bandyopadhyay K. Garre, N. Harth and M. Cahay, Nature Nanotech. **2**, 216 (2007).
- [66] I. Zutic, J. Fabian and S. Das Sarma, Rev. Mod. Phys. **76**, 323 (2004).

- [67] S. Sanvito and A.R. Rocha, *J. Comp. Theo. Nano.* **3**, 624 (2006).
- [68] C. Barraud, P. Seneor, R. Mattana, S. Fusil, K. Bouzheouane, C. Deranlot, P. Graziosi, L. Hueso, I. Bergenti, V.A. Dediu, F. Petroff and A. Fert, *Nature Physics*, **6**, 615-620 (2010).
- [69] S. Ikeda, J. Hayakawa, Y. Ashizawa, Y. M. Lee, K. Miura, H. Hasegawa, M. Tsunoda, F. Matsukura, and H. Ohno, *Appl. Phys. Lett.* **95**, 082508 (2008).
- [70] V.A. Dediu, M. Murgia, F.C. Matacotta, C. Taliani and S. Barbanera, *Sol. State. Commun.* **122**, 181 (2002).
- [71] Z. H. Xiong, D. Wu, Z. V. Vardeny, and J. Shi, *Nature (London)*, **427**, 821 (2004).
- [72] G. Giovannetti, S. Kumar, A. Stroppa, J.V.D. Brink and S. Picozzi, *Phys. Rev. Lett.* **103**, 266401 (2009).
- [73] S. Machida, Y. Nakayama, S. Duhm, Q. Xin, A. Funakoshi, N. Ogawa, S. Kera, N. Ueno and H. Ishii, *Phys. Rev. Lett.* **104**, 156401 (2010).
- [74] P. Gütlich, H.A. Goodwin, in *Spin Crossover in Transition Metal Compounds* (eds. P. Gütlich, H.A. Goodwin) (Springer), *Top. Curr. Chem.* **233**, 1. (2004).
- [75] N. Baadji, M. Piacenza, T. Tugsuz, F. Della Sala, G. Maruccio, S. Sanvito, *Nature Materials*, **8**, 813 (2009).
- [76] M. Diefenbach, K.S. Kim, *Angew. Chem.* **119**, 7784 (2007).
- [77] A. Droghetti and S. Sanvito, *Phys. Rev. Lett.* **107**, 047201 (2011).
- [78] P. Gütlich, H.A. Goodwin, *Spin Crossover in Transition Metal Compounds I*, Springer (2004).
- [79] P. Gütlich, *Metal Complexes*, Springer (1981)
- [80] P. Gütlich, Y. Garcia and H.A. Goodwin, *Chem. Soc. Rev.*, **29**, 419-427 (2000).
- [81] Y. Garcia, V. Niel, M.C. Muñoz and J.A. Real, in *Spin Crossover in Transition Metal Compounds* (eds. P. Gütlich, H.A. Goodwin) (Springer), *Top. Curr. Chem.* **233**, 229 (2004).

- [82] J. Hubbard, Proc. Roy. Soc. A **276**, 238 (1963).
- [83] P.W. Anderson in *Fizika Dielektrikon* edited by G.I. Skanov and K.V. Filippov (Academy of Sciences, Moscow) p. 290, (1960).
- [84] S. Kirkpatrick, C.D. Gelatt and M.P. Vecchi, Science **220**, 4598 (1983).
- [85] W. Lee, N. Jean and S. Sanvito, Phys. Rev. B, **79**, 085120 (2009).
- [86] S.J. Xie, K.H. Ahn, D.L. Smith, A.R. Bishop and A. Saxena, Phys. Rev. B, **67**, 125202 (2003).
- [87] E. Jeckelmann and D. Baeriswyl, Synth. Metal, **65**, 211 (1994).
- [88] E. Jeckelmann, Phys. Rev. B, **57**, 11838 (1998).
- [89] Y.Z. Zhang, C.Q. Wu and H.Q. Lin, Phys. Rev. B, **72**, 125126 (2005).
- [90] P. Sengupta, A.W. Sandvik and D.K. Campbell, Phys. Rev. B, **67**, 245103 (2003).
- [91] Y. Otsuka, H. Seo, Y. Motome and T. Kato, Physics B, **404**, 479 (2009).
- [92] H. Seo, Physics B **405**, S126 (2010).
- [93] P.A. Bobbert, W. Wagemans, F.W.A. van Oost, B. Koopmans and M. Wohlgenannt, Phys. Rev. Lett. **102**, 156604 (2009).
- [94] G. Brehm, M. Reiher and S. Schneider, J. Phys. Chem. A, **106**, 12024-12034 (2002).
- [95] M. Reiher, Inorg. Chem., **41**, 6928-6935 (2002).
- [96] Reference. 36 of C. Wolverton and A. Zunger, Phys. Rev. B, **52**, 12 (1995).
- [97] P. Drude, Annalen der Physik, **306**, 3, 566-613 (1900).
- [98] V. Cataudella, G. De Filippis, and C.A. Perroni, Phys. Rev. B, **83**, 165203 (2011).
- [99] F. Gargiulo, C.A. Perroni, V. M. Ramaglia, and V. Cataudella, Phys. Rev. B, **84**, 245204 (2011).

- [100] A.R. Brown, C.P. Jarrett, D.M. de Leeuw and M. Matters, *Synth. Met.* **88**, 37 (1997).
- [101] J.H. Burroughes, D.D.C. Bradley, A.R. Brown, R.N. Marks, K. Mackay, R.H. Friend, P.L. Burns, and A.B. Holmes, *Nature (London)* **347**, 539 (1990).
- [102] G. Gustafsson, Y. Cao, G.M. Treacy, F. Klavetter, N. Colaneri, and A.J. Heeger, *Nature (London)* **357**, 477 (1992).
- [103] R.H. Friend, R.W. Gymer, A.B. Holmes, J.H. Burroughes, R.N. Marks, C. Taliani, D.D.C. Bradley, D.A. Dos Santos, J.L. Bredas, M. Logdlund, and W.R. Salaneck, *Nature (London)* **397**, 121 (1999).
- [104] P.W.M. Blom and M.J.M. de Jong, *IEEE J. Sel. Top. Quantum Electron.* **4**, 105 (1998).
- [105] D. Eley, *Nature*, **162**, 819 (1948).
- [106] W. Gao, A. Kahn, *Appl. Phys. Lett.* **79**, 4040, (2001), *Org. Electron.* **3**, 53,(2002), *J. Appl. Phys.* **94**, 359, (2003) and *J. Phys.: Condens. Matter* **15**, S2757, (2003).
- [107] C.C. Wu, C.I. Wu, J.C. Sturm, A. Kahn, *Appl. Phys. Lett.* **70**, 11 (1997), Y.H. Tak, K.B. Kim, H.G. Park, K.H. Lee, J.R. Lee, *Thin Solid Films*, **411**, 1, (2002), H. Kim, C.M. Gilmore, A. Pique, J.S. Horwitz, H. Mattoussi, H. Murata, Z.H. Kafafi, D.B. Chrisey, *Journal of Applied Physics*, **86**, 11 (1999).
- [108] C.K. Chan, W. Zhao, S. Barlow, S. Marder, A. Kahn, *Organic Electronics* **9**, 575-58 (2008), V.E. Choong, M.G. Mason, C.W. Tang, Y. Gao, *Appl. Phys. Lett.* **72**, 21 (1998).
- [109] S. Reineke, F. Lindner, G. Schwartz, N. Seidler, K. Walzer, B. Lssem and K. Leo, *Nature* **459**, 234-238 (2009).
- [110] I.N. Hulea, S. Fratini, H. Xie, C.L. Mulder, N.N. Iossad, G. Rastelli, S. Ciuchi and A.F. Morpurgo, *Nature Materials* **5**, 982-986 (2006)
- [111] N. Karl, *Synthetic Materials*, **133**, 647 (2003).
- [112] W. Warta, R. Stehle, N. Karl, *Appl. Phys. A.* **36**, 163 (1985).

- [113] N. Karl, O. Madelung, M. Schulz, H. Weiss (Eds.) Semiconductors, Landolt-Bornstien (Newseries), Group III, Vol 17 (Subvolume 17i), Springer, Berlin, 106-218 (1985).
- [114] O.D. Jurchesu, J. Baas and T.T.M. Palstra, Appl. Phys. Lett. **84**, 3061-3063 (2004).
- [115] A. Troisi and D.L. Cheung, J. Chem. Phys, **131**, 014703 (2009).
- [116] A. Troisi, Chem. Soc. Rev, **40**, 2347-2358 (2011).
- [117] M.E. Gershenson, V. Podzorov and A.F. Morpurgo, Rev. Mod. Phys. **78**, 973-989 (2006)
- [118] K. Hannewald, V.M. Stojanovic, J.M.T. Schellekens, P.A. Bobbert, G. Kresse and J. Hafner, Phys. Rev. B, **69**, 075211 (2004).
- [119] F. Ortman, F. Bechstedt and K. Hannewald, New. J. Phys, **12**, 023011, (2010).
- [120] J. Rivnay, R. Noriega, J.E. Northrup, R.J. Kline, M.F. Toney and A. Salleo, Phys. Rev. B **83**, 121306(R) (2011).
- [121] Z.M. Beiley, E.T. Hoke, R. Noriega, J. Dacua, G.F. Burkhard, J.A. Bartelt, A. Salleo, M.F. Toney, M.D. McGehee, Adv. Energy Mater. **1**, 5, 954-962 (2011).
- [122] Hindelech, J. Phys. C, Solid State Physics (1988).
- [123] J.E. Anthony, D.L. Eaton and S.R. Parkin, Org. Lett, **4**, 15 (2002).
- [124] K.P. Goetz, Z. Li, J.W. Ward, C. Bougher, J. Rivnay, J. Smith, B.R. Conrad, S.R. Parkin, T.D. Anthopoulos, A. Salleo, J.E. Anthony, O.D. Jurchescu, Adv. Mater, **23**, 3698-3703 (2011).
- [125] V. Ambegaokar, B.I. Halperin and J.S. Langer, Phys. Rev. B, **4**, 2612 (1971).
- [126] D.A. Da Silva, E.G. Kim and J.L. Bredas, Adv. Mater, **17**, 8 (2005).
- [127] D.E. Janzen, M.W. Burand, P.C. Ewbank, T.M. Pappenfus, H. Higuchi, D.A. da Silva, V.G. Young, J.L. Bredas, K.R. Mann, J. Am. Chem. Soc, **126**, 15295 (2004).
- [128] J.E. Anthony, J.S. Brooks, D.L. Eaton, S.R. Parkin, J. Am. Chem. Soc, **123**, 9482 (2001).

- [129] S. Datta, *Electronic Transport in Mesoscopic Systems*. New York: Cambridge University Press. pp. 57-111, (1997).
- [130] N.F. Mott, Proc. R. Soc. Lond. A, **153**, 699-717 (1936).
- [131] S. Yuasa, T. Nagahama, A. Fukushima, Y. Suzuki and K. Ando, Nature Materials, **3**, 868-871 (2004) and S.P. Parkin, C. Kaiser, A. Panchula, P.M. Rice, B. Hughes, M. Samant and S. Yang, Nature Materials, **3**, 862-867 (2004).
- [132] T.D. Nguyen, G. Hukic-Markosian, F. Wang, L. Wojcik, X. Li, E. Ehrenfreund and Z.V. Vardeny, Nature Materials, **9**, 345, 352 (2010).
- [133] N.J. Rolfe, M. Heeney, P.B. Wyatt, A.J. Drew, T. Kreouzis and W.P. Gillin, Phys. Rev. B, **80**, 241201 (2009).
- [134] K. Schulten and P. Wolynes, J. Chem. Phys, **68**, 3292-3297 (1978).
- [135] P.A. Bobbert, Nature Materials, **9**, 288-290 (2010).
- [136] H.M. McConnell, J. Chem. Phys, **24**, 764-766 (1956).
- [137] D. R. McCamey, K.J. van Schooten, W.J. Baker, S.Y. Lee, S.Y. Paik, J. M. Lupton and C. Boehme, Phys. Rev. Lett, **104**, 017601 (2010).
- [138] M. Julliere, Phys. Lett. A, **54**, 225-226 (1975).
- [139] V. Dediu, L.E. Hueso, I. Bergenti, A. Riminucci, F. Borgatti, P. Graziosi, C. Newby, F. Casoli, M.P. De Jong, C. Taliani and Y. Zhan, Phys. Rev. B, **78**, 115203 (2008).
- [140] F.J. Wang, C.G. Yang and Z.V. Vardeny, Phys. Rev. B, **75**, 245324 (2007).
- [141] R.J. Elliott, Phys. Rev., **96**, 266-279 (1954).
- [142] S. Bandyopadhyay, Phys. Rev. B, **81**, 153202 (2010).
- [143] J.J.H.M. Schoonus, P.G.E. Lumens, W. Wagemans, J.T. Kohlhepp, P.A. Bobbert, H.J.M. Swagten and B. Koopmans, Phys. Rev. Lett. **103**, 146601 (2009).
- [144] Y.A. Bychkov and E.T. Rashba, J. Phys. C, **17**, 6039 (1984).

- [145] Z.G. Yu, Phys. Rev. Lett. **106**, 106602 (2011).
- [146] Z.G. Yu, Phys. Rev. B. **85**, 115201 (2012).
- [147] R. Kubo, J. Phys. Soc.Jpn **12**, 570 (1957).
- [148] A.J. Drew *et al.*, Nature Mater. **8**, 109-114 (2009).
- [149] M. Cinchetti, K. Heimer, J. Wüstenberg, O. Andreyev, M. Bauer, S. Lach, C. Ziegler, Y. Gao and M. Aeschlimann, Nature Mater. **8**, 115-119 (2009).
- [150] M. Rosenblatt, Ann. Math. Statist. **27**, 3, 832-837 (1956).
- [151] M. Kikkawa and D.D. Awschalom, Nature, 397, 139141 (1999).
- [152] *Calculation of NMR and EPR Parameters: Theory and Applications* edited by M. Kaupp, M. Bühl, V.G. Malkin, Wiley (2004).
- [153] Optical Orientation, ed. F. Meier and B.P. Zachachrenya, North-Holland, Amsterdam, The Netherlands, Modern Problems in Condensed Matter Science series, vol. 8 edn, 1984.
- [154] Spin Electronics, ed. M. Ziese and M.J. Thornton, Springer-Verlag, Heidelberg, Germany, Lecture Notes in Physics series, vol. 569 edn, 2001.
- [155] A. Kirilyuk, A.V. Kimel and T. Rasing, Rev. Mod. Phys., **82**, 2731-2784 (2010).
- [156] V.C. Sundar, J. Zaumseil, V. Podzorov, E. Menard, R.L. Willett, T. Someya, M.E. Gershenson and J.A. Rogers, Science, **303**, 1644 (2004).
- [157] R.W.I. De Boer, T.M. Klapwijk, A.F. Morpurgo, Appl. Phys. Lett. **83**, 4345 (2003).
- [158] J. Takeya, C. Goldmann, S. Haas, K.P. Pernstich, B. Ketterer and B. Batlogg, J. Appl. Phys. **94**, 5800 (2003).
- [159] T. Hasegawa and J. Takeya, Sci. Technol. Adv. Mater. **10**, 024314 (2009).
- [160] J. Takeya, K. Tsukagoshi, Y. Aoyagi, T. Takenobu and Y. Iwasa, Japan J. Appl. Phys. **44**, L1393 (2005).

- [161] V. Podzorov, E. Menard, A. Borissov, V. Kiryukhin, J.A. Rodgers and M.E. Gershenson, Phys. Rev. Lett **93**, 086602 (2004).
- [162] T. Sekitani, Y. Takamatsu, S. Nakano, T. Sakurai and T. Someya, Appl. Phys. Lett. **88**, 253508 (2006).
- [163] I. Yagi, K. Tsukagoshi and Y. Aoyagi, Appl. Phys. Lett. **84**, 813 (2004).
- [164] N. Sai, M.L. Tiago, J.R. Chelikowsky and F.A. Reboredo, Phys. Rev. B **77**, 161306(R) (2008).
- [165] R.J. Needs, M.D. Towler, N.D. Drummond, and P. Lopez Ros, CASINO Version 2.0 User Manual University of Cambridge, Cambridge (2006).
- [166] N. Sato, K. Seki, and H.J. Inokuchi, J. Chem. Soc., Faraday Trans. 2, **77**, 1621 (1981).
- [167] Z. Zhi-lin, J. Xue-yin, X. Shao-hong, T. Nagatomo and O. Omoto, J. Phys. D: Appl. Phys. **31**, 32-35 (1998) and Z.Q. Li *et al.* Phys. Rev. Lett, **99**, 016403 (2007).
- [168] <https://aimsclub.fhi-berlin.mpg.de/>
- [169] J. Takeya, M. Yamagishi, Y. Tominari, R. Hirahara, Y. Nakazawa, T. Nishikawa, T. Kawase, T. Shimoda and S. Ogawa, Applied Physical Lett., **90**, 102120 (2007).
- [170] J.H. Shim, K.V. Raman, Y.J. Park, T.S. Santos, G.X. Miao, B. Satpati and J.S. Moodera, Phys. Rev. Lett **100**, 226603 (2008).
- [171] H. Ding, C. Reese, A.J. Mkinen, Z. Bao and Y. Gao, Appl. Phys. Lett. **96**, 222106 (2010).
- [172] J. Kirkpatrick, V. Marcon, J. Nelson, K. Kremer and D. Andrienko, Phys. Rev. Lett. **98**, 227402 (2007).
- [173] N. Marzari and D. Vanderbilt Phys. Rev. B, **56**, 12847 (1997).
- [174] N. Marzari, A.A. Mostofi, J.R. Yates, I. Souza, D. Vanderbilt, Rev. Mod. Phys. **84**, 1419 (2012).
- [175] N. Marzari, I. Souza, D. Vanderbilt, Psi-K Newsletter **57**, 129 (2003).

- [176] I. Souza, N. Marzari and D. Vanderbilt, *Phys. Rev. B* **65**, 035109 (2001).
- [177] E.I. Blount, *Formalisms of band theory in Solid State Physics*, vol 13, pp-305-373, New York: Academic Press (1962).
- [178] A.A. Mosfoti, J.R. Yates, Y.S. Lee, I. Souza, D. Vanderbilt and N. Marzari, *Comput. Phys. Commun.* **178**, 685 (2008).
- [179] O.D. Jurchescu, A. Meetsma, and T.M.T. Pastra, *Acta Crystallogr., Sec.B: Struct. Sci.* **62**, 330 (2006).
- [180] S. Bhattacharya, M.S. Ferreira and S. Sanvito, *J. Phys.: Condens. Matter* **23**, 316001 (2011).
- [181] S. Sanvito, *Chem. Soc. Rev.*, **40**, 3336-3355 (2011).
- [182] A. Girlando, L. Grisanti, M. Masino, I. Bilotti, A. Brillante, R.G. Della Valle and E. Venuti, *Phys. Rev. B*, **82**, 035208 (2010).
- [183] J. Veres, S. Ogier and G. Lloyd, *Chem. Mater.*, **16** (23), 4543-4555 (2004).
- [184] E.I. Blount, *Solid State Physics*, **13**, 305 (1962).
- [185] D. Vanderbilt and R.D. King-Smith, *Phys. Rev. B*, **48**, 4442 (1993), R.D. King-Smith and D. Vanderbilt, *Phys. Rev. B*, **47**, 1651 (1993) and R.D. King-Smith and D. Vanderbilt, *Phys. Rev. B*, **49**, 5828 (1994).
- [186] Z. Ning and H. Tian, *Chem. Commun.* 5483 (2009).
- [187] J.P. Hill, W. Jin, A. Kosaka, T. Fukushima, H. Ichihara, T. Shimomura, K. Ito, T. Hashizume, N. Ishii and T. Aida, *Science*, **304**, 5676 (2004); W.J. Blau and A.J. Fleming, *Science*, **4**, 1457-1458 (2004).
- [188] Z. Bao, A. Dodabalapur and A.J. Lovinger, *Appl. Phys. Lett.* **69**, 4108 (1996).
- [189] E. Moulin, F. Niess, M. Maaloum, E. Buhler, I. Nyrkova and N. Giuseppone, *Angew. Chem. Int. Ed.* **49** 6974 (2010).

- [190] V. Faramarzi, F. Niess, E. Moulin, M. Maaloum, J.F. Dayen, J.B. Beaufrand, S. Zanettini, B. Doudin and N. Giuseppone, *Nature Chemistry* **4**, 485 (2012).
- [191] R.A. Marcus, *J. Chem. Phys.* **24**, 966 (1956) and R. A. Marcus, *Rev. Mod. Phys.* **65**, 599 (1993).
- [192] G.R. Hutchison, M.A. Ratner and T.J. Marks, *J. Am. Chem. Soc.* **127**, 16866 (2005).
- [193] W.Q. Deng and W.A. Goddard III, *J. Phys. Chem. B.* **108**, 8614 (2004).
- [194] G.D. Mahan, *Many-Particle Physics*, Kluwer Academic/ Plenum Publishers.
- [195] (a) C. Lee, W. Yang, R.G. Parr, *Phys. Rev. B.* **37**, 785 (1988): (b) A.D. Becke, *J. Chem. Phys.* **98**, 5648 (1993)
- [196] W.P. Su, J.R. Schrieffer and A.J. Heeger, *Phys. Rev. Lett.* **42**, 1698 (1979) and *Phys. Rev. B* **22**, 2099 (1980).
- [197] T. Yanai, D. Tew and N. Handy, *Chem. Phys. Lett.* **393**, 51 (2004).
- [198] Y. Zhao and D.G. Truhlar, *Theor. Chem. Acc.* **120**, 215 (2008).
- [199] M.J. Frisch *et al.*, *Gaussian 09, Revision A.01*, Gaussian Inc. Wallingford CT (2009).
- [200] X. Li and M.J. Frisch, *J. Chem. Theory and Comput.* **2**, 835 (2006).
- [201] P. Giannozzi *et al.* *J. Phys.: Condens. Matter* **21**, 395502 (2009).
- [202] D. Vanderbilt, *Phys. Rev. B*, **41**, 7892 (1990).
- [203] B. Yang, S.K. Kim, H. Xu, Y.I. Park, H. Zhang, C. Gu, F. Shen, C. Wang, D. Liu, X. Liu, M. Hanif, S. Tang, W. Li, F. Li, J. Shen, J.W. Park, Y. Ma, *Chem. Phys. Chem* **9**, 2601 (2008).
- [204] B.C. Lin, C.P. Cheng and Z.P.M. Lao, *J. Phys. Chem. A* **107**, 5241 (2003).
- [205] M. Malagoli and J.L. Brédas, *Chem. Phys. Lett.* **327**, 13 (2000).

- [206] G. Meijer, G. Berden, W.L. Meerts, H. Hunziker, M.S. deVries, H.R. Wendt, *Chem. Phys.* **163**, 209 (1992).
- [207] B.C. Wang, H.R. Liao, J.C. Chang, L. Chen and J.T. Yeh, *J. Lumin.* **124**, 333 (2007).
- [208] Z. Shuai, L. Wang and C. Song, *Theory of Charge Transport in Carbon Electronic Materials*, (Springer) (2012)
- [209] J. Kirkpatrick and J. Nelson, *J. Chem. Phys.* **123**, 084703 (2005).
- [210] J.L. Brédas, D. Beljonne, V. Coropceanu and J. Cornil, *Chem. Rev.* **104**, 4971 (2004).
- [211] B.C. Lin, C.P. Cheng, Z.Q. You and C.P. Hsu, *J. Am. Chem. Soc.* **127**, 66 (2005).
- [212] X.K. Chen, L.Y. Zou, A.M. Ren and J.X. Fan, *Phys. Chem. Chem. Phys.* **13**, 19490 (2011).
- [213] E.F. Valeev, V. Coropceanu, D.A. da Silva Filho, S. Salman and J.L. Brédas, *J. Am. Chem. Soc.* **128**, 9882 (2006).
- [214] X. Yang, Q. Li and Z. Shuai, *Nanotechnology* **18**, 424029 (2007).
- [215] S. Kwon, K.R. Wee, J.W. Kim, C. Pac, and S.O. Kang, *J. Chem. Phys.* **136**, 204706 (2012).
- [216] V. Coropceanu, J. Cornil, D.A. da Silva Filho, Y. Olivier, R. Silbey and J.L. Brédas, *Chem. Rev.* **107**, 926 (2007).
- [217] M. Pope and C.E. Swenberg, *Electronic Processes in Organic Crystals and Polymers*, (Oxford University Press: New York) (1999).
- [218] A. Troisi and G. Orlandi, *Phys. Rev. Lett.* **96**, 086601 (2006).
- [219] A. Troisi, *Adv. Mat.* **19**, 2000 (2007).
- [220] A. Troisi, *Organic Electronics*, **12**, 12, 19881991 (2011).
- [221] T. Clark, J. Chandrasekhar, G.W. Spitznagel and P.v.R. Schleyer, *J. Comp. Chem.* **4**, 294-301 (1983) and M.J. Frisch, J.A. Pople and J.S. Binkley, *J. Chem. Phys.* **80**, 3265-69 (1984).

- [222] H. Elsinger *et al.*, Phys. Rev. Lett. **84**, 6098 (2000), Y. Shimizu *et al.*, Phys. Rev. Lett. **91**, 107001 (2003), Y. Kurosaki *et al.*, Phys. Rev. Lett. **95**, 177001 (2005), F. Kagawa *et al.*, Nature (London) **436**, 534 (2005).
- [223] S. Kim , J.K. Lee , S.O. Kang , J. Ko , J.H. Yum , S. Fantacci , F.De. Angelis , D.Di. Censo , Md. K. Nazeeruddin and M. Grätzel, J. Am. Chem. Soc. **128** (51), pp 16701-16707, (2006).
- [224] Z. Ning , Q. Zhang , W. Wu , H. Pei , B. Liu and H. Tian, J. Org. Chem. **73** (10), pp 3791-3797 (2008).
- [225] Dimitrakopoulos *et al.*, Adv. Mater. **14**, 99 (2002), Synthetic Metals **92**, 47 (1998) and Y. Yamashita, Sci. Technol. Adv. Mater. **10**, 024313 (2009).
- [226] Li *et al.*, Scientific Reports, **754**, 1 (2012).
- [227] Nature Materials, **8**, 691 (2009).
- [228] T.L. Francis, O. Mermer, G. Veeraraghavan and M. Wohlgenannt New J. Phys. **6**, 185 (2004).
- [229] T.D. Nguyen, Y.G. Sheng, J. Rybicki, G. Veeraraghavan and M. Wohlgenannt, J. Mater. Chem. **17** (19), 1995 (2007).
- [230] T.D. Nguyen, Y. Sheng, M. Wohlgenannt and T.D. Anthopoulos, Synth. Met. **157**(22-23), 930 (2007).
- [231] O. Mermer, G. Veeraraghavan, T.L. Francis, Y. Sheng, D.T. Nguyen, M. Wohlgenannt, A. Kohler, M.K. Al-Suti and M.S. Khan, Phys. Rev. B **72** (20), 205202 (2005).
- [232] M. Wohlgenannt, Phys. Status. Solidi RRL **6**, No. 6, 229-242 (2012) .
- [233] A.R.B.M. Yusoff, W.J. da Silva, J.P.M. Serbena, M.S. Meruvia, and I.A. Himmolgen, Appl. Phys. Lett. **94**, 253305 (2009).
- [234] H.C. Kandpal, I. Opahle, Y. Zhang, H.O. Jeschke and R. Valent, Physical Review Letters, **103**, 067004 (2009).

[235] K. Blum, *Density matrix theory and applications*, Springer 3rd edition (2012).

[236] F. Ortmann, F. Bechstedt, and K. Hannewald, *Phys. Rev. B* **79**, 235206 (2009).

Charge and spin transport through organic semiconductors

Sandip Bhattacharya

Over the past decade a great body of research has been devoted to the field of *organic spintronics*. This is primarily because of its potential to open new ways to cheap, low weight, mechanically flexible, chemically inert and bottom up fabricated spin-devices for high density data storage and logic applications. The main advantage of using organic semiconductors (OSCs) for spintronics applications is that the device structure can be conveniently designed based on the experiences from an industrially well established field, namely that of *organic electronics*. However, the intrinsic transport properties of OSCs are poorly understood from both an experimental and a theoretical perspective. The work presented in this thesis provides the first comprehensive and robust procedure to investigate in detail the charge and spin transport properties of such OSCs from first principles.

The technique involves representing all the essential interactions in OSCs with a tight-binding model including in particular the coupling of the charge carriers to phonons. Thereafter the *ab initio* Hamiltonian parameters are extracted from Density Functional Theory (DFT) and the maximally localized Wannier functions scheme. Furthermore, the Hamiltonian representing the organic material also incorporates carriers' spin relaxation mechanisms, i.e. hyperfine interactions and spin-orbit coupling. We evaluate the finite temperature properties of the system by evolving the classical fields in the Hamiltonian via Monte Carlo simulations. Thereafter the mobility is obtained from the Kubo formula and the spin diffusion length from a Landauer-Büttiker approach, implemented within the Monte Carlo scheme.

The results from the work in this thesis can be divided into three main parts. Firstly, we explore in detail the phase diagram of the model to understand the effect of the various parameters on the physical observables. This is particularly crucial in order to optimize the different interactions in the OSC. Furthermore, we also understand the charge and spin transport properties of the model from such a microscopic approach. Secondly, we present in detail a DFT characterization of rubrene molecular crystals, which has the highest charge carrier mobility among OSCs. We shall then demonstrate that the first principles estimates of its carrier mobilities are very close to those measured in single-crystal rubrene-based organic field effect transistors and the spin diffusion lengths are also similar to that estimated in experiments on rubrene-based spin valves.

Thirdly, we will discuss the use of a similar multiscale procedure to predict the *ab initio* charge and spin transport characteristics of triarylamine based organic nanowires. Such organic nanowires were recently synthesized from a light activated self-assembly process and were demonstrated to have almost metallic type transport characteristics. We obtain quite exceptional estimates for the hole mobilities in such nanowires thereby confirming the experiments. Also the spin transport properties of such nanowires that we obtain are quite exceptional. As such, we predict that triarylamine based self-assembled organic nanowires can be promising candidates for organic spintronics.